

Air Mouse: An Everyday Mouse for the Ease of Computing

P.S. Venkateswaran, Vivek Kaundal, Amit Kumar Mondal, Abhishek Sharma, Vindhya Devalla and Shival Dubey

Abstract There are several ways for human computer interaction in the modern era of electronics. In the present day, computers motion recognition is used very efficiently for playing games. The work done in this paper presents a simple and low-cost device for the movement of cursor on computer screen or to rotate the three-dimensional images. For the movement of cursor the data of accelerometer sensor (according to hand movement) is fed to the controller unit and after processing it is sent serially to the computer through RS 232 protocol. The developed device is used for all applications as accomplished with mouse. The proposed device senses the end user action with the help of accelerometer and push buttons. The air mouse is comfortable to wear, and does not considerably obstruct entering. It functions completely as serial mouse available in the market, and even has the feature of scrolling as the conventional mouse. This innovative approach improves the end user's experience with day-to-day task and playing games in computer.

Keywords Mouse · ATmega32 · Dual-axis accelerometer · ADC

1 Introduction

A mouse is a representative device specially in computing. The operation of which depends on recognition of gestures in two-dimensional space. Materially, a mouse is a device made up of optical sensor embedded with electronic components. It at times features other elements, such as “wheels”, which permit the user to execute various system-reliant processes, or additional controls or features can add extra dimensional input. The present technology in mouse needs it to rest on a hard surface and there will be variations in the sensitivity as and when the surface is changed and there is also a need for us to move back and forth between the mouse

P.S. Venkateswaran · Vivek Kaundal · A.K. Mondal (✉) ·
Abhishek Sharma · Vindhya Devalla · Shival Dubey
University of Petroleum and Energy Studies, Dehradun, India
e-mail: akmondal1603@gmail.com

and the screen during presentations [1, 2]. By resting our hands on a hard surface, it weakens the muscles and creates carpal tunnel syndrome [1, 3, 4]. But air mouse which can be worn as a glove and one can type and at the same time by moving one's hands, user can move the mouse pointer on the screen.

2 Materials and Method

2.1 Design and Outlook

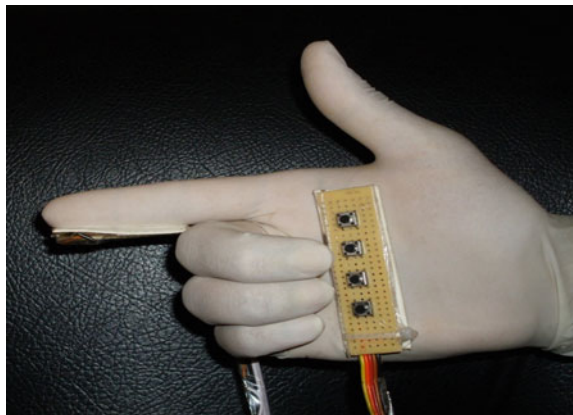
All the technologies which have been used so far needs the mouse to be placed on a hard surface and all these technologies uses optical or mechanical means for position tracking. Air mouse uses an accelerometer sensor which gives the acceleration of the hand in the XY plane in air and this motion is transformed to point the cursor on the screen. This transformation is done using a high-speed microcontroller with an inbuilt ADC and sending the serial data via a cable to the computer. There is a filtering circuit for removing noise and an amplifier circuit to increase the gain of the signal. The total functioning of the device is like a serial mouse to make it cost efficient but the special thing about it is that since it makes use of the accelerometer sensor it can be used in midair, as shown in Fig. 1.

2.2 Components and Fabrication

The air mouse device consists of the following components

- a. Accelerometer: The ADXL 203 is sized at $5 \times 5 \times 2 \text{ mm}^3$. The main features of it include the high rate of precision, low power consumption and dual-axis

Fig. 1 Air mouse



accelerometer that gives signal-conditioned output voltage. It measures acceleration with a full-scale range of ± 1.7 g. It is able to measure only two types of dynamic and static acceleration. Its bandwidth is less than 60 Hz and is been selected by the user by inbuilt capacitor and output pins.

- b. **Amplifier and Filter Circuit:** In order to remove the unwanted frequency noise at the input terminals of ADXL IC, a lowpass filter was used. Then a dual-operational amplifier LM358 is used. It comprises of two-operational amplifiers having features including high gain and better stability. They work on same power supply. The differential part amplifies the accelerometer output. On providing suitable gain into the accelerometer, output results into higher resolution with the ADC.
- c. **ATmega32 microcontroller:** The ATmega32 is an 8-bit microcontroller fabricated on the CMOS technology and its architecture is based on the advanced virtual RISC architecture. In a single clock cycle, with the help of executing instructions ATmega32 has the capability of providing the throughputs at the speed of 1 MIPS per MHz. This feature allows the system with optimized power consumption and high processing speed. It has a 10-bit ADC that converts the analog signal into digital using the successive approximation technique. PORT A is the ADC port in ATmega32. The controller used in this paper is used to convert the analog filtered signals to computer compatible format, i.e., 2's compliment format.
- d. **Max 232A (RS232 to TTL):** Max232A [5] it requires +5 V dc voltage and also external capacitors for the proper operation. It uses a voltage inverter with the rating of 10 V. According to RS-232 protocol the 0 V is taken in the range of +5 to +15 V and for the 1 V range varies from -5 to -15 V. Most of the micro-controllers do not have capability to generate this range of voltage. In order to connect a microcontroller SCI port to a true RS-232 device, for this it is necessary to convert the range of TTL voltage (0 and +5 V) into voltage range of -10 to +10 V.

3 Operation and Program Design Flow

3.1 Hardware Operation

The operation of the air mouse is focused on information gathering and processing. Output of the accelerometer passes through three stages to pass through lowpass filter to remove noise due to high frequency. The second stage is known as differential amplifier stage. Second stage is of differential stage amplifier, it amplifies the signal by a factor of two and increases the accelerometer output from 1.5 to 3.5 V for -1 to 1G to 0.5 to 4.5 V. Thus by introducing the suitable gain into the output given by accelerometer will improve the resolution of the inbuilt ADC. There is generation of negative and positive voltage which is used as the differential

input for both accelerometer and potentiometer output. Potentiometer helps to tune the accelerometer 0 G level to a voltage of the desired choice. By providing the output of the amplifier through a resistor ADC circuit is prevented from exposure of high current. Combination of diode and resistor generates the +5 V output. The output is taken from the junction of potential divider circuit formed by the combination of resistor and diode. It also prevents the following things:

- i. Generation of output voltage from amplifier not more than 5 V.
- ii. The threshold voltage of the diode (0.67 V in case of Si).

Besides these two accelerometer inputs, there are four push-buttons inputs in the form of enable/disable functionality, left click, right click, and mouse scrolling of the mouse to the microcontroller, the same has been shown in Fig. 2.

3.2 Program Operation Flow

Figure 3 is representing the flow diagram of the air mouse program. Initially user has to wait for the computer to toggle the RTS line. When it does, “MZ” signal is

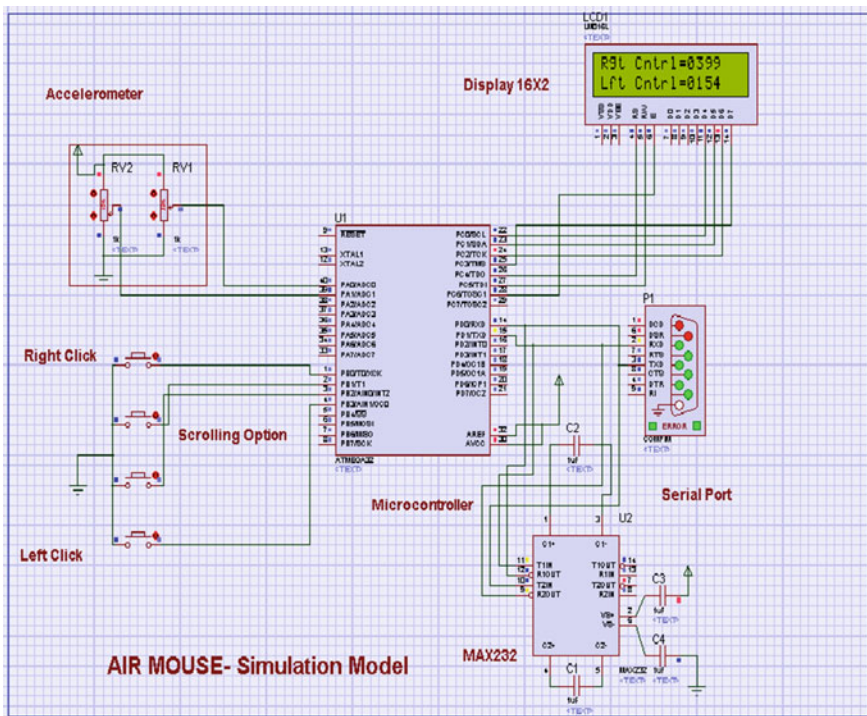


Fig. 2 Simulation model for air mouse

sent indicating that it is a Microsoft serial scroll mouse. The response for five queries is done, then deactivate query response is functionalized and finally the start mouse operation is performed.

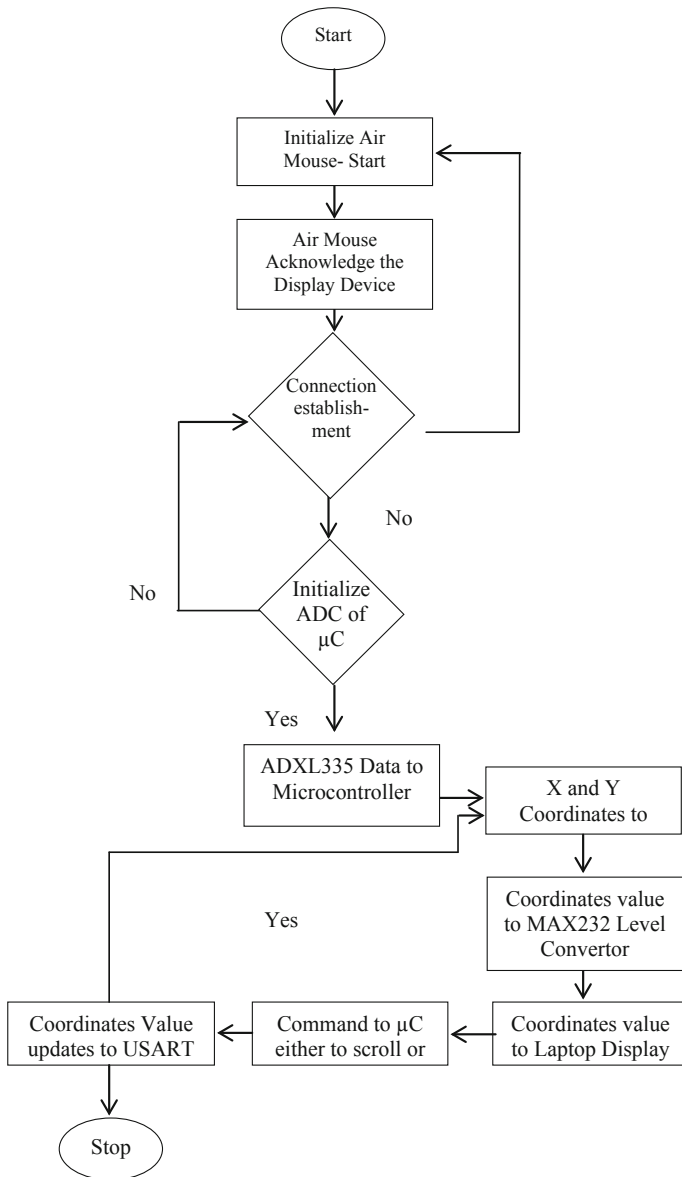


Fig. 3 Flowchart of the air mouse program operation

If the mouse is inactive, the program cycles through the button sampling until the mouse is active. After the sampling of button is made, mouse is empowered and acceleration axis checking is been done. If X has not been sampled, set the sample multiplexer to Y , sleep until X is prepared, and sample X . The multiplexer is fixed to Y before X is been sampled because the present sample being processed is continuously taken off of the current multiplexer value, which is X , if X has not been sampled. If X has been sampled, Y has to be checked to see whether it has been sampled or not. If it has not been, set the multiplexer to X , sleep until Y is prepared, and sample Y . If Y has been sampled, adjust the samples to the correct two's complement numbers, scale them, and create the serial packets. Send the serial packets, indicate that X needs to be sampled, and return to the beginning of the loop. The mouse is enabled and disabled by one of the sampled buttons.

```

Initialize ADC of  $\mu\text{C}$ 
Initialize USART of  $\mu\text{C}$ 
char data;
int main ( )
Calculate XYcor;
end for
Display to LCD
end for
Cmd to USART;
Locate XYcor to Screen;
end for
Updt_USART;
end for
Finding new XYcor;
Return to finding XYcor;
end for

```

Notations:

char: Character initialization of 8 bit
 XYcor: Locate coordinates of screen in two dimension
 Updt_USART: updating of USART value
 USART: Universal synchronous asynchronous Receiver Transmitter
 ADXL_Sensor: Accelerometer Sensor value in XY coordinates

3.3 Applications

- i. For ease of conducting seminars or official meetings in a large hall since it requires wearing of a simple glove which acts as the mouse. Also, many of the tasks where both the keyboard and mouse are required, makes the user frustrating and awkward to switch back and forth between them. The same can be easily solved by the proposed solution.
- ii. Air mouse prevents its users from occupational disorders like Carpal Tunnel Syndrome. This is caused by resting wrist on a hard surface as in the case of conventional mouse. No need to move back and forth between the projected slide and the system to open or close any related files. It is an innovative way to maintain proper ergonomics.

The tricky part of this algorithm is its timing and the conversion of the accelerometer output to the proper 2's complement number. There might be some issues pertaining to the accelerometer readings probably when the sensor is moved on the NW–SE plane. But for getting good readings the microprocessor can be put to sleep until the reading becomes ready.

4 Conclusion

The design is aimed at the utilization of movement of hand to yield a cursor velocity, and the desired results are easily achievable. The device will work well if the pitch and roll functions are taken into consideration properly. Rolling the device counter-clockwise or clockwise moves the mouse to the left or to the right. Pitching the device towards one or away moves the mouse down or up. The vertical motion of the mouse is reversed, like a joystick. This type of gesture is simple to acclimatize to than having the pitch non-inverted. The present model of the Air mouse is a hand glove type hence there might be problems of varying size of human hands. Moreover there is always a need of a cable attached to the computer. This can be avoided by devising the circuitry in a wireless environment. In extended forms of this project, one can use a gyro the cost of which is very low. So that gravity in the motion sensing can also be taken into account for achieving perfection in positioning of the device in the free space.

References

1. Seelye, A., et al., *Computer mouse movement patterns: A potential marker of mild cognitive impairment*. *Alzheimer's & Dementia: Diagnosis, Assessment & Disease Monitoring*, 2015. **1**(4): p. 472–480.
2. Onyebeke, L.C., et al., *Effects of forearm and palm supports on the upper extremity during computer mouse use*. *Applied Ergonomics*, 2014. **45**(3): p. 564–570.
3. Fogleman, M. and G. Brogmus, *Computer mouse use and cumulative trauma disorders of the upper extremities*. *Ergonomics*, 1995. **38**(12): p. 2465–2475.
4. Van Niekerk, S.M., S.M. Fourie, and Q.A. Louw, *Postural dynamism during computer mouse and keyboard use: A pilot study*. *Applied Ergonomics*, 2015. **50**: p. 170–176.
5. Devalla, V., et al., *Design and Development of Object Recognition and Sorting Robot for Material Handling in Packaging and Logistic Industries*. *International Journal of Science and Advanced Technology*, 2012. **2**(9).

An Improved Approach for Denoising MRI using Non Local Means Filter

Nikita Joshi

Amity School of Engg. & Tech.
Amity University Uttar Pradesh
Noida, India
nikitajoshi502@gmail.com

Sarika Jain

Amity Inst. of Inf. Tech.
Amity University Uttar Pradesh
Noida, India
ashusarika@gmail.com

Amit Agarwal

Univ. of Petroleum and Energy Studies
Dehradun, India
coer.info@gmail.com

Abstract—Various types of noise affect Magnetic Resonance Images and consequently interrupt in correct diagnosis. Thus, noise reduction is a major task while working with Magnetic Resonance (MR) Images. The process of denoising reduces the undesirable noise, but at the same time the denoising process needs to preserve the image features as well. Various techniques are available for noise removal from MR Images. Non local means filtering approach is a popular denoising technique for MR images. Modifications have been performed on the original Non Local Means algorithm to apply it on numerous applications. The aim of this paper is to denoise MRI by a novel approach, making use of a median and wiener filter in conjunction with the Non local means filtering technique.

Keywords—Non local means filtering; Wiener Filter; Median Filter; Magnetic resonance imaging

I. INTRODUCTION

Today's medical diagnosis and research is greatly supported by Magnetic Resonance Imaging (MRI). Accurate medical diagnosis depends upon the quality of the acquired image. These MR images get affected by noise during the image acquiring process, thus making filtering a necessary pre processing step for numerous medical diagnoses like segmentation, classification, 3D reconstruction and registration tasks. MRIs contain noises from various sources, including noise from stochastic variation, noise arising from eddy currents and numerous physiological processes, artefacts due to magnetic sensitivity between neighbouring tissues, rigid and non rigid body motion and other sources [1, 2]. The electrically conducting tissues in the patient's body produce thermal noise which is a major source of noise in MRI [3]. As a result, uncertainties are introduced while measuring different parameters, leading to inaccurate computer analysis. Therefore noise removal becomes a necessary task when handling images. All the signal frequencies in MR images get affected by noise. It can be considered that the noise existing in the image is complex Additive White Gaussian Noise (AWGN) which possesses a zero mean value [4], if the noise is independent of the signal. In case of MR images, the real and imaginary

parts of the spatial distribution of noise usually depends on signal and ensues a Rician distribution [5, 6], when the signal-to-noise ratio (SNR) of the noise signal intensities has a value less than 2. If the value of SNR is quite high, then it is seen that the Rician distribution follows a Gaussian distribution. The noise present in MR images can be removed by various techniques such as spatial and temporal filter, anisotropic diffusion filtering, non local means algorithm (NLM), bilateral and trilateral filters, wavelet transformation, curvelet and the contourlet transformation, linear minimum mean square error estimation, maximum likelihood approach, statistics/estimation of nonparametric neighbourhood and singularity function analysis [7].

II. RELATED WORK

Eng *et al.* [8] proposed a novel filter known as Noise Adaptive Soft-Switching Median (NASM) filter. It was a median filter based on the fuzzy-set theory integrated with switching. Impulse noise was removed while maintaining signal details and effectively handled noise density variations. Lin *et al.* [9] proposed a filter using the minimum mean square error of the wiener filter. This filter was applied in wavelet domain along with non local means filter. Chan *et al.* [10] combined median filtering technique and the non local means method, to obtain a stronger estimation of weights. Mohan *et al.* [3] proposed a unique technique for removing Rician noise from magnetic resonance images. It was based on wiener filter's Neutrosophic set. The experiments were carried out on a set of simulated images obtained from Brainweb database with addition of Rician noise. This method preserved image details. Salvadeo *et al.* [11] proposed a technique to filter noise in Computed Tomography images by making use of Non Local Means and Generalized Wiener Filter (GWF). GWF is a contextual version of Wiener Filter. This method delivers significant results without much increase in the computational cost. Vega *et al.* [12] presented a novel method for denoising of Diffusion Weighted Images which worked in conjunction with wiener filter and non local means filter. Huang *et al.* [13] proposed an enhanced non-local means method by using a novel weighted kernel for preprocessing, thereby preserving image features. Joshi *et*

al. [14] enumerated various optimization techniques developed for Non Local Means filtering approach, used particularly with MR images.

III. METHODOLOGY

The proposed approach in this paper removes noise from MR images and also preserves the edges and fine structures, without causing much blurring of the image. To accomplish this, denoising has been performed in spatial domain by using union of median filter and wiener filter with a NLM filter. In this algorithm, the noisy MR Image has been firstly pre-processed with median filter. After pre-processing, the image is filtered using wiener filter in spatial domain. This filtered image is further denoised using NLM filter. Figure 1 illustrates the simplified block diagram of this proposed approach.

A. Wiener Filter

Wiener filtering is a general approach for reconstructing a noisy signal. Wiener2 function makes use of adaptive Wiener method and utilizes the statistical data which has been approximated from the local neighborhood of every pixel in the image. The wiener2 function adaptively employs Wiener filter on the noisy MR image and gets adjusted to the variance of the local image. Wiener2 accomplishes little smoothing where the value of variance is high and vice versa. This approach generally yields improved results as compared to linear filtering. This adaptive filter is better as compared to linear filter as it preserves edges and other high frequency components of the image. While using wiener2 function it is considered that the signal has been corrupted by white Gaussian noise. This white Gaussian noise is signal independent and possesses zero mean.

B. Median Filter

Although the median filter shares some similarity with the mean filter in reducing noise in an image, it proves to be better than the mean filter in preserving useful image details. Each pixel in the noisy image is replaced with the median value of its nearby neighbouring pixels. The median of this block of pixels is computed by first arranging all the surrounding neighbourhood pixel values into a numerical order and then replacing the desired pixel with the value of the centre pixel.

C. Non Local Means

Buades *et al.* [15] suggested a powerful noise removal approach known as Non Local Means filter. It was constituted on the basic theory of averaging all the non local pixels in the image. A specific pixel's gray level is compared with the geometrical composition in its entire surroundings.

According to Buades *et al.* [15], when a distinct image i (consisting of some noise) is taken into consideration such that

$$i = \{i(x) | x \in I\}$$

the approximate non-local means value $NL(i(x))$, for a pixel x , is calculated as

$$NL(i(x)) = \sum_{y \in I} w(x,y) i(y)$$

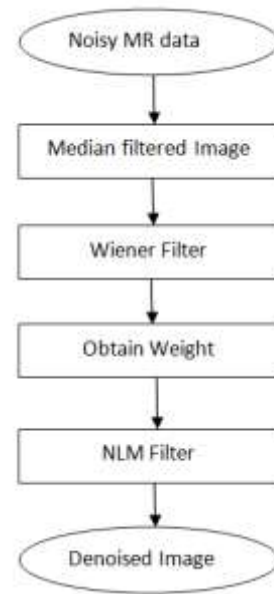


Fig. 1. Block diagram of the proposed approach

where the set of weights $\{w(x,y)\}_y$ is dependent upon the amount of similarity that exists between the pixels x and y and fulfill the given condition

$$0 \leq w(x,y) \leq 1 \text{ and } \sum_y w(x,y) = 1$$

$NL(i(x))$ denote the weighted average of the image's pixels. The similarity that exists between the two pixels x and y is determined by intensity gray level vectors $i(N_x)$ and $i(N_y)$, where N_k correspond to the pixel neighborhood having a square configuration and centered at a pixel k and having a fixed size. The Euclidean distance d (a decaying function), which is also weighted in nature, is used for measuring the similarity between the pixels and is given by

$$d = \|i(N_x) - i(N_y)\|_{2,p}^2$$

where $p > 0$ depicts the standard deviation of the Gaussian kernel. If the gray level neighborhood of a pixel are similar as that of $i(N_x)$, then it possess larger weights in computing the average as compared to other pixels in the image. The weights are determined as

$$w(x,y) = \frac{x}{Z(x)} e^{-\left(\frac{\|i(N_x) - i(N_y)\|_{2,p}^2}{h^2}\right)}$$

where $Z(x)$ is the normalizing constant

$$Z(x) = \sum_y e^{-\left(\frac{\|i(N_x) - i(N_y)\|_{2,p}^2}{h^2}\right)}$$

and parameter h represents the degree of filtering and it controls the decay of the exponential function. Norm

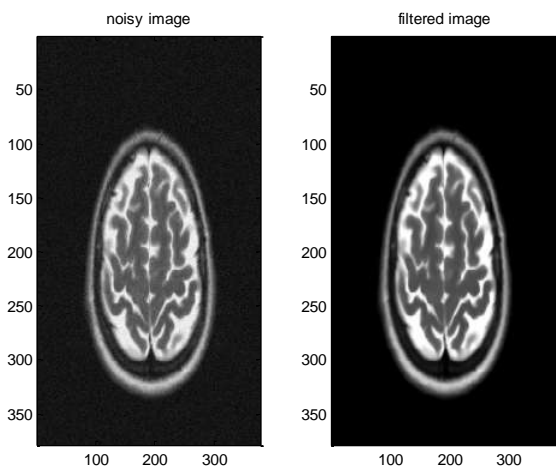
function is denoted by the symbol $\|\cdot\|$. In 3-D, a voxel is a volumetric pixel. In a 3-D object, the voxel represents the smallest distinct element and is used to analyze data from various medical imaging machines. Associating a particular voxel to all other rest of the voxels in the image will greatly increase the computational time. In order to avoid this, the number of voxels to be considered for computing the weighted average are restricted only to a “search volume” V_i , centered at the current voxel i_x , instead of the entire image. In [16], Buades *et al.* proved that the Non Local Means filter gave remarkable output while using various set of 2-D images.

IV. EXPERIMENTAL RESULTS

The experiment has been performed using various simulated MR images of brain by addition of Gaussian noise with different values of sigma such as 6, 9, 13, 20, 25 and results compared with the original NLM technique. It was observed that for various values of sigma, the peak signal to noise ratio (PSNR) got increased where as the Mean Square Error (MSE) was decreased compared to the original NLM. The following tables and figures show the various results for different values of sigma.

Table 1
SIGMA =6

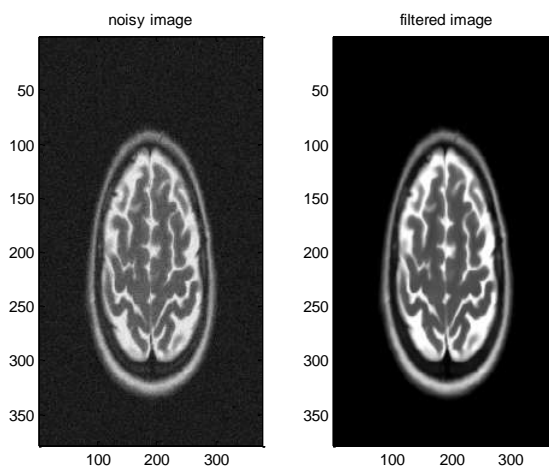
Technique	PSNR	MSE
Wiener enhanced NLM	41.01	5.18
Original NLM	40.13	6.35



SIGMA =6
Figure 1

TABLE 2
SIGMA =9

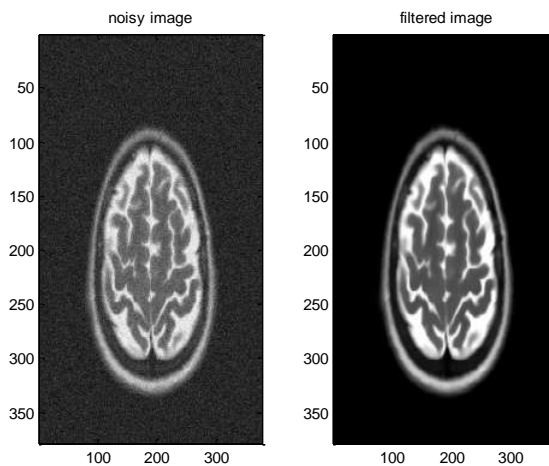
Technique	PSNR	MSE
Wiener enhanced NLM	40.31	6.091
Original NLM	39.22	7.82



SIGMA =9
Figure 2

TABLE 3
SIGMA =13

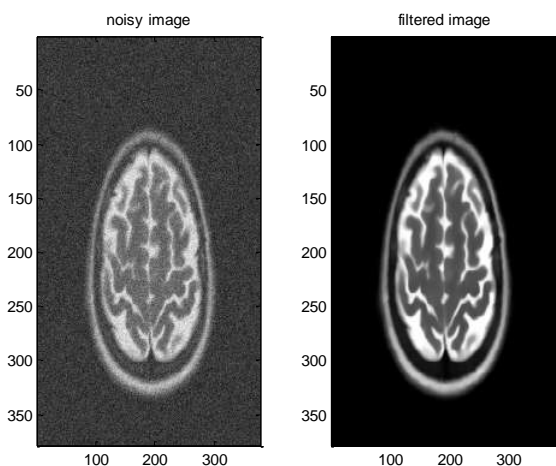
Technique	PSNR	MSE
Wiener enhanced NLM	39.30	7.69
Original NLM	36.96	13.19



SIGMA =13
Figure 3

TABLE 4
SIGMA =20

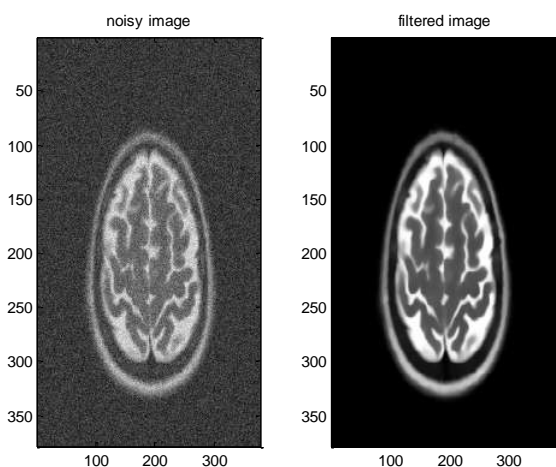
Technique	PSNR	MSE
Wiener enhanced NLM	37.644	11.27
Original NLM	34.06	25.72



SIGMA =20
Figure 4

TABLE 5
SIGMA =25

Technique	PSNR	MSE
Wiener enhanced NLM	36.58	14.37
Original NLM	32.43	37.38



SIGMA =25
Figure 5

V. CONCLUSIONS

In this paper a novel technique has been discussed for denoising MRI using the median filter and wiener filter in combination MRI with the non local means filter. Performance of this approach has been assessed qualitatively and quantitatively with PSNR and MSE measures, on various simulated MR images of brain. Better results are obtained as compared to NLM. However, computation time is increased.

REFERENCES

- [1]. T. W. Redpath, "Commentary signal-to-noise ratio in MRI", *Br. J. Radiol.* 71, pp. 704–707, 1998.
- [2]. H. Zhu, Y. Li, J. G. Ibrahim, X. Shi, H. An, Y. Chen, W. Gao, W. Lin, D. B. Rowe, B. S. Peterson, "Regression models for identifying noise sources in magnetic resonance imaging", *J. Am. Stat. Assoc.* 104, pp. 623–637, 2009.
- [3]. J. Mohan, V. Krishnaveni, Y. Guo, "MRI denoising based on neutrosophic wiener filtering", In *IEEE International Conference on Imaging Systems and Techniques*, pp. 327-331, 2012.
- [4]. N. W. Daessle, S. Prima, P. Coupe, S. P. Morrissey, C. Barillot, "Rician noise removal by Non-Local Means filtering for low signal-to-noise ratio MRI: applications to DT-MRI", in *11th International Conference on Medical Image Computing and Computer-Assisted Intervention*, pp. 171–179, 2008.
- [5]. H. Gudbjartsson, S. Patz, "The rician distribution of noisy mri data", *Magnetic Resonance in Medicine*, 34(6), pp. 910–914, 1995.
- [6]. A. Macovski, "Noise in MRI", *Magnetic Resonance in Medicine*, 36, pp. 494–497, 1996.
- [7]. J. Mohan, V. Krishnaveni, Y. Guo, "A survey on the magnetic resonance image denoising methods", *Biomed. Signal Processing and Control*, 9(1), pp. 56-69, 2014.
- [8]. H. L. Eng, K. K. Ma, "Noise Adaptive Soft-Switching Median Filter", *IEEE Trans. on Image Processing*, 10(2), pp. 242-251, Feb. 2001.
- [9]. L. Lin, K. Lingfu, "Image Denoising Based on Non-local means with Wiener Filtering in Wavelet Domain", in *Fifth International Conference on Intelligent Information Hiding and Multimedia Signal Processing*, pp. 471-474, 2009.
- [10]. C. Chan, R. Fulton, D. D. Feng, S. Mielke, "Median Non-local Means Filtering for Low SNR Image Denoising: Application to PET with Anatomical Knowledge", in *IEEE Nuclear Science Symposium and Medical Imaging Conference*, pp. 3613 - 3618, 2010.
- [11]. D. H. P. Salvadeo, N. D. A. Mascarenhas, A. L. M. Levada, "Contextual Filtering of CT Images Using Markovian Wiener Filters With a Non Local Means Approach for Statistical Estimation", in *25th SIBGRAPI Conference on Graphics, Patterns and Images*, pp. 16-23, 2012.
- [12]. A. T. Vega, V. Brion, G. V. Sanchez-Ferrero, Santiago Aja-Fernandez, "Merging squared-magnitude approaches to DWI denoising: An adaptive Wiener filter tuned to the anatomical contents of the image", In *35th Annual International Conference of the IEEE EMBS*, 2013.
- [13]. L. Huang, "Improved Non-Local Means Algorithm for Image Denoising", *J. of Computer and Communications*, 3, pp. 23-29, 2015.
- [14]. N. Joshi, S. Jain, " Optimization of Non local means filtering technique for denoising Magnetic Resonance Images: A review", In *Proceedings of Fifth International Conference on Soft Computing for Problem Solving, Advances in Intelligent Systems and Computing*, Vol. 436, pp 1-15, 2015.
- [15]. A. Buades, B. Coll, J.M. Morel, "A non local algorithm for image denoising", In *IEEE Computer Society Conference on Computer Vision and Pattern Recognition*, San Diego, pp. 60-65, 2005.
- [16]. A. Buades, B. Coll, J. M. Morel, "A review of image denoising algorithms, with a new one", *Multiscale Model. & Simul.* 4, pp.490-530, 2005.

Analysis of Beaconing performance in IEEE 802.11p on Vehicular Ad-hoc Environment

Ravi Tomar
School of Computer Science and Engineering
University of Petroleum and Energy Studies Dehradun,
India
rtomar@ddn.upes.ac.in

¹Manish Prateek, ²Hanumat G. Sastry
School of Computer Science and Engineering
University of Petroleum and Energy Studies Dehradun, India
¹mprateek@ddn.upes.ac.in ²hsastry@ddn.upes.ac.in

Abstract— VANET is special kind of Mobile Ad-hoc Network(MANET), rapid change in mobile nodes(car/vehicles) in case of VANET makes it different from MANET while sharing all other features of MANET. VANET has many advantages including minimising traffic, reducing car accidents, co-operative awareness, and environmental safety by monitoring CO2 emission. All these applications require proper information dissemination among nodes. This is achieved through Vehicle to Vehicle (V2V), Vehicle to Infrastructure (V2I) or a hybrid approach. For this communication, U.S. FCC allotted Dedicated Short-Range Communication (DSRC) spectrum of 75MHz in the frequency band of 5GHz(5.85 GHz to 5.925 GHz) [1]. This 75MHz spectrum is divided into seven 10 MHz-wide channels, One channel is the control channel (CCH) and the remaining six channels are the service channels (SCHs). Short messages are exchanged among the nodes to create cooperative awareness. These short messages are referred as Beacons, and the process is called as beaconing. Beaconing is always carried on CCH. This paper provides analysis of the beaconing performance of IEEE 802.11p when only the control channel is used for beaconing. Simulation experiments are conducted using OMNET++ and VEINS framework. SUMO is used to create the platoon of vehicles being deployed on the model and beaconing performance is evaluated using different intervals.

Index Terms— VANET, SUMO, OMNeT++, VEINS, ITS, Beaconing, IEEE 802.11p, IEEE1609.4.

I. INTRODUCTION

Vehicular ad hoc networking (VANET) is the recent trend in research and industry, the application of VANET is evident in many domains like safety, infotainment, traffic management, cruise control, advertisements and online gaming. The basic need for all such applications is communication between the vehicle nodes. VANET is a specialized class of MANET where high mobility of nodes is a crucial parameter to consider and energy has negligible limitations, as vehicles are capable of generating energy on the go. For this special class of mobile nodes, the 75 MHz (5.85 to 5.925 GHz) of Dedicated Short-Range Communication (DSRC) spectrum is allotted by U.S. Federal Communication Commission [1]. Seven 10 MHz-wide channels are formed from this 75MHz channel. One channel is

the control channel (CCH) and the remaining six channels are the service channels (SCHs). The IEEE has defined amendment in IEEE 802.11p for Vehicular Ad-hoc Networks also called as Wireless Access for Vehicular Environment (WAVE). WAVE defines the specifications following which any wireless devices can interoperate in the allotted frequency. These specifications describe how multiple wireless devices using the same IEEE 802.11p devices can communicate directly [2]. To enable proper communication and create a cooperative awareness among different nodes small periodic messages are broadcasted. These messages are known as the beacon and the process is referred as beaconing. These beacons contain kinematics of vehicles such as position, acceleration, velocity, direction etc. and are of approximately 400 bytes including security fields [3]. To ensure the fast dissemination of this information beaconing is always done on CCH. However, there are always other non-critical message packets to be delivered which are usually transmitted on SCH. The IEEE 802.11p also specifies Medium Access Control (MAC) protocol for single channel operations [4]. Furthermore, IEEE has also specified IEEE 1609.4 standard which enables multi-channel operation over IEEE 802.11p using Enhanced Distributed Channel Access (EDCA). This implementation impacts the beaconing performance because it uses time division between CCH and SCH. This research studies the beaconing performance on variable nodes at a variable frequency of beacons under continuous access mode.

II. WAVE SYSTEM ARCHITECTURE

For use of wireless communication in Intelligent Transportation System(ITS), IEEE came up with amendments in IEEE 802.11 protocol as IEEE 802.11p which is also known as Wireless Access for Vehicular Environment(WAVE). However, being an amendment in existing architecture it seems to be an entirely new architecture bearing characteristics of IEEE 802.11a, IEEE 802.11e and IEEE 802.11q. The amendments can be classified into two parts PHY and MAC.

A. PHY Amendment in IEEE 802.11

There are very few changes at PHY in 802.11p. The communication between Vehicle to Vehicle is established using Dedicated Short-Range Communication (DSRC) spectrum in the frequency band of 5GHz (5.85 to 5.925 GHz) [1]. The entire spectrum of 75MHz is divided into seven intervals. Each channel has a bandwidth of 10MHz. One channel is the control channel (CCH) which serves critical messages, management frames, WAVE service advertisements and the other six channels are the service channels (SCHs) which are solely for the non-critical applications. SCH (174,176) and SCH (180, 182) may be used as single 20 MHz channel respectively if required.

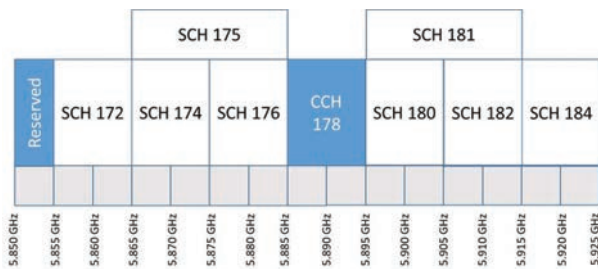


Figure 1: Channel Distribution of WAVE system

B. MAC Amendment in IEEE 802.11

For very basic understanding Medium Access Control (MAC) is a sub layer between Physical and Data Link layer in the OSI reference model. The main role of MAC layer in WAVE is to enable different nodes to communicate with each other wirelessly, faster and more efficient. Thus, we can conclude that this is the main amendment in WAVE vs 802.11 protocol. In 802.11 wireless application, one has to get the SSID of the access point to be in the same network followed by different steps of authentication. In contrast with the Service Set identification (SSID) used in wireless Basic Service Set (BSS), there is Wave Basic Service Set (WBSS) used in WAVE architecture. This WBSS also called as Wave mode is a simple

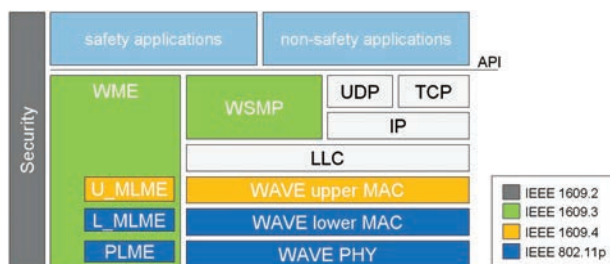


Figure 2: DSRC standards and communication stack copied from [1]

method to create instantaneous communication between two vehicles, which usually have very less time to establish communication. This improves the efficiency of the network. Furthermore, IEEE has also specified IEEE 1609.4 standard for

MAC layer which enables multi-channel operation over IEEE 802.11p which uses Carrier Sense Multiple Access Protocol with Collision Avoidance (CSMA/CA) [5]. This implements that if a node is willing to send a message it will first listen to Arbitration Inter Frame Spacing (AIFS) period. If the channel is busy it chose a random Back-off time from $[0-CW]$ and transfer only when back off timer is elapsed or sends directly if the channel is idle. QoS is also provided in IEEE 802.11p using Enhanced Distributed Channel Access(EDCA).

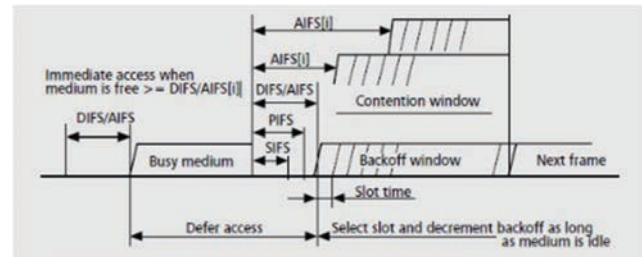


Figure 3: EDCA Inter Frame Spacing Relations, copied from [5]

EDCA works by classifying the beacons based on four access category(AC) namely Video Traffic (VI), Voice Traffic (VO), Best effort Traffic (BE) and Background Traffic (BK). These four AC differs by using different CW_{min} , CW_{max} and AIFSN.

III. BEACONING

To create cooperative awareness among the highly mobile vehicle nodes small periodic messages are broadcasted. These messages are known as a beacon and the process is referred as beaconing. These beacons contain kinematics of vehicles such as position, acceleration, velocity, direction etc. and are of approximately from 20 bytes [6] to 400 bytes including security fields [3]. To ensure the fast dissemination of this information beaconing is always done on CCH. The Beacons can be propagated in either one-hop or multi-hop. In one-hop, the message is only propagated once and the receiving node does not forward it, while in multi-hop the receiving node rebroadcast the message to its neighbours and this process goes on till any of the termination conditions reaches. In a multi hop, the information is obviously disseminated at the larger area but it introduces the famous broadcast storm problem resulting in packet collision and hidden terminal problem. Most of the research are done in controlling the multi hop broadcasting based on geography, counter based, delay based methods.

IV. SIMULATION

Simulation is needed where physical implementation is not feasible to test some rough concepts, among many road traffic and safety is one of the major problem concern of this modern world. Critical traffic problems such as accidents and traffic congestion require the development of new transportation systems [7]. The need for some mechanism comes where one

can model the real traffic in simulation and then dive in to propose solutions to the problems like traffic congestion, alternate route finding, minimizing red light stoppage, Co2 emission by controlling the flow of vehicles and much more.

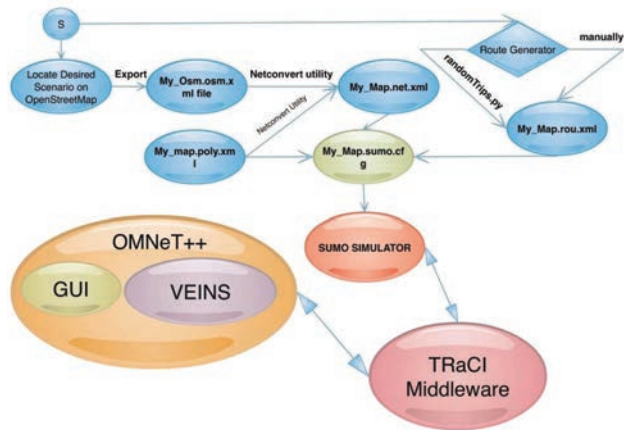


Figure 4 : Process flow for entire simulation

Post modelling it is needed to make those simulated vehicles intelligent so to make decisions and establish communication among each other for coming to some decision. VANET has a major challenge of Vehicles come and lose contact in a matter of seconds as speed is measured in miles per hour [8]. Here come network simulators in the picture which considers these vehicles as nodes and enables them to communicate with each other for real time decision making and behaving. During simulation data is processed and an overall decision is being taken for platoons of vehicles through which they behave. To start with modelling, we need to have some geographic location such as a city or some specific area, which will be our area where we want to do some simulation. For this purpose we will be taking maps from OpenStreetMap [9] [10], these maps will be then fed into SUMO [11] for modelling and then VEINS [12] framework will be used to make a realistic Vehicular Simulation using mobility from SUMO and Network from OMNeT++ [13]. Any VANET application, which needs simulation, will obviously have to pass through all above-mentioned phases. However, there are different tools and techniques available to attain the goal each having its own merit and demerits. We selected the most used and reliable method. The flow of the entire process is shown in Figure 4 and simulation screenshot is shown in Figure 5.

A. Simulation Scenario

The Scenario for simulation is generated in SUMO [10]. This work studies the beaconing performance on variable nodes at a variable frequency of beacons under continuous access mode. The model consists of a single lane of vehicles running at an interval of 3 seconds with parameters defined in Table 1. The simulation is carried out for 200s during which total of 67 vehicles enters the simulation. As this work focuses on

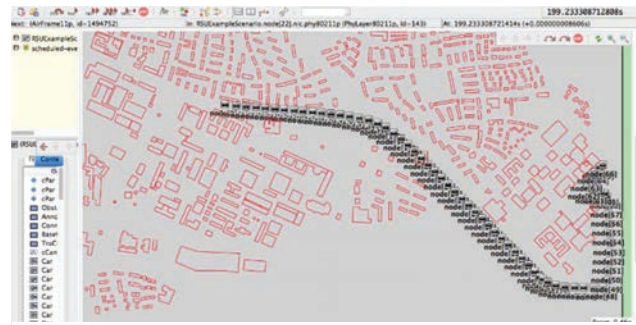


Figure 5 : Screenshot of running Simulation

beaconing so no other type of messages is taken into consideration hence the vehicles are running under the normal condition without any event of accident or emergency.

TABLE 1: SUMO SIMULATION PARAMETERS

Parameter	Value
Acceleration	2.6 m/s ²
Deceleration	4.5m/s ²
Sigma	0.5
Length	2.5m
MiniGap	2.5m
MaxSpeed	14m/s or 50kmph

B. Simulation Parameters

The Simulation is carried out in OMNET++ and VEINS framework using the parameters given below in Table 2. The *SimpleObstacleShadowing* obstacle model used to depict real world conditions.

TABLE 2 : OMNET++ SIMULATION PARAMETERS

Parameter	Value
txPower	20mW
bitrate	6Mbps
sensitivity	-89dBm
thermalNoise	-110dBm
usePropagationDelay	True
dataOnSch	false

C. Beaconing Frequency

The three simulations are carried out by taking variable beaconing frequency of 1Hz, 2Hz, .5Hz respectively. Each vehicle node which is generated at an interval of 3s through SUMO enters simulation and starts sending a beacon message to other nodes. A number of beacons generated become a cross product of all nodes in the simulation gradually when the number of vehicles grows. The results are obtained by setting

beacon generation rate of 1 beacon per sec, 2 beacons per sec and 1 beacon per 2 seconds.

D. Simulation Results

As the simulation executed for 200 seconds, 67 vehicles participated and node 0 started to send the beacons as soon as it entered the simulation. Figure 6 shows a number of beacons

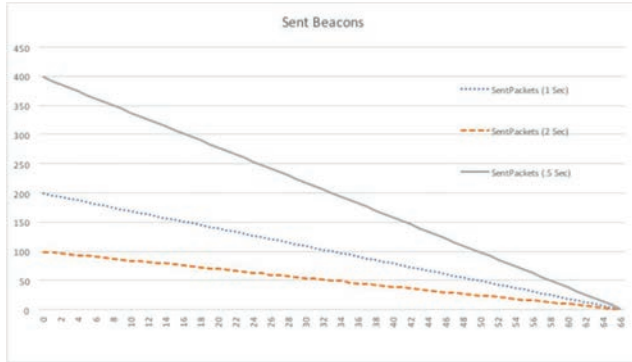


Figure 6 : Sent Beacons

generated by different nodes for different frequency of beaconing. We can observe that Node 0 has generated the maximum beacons as it stayed for longest time in all the

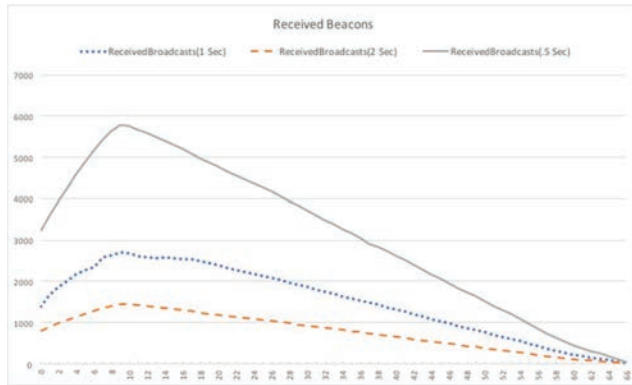


Figure 7 : Received Beacons

simulated scenarios while node at the right side has generated less number of beacon. This happened because beacon generation is the function of time and no other factor is responsible to alter the generation of beacons. If we look at Figure 7, which displays the number of received beacon messages at respective nodes. As we can see there are no straight lines we, observe a curve in the graph at Node 9, this curve is the result of maximum messages received at this node in all three simulated cases, this happened due to the reason of being node 9 in the vicinity of all the vehicles during the simulation. As we have used *SimpleObstacleShadowing* model to depict the real world scenario, it is also clear from the simulation model in Figure 5 that when vehicles are in direct line of sight there is no obstacle in between and they can transmit to their full range. Also, node 9 receives the messages from node ahead it and nodes

following it. This increased the reception of messages and hence raised the total channel busy time for Node 9, as shown in Figure 8. As Node 9 is receiving more messages so more back off time is required as compared to all other nodes, however, backoff time is dependent on CW values but in case of beaconing, the CW time is not doubled [3] as it is doubled in case of SCH messages. Therefore, there is no significant difference in backoff time of node 9 as shown in Figure 9. The last observation in

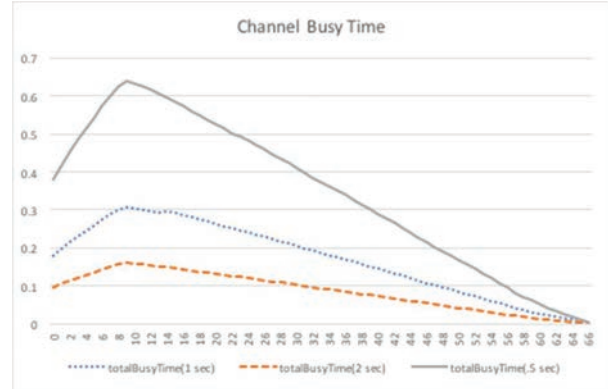


Figure 8 : Channel Busy Time

Figure 10 shows the number of time an individual node gets into the Backoff time, this is again dependent on the channel availability. Backoff is the event which occurs when the node wants to transmit the message but the channel is sensed as busy. This makes a message to wait for a specific time and that time is called as backoff time, while the number of time backoff occurred is the count of how many time an individual node has suffered backoff.

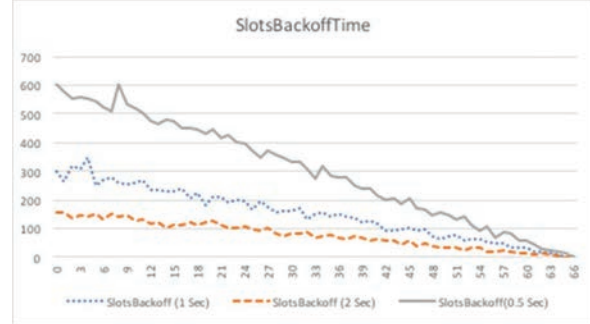


Figure 9 :Slots Backoff Time

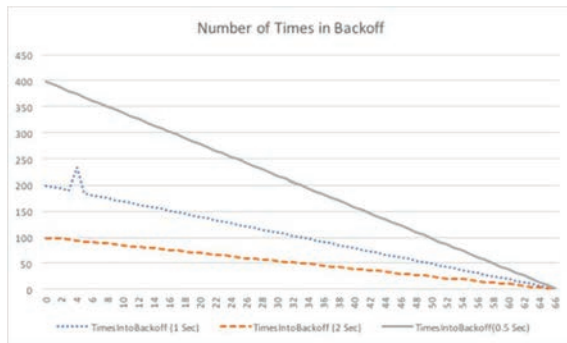


Figure 10 : Time in Backoff

V. Conclusion and Future Work

In this work, we have simulated the beaconing of messages at different intervals and have understood the behaviour of IEEE 1609.4 MAC layer, this work has observed only the CCH channel because beacons use Control Channel for transmission. We have used the flooding technique to make transmission to a maximum node within the network. Each node generates message as per the frequency allotted. We have also observed that there is a node X which falls at a specific location where message reception is more as compared to other nodes. Future work may be considered to reduce the number of Backoff per node and minimize the channel busy time. Impact of messages other than beacons on the channel and overall performance is also the area to look in future.

VI. References

- [1] L. D. D. Jiang, "Towards an International Standard for Wireless Access in Vehicular Environments," in *Vehicular Technology Conference, VTC*, 2008.
- [2] C. Y. H. C. Huang, "An Effective Channel Utilization Scheme for IEEE 1609.4 Protocol," in *Ubiquitous Information Technologies & Applications*, 2009.
- [3] A. v. d. V. G. K. M. van Eenennaam, "Impact of IEEE 1609.4 channel switching on the IEEE 802.11p beaconing performance," in *Wireless Days (WD)*, 2012 IFIP, Dublin, Ireland, 2012.
- [4] "IEEE Standard for Information technology," *IEEE Std 802.11p-2010 (Amendment to IEEE Std 802.11-2007 as amended by IEEE Std 802.11k-2008, IEEE Std 802.11r-2008, IEEE Std 802.11y-2008, IEEE Std 802.11n-2009, and IEEE Std 802.11w-2009)*, pp. 1-51, 15 July 2010.
- [5] L. Hendriks, "Effects of Transmission Queue Size, Buffer and Scheduling Mechanisms on the IEEE 802.11p Beaconing Performance," in *15th Twente Student Conference on IT*, Enschede, 2011.
- [6] R. F. M. M. Dario Rossi, "VANETs: Why Use Beaconing at All?," in *Communications, 2008. ICC '08.*, Beijing, 2008.
- [7] V. S. M. Motani, "Cross layer design: a survey and road ahead," *IEEE Communication Magazine*, vol. 43, no. 12, pp. 112-119, 2005.
- [8] M. P. G. S. R. Tomar, "Vehicular Ad Hoc Network(VANET)- An Introduction," *International Journal of control theory and application*, vol. 9, no. 18, pp. 8883-8888, 2016.
- [9] "http://en.wikipedia.org/wiki/OpenStreetMap," Wikipedia. [Online]. [Accessed 04 July 2017].
- [10] "DLR and contributors, SUMO Homepage," [Online]. Available: http://www.dlr.de/ts/desktopdefault.aspx/tabid-9883/16931_read-41000/. [Accessed 05 July 2017].
- [11] [Online]. Available: <http://sumo.dlr.de/wiki/Networks/Import/OpenStreetMap>. [Accessed 04 July 2017].
- [12] R. G. a. F. D. Christoph Sommer, "Bidirectionally Coupled Network and Road Traffic Simulation for Improved IVC Analysis," *IEEE Transactions on Mobile Computing*, vol. 10, no. 1, pp. 3-15, January 2011.
- [13] András Varga and team, "OMNeT Homepage," [Online]. Available: <https://omnetpp.org/>. [Accessed 05 July 2017].

Analysis of Beaconing performance in IEEE 802.11p on Vehicular Ad-hoc Environment

Ravi Tomar
School of Computer Science and Engineering
University of Petroleum and Energy Studies Dehradun,
India
rtomar@ddn.upes.ac.in

¹Manish Prateek, ²Hanumat G. Sastry
School of Computer Science and Engineering
University of Petroleum and Energy Studies Dehradun, India
¹mprateek@ddn.upes.ac.in ²hsastry@ddn.upes.ac.in

Abstract— VANET is special kind of Mobile Ad-hoc Network(MANET), rapid change in mobile nodes(car/vehicles) in case of VANET makes it different from MANET while sharing all other features of MANET. VANET has many advantages including minimising traffic, reducing car accidents, co-operative awareness, and environmental safety by monitoring CO2 emission. All these applications require proper information dissemination among nodes. This is achieved through Vehicle to Vehicle (V2V), Vehicle to Infrastructure (V2I) or a hybrid approach. For this communication, U.S. FCC allotted Dedicated Short-Range Communication (DSRC) spectrum of 75MHz in the frequency band of 5GHz(5.85 GHz to 5.925 GHz) [1]. This 75MHz spectrum is divided into seven 10 MHz-wide channels, One channel is the control channel (CCH) and the remaining six channels are the service channels (SCHs). Short messages are exchanged among the nodes to create cooperative awareness. These short messages are referred as Beacons, and the process is called as beaconing. Beaconing is always carried on CCH. This paper provides analysis of the beaconing performance of IEEE 802.11p when only the control channel is used for beaconing. Simulation experiments are conducted using OMNET++ and VEINS framework. SUMO is used to create the platoon of vehicles being deployed on the model and beaconing performance is evaluated using different intervals.

Index Terms— VANET, SUMO, OMNeT++, VEINS, ITS, Beaconing, IEEE 802.11p, IEEE1609.4.

I. INTRODUCTION

Vehicular ad hoc networking (VANET) is the recent trend in research and industry, the application of VANET is evident in many domains like safety, infotainment, traffic management, cruise control, advertisements and online gaming. The basic need for all such applications is communication between the vehicle nodes. VANET is a specialized class of MANET where high mobility of nodes is a crucial parameter to consider and energy has negligible limitations, as vehicles are capable of generating energy on the go. For this special class of mobile nodes, the 75 MHz (5.85 to 5.925 GHz) of Dedicated Short-Range Communication (DSRC) spectrum is allotted by U.S. Federal Communication Commission [1]. Seven 10 MHz-wide channels are formed from this 75MHz channel. One channel is

the control channel (CCH) and the remaining six channels are the service channels (SCHs). The IEEE has defined amendment in IEEE 802.11p for Vehicular Ad-hoc Networks also called as Wireless Access for Vehicular Environment (WAVE). WAVE defines the specifications following which any wireless devices can interoperate in the allotted frequency. These specifications describe how multiple wireless devices using the same IEEE 802.11p devices can communicate directly [2]. To enable proper communication and create a cooperative awareness among different nodes small periodic messages are broadcasted. These messages are known as the beacon and the process is referred as beaconing. These beacons contain kinematics of vehicles such as position, acceleration, velocity, direction etc. and are of approximately 400 bytes including security fields [3]. To ensure the fast dissemination of this information beaconing is always done on CCH. However, there are always other non-critical message packets to be delivered which are usually transmitted on SCH. The IEEE 802.11p also specifies Medium Access Control (MAC) protocol for single channel operations [4]. Furthermore, IEEE has also specified IEEE 1609.4 standard which enables multi-channel operation over IEEE 802.11p using Enhanced Distributed Channel Access (EDCA). This implementation impacts the beaconing performance because it uses time division between CCH and SCH. This research studies the beaconing performance on variable nodes at a variable frequency of beacons under continuous access mode.

II. WAVE SYSTEM ARCHITECTURE

For use of wireless communication in Intelligent Transportation System(ITS), IEEE came up with amendments in IEEE 802.11 protocol as IEEE 802.11p which is also known as Wireless Access for Vehicular Environment(WAVE). However, being an amendment in existing architecture it seems to be an entirely new architecture bearing characteristics of IEEE 802.11a, IEEE 802.11e and IEEE 802.11q. The amendments can be classified into two parts PHY and MAC.

A. PHY Amendment in IEEE 802.11

There are very few changes at PHY in 802.11p. The communication between Vehicle to Vehicle is established using Dedicated Short-Range Communication (DSRC) spectrum in the frequency band of 5GHz (5.85 to 5.925 GHz) [1]. The entire spectrum of 75MHz is divided into seven intervals. Each channel has a bandwidth of 10MHz. One channel is the control channel (CCH) which serves critical messages, management frames, WAVE service advertisements and the other six channels are the service channels (SCHs) which are solely for the non-critical applications. SCH (174,176) and SCH (180, 182) may be used as single 20 MHz channel respectively if required.

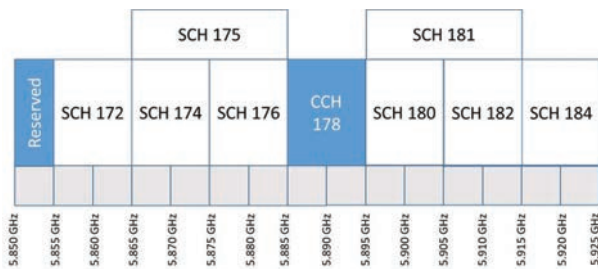


Figure 1: Channel Distribution of WAVE system

B. MAC Amendment in IEEE 802.11

For very basic understanding Medium Access Control (MAC) is a sub layer between Physical and Data Link layer in the OSI reference model. The main role of MAC layer in WAVE is to enable different nodes to communicate with each other wirelessly, faster and more efficient. Thus, we can conclude that this is the main amendment in WAVE vs 802.11 protocol. In 802.11 wireless application, one has to get the SSID of the access point to be in the same network followed by different steps of authentication. In contrast with the Service Set identification (SSID) used in wireless Basic Service Set (BSS), there is Wave Basic Service Set (WBSS) used in WAVE architecture. This WBSS also called as Wave mode is a simple

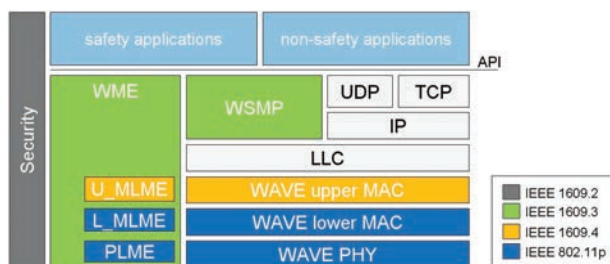


Figure 2: DSRC standards and communication stack copied from [1]

method to create instantaneous communication between two vehicles, which usually have very less time to establish communication. This improves the efficiency of the network. Furthermore, IEEE has also specified IEEE 1609.4 standard for

MAC layer which enables multi-channel operation over IEEE 802.11p which uses Carrier Sense Multiple Access Protocol with Collision Avoidance (CSMA/CA) [5]. This implements that if a node is willing to send a message it will first listen to Arbitration Inter Frame Spacing (AIFS) period. If the channel is busy it chose a random Back-off time from $[0-CW]$ and transfer only when back off timer is elapsed or sends directly if the channel is idle. QoS is also provided in IEEE 802.11p using Enhanced Distributed Channel Access (EDCA).

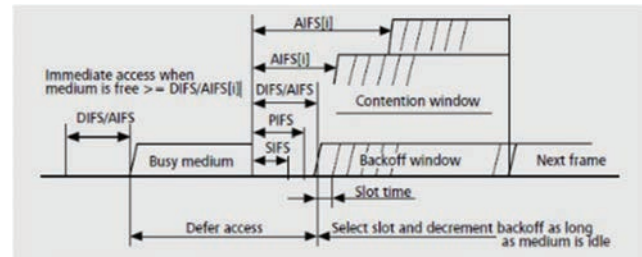


Figure 3: EDCA Inter Frame Spacing Relations, copied from [5]

EDCA works by classifying the beacons based on four access category (AC) namely Video Traffic (VI), Voice Traffic (VO), Best effort Traffic (BE) and Background Traffic (BK). These four AC differs by using different CW_{min} , CW_{max} and AIFSN.

III. BEACONING

To create cooperative awareness among the highly mobile vehicle nodes small periodic messages are broadcasted. These messages are known as a beacon and the process is referred as beaconing. These beacons contain kinematics of vehicles such as position, acceleration, velocity, direction etc. and are of approximately from 20 bytes [6] to 400 bytes including security fields [3]. To ensure the fast dissemination of this information beaconing is always done on CCH. The Beacons can be propagated in either one-hop or multi-hop. In one-hop, the message is only propagated once and the receiving node does not forward it, while in multi-hop the receiving node rebroadcast the message to its neighbours and this process goes on till any of the termination conditions reaches. In a multi hop, the information is obviously disseminated at the larger area but it introduces the famous broadcast storm problem resulting in packet collision and hidden terminal problem. Most of the research are done in controlling the multi hop broadcasting based on geography, counter based, delay based methods.

IV. SIMULATION

Simulation is needed where physical implementation is not feasible to test some rough concepts, among many road traffic and safety is one of the major problem concern of this modern world. Critical traffic problems such as accidents and traffic congestion require the development of new transportation systems [7]. The need for some mechanism comes where one

can model the real traffic in simulation and then dive in to propose solutions to the problems like traffic congestion, alternate route finding, minimizing red light stoppage, Co2 emission by controlling the flow of vehicles and much more.

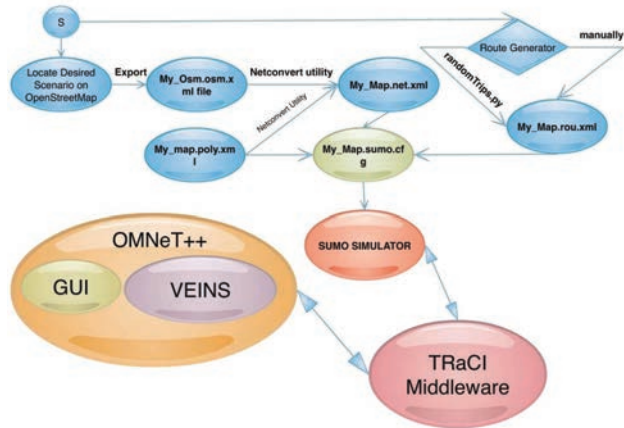


Figure 4 : Process flow for entire simulation

Post modelling it is needed to make those simulated vehicles intelligent so to make decisions and establish communication among each other for coming to some decision. VANET has a major challenge of Vehicles come and lose contact in a matter of seconds as speed is measured in miles per hour [8]. Here come network simulators in the picture which considers these vehicles as nodes and enables them to communicate with each other for real time decision making and behaving. During simulation data is processed and an overall decision is being taken for platoons of vehicles through which they behave. To start with modelling, we need to have some geographic location such as a city or some specific area, which will be our area where we want to do some simulation. For this purpose we will be taking maps from OpenStreetMap [9] [10], these maps will be then fed into SUMO [11] for modelling and then VEINS [12] framework will be used to make a realistic Vehicular Simulation using mobility from SUMO and Network from OMNeT++ [13]. Any VANET application, which needs simulation, will obviously have to pass through all above-mentioned phases. However, there are different tools and techniques available to attain the goal each having its own merit and demerits. We selected the most used and reliable method. The flow of the entire process is shown in Figure 4 and simulation screenshot is shown in Figure 5.

A. Simulation Scenario

The Scenario for simulation is generated in SUMO [10]. This work studies the beaconing performance on variable nodes at a variable frequency of beacons under continuous access mode. The model consists of a single lane of vehicles running at an interval of 3 seconds with parameters defined in Table 1. The simulation is carried out for 200s during which total of 67 vehicles enters the simulation. As this work focuses on

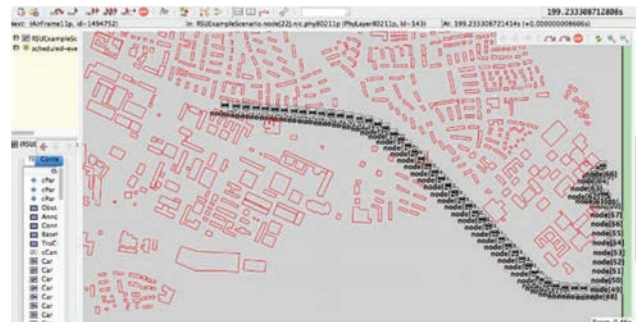


Figure 5 : Screenshot of running Simulation

beaconing so no other type of messages is taken into consideration hence the vehicles are running under the normal condition without any event of accident or emergency.

TABLE 1: SUMO SIMULATION PARAMETERS

Parameter	Value
Acceleration	2.6 m/s ²
Deceleration	4.5m/s ²
Sigma	0.5
Length	2.5m
MiniGap	2.5m
MaxSpeed	14m/s or 50kmph

B. Simulation Parameters

The Simulation is carried out in OMNET++ and VEINS framework using the parameters given below in Table 2. The *SimpleObstacleShadowing* obstacle model used to depict real world conditions.

TABLE 2 : OMNET++ SIMULATION PARAMETERS

Parameter	Value
txPower	20mW
bitrate	6Mbps
sensitivity	-89dBm
thermalNoise	-110dBm
usePropagationDelay	True
dataOnSch	false

C. Beaconing Frequency

The three simulations are carried out by taking variable beaconing frequency of 1Hz, 2Hz, .5Hz respectively. Each vehicle node which is generated at an interval of 3s through SUMO enters simulation and starts sending a beacon message to other nodes. A number of beacons generated become a cross product of all nodes in the simulation gradually when the number of vehicles grows. The results are obtained by setting

beacon generation rate of 1 beacon per sec, 2 beacons per sec and 1 beacon per 2 seconds.

D. Simulation Results

As the simulation executed for 200 seconds, 67 vehicles participated and node 0 started to send the beacons as soon as it entered the simulation. Figure 6 shows a number of beacons

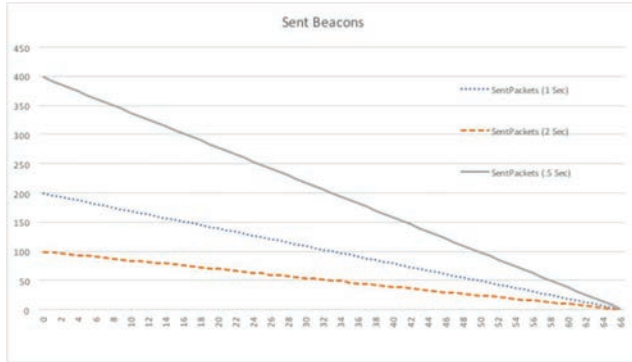


Figure 6 : Sent Beacons

generated by different nodes for different frequency of beaconing. We can observe that Node 0 has generated the maximum beacons as it stayed for longest time in all the

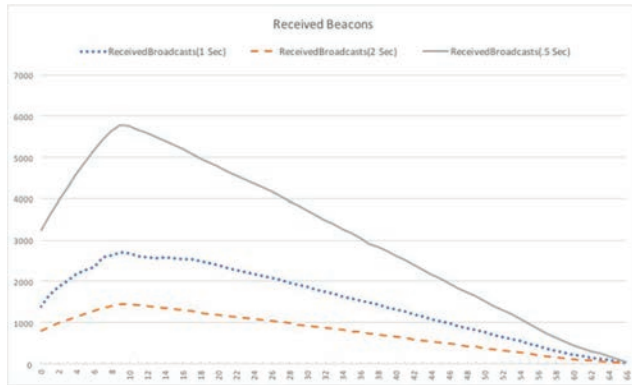


Figure 7 : Received Beacons

simulated scenarios while node at the right side has generated less number of beacon. This happened because beacon generation is the function of time and no other factor is responsible to alter the generation of beacons. If we look at Figure 7, which displays the number of received beacon messages at respective nodes. As we can see there are no straight lines we, observe a curve in the graph at Node 9, this curve is the result of maximum messages received at this node in all three simulated cases, this happened due to the reason of being node 9 in the vicinity of all the vehicles during the simulation. As we have used *SimpleObstacleShadowing* model to depict the real world scenario, it is also clear from the simulation model in Figure 5 that when vehicles are in direct line of sight there is no obstacle in between and they can transmit to their full range. Also, node 9 receives the messages from node ahead it and nodes

following it. This increased the reception of messages and hence raised the total channel busy time for Node 9, as shown in Figure 8. As Node 9 is receiving more messages so more back off time is required as compared to all other nodes, however, backoff time is dependent on CW values but in case of beaconing, the CW time is not doubled [3] as it is doubled in case of SCH messages. Therefore, there is no significant difference in backoff time of node 9 as shown in Figure 9. The last observation in

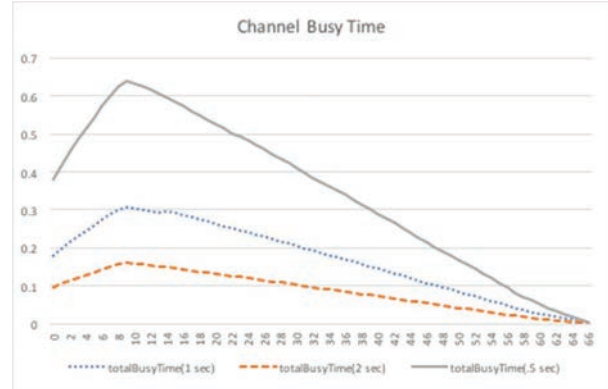


Figure 8 : Channel Busy Time

Figure 10 shows the number of time an individual node gets into the Backoff time, this is again dependent on the channel availability. Backoff is the event which occurs when the node wants to transmit the message but the channel is sensed as busy. This makes a message to wait for a specific time and that time is called as backoff time, while the number of time backoff occurred is the count of how many time an individual node has suffered backoff.

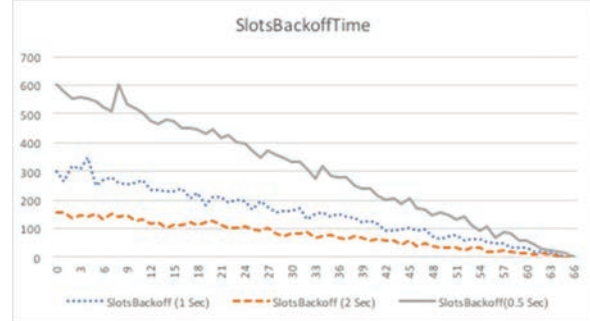


Figure 9 :Slots Backoff Time

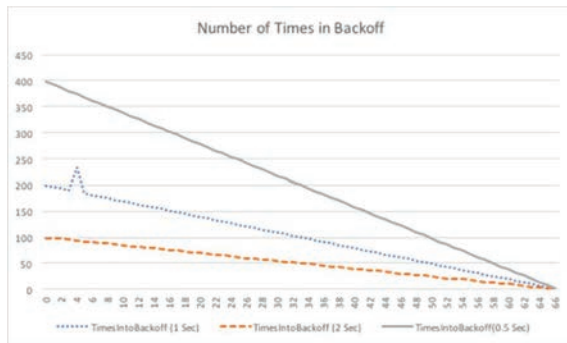


Figure 10 : Time in Backoff

V. Conclusion and Future Work

In this work, we have simulated the beaconing of messages at different intervals and have understood the behaviour of IEEE 1609.4 MAC layer, this work has observed only the CCH channel because beacons use Control Channel for transmission. We have used the flooding technique to make transmission to a maximum node within the network. Each node generates message as per the frequency allotted. We have also observed that there is a node X which falls at a specific location where message reception is more as compared to other nodes. Future work may be considered to reduce the number of Backoff per node and minimize the channel busy time. Impact of messages other than beacons on the channel and overall performance is also the area to look in future.

VI. References

- [1] L. D. D. Jiang, "Towards an International Standard for Wireless Access in Vehicular Environments," in *Vehicular Technology Conference, VTC*, 2008.
- [2] C. Y. H. C. Huang, "An Effective Channel Utilization Scheme for IEEE 1609.4 Protocol," in *Ubiquitous Information Technologies & Applications*, 2009.
- [3] A. v. d. V. G. K. M. van Eenennaam, "Impact of IEEE 1609.4 channel switching on the IEEE 802.11p beaconing performance," in *Wireless Days (WD)*, 2012 IFIP, Dublin, Ireland, 2012.
- [4] "IEEE Standard for Information technology," *IEEE Std 802.11p-2010 (Amendment to IEEE Std 802.11-2007 as amended by IEEE Std 802.11k-2008, IEEE Std 802.11r-2008, IEEE Std 802.11y-2008, IEEE Std 802.11n-2009, and IEEE Std 802.11w-2009)*, pp. 1-51, 15 July 2010.
- [5] L. Hendriks, "Effects of Transmission Queue Size, Buffer and Scheduling Mechanisms on the IEEE 802.11p Beaconing Performance," in *15th Twente Student Conference on IT*, Enschede, 2011.
- [6] R. F. M. M. Dario Rossi, "VANETs: Why Use Beaconing at All?," in *Communications, 2008. ICC '08.*, Beijing, 2008.
- [7] V. S. M. Motani, "Cross layer design: a survey and road ahead," *IEEE Communication Magazine*, vol. 43, no. 12, pp. 112-119, 2005.
- [8] M. P. G. S. R. Tomar, "Vehicular Ad Hoc Network(VANET)- An Introduction," *International Journal of control theory and application*, vol. 9, no. 18, pp. 8883-8888, 2016.
- [9] "http://en.wikipedia.org/wiki/OpenStreetMap," Wikipedia. [Online]. [Accessed 04 July 2017].
- [10] "DLR and contributors, SUMO Homepage," [Online]. Available: http://www.dlr.de/ts/desktopdefault.aspx/tabid-9883/16931_read-41000/. [Accessed 05 July 2017].
- [11] [Online]. Available: <http://sumo.dlr.de/wiki/Networks/Import/OpenStreetMap>. [Accessed 04 July 2017].
- [12] R. G. a. F. D. Christoph Sommer, "Bidirectionally Coupled Network and Road Traffic Simulation for Improved IVC Analysis," *IEEE Transactions on Mobile Computing*, vol. 10, no. 1, pp. 3-15, January 2011.
- [13] András Varga and team, "OMNeT Homepage," [Online]. Available: <https://omnetpp.org/>. [Accessed 05 July 2017].

Capacitive Coupled Rectangular Microstrip Patch Antenna for Ku Band

Praful Ranjan¹, Prof. G. S. Tomar²

Department of Electronics & Communication

^{1,2}THDC Institute of Hydropower Engineering & Technology
 Tehri, India

¹prf98354@rediffmail.com

Dr. R. Gowri³

Department of Electronics Engineering
 University of Petroleum & Energy Studies

Dehradun, India

³ravigowri07@gmail.com

Abstract—This Paper has presented a new approach to design and simulation for Ku band. This proposed designed antenna is very useful for satellite communication. Coplanar capacitive coupled feeding technique was used to reduce probe inductance. This feeding technique is mutually coupled with this patch and feeding patch. This microstrip rectangular patch antenna has two dielectric substrates. First substrate which is just below the patch is RT Duroid ($\epsilon_r=3$) and above the ground second dielectric is Air($\epsilon_r=1$). Both dielectric materials has sandwich. So that bandwidth of the antenna. The resonating frequency of capacitive coupled double dielectric rectangular patch is 16GHz. Design and analysis of this rectangular patch antenna has been done in HFSS software. Bandwidth of simulated antenna is 4.5GHz. Return loss of this antenna is around $-30dB$.

Keywords—Microstrip; Capacitive coupled; Ku Band; Rectangular Patch; Double Dielectric Materials

I. INTRODUCTION

Microstrip patch antenna is playing a main role of Digital communication, Satellite Communication, Wireless communication, Cellular Communication. Microstrip patch antenna has so many advantages like easily fabrication, durable, light weight, easy to handle, low cost. In some instant, it has some boundary conditions. It can design in rectangular shape, square shape, triangular shape and also different shape and sizes [1]. It can be flexible in different shape and size. So it is compatible to any applications like Mobile handset, Bluetooth application, WIFI applications and many more according to its shape. It has also multi resonating frequencies. In one antenna can work multi band like in Mobile, there are several applications such as subscriber calling GSM, CDMA band, Bluetooth and WIFI applications [2]-[4].

There is several feeding technique in microstrip patch antenna like edge feeding, side feeding, coaxial feeding, and proximately feeding, coplanar feeding [5]-[7]. This paper has introduced an approach of capacitive coupled. Feed pitch length and width has

decided according to bandwidth using approximation method [14]-[15]. The general structure of designed antenna is shown in Fig 1. In figure (a) top view and (b) side view of antenna. Antenna geometry is discussed in next section.

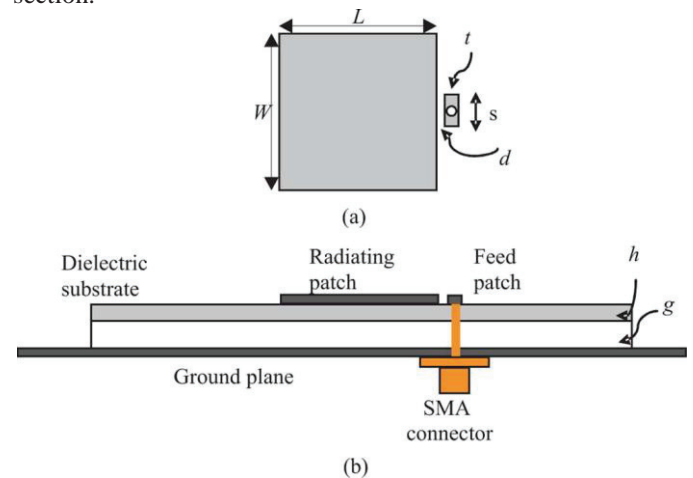


Fig.1. Overview of Patch Antenna (a) Top View (b) Side View

II. DESCRIPTION OF ANTENNA

The designed microstrip antenna is in rectangular shape where patch length and width are L & W respectively. Radiating patch is on the top of first dielectric (RT Duroid $\epsilon_r=3$). Thickness of substrate is h. Below the RT Duroid, second dielectric is air ($\epsilon_r=1$) and thickness of second dielectric is g [8]-[10]. The feeding patch is just side of patch. Feed patch length and width are denoted s and t respectively. Thickness of substrate is very thin. Feeding of this proposed antenna, connected through SMA connector [16]-[17]. Calculation of all parameters is done by Equations (1) - (5).

Width (W) of proposed patch antenna is calculated as [11]-[13].

$$W = \frac{1}{2f_r \sqrt{\mu_0 \epsilon_0}} \sqrt{\frac{2}{\epsilon_r + 1}} = \frac{c}{2f_r} \sqrt{\frac{2}{\epsilon_r + 1}} \quad (1)$$

Dielectric constant (effective) is calculated from:

$$\epsilon_{eff} = \frac{\epsilon_r + 1}{2} + \frac{\epsilon_r - 1}{2} \left(\frac{1}{\sqrt{1 + \frac{12h}{w}}} \right) \quad (2)$$

The actual length of the Patch (L)

$$L = L_{eff} - 2\Delta L \quad (3)$$

Where

$$L_{eff} = \frac{c}{2f_r \sqrt{\epsilon_{eff}}} \quad (4)$$

Calculation of Length Extension

$$\frac{\Delta L}{h} = 0.412 \frac{(\epsilon_{eff} + 0.3) \left(\frac{w}{h} + 0.264 \right)}{(\epsilon_{eff} - 0.258) \left(\frac{w}{h} + 0.8 \right)} \quad (5)$$

Where,

- ϵ_{reff} = Effective dielectric constant,
- ϵ_r = Dielectric constant of substrate,
- h = Height of dielectric substrate,
- W = Width of the Patch,
- L = Length of the Patch,
- ΔL = Effective Length,
- f_r = Resonating Frequency

All calculated parameter had done by these equations. We use optimization technique for enhance the radiation properties of proposed antenna also done in HFSS software. All d related values are shown in Table I.

TABLE I
SPECIFICATION OF ANTENNA PARAMETERS

Parameters	Value
Operating Frequency	16GHz
Length (L)	4.285mm
Width (W)	4.5mm
Length of feed patch(s)	2.0mm
Width of feed patch (t)	1.6mm
Separation of feed strip from the patch (d)	0.28mm
Air gap between the substrates (g)	1.0mm
Thickness of substrate (h)	1.56mm
Ground plane size	$12.56 \times 12.56mm^2$

Length of patch and height is also depending on dielectric height as (g + h) Height of air dielectric is calculated by equation (6) [7]-[9]. Calculating the height of air gap by

$$g \cong 0.16\lambda_0 - h\sqrt{\epsilon_r} \quad (6)$$

Variations in value of g depend upon optimization method in HFSS software. The value of air height (g) and bandwidth is shown in Table II. When g is 1mm, bandwidth of the antenna is maximum. Hence air gap or height of second dielectric we have taken in 1mm.

TABLE II
OPTIMIZATION OF AIR THICKNESS AND OTHER ANTENNA PARAMETERS

Air Gap Height (g) in mm	Feed Strip (s × t) in mm	Bandwidth in GHz
0.2	2 × 1.6	4.01
0.4	2 × 1.6	4.21
0.6	2 × 1.6	4.33
0.8	2 × 1.6	4.42
1.0	2 × 1.6	4.50
1.2	2 × 1.6	4.46
1.4	2 × 1.6	4.47
1.6	2 × 1.6	4.45

TABLE III
OPTIMIZATION OF FEED PATCH LENGTH WITH OTHER ANTENNA PARAMETERS

Feed Strip (s × t) in mm	Air Gap Height (g) in mm	Bandwidth in GHz
0.5 × 1.6	1.0	4.03
1.0 × 1.6	1.0	4.16
1.5 × 1.6	1.0	4.21
2.0 × 1.6	1.0	4.50
2.5 × 1.6	1.0	4.48
3.0 × 1.6	1.0	4.47
3.5 × 1.6	1.0	4.46

TABLE IV

OPTIMIZATION OF FEED PATCH WIDTH WITH OTHER ANTENNA PARAMETERS

Feed Strip (s × t) in mm	Air Gap Height (g) in mm	Bandwidth in GHz
2.0 × 1.0	1.0	4.42
2.0 × 1.2	1.0	4.45
2.0 × 1.4	1.0	4.49
2.0 × 1.6	1.0	4.50
2.0 × 1.8	1.0	4.49
2.0 × 2.0	1.0	4.46
2.0 × 2.2	1.0	4.45

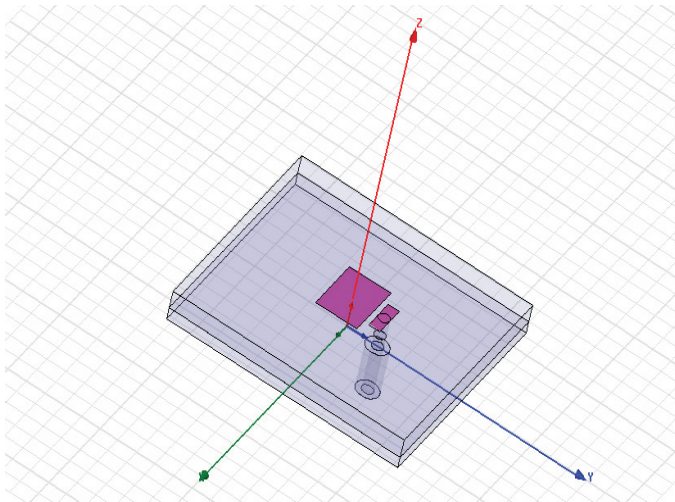


Fig.2. Simulated structure of proposed antenna

When variation in feed strip length and feed strip width with constant air gap height, the bandwidth variations are shown in Table III and Table IV. So feed strip length and width (2 × 1.6)mm has given a maximum bandwidth. Simulated structure of antenna is shown in Fig 2.

III. RESULTS AND DISCUSSION

Proposed antenna is designed and simulated in HFSS. Good return loss is achieved around -30 dB for this capacitive coupled rectangular microstrip patch antenna. Graph of return loss versus frequency are shown in Fig 3. E field pattern and H field pattern of simulated antenna is presented in Fig 4 & Fig 5. VSWR of this simulated antenna is almost 1 which is shown in Fig 6. Impedance matching is also 50Ω. It means it is clearly indicates that the maximum power transfer theorem is achieved indicate in Fig 7. Hence antenna is perfectly matched. Gain of antenna is achieved around 6dBi. Gain of antenna is clearly shown in Fig 8.

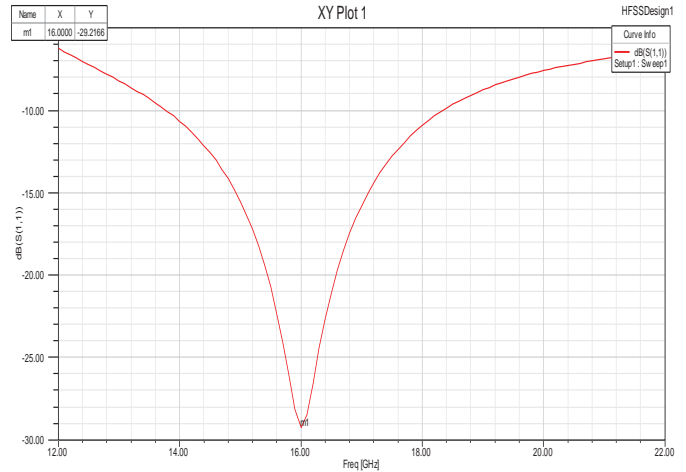


Fig.3. Return loss of coplaner capacitive coupled antenna

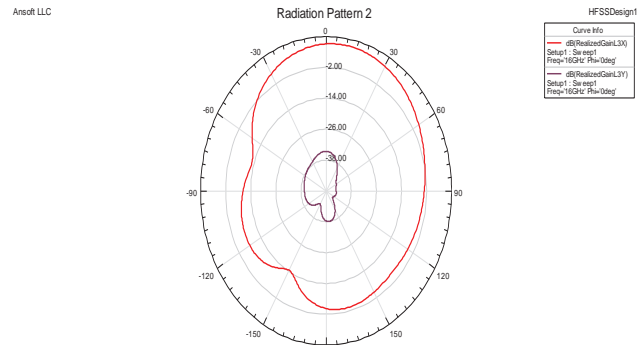


Fig.4. E field pattern of simulated antenna

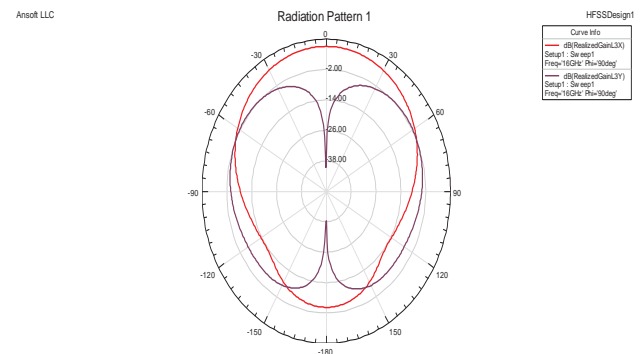


Fig.5. H field pattern of simulated antenna

By investigation of all the results it is observed that antenna has good return loss, impedance matching and VSWR values. Bandwidth of 4.50GHz is achieved which is already in Fig 1.

Table V shows the result of bandwidth which is achieved of simulated antenna. Bandwidth % is approximately 28.12.

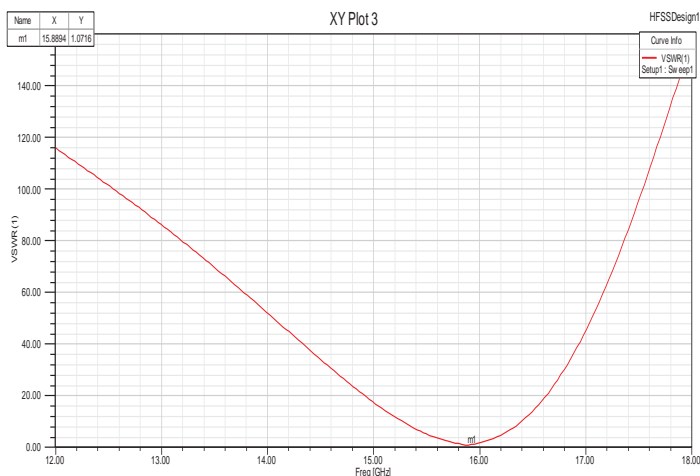


Fig.6. VSWR of simulated capacitive coupled antenna

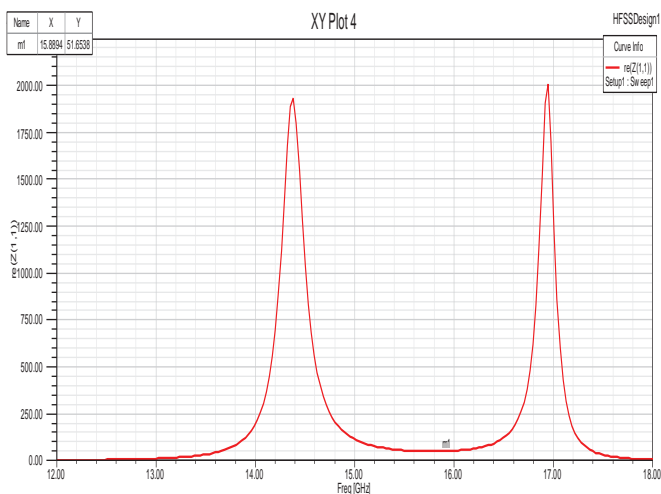


Fig.7. Impedance matching of simulated antenna

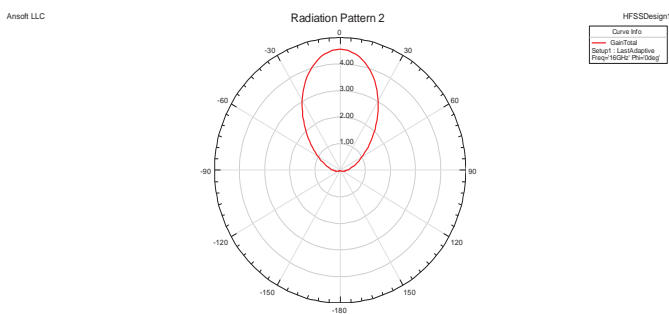


Fig.8. Gain of the antenna

Directivity of the antenna is also shown in Fig 9. A good directive pattern shows that the antenna is useful in satellite communication applications.

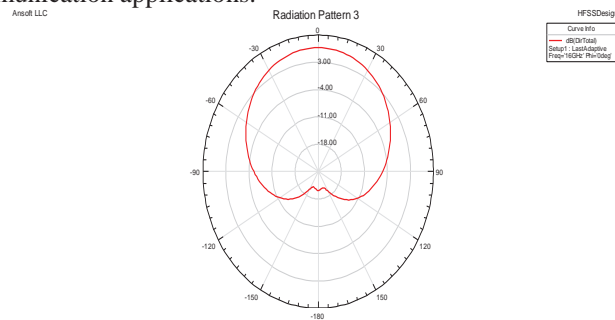


Fig.9. Directivity of the simulated antenna

TABLE V
ANALYSIS OF BANDWIDTH OF SIMULATED ANTENNA

Resonant Frequency (GHz)	Frequency Range	Bandwidth (GHz)	% Bandwidth
16	13.78-18.28	4.50	28.12

V. CONCLUSION

In this paper a capacitive coupled with double dielectric rectangular microstrip patch antenna has been simulated at 16GHz. This simulated antenna is achieved approx. -30dB return loss and 4.50GHz bandwidth. Gain of this designed antenna is 6.0dBi. Proposed designed structure is very compact than previous work in Ku band. Purpose of the antenna is designed for improving the bandwidth. In satellite communication it is compulsory because huge number of channels, so that it is mandatory to improve the bandwidth. Area of the patch is less as compare to conventional antenna. It can be very useful in satellite communication. It shows good agreement with antenna design parameters. Future scope is to improve the gain using array of patches.

REFERENCES

- [1] M. Ben Ahmed, M. Bouhorma, F. Elouaai, A. Mamouni, "Design of new multistandard patch antenna GSM/PCS/UMTS/HIPERLAN for mobile cellular phones", European journal of scientific research ISSN 1450-216X vol.32 No.2(2009), pp 151-157.
- [2] W.L. Stutzman, G.A. Thiele, "Antenna Theory and design", John Wiley & Sons, 2nd Ed., New York, 1998.
- [3] David M. Pozar, "Microwave Engineering", 3rd Edition, John Wiley & Sons, 2004.
- [4] R. E. Collin, Field theory of guided waves, Piscataway, NJ: IEEE Press, 1990.

- [5] Constantine A. Balanis, "Antenna Theory and Design", John Wiley & Sons, Inc., 1997.
- [6] J. S. Colburn and Y. Rahmat-Samii, "Patch antennas on externally perforated high dielectric constant substrates," IEEE Trans. Antennas Propag., vol. 47, no.12, pp. 1785-1794, Dec. 1999.
- [7] A. D. Yaghjian and S. R. Best, "Impedance, Bandwidth, and Q of Antennas," IEEE Trans. on Antennas and Propagation, Vol. 53, No. 4, pp. 1298-1324, 2005.
- [8] Prof. G.S. Tomar, Praful Ranjan, Dr. R. Gowri, "Metamaterial Loaded Shorted Post Circular Patch Antenna" published in International Journal of signal Processing and Pattern Recognition Vol. 9, No. 10, (2016) pp.217-226.
- [9] N. Prashanti, Praful Ranjan, "Cylindrical Metallic pin structure microstrip patch antenna for wideband application," ICICCD 2016 Springer SBIN 978-981-10-1708-7, Vol-479, 2016.
- [10] Ramesh Garg, Prakash Bartia, Inder Bahl, Apisak Ittipiboon, "Microstrip Antenna Design Handbook", pp 1-68, 253-316 Artech House Inc. Norwood, MA, 2001.
- [11] A. K. Verma, D. Chakraverty and N. V. Tyagi, "Input impedance of probe fed multilayer rectangular microstrip patch antenna using the modified Wolff model," Microwave Opt. Technology Lett., pp. 237-239, vol. 31, no. 3, 2001.
- [12] Saurabh Mishra, Praful Ranjan "Design of Circularly Polarized Rectangular Patch Antenna with single cut," CAC2S 2013, Atlantis Press, pp 174-177, 2013.
- [13] R. Gowri, Praful Ranjan and N. Prashanti, "Design of Double sided Metamaterial Antenna for Mobile Handset Applications," SPIN 2014, IEEE 978-1-4799-2866-8/14 pp 675-678, 2014.
- [14] F. Abboud, A. Papiernik, and J. P. Damiano, "Simple model for the input impedance of the coax-feed rectangular microstrip patch antenna for CAD," Proc. Inst. Electrical Eng., pp. 323-326, vol. 135, no. 5, 1988.
- [15] Prasana L. Zade, Sachin S Khade, Dr. N. K. Choudhary, "Modelling and designing of Circular Microstrip antenna for wireless communication", IEEE, 2009.
- [16] K. Suell, H. Mosallei and K. Sarabandi, "A substrate for small patch antenna providing tunable miniaturization", IEEE Trans. Microwave theory Tech, Vol-54, January 2006.
- [17] P. Ikonen, K.N. Rozanov, A. V. Osipov and S.A. Tretykov, "Magneto dielectric substrates on antenna miniaturizations. Potential and limitation", IEEE Trans. Antenna Propg. Vol 154, Nov. 2006.

Cloud Security Ecosystem for Data Security and Privacy

Akshay Arora
Information Security Associate
Fiserv India Pvt Ltd
Noida, India
akshay.arora@fiserv.com

Anmol Rastogi
Associate Software Engineer
KPIT Technologies
Pune, India
Anmol.Rastogi@kpit.com

Abhirup Khanna
Centre for Information Technology
University of Petroleum and Energy Studies
Dehradun, India
abhirupkhanna@yahoo.com

Amit Agarwal
Centre for Information Technology
University of Petroleum and Energy Studies
Dehradun, India
aagarwal@ddn.upes.ac.in

Abstract—In the past couple of years Cloud Computing has become an eminent part of the IT industry. As a result of its economic benefits more and more people are heading towards Cloud adoption. In present times there are numerous Cloud Service providers (CSP) allowing customers to host their applications and data onto Cloud. However Cloud Security continues to be the biggest obstacle in Cloud adoption and thereby prevents customers from accessing its services. Various techniques have been implemented by provides in order to mitigate risks pertaining to Cloud security. In this paper, we present a Hybrid Cryptographic System (HCS) that combines the benefits of both symmetric and asymmetric encryption thus resulting in a secure Cloud environment. The paper focuses on creating a secure Cloud ecosystem wherein we make use of multi-factor authentication along with multiple levels of hashing and encryption. The proposed system along with the algorithm are simulated using the CloudSim simulator. To this end, we illustrate the working of our proposed system along with the simulated results.

Keywords—Cloud Security; Data Security; Data Privacy; CloudSim

I. INTRODUCTION

In today's times Cloud computing has a significant impact on the IT industry. With growing popularity more and more organizations are making use of cloud services [1]. Although cloud services have a widespread acceptance but the fear pertaining to security and privacy of these services still continue to be an open challenge. With rapid technological advancements these services could be easily accessed through smart phones thus allowing users to share pictures, video, documents and other important data across various platforms on a real time basis [2]. However, a security breach in there

cloud account could lead to stolen data which would indeed result in huge losses.

Security has always been a concern in the domain of information technology. With Cloud services handling critical data which can be accessed from anywhere through the internet makes security a prominent concern [3]. The pervasive nature of Cloud and its disbursement of data across various geographical locations amounts to high security risks. While talking of Cloud Security there are many aspects which one needs to consider such as, trusted authentication, appropriate authorization, data security and privacy. These are some of the basic security goals which are extremely essential for every cloud provider to incorporate [4]. Since security has been seen as an attribute for information technology, data encryption has been one of its key measures in ensuring data security protection. Many algorithms in the past have been proposed for conducting efficient data encryption. These algorithms range from Diffie-Hellman, RSA, DES to AES, RC4 and 3DES. Each of these algorithms have their own advantages along with their demerits. These algorithms are broadly classified as being symmetric or asymmetric in nature.

Our focus here would be to create a Secure Cloud Ecosystem that leverages from the benefits of both symmetric and asymmetric encryption. We make use of RSA (Asymmetric) and AES (Symmetric) algorithms for carrying out data encryption. We aim at creating a comprehensive Cloud Environment that has security measures at all levels from creating and storing username and password, multifactor authentication, transmission of user data and data encryption.

The rest of the paper is categorized as follows: Section II talks about security concerns pertaining to Cloud Computing.

Section III elucidates the proposed work wherein the proposed system and its working are explained. Section IV discusses the algorithm that depicts the workflow of the entire system, whereas its successful simulation and its results are discussed in Section V. Finally, Section VI concludes the paper.

II. SECURITY CONCERNS IN CLOUD

Security in cloud plays an important role in creating a sense of belief and confidence between the customer and Cloud Service Provider (CSP). Since, all the user data is stored, managed and processed at the cloud end thus it is the duty of the CSP to mitigate any kind of risk pertaining data security and privacy. Following are certain Cloud security which a CSP needs to keep in mind while dealing with user data.

- **Data Protection:** Cloud computing poses several data protection risks for cloud users, providers and brokers. There are different kinds of SLAs involved between the cloud user, provider and broker leading to certain kinds of data leaks. Many of times it is seen that it becomes difficult for the cloud user to have a check on the data handling practices of the cloud provider [5]. Further there can be challenges due to the complex network topology between cloud and the end user that gives scope to many network related attacks.
- **Loss of Data:** Mission critical applications involving the use of crucial data are not preferred to be offloaded to cloud. Due to the presence of common resource pools, applications run on the same platform that could lead to disclosure of user's information through its application. In many cases proper encryption schemes for secure processing are not adopted for data transfer and its storage by the cloud vendor.
- **Traffic hijacking:** is also one of the prominent threats that end users face while leveraging form cloud computing. In 2013 Cloud Security Alliance ranked it as the third most extreme threat to cloud security. In such kind of an attack, hackers tend to obtain a user's security credentials and proclaim unauthorized access to its data. After which all the activities of a user including its confidential transactions happening on the cloud are now open to a hacker [6]. The hacker can easily tamer the users data along with have access to its applications running on cloud. A similar kind of an attack was faced by Amazon in 2010 when the hackers had stolen the session IDs and had access to client's credentials.
- **Isolation of Resources:** In present times the two main characteristics of cloud computing are multi-tenancy and shared resources. This risk category caters to processes that work and manage resources like storage, memory, bandwidth and even reputation

between different tenants. Cloud provides a shared platform for different kind of applications from different users. This common resource pool adds problems relating to security thus making the user data more vulnerable to data breaches.

- **Malicious Insider:** Usually, the damage which may be caused by malicious insiders is often far greater than expected. Such type of attackers uses their own device as a medium to inject the unsecure code to the cloud. This code behaves maliciously when properly injected and the control of which lies in hands of the user operating it [7]. This code can provide access of information to the malicious user, criticality of which depends on the capability of the designed code and the level of security measures taken by the cloud.

III. PROPOSED WORK

Over the years, many security models have been presented with regard to Cloud computing but most of them had their focus on a particular security threat rather than catering to the entire system. In this section we, discuss our proposed Secure Cloud Ecosystem which intends to provide security measures on a pan Cloud basis. The aim of our system is to ensure data security and privacy right from the process of user authentication to data being stored on Cloud. We make use of multiple algorithms for ensuring the efficiency of our system. Our primary focus in this section would be to illustrate upon our encryption & decryption process along with describing our system architecture.

A. Data Encryption

In this sub section, we would be talking about the ways in which data encryption takes place at the Cloud end. The following is a flow chart which clearly depicts the working of our proposed system.

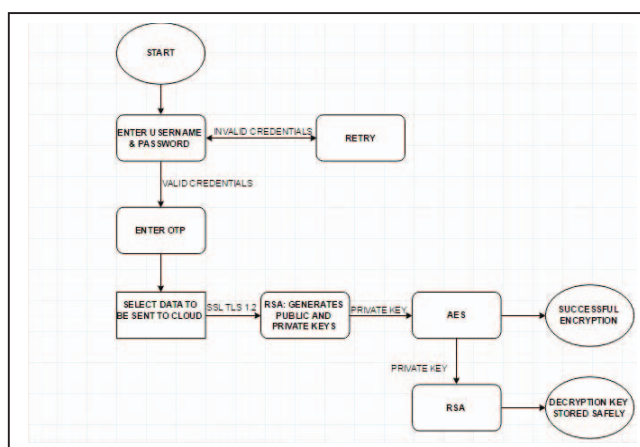


Fig. 1. Encryption Process Flowchart

As it can be seen in the figure, no unauthorized user will have access to and kind of user data. This is ensured by making use of multifactor authentication in form of One Time

Password (OTP). Once a legitimate user enters its login credentials an OTP is sent to its registered mail which one needs to enter in order to make certain successful login. Upon successful login the user can anytime send or retrieve data from Cloud. If a user wishes to store its data onto the Cloud, in this case the data is allowed to pass through a secure network channel so as to protect it from any kind of hackers residing over the network. Once the data reaches the Cloud end it undergoes encryption through our Hybrid Cryptographic System. At first the RSA generates Public and Private Keys which are later used by the AES in order to commence data encryption. The Private key of the AES again undergoes encryption through RSA and is saved in the data base after adding salt to it. In this way the user data is stored in an encrypted form at the Cloud end and whenever the user wishes to access it will be available after successful decryption.

B. System Architecture

In this sub section, we would be discuss the system architecture of our proposed Secure Cloud Ecosystem. The system architecture comprises of various physical entities that constitute the entire ecosystem. Here we would be talking about all different actors that constitute the Cloud, their roles, basic functionalities and the security services which our system provides. The following figure exemplifies our system architecture.

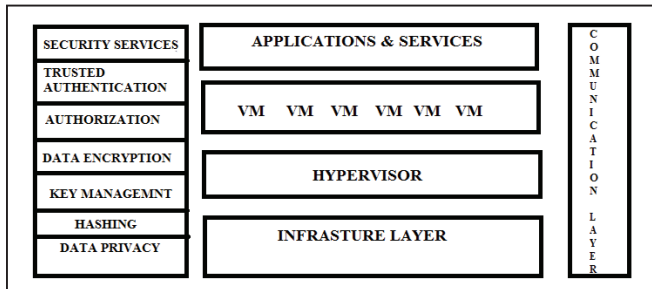


Fig. 2. System Architecture

The list of security services which our Secure Cloud Ecosystem ensure are:

- **Trusted Authentication:** Only a legitimate user will be allowed to access services and data being hosted on Cloud.
- **Authorization:** The system ensures proper authorization by only allowing system admin to have access to decryption keys. It is only the Cloud admin who is aware of the salted value added to every user password and Decryption Key before being saved in the database.
- **Data Encryption:** The system makes use of Hybrid Encryption by allowing RSA and AES algorithms to encrypt user data. The proposed system leverages the benefits of both symmetric and asymmetric data

encryption. We make use of RSA2048 and AES256 for our encryption process.

- **Hashing:** SHA512 and bcrypt functions are used for securing user password.
- **Key Management:** The Private Key of AES is encrypted and salted and safely stored into the database. The decryption keys are also saved soon after the encryption gets over. The SHA512 key is protected using keyed-hash message authentication code (HMAC).

IV. ALGORITHM

The working of our proposed system is explained through the illustration of the algorithm that forms the core for it. The algorithm depicts the functioning of the system by representing the entire process from user authentication to storage and retrieval of user data from Cloud.

- STEP 1:** Create Username and Password
- STEP 2:** Password creation using CSPRNG
- STEP 3:** SHA512 and bcrypt function used for password protection
- STEP 4:** SHA512 key is protected using HMAC algorithm
- STEP 5:** Enter login credentials
- STEP 6:** Make use of OTP for multifactor authentication. Validity of OTP is 5 minutes.
- STEP 7:** User stores data on Cloud
- STEP 8:** SSL and TLS 1.2 are used for conducting transfer user data over the network
- STEP 9:** RSA algorithm is used for Public Private Key generation
- STEP 10:** AES algorithm encrypts data using RSA Private Key
- STEP 11:** Private Key encrypted using RSA
- STEP 12:** User request to access data
- STEP 13:** RSA generates Decryption Keys
- STEP 14:** Decryption process takes place

STEP 1 to STEP 6 depict the authentication process wherein trusted authentication takes place through the use of original user credentials. Multifactor authentication has also been performed by making use of One Time Password (OTP), which is sent to the registered email-id of the user. In STEP 2, we make use of CSPRNG (Cryptographically Secure Pseudo-Random Number Generator) which is a salting technique used for protecting passwords in case there is an attack on credential database. In STEP 3, hashing functions such as SHA512 and bcrypt have been used for ensuring password protection. STEP 9 to STEP 11 illustrate the process of data encryption that happens at the Cloud end. STEP 12 to STEP 14 demonstrate the decryption process in case the user needs to access its data.

V. IMPLIMENTATION & SIMULATION

The above mentioned algorithm is implemented on CloudSim framework. CloudSim [8] is a simulation toolkit which comprises of various predefined classes that provide a simulation environment for Cloud computing. It is a java based simulation toolkit and can be implemented either using Eclipse or NetBeans IDE. In our case we would be using the eclipse IDE. To run CloudSim on eclipse, we first need to download the eclipse IDE and install it. After successful installation of eclipse IDE, download the latest CloudSim package, extract it and import it in eclipse. Talking of our proposed work we have created our own classes in CloudSim and have portrayed our algorithm in form of java code. Through our simulation we intend to depict two specific scenarios i.e. Authentication Process and Data Encryption. The following are the screenshots that depict the working of our algorithm on CloudSim framework.

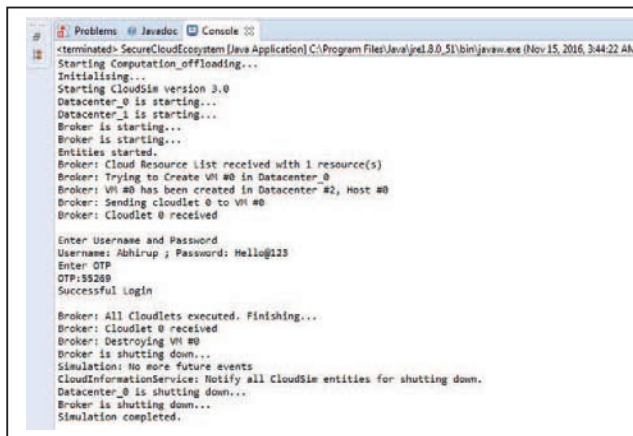


Fig. 3. Simulation: Authentication Process

The above mentioned screenshot depicts the working of our offloading model. Some pre-defined functions such as createCloudlet(),createBroker() and createDatacenter() from CloudSim have been used extensively throughout this experiment for creating various entities such as Cloudlets (Application), Virtual Machines, broker and Datacenter. In this experiment, we aim at portraying the Authentication Process of our proposed system. As explained in the algorithm itself, the first step would be to ensure trusted authentication thereby asking the username and password along with the OTP.

The following figure showcases the process of data encryption which takes place after successful user authentication. User data is stored at the Cloud end after undergoing data encryption.

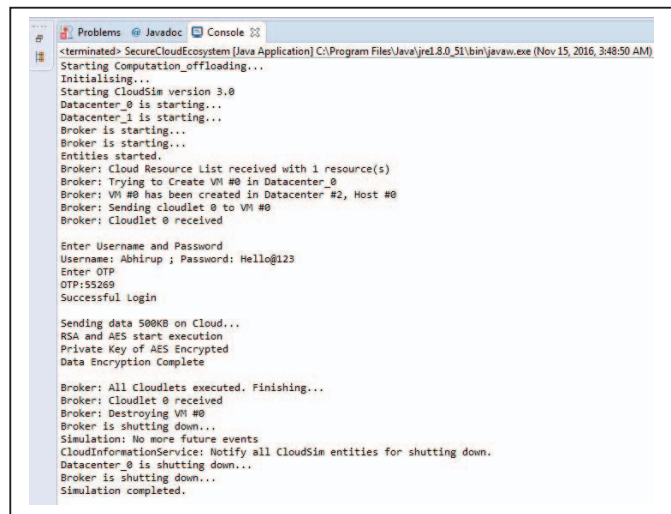


Fig. 4. Simulation: Encryption Process

VI. CONCLUSION & FUTURE WORK

In this paper, we present a Hybrid Cryptographic System (HCS) that combines the benefits of both symmetric and asymmetric encryption. The Secure Cloud Ecosystem which we propose ensures data security and privacy by implementing different encryption techniques at various levels. The system also makes use of certain hashing and salting techniques which even strengthens the entire encryption process. During the design of our system we also made sure of trusted authentication thereby allowing the feature of One Time Password (OTP). In future we wish to incorporate definite steps that would enhance the efficiency and generality of our system. This could be in form of extending our system to work for a multi cloud environment and add certain backup and recovery features which would prevent data loss in case of an attack.

REFERENCES

- [1] Subashini, Subashini, and Veeraruna Kavitha. "A survey on security issues in service delivery models of cloud computing." *Journal of network and computer applications* 34.1 (2011): 1-11.
- [2] Pawar, Pramod S., et al. "Security-as-a-service in multi-cloud and federated cloud environments." *IFIP International Conference on Trust Management*. Springer International Publishing, 2015.
- [3] Nair, Nikhitha K., K. S. Navin, and Soya Chandra. "Digital Signature and Advanced Encryption Standard for Enhancing Data Security and Authentication in Cloud Computing." (2015).
- [4] Wang, Cong, et al. "Privacy-preserving public auditing for data storage security in cloud computing." *INFOCOM, 2010 Proceedings IEEE. Ieee*, 2010.
- [5] Hendre, Amit, and Karuna Pande Joshi. "A semantic approach to cloud security and compliance." *2015 IEEE 8th International Conference on Cloud Computing*. IEEE, 2015.
- [6] Khanna, Abhirup, Sarishma. (2015). *Mobile Cloud Computing: Principles and Paradigms*. IK International.

- [7] Khanna, Abhirup. "RAS: A novel approach for dynamic resource allocation." Next Generation Computing Technologies (NGCT), 2015 1st International Conference on. IEEE, 2015.
- [8] Calheiros, Rodrigo N., et al. "CloudSim: a toolkit for modeling and simulation of cloud computing environments and evaluation of resource provisioning algorithms." Software: Practice and Experience 41.1 (2011): 23-50.
- [9] Huang, Wei, et al. "The State of Public Infrastructure-as-a-Service Cloud Security." ACM Computing Surveys (CSUR) 47.4 (2015): 68.
- [10] Aich, Asish, Alo Sen, and Satya Ranjan Dash. "A Survey on Cloud Environment Security Risk and Remedy." Computational Intelligence and Networks (CINE), 2015 International Conference on. IEEE, 2015.
- [11] Singh, Aarti, and Manisha Malhotra. "Security Concerns at Various Levels of Cloud Computing Paradigm: A Review." International Journal of Computer Networks and Applications 2.2 (2015): 41-45.

Design and Development of Low-Cost Wireless Parameter Monitoring System for Nuclear Power Plant

Tanisha Gupta, Rohit Sanket, Rajesh Singh, Anita Gehlot,
Eesh Mehandiratta, Ateev Agarwal and Sushabhan Choudhury

Abstract Safety is of utmost importance in any nuclear power plant, as even minor accidents may pose huge danger due to radiation leakage. The paper highlights the need of radiation leakage monitoring for nuclear power plant. Whenever radioactive radiations would increase beyond the safety level, alarms would indicate it. Thus, it will help to take safety measures before leading to serious problems. The system comprises of radiation sensor, fire sensors, and temperature sensors to detect any possibility of leakage and fire. XBee is used as communication media for the system. All the information is collected at a control room and analyzed through LabVIEW.

Keywords Fire sensor · Gas sensor · Radiation · Nuclear power plant · XBee

1 Introduction

Radiation leakage in nuclear power plants is posing health risks to people in and around nuclear power plants. This affects plant efficiency and harmful for animal life. Once any explosion takes place, repair takes a lot of time which reduces power generation. Fire in any part of the plant also leads to explosion and releases huge amount of radiations into the environment. Lin et al. discussed wireless sensor networks and used it to acquire and process data. This paper presents the current growth in WSN applications and its use in real-time monitoring of nuclear power plant [1]. Kim et al. discussed and analyzed internal parameters for nuclear power sites for two years [2]. Jang et al. deals with wireless sensor technology to monitor conditions in and around buildings. Sensor is programmed to process signals received in a suitable format through an open-source operating system [3]. Khedo et al. discussed the use of WSN-based air pollution monitoring system in Mauritius.

Tanisha Gupta · Rohit Sanket (✉) · Rajesh Singh · Anita Gehlot ·
Eesh Mehandiratta · Ateev Agarwal · Sushabhan Choudhury
University of Petroleum and Energy Studies, Dehradun, India
e-mail: rohitsanket@gmail.com

Recursive Converging Quartiles algorithm merges data to remove duplicates, filter out invalid readings and convert it into simpler form which reduces the amount of data to be transmitted to the sink which helps in saving energy [4]. Lopez et al. describes the steps which are essential for developing a good WSN [5]. Ding et al. discussed the research deals in a GPS-enabled wireless sensor network as solution to monitor nuclear radiation. The node size is kept small to ensure the functions of communication. ZigBee multi-hop mesh routing protocol is used for wireless communication [6]. Shen et al. discussed a system, which is designed to predict wind power. Wireless sensor network is proposed for the collection and communication of the correlative real-time data [7]. Akyildiz et al. discussed sensor networks and the working of sensors, their potential applications and the communication setup for sensor networks [8]. Hashemian et al. discussed an integrated wireless system for condition monitoring with essential equipment in nuclear reactors by analysis and Measurement Services Corporation. AMS examined the electromagnetic compatibility of the wireless system with existing plant equipment [9]. Gomaa et al. discussed a WSN-based system for real-time monitoring of radiation levels at nuclear facilities by developing a prototype of wireless sensor node. The wireless node comprises of ZigBee technology for wireless communication, Arduino platform, TI CC2530 chips for implementation and Geiger Muller tube-based radiation detector [10]. Gomaa et al. discussed the prototype for a wireless sensor network that allows a real-time monitoring of radiation levels at nuclear facilities [11]. Bin et al. discussed the structure with a wireless system, compiled with a radiation sensor and associated peripherals implemented upon ZigBee technology using TI CC2530 chip to monitor radiation at nuclear facilities [12]. Chiti et al. discussed the main features of a wireless network and its use in disaster management system [13]. Fu et al. discussed the design of a wireless sensor network for gamma rays monitoring and also explains the requirements environment monitoring system for nuclear power plant [14]. Sav et al. discussed the mechanical properties of the prototype developed for sodium leakage in plant. Paper also discussed the fast breeder reactor component materials under the influence of sodium [15].

2 Proposed System

The concept is to design a low-cost system, which is capable of monitoring environmental parameters in the premises of the nuclear power plant. The information is collected with sensor nodes deployed at appropriate locations to monitor the radiation leakage, fire, gas temperature, and humidity of the surroundings to take action before leakage would take uncontrollable shape. All the data is collected at control room and analyzed with LabVIEW. A wireless sensor network is deployed with XBee as communication media. The system comprises of sensor nodes and a control room. If any of the parameter exceeds to its limit then the LED at control room will start blinking and hooter will on to alert about danger (Fig 1).

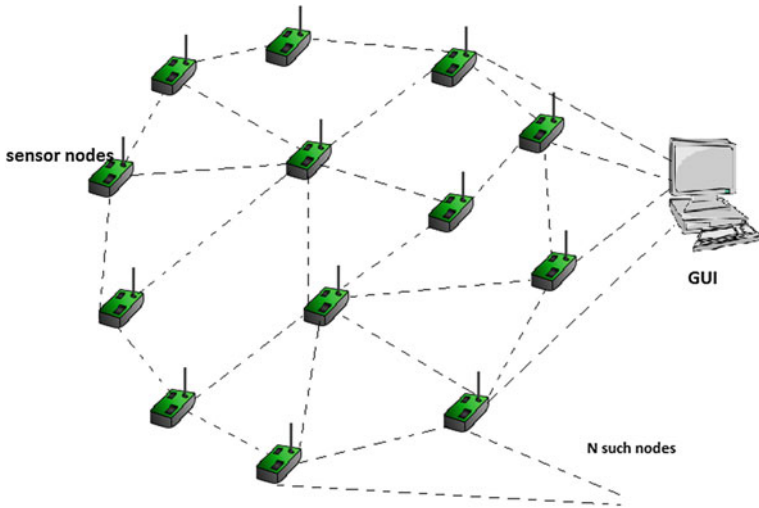


Fig. 1 Generalized block diagram

2.1 Sensor Node

It comprises of controller (Arduino uno), LCD (to display the content), RF modem (XBee), radiation sensor, fire sensor, gas sensor, temperature, and humidity sensor (as shown in Fig. 2).

Fig. 2 Block diagram for sensor node

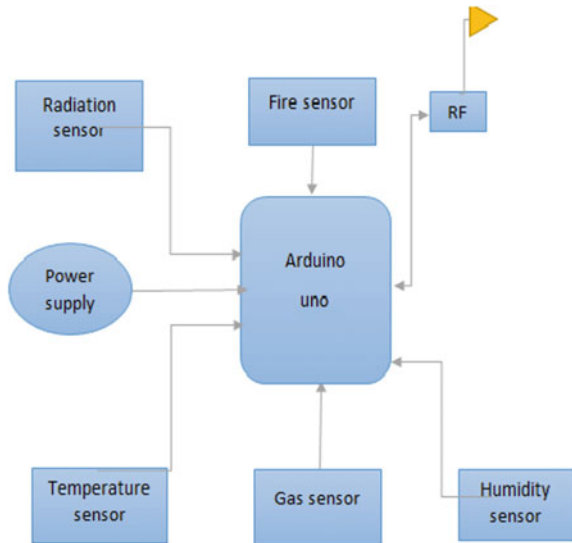
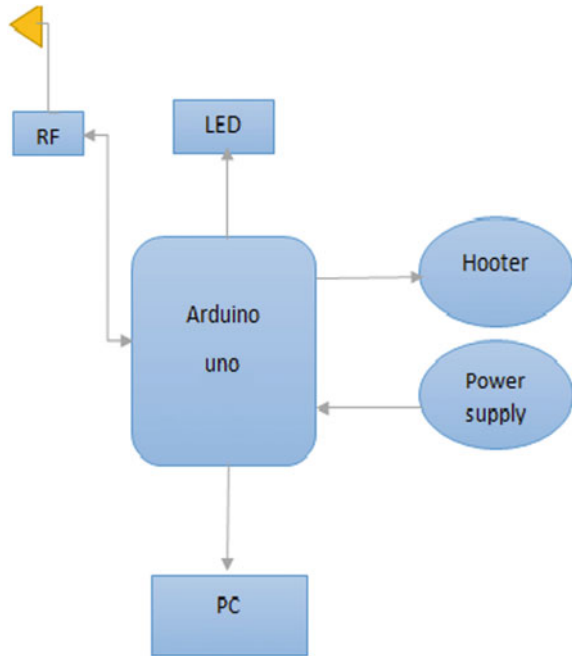


Fig. 3 Block diagram for control room



2.2 Radiation Sensor

It detects the radiation leakage in and around the plant. Temperature sensor—measures the temperature. Gas sensor—detects the harmful gases. Fire sensor—detects the occurrence of fire. Humidity sensor—measures the humidity inside the plant.

2.3 Control Room

All the data measured by sensor nodes is collected at control room wirelessly through XBee. The node comprises of controller (Arduino uno), LED, RF modem (XBee), hooter, and desktop for LabVIEW as data logger and analysis (Fig. 3).

3 Circuit and Simulation

The fire sensor is connected to digital pin as it activates only in case of fire and rest of the sensors are connected to analog pins which display the data continuously on the LCD attached to the node and transmits all the data to the receiver node via

XBee (RF modem) which can transmit data over long distance by passing data through a mesh network of intermediate devices.

The receiver has a GUI, sound alarm, LEDs, and a XBee attached to it. The receiver collects all the data from transmitter via XBee and displays it on the GUI. In case of fire, increased level of radiation or in presence on harmful gas—the sound alarm/hooter gets activated and the LED starts glowing (Figs. 4, 5 and 6).

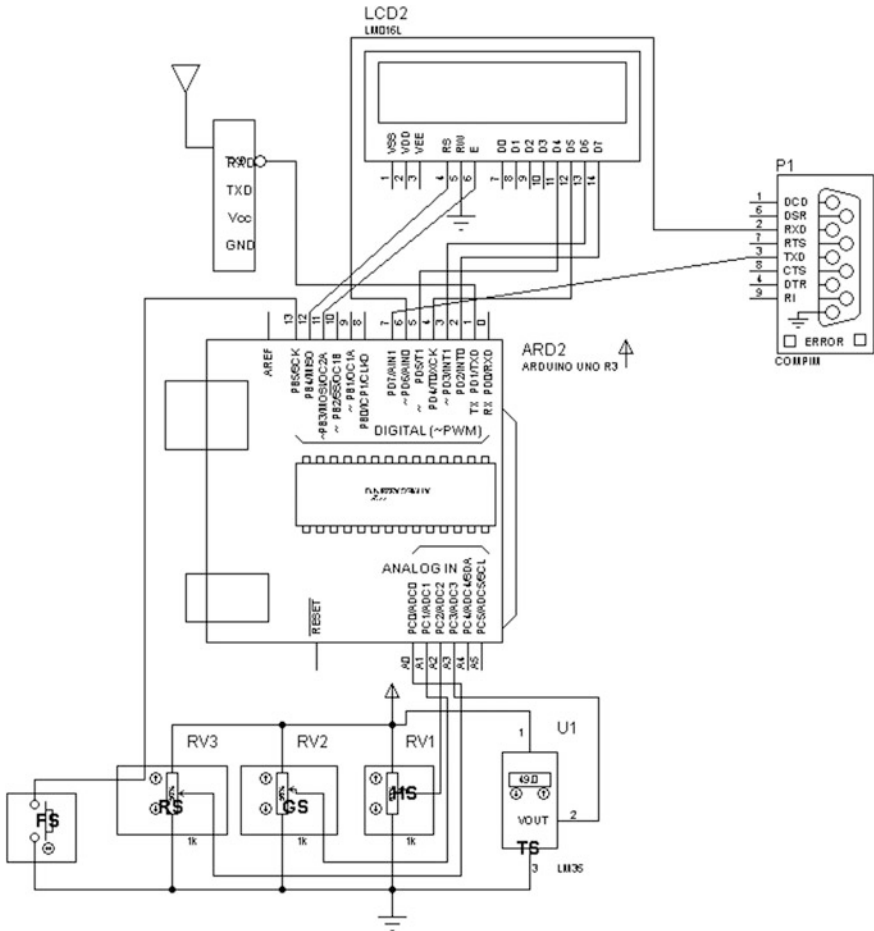


Fig. 4 Circuit diagram for sensor node

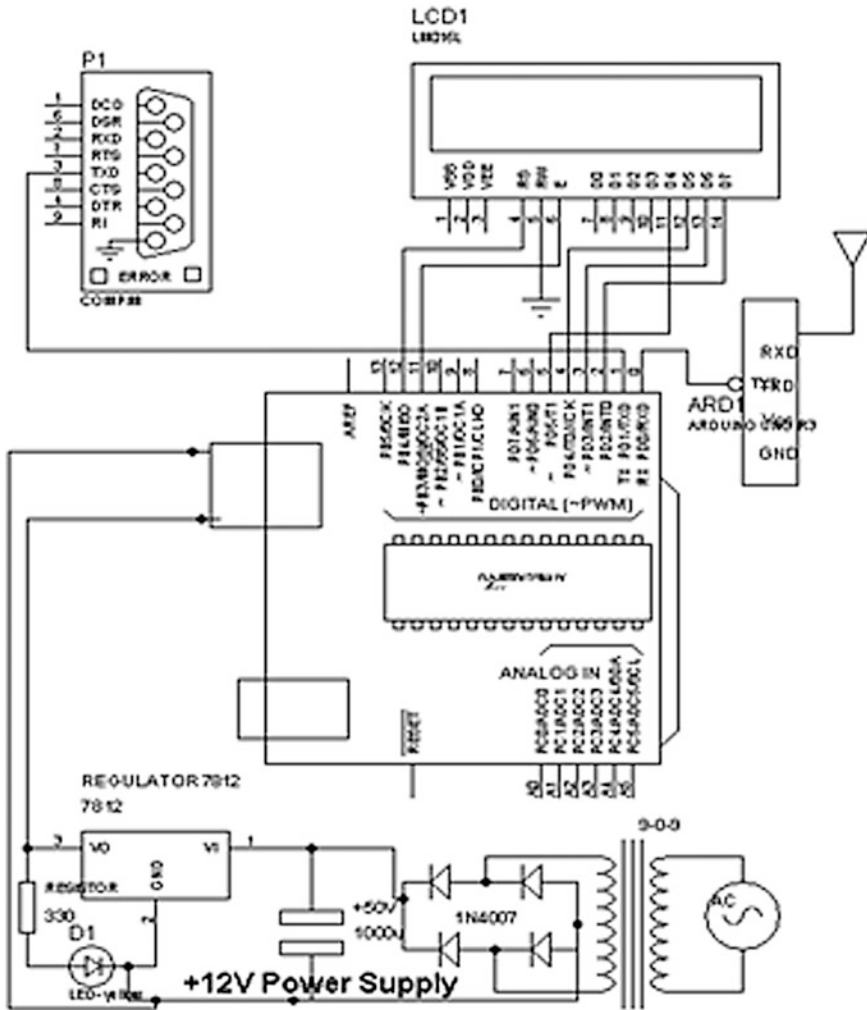


Fig. 5 Circuit diagram for receiver section/control room

4 Deployment Strategy of ‘N’ Nodes

Multiple sensor nodes are placed across the area. Let say A, B, C, D, E are five nodes placed at a location as shown in Fig. 7, have following duties:

A: Coordinator, B: End device, C: End device, D: End device, and E: End device

Node A acts as a coordinator for communicating to control room. All other nodes acts as transmitter node and communicate with coordinator. Node ‘A’ is in range of node ‘B’ and ‘C’ while node ‘D’ and ‘E’ are out of range for node ‘A’ but node ‘E’ and ‘D’ are in the range of node ‘B’ and ‘C,’ respectively. This network

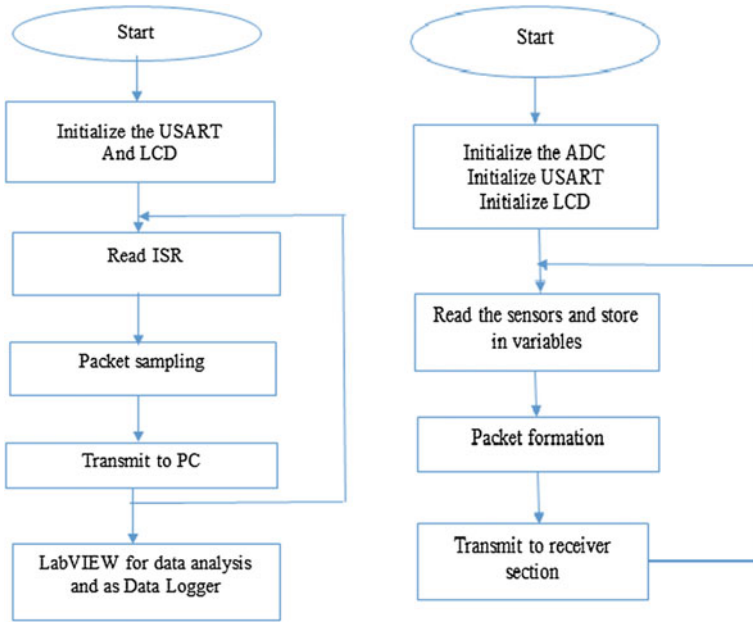
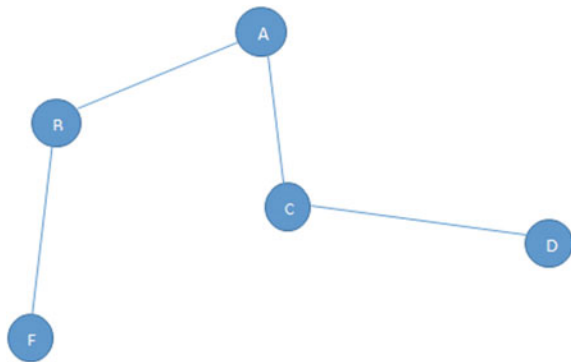


Fig. 6 Working flow chart for sensor node and control room

Fig. 7 Placement of sensor nodes



follows star and mesh networking to transmit the data. Node 'B' and 'C' directly transmits the data to node 'A,' forming a star network while node 'D' hop the data from node 'C' to 'A' similarly node E hops the data from node 'B' to 'A' forming a mesh network.

In the same way 'N' number of nodes communicate with each other and transmits their data by hopping the data from one node to another or directly transmitting the data when the node within the reach of receiver node.

5 Proteus Simulation

The sensor nodes are analyzed using Proteus professional software for integrated circuit designing. An Arduino uno board microcontroller is used for every node. Here we are presenting the working strategy making use of just two nodes—the transmitter node which transmits data received from the five sensors used, to the receiver node which further transmits the data to the data logger. The transmitter node uses an Arduino uno board which receives a constant power supply of 12 V. The four analog sensors namely fire sensor (represented by FS on the IC), gas sensor (represented by GS on the IC), radiation sensor (represented by RS on the IC), and the humidity sensor (represented by HS on the IC) are connected to the analog pins of the IC. The digital temperature sensor is connected to one of the digital pins of the IC. The five sensors run using a 5 V power supply. One LCD is attached to this node which simultaneously displays data of the sensors on the LCD screen. An RF modem simultaneously receives data displayed on LCD through its RXD pin and transmits it wirelessly via XBee to the receiver node. The receiver node also has similar structure as that of the transmitter node besides having a data logger (COMPIM). The receiver node transmits the data received from the transmitter node to the data logger besides sending its own sensors' data. It displays its own data simultaneously on the LCD attached to it. A code is used to give to command to the setup of the nodes on the Proteus professional software (Fig. 8 and Table 1).

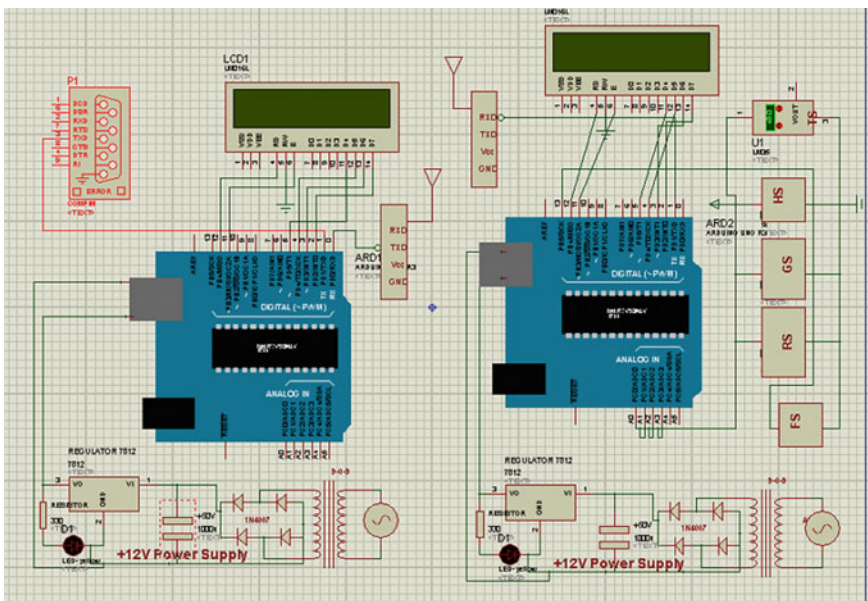


Fig. 8 Proteus simulation of model

Table 1 Components used for development

S. No.	Component	Model name	Description
1	Microcontroller board	ArduinUNO ATmega328P microprocessor	It is a 16 MHz, 8-bit microcontroller
2	XBee module	2.4 GHz XBee XB24Z7WIT-004 (ZigBee/802.15.4 modules) module from Digi. Series2	It has a frequency of 2.4 GHz, data range of 133–400 ft and transmits data at the rate of 250 kbps
3	Radiation sensor	RD2014 from Teviso Sensor Technologies Ltd.	It is a nuclear radiation sensor. It detects beta and gamma radiation and X-rays
4	Fire sensor	BE0010	It detects flame or wavelength at 760 nm range
5	Gas sensor	AS-MLV-P2 by ams	It is a multi-oxide semiconductor air quality sensor
6	Temperature sensor	1211 by Sunrom Technologies Ltd.	It can read temperatures from 2 to 60 °C
7	Humidity sensor	1211 by Sunrom Technologies Ltd.	It measures relative humidity from 1 to 100 %

6 Analysis with LabVIEW

The data of all the five sensors is displayed on the LabVIEW front panel. The graphs on the front panel indicate changes in the readings of the five sensors. The data from the designed system on Proteus professional is directly sent to LabVIEW using a visual serial ports emulator. The Proteus professional's data are sent from port designated as COM2. The LabVIEW receives this data on port designated COM1. The two ports are paired using visual serial ports emulator. Thus all the data sensed on one software is directly transmitted to another software using an emulator. Thus, LabVIEW actually displays the same data that was sensed by Proteus professional's setup (Figs. 9 and 10).

7 Results and Discussion

The prototype of the XBee-based wireless sensor network for nuclear radiation detection is successfully developed and tested. The prototype consisting of two sensor nodes—one as a transmitter node and the other as a receiver node has also been simulated using Proteus professional software and LabVIEW. The data for temperature, humidity, air quality, and radiation have been correctly obtained. Such sensor networks using sensor nodes transmitting data using XBee modules can be used in any desired area. The range of transmission can be changed by applying the specific network topology either mesh, star, and multi-mesh hop (Fig. 11).

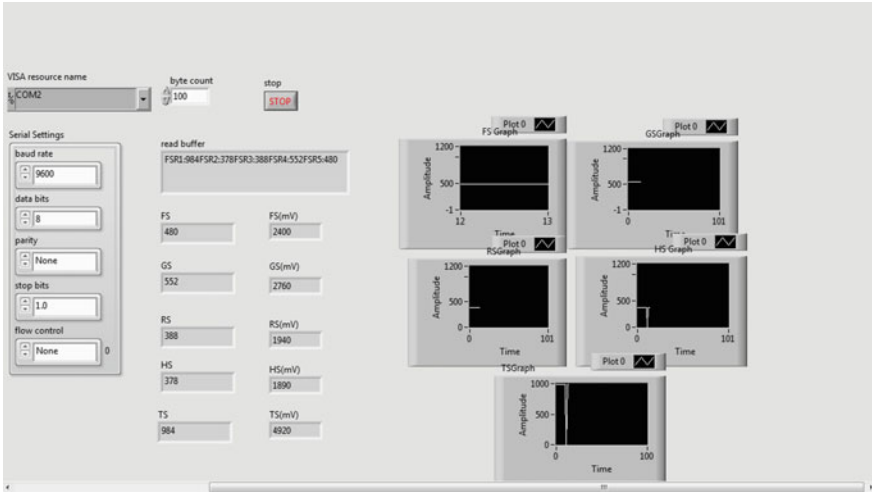


Fig. 9 LabVIEW front panel

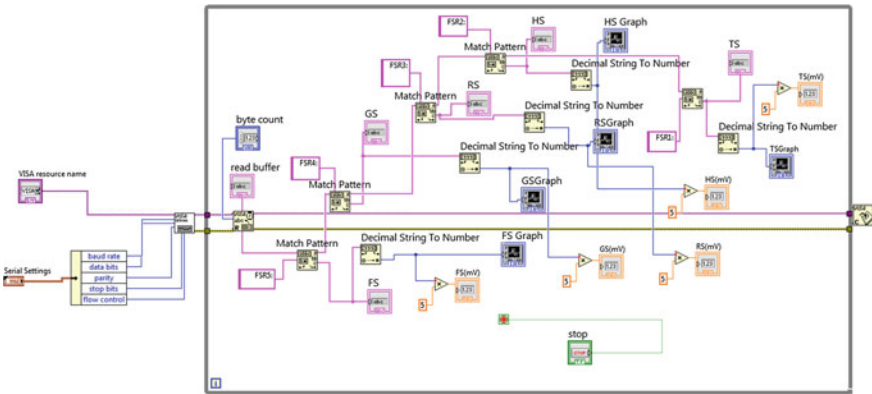


Fig. 10 LabVIEW back panel

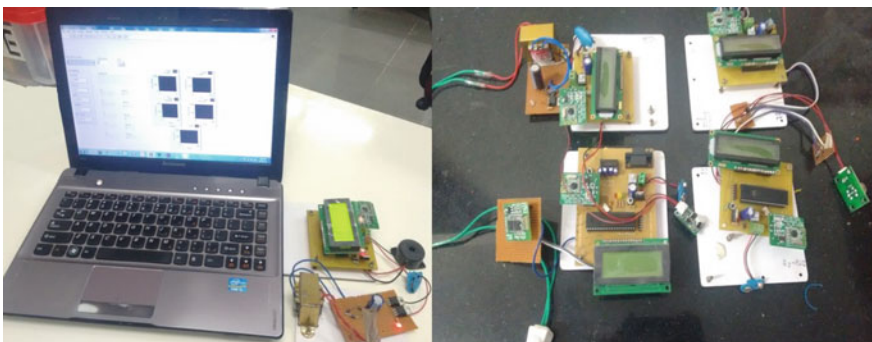


Fig. 11 Snapshot for developed prototype

8 Conclusion

This paper provides the study of XBee-based wireless sensor networks primarily for use in nuclear radiation detection, i.e., for safety purpose in nuclear power plant. It is just to provide alerts before any dangerous outcome like radiations going beyond the safety level. So, this WSN monitoring system helps to increase safety of the plant and prevent danger. These safety measures will reduce power plant repair cost because problem will be detected before it gets serious. Lives of people in and the around the plant would be saved. The environment would also be protected. Such high-level safety through WSN monitoring will popularize nuclear power as an alternative, clean source of power and reduce energy threats to the world. Also just by changing the type of sensor used, this type of WSN can be used for monitoring any kind of power plant or other area.

References

1. Lin, Ruizhong, Zhi Wang, and Youxian Sun. "Wireless sensor networks solutions for real time monitoring of nuclear power plant." *Intelligent Control and Automation*, 2004. WCICA 2004. Fifth World Congress on. Vol. 4. IEEE, 2004.
2. Kim, E. H., et al. "Analysis of the site characteristics of Korean nuclear power sites from the meteorological aspects." *Annals of Nuclear Energy* 34.9 (2007): 719–723.
3. Jang, Won-Suk, William M. Healy, and Mirosław J. Skibniewski. "Wireless sensor networks as part of a web-based building environmental monitoring system." *Automation in Construction* 17.6 (2008): 729–736.
4. Khedo, Kavi K., Rajiv Perseedoss, and Avinash Mungur. "A wireless sensor network air pollution monitoring system." arXiv preprint [arXiv:1005.1737](https://arxiv.org/abs/1005.1737) (2010).
5. Lopez, Javier, et al. "Trust management systems for wireless sensor networks: Best practices." *Computer Communications* 33.9 (2010): 1086–1093.
6. Ding, Fei, et al. "A GPS-enabled wireless sensor network for monitoring radioactive materials." *Sensors and Actuators A: Physical* 155.1 (2009): 210–215.
7. Shen, Liangping, et al. "Application of wireless sensor networks in the prediction of wind power generation." *Wireless Communications, Networking and Mobile Computing*, 2008. WiCOM'08. 4th International Conference on. IEEE, 2008.
8. Akyildiz, Ian F., et al. "Wireless sensor networks: a survey." *Computer networks* 38.4 (2002): 393–422.
9. Hashemian, H. M., et al. "Wireless sensors for equipment health and condition monitoring in nuclear power plants." *Future of Instrumentation International Workshop (FIIW)*, 2011. IEEE, 2011.
10. Gomaa, Rania, et al. "ZigBee wireless sensor network for radiation monitoring at nuclear facilities." *Wireless and Mobile Networking Conference (WMNC)*, 2013 6th Joint IFIP. IEEE, 2013.
11. Gomaa, Rania Ibrahim, et al. "Real-Time Radiological Monitoring of Nuclear Facilities Using ZigBee Technology." *Sensors Journal*, IEEE 14.11 (2014): 4007–4013.
12. Bin, Cai, et al. "Application research on temperature WSN nodes in switchgear assemblies based on TinyOS and ZigBee." *Electric Utility Deregulation and Restructuring and Power Technologies (DRPT)*, 2011 4th International Conference on. IEEE, 2011.

13. Chiti, Francesco, et al. "A broadband wireless communications system for emergency management." *Wireless Communications, IEEE* 15.3 (2008): 8–14.
14. FU, Hai-long, Ming-chun JIA, and Gui-chu PENG. "Research on Continuous Environmental Radiation Monitoring System for NPP Based on Wireless Sensor Network [J]." *Nuclear Electronics & Detection Technology* 6 (2010): 028.
15. SAV, Satya Murty, et al. "Wireless sensor network for sodium leak detection." *Nuclear Engineering and Design* 249 (2012): 432–437.

Design of Beam Steered Weighted Array with Sidelobe Cancellation

Apurva Garg, Akansha Sharma, Dr V.P. Dubey
 {Dept. of Electronics & Communication
 Engineering}
 Graphic Era Hill University
 Dehradun, India

Dr R. Gowri
 {Dept. of Electronics & Communication
 Engineering}
 University of Petroleum and Energy Studies
 Dehradun, India

Abstract: Smart antenna is one of the fastest emerging technologies. An antenna array is a set of individual antennas that are used for transceiving the electromagnetic signals. In this paper weighting method is used to control the behaviour of the array along with sidelobe cancellation techniques. Three basic algorithms that are Kaiser-Bessel, Blackman and Gaussian are used to find the array weights. As a result an array factor of amplitudes 1, 0.6561, 0.2521 with side lobes which are being cancelled to yield maximum directional beam.

Index Terms— Kaiser-Bessel, Blackman, Gaussian, Side-lobe cancellation techniques, Array factor, HPBW

I. INTRODUCTION

With advancement in both size and power efficient computing, the concept of smart antennas has quickly emerged as a legitimate topic due to current exponential growth in all forms of wireless communication and sensing. This advancement has been facilitated by advancing digital signal processing hardware and also by the global interest in wideband wireless applications.

An array of antennas mounted on vehicles, ships, aircrafts, satellites and base stations is expected to play an important role in fulfilling these services and increased demand for channels. The term 'smart antenna' generally refers to any antenna array in a processor which can be adjusted or can adapt according to EM environment, its own beam pattern in order to emphasize signals of interest and to minimize interfering signals. The rapid growth of smart antennas is fueled by two reasons; First, the technology for high speed analog-to-digital converter (ADC) and high speed digital signal processing is at an rapid high rate[1]. It is a well-known fact that the performance of beam forming array has been degraded because of interfering signals.

Important characteristics [2]. The power radiated should be in desired direction with effective sidelobe cancellation. The side lobe cancellation can be obtained by applying high power to the central element and comparatively low power levels to the periphery elements [2]. So, physical implementation of the defined array is difficult than that in uniformly excited arrays. To implement such arrays, variable phase shifters and/or attenuators are required for each antenna element. The use of digital phase shifters and/or attenuators results in deviation (error) from the desired values of amplitude and phase excitations. Because of the deviation obtained we can also obtain some amplitude at undesired directions which can be called as side lobes. In many applications, a less costly and complex system is desirable where only few elements are arranged to have the main side lobe [3]. Towards this goal many approaches have been proposed; for example, see [4]-[8].

In [4], the advantages of using uniformly excited arrays have been proposed in order to get main lobe in desired direction. In [5], the authors define a method for side lobe cancellation of linear and planar arrays by adjusting the amplitude and phase. For this purpose the authors have used genetic algorithm so as to define that by how much factor the amplitude and phase should be readjusted so as to minimize the side lobe level.

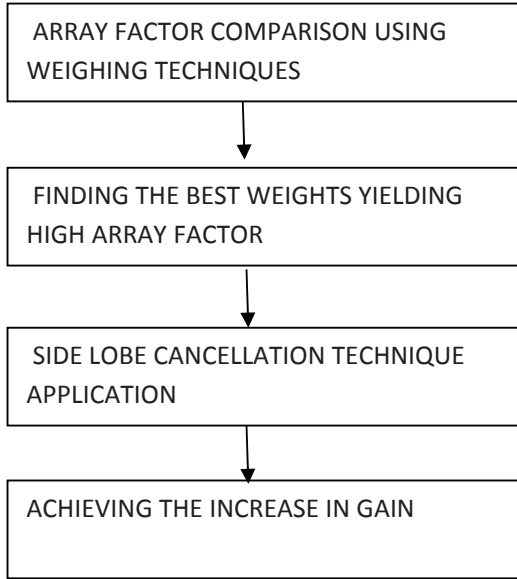
Nowadays, there is an immense interest in reconfigurable arrays for which a single antenna is used to radiate many patterns with common excitation or it uses the concept of tapering the elements [7]- [8].

In this paper, we propose three algorithms i.e. Gaussian algorithm, Blackman algorithm, and Kaiser-Bessel algorithm to calculate the weights, these weights are used to calculate the array factor and then the one with maximum array factor is being chosen. Moreover side lobe cancellation techniques are being applied to cancel the sidelobes obtained in the array factor and hence generate null over a wide angular region. Then the gain is being

calculated for the respective array factor.

The paper is organized as follows. The mathematical formulation is reported in Section II, while the numerical results are being reported in Section III to assess the accuracy and the flexibility in the proposed design. The directivity and gain are also drawn in this section for the main lobe obtained after side lobe cancellation. Eventually conclusion is drawn in Section IV.

II. PROPOSED DESIGN



A. Design of Weighted Array

Smart antennas are composed of a collection of two or more antennas called array of antennas and works to establish a unique radiation pattern for the electromagnetic environment. The behavior of array transcends the specific elements used and this array can take any geometrical form.

For an antenna array, array factor (AF) is calculated which depends on the geometric arrangement of array elements, the spacing of the elements and the electrical phase of the elements. It is considered that the elements are equally spaced but their amplitudes are different due to weighing factors. The technique used to calculate their amplitude is known as array weighting [2]. The weights w_n can be chosen to meet the specific criteria. Generally the criterion is to minimize the side lobes or to achieve null in the undesired directions.

Considering a symmetric linear array with an even number of elements N . The array is symmetrically weighted with

weights. The array factor for even number of elements is found by summing the weighted outputs of each element such that [2]:

$$AF_{\text{even}} = w_m e^{-\frac{j(2M-1)Bd \sin \theta}{2}} + \dots + w_1 e^{-\frac{jBd \sin \theta}{2}} + w_1 e^{\frac{jBd \sin \theta}{2}} + \dots + w_m e^{\frac{j(2M-1)Bd \sin \theta}{2}} \quad (1)$$

The array factor for odd number of elements is found by [2]:

$$AF_{\text{odd}} = \sum_{n=1}^{M+1} w_n \cos(2(n-1)u) \quad (2)$$

$$\text{where } u = \pi d / \lambda \sin \theta$$

There are various possible window functions available that can provide weights for use with linear arrays. The algorithms used for weight calculation are as follows:

a) BLACKMAN

The Blackman weights are defined by [2]:

$$w(k+1) = .42 - .5 \cos\left(\frac{2\pi k}{N-1}\right) + .08 \cos\left(\frac{4\pi k}{N-1}\right)$$

$$k = 0, 1, 2, \dots, N-1 \quad (3)$$

b) GAUSSIAN

The Gaussian weights are determined by the Gaussian function to be [2]:

$$w(k+1) = e^{\left(-\frac{1}{2}a \frac{(k-\frac{N}{2})^2}{\frac{N}{2}}\right)^2}$$

$$k = 0, 1, 2, \dots, N-1 \quad a \geq 2 \quad (4)$$

c) KAISER-BESSEL

The Kaiser-Bessel weights are determined by [2]:

$$w(k) = \frac{I_0 \left[\pi a \sqrt{1 - \left(\frac{k}{\frac{N}{2}}\right)^2} \right]}{I_0[\pi a]}$$

$$k = 0, 1, 2, \dots, \frac{N}{2} \quad a > 1 \quad (5)$$

B. Calculation Of Weights

The weights were found using the three equations as specified in Blackman, Gaussian and Kaiser-Bessel (1) to (3). The Normalized array factor was calculated and plotted v/s angle. Then the three were compared to find out the best one yielding maximum array factor [2]. It was noted that Kaiser-Bessel weights provided one of the lowest array side lobe levels while still maintaining nearly the same beamwidth as uniform weights.

C. Side Lobe Cancellation

The basic goal of side lobe cancellation is to choose array weights such that a null is placed in the direction of interference while the main lobe maximum is in the direction of interest. In our current development we have discussed fixed side lobe cancellation for one fixed known desired angle and two fixed undesired interferers. We have assumed that all signals are operating at same carrier frequency.

Assuming a 6-element array with desired angle and interferers, the array factor is given by

$$a(\theta) = \begin{bmatrix} e^{-2.5jkdsin\theta} \\ e^{-1.5jkdsin\theta} \\ e^{-0.5jkdsin\theta} \\ 1 \\ e^{0.5jkdsin\theta} \\ e^{1.5jkdsin\theta} \\ e^{2.5jkdsin\theta} \end{bmatrix} \quad (6)$$

Array weights are calculated as

$$w^T = [w_1 w_2 w_3 w_4 w_5 w_6] \quad (7)$$

The total array output for six element array can be given as:

$$S = w^T \cdot a = w_1 e^{-2.5jkdsin\theta} + w_2 e^{-1.5jkdsin\theta} + w_3 e^{-0.5jkdsin\theta} + w_4 e^{0.5jkdsin\theta} + w_5 e^{1.5jkdsin\theta} + w_6 e^{2.5jkdsin\theta} \quad (8)$$

The array output for the desired signal will be designated as S_D whereas the array output for the interfering signals will be designated by S_1, S_2, S_3, S_4 and S_5 [1]. For side lobe cancellation the array weights are calculated, which must satisfy the three conditions that is the total array output should be made unity and for the interfering signals the

output should be made null. The conditions can be specified as:

$$S_D = w_1 e^{-2.5jkdsin\theta D} + w_2 e^{-1.5jkdsin\theta D} + w_3 e^{-0.5jkdsin\theta D} + w_4 e^{0.5jkdsin\theta D} + w_5 e^{1.5jkdsin\theta D} + w_6 e^{2.5jkdsin\theta D} = 1 \quad (9)$$

$$S_1 = w_1 e^{-2.5jkdsin\theta_1} + w_2 e^{-1.5jkdsin\theta_1} + w_3 e^{-0.5jkdsin\theta_1} + w_4 e^{0.5jkdsin\theta_1} + w_5 e^{1.5jkdsin\theta_1} + w_6 e^{2.5jkdsin\theta_1} = 0 \quad (10)$$

$$S_2 = w_1 e^{-2.5jkdsin\theta_2} + w_2 e^{-1.5jkdsin\theta_2} + w_3 e^{-0.5jkdsin\theta_2} + w_4 e^{0.5jkdsin\theta_2} + w_5 e^{1.5jkdsin\theta_2} + w_6 e^{2.5jkdsin\theta_2} = 0 \quad (11)$$

$$S_3 = w_1 e^{-2.5jkdsin\theta_3} + w_2 e^{-1.5jkdsin\theta_3} + w_3 e^{-0.5jkdsin\theta_3} + w_4 e^{0.5jkdsin\theta_3} + w_5 e^{1.5jkdsin\theta_3} + w_6 e^{2.5jkdsin\theta_3} = 0 \quad (12)$$

$$S_4 = w_1 e^{-2.5jkdsin\theta_4} + w_2 e^{-1.5jkdsin\theta_4} + w_3 e^{-0.5jkdsin\theta_4} + w_4 e^{0.5jkdsin\theta_4} + w_5 e^{1.5jkdsin\theta_4} + w_6 e^{2.5jkdsin\theta_4} = 0 \quad (13)$$

$$S_5 = w_1 e^{-2.5jkdsin\theta_5} + w_2 e^{-1.5jkdsin\theta_5} + w_3 e^{-0.5jkdsin\theta_5} + w_4 e^{0.5jkdsin\theta_5} + w_5 e^{1.5jkdsin\theta_5} + w_6 e^{2.5jkdsin\theta_5} = 0 \quad (14)$$

By using this method the array weights for side lobe cancellation are being calculated and are simulated.

III. DIRECTIVITY

The beamwidth of a linear array is determined by the angular distance between the half-power points of the main lobe. The two half power points ($\theta + \text{and} \theta -$) are found.

To solve for $\theta \pm$ we get [2]:

$$\theta \pm = \sin^{-1} \left(\frac{1}{B_d} \left(\pm \frac{2.782}{N} - \delta \right) \right) \quad (15)$$

The half-power beam width (HPBW) is now easily shown to be [2]:

$$HPBW = |\theta(+) - \theta(-)| \quad (16)$$

The directivity can now be evaluated as [2]

$$D = \frac{41600}{(HPBW)^2} \quad (17)$$

To calculate gain we have used the equation [2] (17)

$$Gain = B.D \tag{18}$$

IV. SIMULATION RESULTS

In this section, the values of different weights calculated using Gaussian, Blackman, and Kaiser-Bessel algorithm are shown. These weights were compared and the best out of the three was found to be Kaiser-Bessel. The calculated weights are depicted in TABLE I.

TABLE I

CALCULATION OF WEIGHTS

Weights	Gaussian	Kaiser-Bessel	Blackman
W1	1	1	1
W2	0.3679	0.6561	0.2364
W3	0.0498	0.2152	0

The weights of the three algorithm obtained were used to obtain the array factor and was then plotted with respect to the angle (degrees) as given in Equation (1). The graph is depicted in Figure 1, which shows the impact of undesired signals in the form of side lobe, and the desired signal shows the maximum amplitude in the desired angle which is giving the amplitude of 1.8 approximately in case of Kaiser Bessel.

Now from Figure 1 the value of the undesired angles from the graph are calculated to obtain the weights for side lobe cancellation. The undesired angles (degree) were found to be $\theta_1 = -70, \theta_2 = -75, \theta_3 = -80, \theta_4 = -85, \theta_5 = -90$.

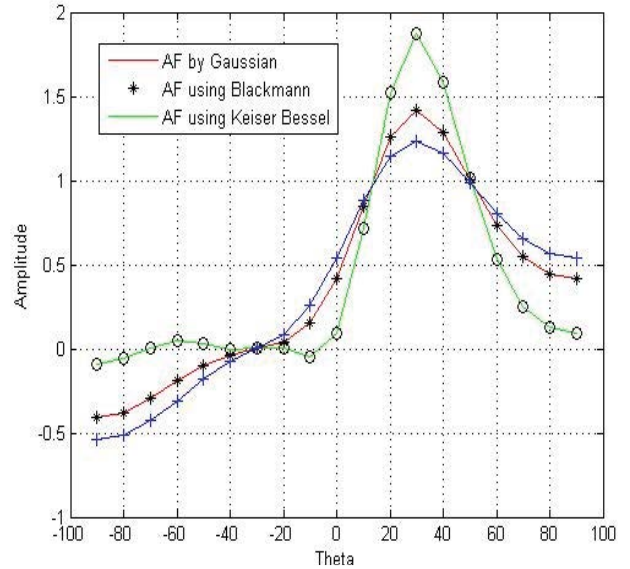


Fig.1 Comparison of weights using different algorithm i.e. Gaussian, Blackman and Kaiser-Bessel

The calculated weights using side lobe cancellation technique by the use of mentioned desired angle is shown in TABLE II.

TABLE II

CALCULATION OF WEIGHTS WITH SIDELOBES

Weights	WITHSIDELOBES	WITHOUT SIDELOBES
W1	1	$0.1464 \pm 0.0269i$
W2	0.6561	$0.7381 \pm 0.0809i$
W3	0.2152	$1.4824 \pm 0.054i$

It is known that the side lobes behaviour is a pattern feature quite sensitive to the tolerances of the amplitude and phase coefficients. This paper deals with the effect of side lobe cancellation and steering the antenna mainlobe in the

desired direction. For that purpose we have chosen the Kaiser Bessel algorithm and calculated its weights without side lobe cancellation which is depicted in Table II.

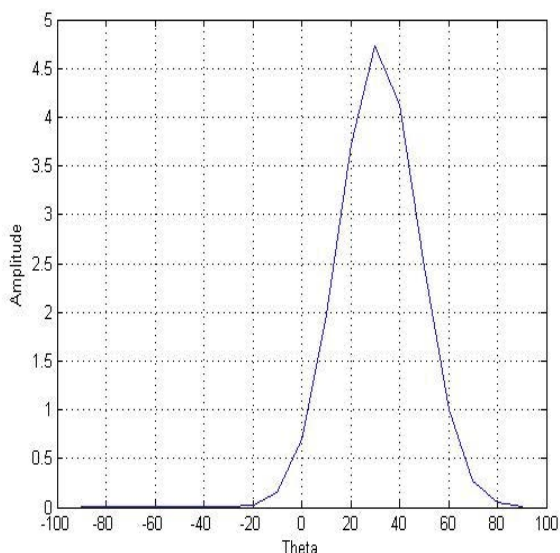


Fig.2 Graph depicting sidelobe cancellation and main beam at 30°

The new weights thus obtained using the undesired angle is now used to calculate the value of array factor and is then plotted. Figure 2 depicts the side lobe cancellation at all the undesired angles and the beam is steered only at desired angle that is 30° . The half power beam width thus obtained for the mainlobe result 17.2095, Directivity is 140.4608 and the gain in the desired direction obtained is 98.3226.

V. CONCLUSION

A computationally efficient and analytical method is being proposed for comparing the array factors of Gaussian, Kaiser-Bessel and Blackman algorithms using MATLAB.

The array factor thus obtained was used to choose the best out of the three algorithms which is found to be Kaiser Bessel giving the maximum value of array factor. It has been shown that the side lobe cancellation over a wide range in the uniformly excited planar array can be obtained by readjusting the amplitudes. Finally beam was steered at desired angle of 30 degrees by having only main beam with all sidelobe's intensity nullified.

REFERENCES

- [1] Daniel E. Lawrence, Member, IEEE, "Low Probability of Intercept Antenna Array Beam forming", *IEEE Trans. Antennas Propag.*, vol. 58, no. 9, 9 Sept, 2010.
- [2] Frank B. Gross, Phd (Senior System Engineer, Argon ST, Fairfax, Virginia) in 'Smart antennas for wireless Communications'.
- [3] J. R. Mohammed and K.H. Sayidmarie, "Side Lobe Cancellation for Uniformly Excited Planar Array Antennas by Controlling the Side Elements", *IEEE Antennas and Wireless Propagation Letters*, Vol. 13, 2014.
- [4] A.F. Morabito and T. Isemia, "Direct Radiating Arrays for Satellite Communication via Aperiodic Tiling," *Prog. Electromagn Res.*, vol. 93, pp. 107-124, 2009
- [5] P. Lopez, J. A. Rodriguez, F. Ares, and E. Moreno, "Low Sidelobe Patterns from Linear and Planar Arrays With Uniform Excitation Except for Phases of a small Number of Elements," *Electron Lett.*, vol. 37, no. 25, pp. 1495-1497, Dec 2001.
- [6] A.F. Morabito, A. Massa, P. Rocca, and T. Isemia "An Effective approach to the synthesis of phase only reconfigurable linear arrays," *IEEE Trans. Antennas Propag.*, vol. 60, no. 8, pp. 3622-3631, Aug 2012
- [7] J. A Rodriguez, A. Trastoy, J. C. Bregains, F. Ares, and G. Franceschetti, "Beam reconfiguration of linear arrays using parasitic elements," *Electron Lett.*, vol.42, no. 03, pp. 131-133, Feb 2006.
- [8] J. R. Mohammed, "Phased Array antenna With Ultra low sidelobes", *Electron Lett.*, vol. 49, no.17, pp. 18-19,2013.

Design of Wearable Device for Muscle Fatigue Monitoring

Sweety Siwach, Anita Gehlot and Anshuman Prakash

Abstract Exercise is very beneficial to our health but evidence show that intense training and heavy exercises out by fortitude athletes can cause skeletal muscle damage, which is known as muscle fatigue. For athletes, muscle fatigue is perhaps one of the major causes of degradation in their performance. There are various methods to monitor the muscle fatigue, of which surface electromyography is an important one. In this research work, a system is proposed to monitor muscle fatigue continuously and transmit the data wirelessly to a handheld portable device using RF module. A threshold point is set by calculating the average mean and in case of any danger a notification will be given by the device indicating onset of fatigue.

Keywords Muscle fatigue monitoring · sEMG · Microcontroller · Wearable sensor

1 Introduction

In the nineteenth century the prevailing view was that fatigue was caused by processes in the central nervous system. Mosso (1892) has been quoted as advocating this view, but actually he clearly demonstrated that muscle fatigue could be entirely peripheral. Mosso was the first to record the decrease in muscle force by means of an “ergograph” during fatiguing contractions in humans, and he found a comparable decline in force both during voluntary contractions and during stimulation of the muscle. There are mainly two types of fatigue, high frequency and low frequency fatigue. In high frequency fatigue, the muscle fatigues very rapidly on continuous workout but also recovers after a short rest while low frequency fatigue is one in which fatigue develops more slowly with low intensity. Fatigue represents a reduction in the capability of muscle to generate force. So far two main causes of

Sweety Siwach (✉) · Anita Gehlot · Anshuman Prakash
University of Petroleum and Energy Studies, Bidholi via Prem Nagar, Dehradun, India
e-mail: ssiwach112@gmail.com

muscle fatigue are discovered, first one was observed when nerve's ability to generate a sustained signal is limited and second comes the declined ability of the muscle fiber to contract while some other causes lack of essential nutrients and oxygen in muscle and also accumulation of waste products mainly lactic acid.

Many systems are developed based on different techniques to monitor the muscle fatigue. [1] Dayan, et al. proposed a system a signal spike and peak counter system which is then correlated with median frequency for monitoring the muscle fatigue [2] Ahamed, et al. proposed a system in which muscle fatigue is monitored by calculating average EMG, the highest peak of the signal and root mean square (RMS) values after recording the EMG values. [3] Tanaka, et al. proposed a system which uses myoelectric signals to monitor the muscle condition. [4] Pioggia, et al. proposed a system in which a wearable platform is developed to monitor the muscle fatigue by observing the sEMG in absence and presence of fatigue after which STFT of signal is calculated in absence and presence on fatigue. [5] Karagözoğlu, et al. proposed a system which used FFT on platform MATLAB to calculate the power spectrum of the signals obtained. [6] Na, et al. developed a muscle fatigue monitoring system by observing the variation in the muscles before the fatigue is approached and after the fatigue is approached. [7] Cifrek, et al. proposed a system where classical and modern signal processing techniques are explained which includes frequency domain, time domain, time–frequency, and time scale representations. [8] Kang-Ming, et al. proposed a system in which (DWT), (EMD), and (EEMD) are calculated to monitor the muscle fatigue progression.

1.1 Proposed System

The system consists of a real-time monitoring of muscles and wirelessly transmit the data using RF module to a handheld portable device and also will notify the user when the fatigue is approached (Fig. 1).

2 Methodology

The methodology behind this work started from developing a data logger in lab VIEW. The data logger consists of a wave form diagram indicating EMG values in amplitude and time relationship form other part consists of a table having EMG value in volts with date and time of recording data. Next step started by collecting muscle fatigue data of two specific groups, one those who were suffering from muscle fatigue and other who were not suffering from muscle fatigue and after collecting data it was observed that the average mean values of both the groups were different. After observing the average mean values, a range was set with the lowest value of muscle fatigue and the maximum value of muscle fatigue, i.e.,

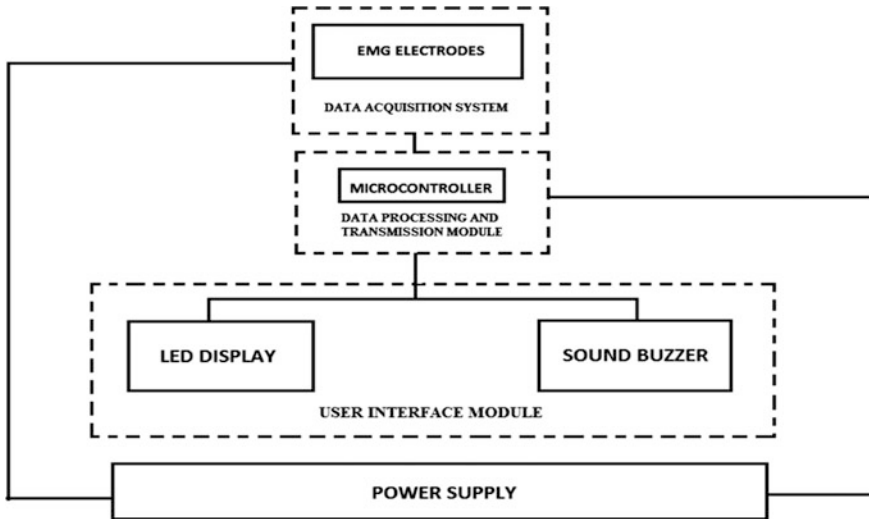


Fig. 1 System block diagram showing the main modules used in the system. The data acquisition system consists of EMG electrodes through which data is recorded. Data processing and transmission module consists of arduino uno which is a 8 bit microcontroller and works on 16 MHz frequency. Next part consists of user interface module containing led display or sound buzzer depending on user requirement

indicating onset of fatigue. Now when the real-time monitoring of muscles will be carried out, if the value exceeds the specified range, a notification will be sent to the user or the coach regarding the danger.

3 Algorithm

The flow chart shows the working model of the proposed system in which data from EMG sensor is continuously monitored and wirelessly transmitted through RF module to a handheld device to indicate the status of subject. A threshold value is set after careful examination of both the groups, first group having person affected of muscle fatigue and second group having persons suffering from muscle fatigue. If the recorded value is same as the threshold value, a notification in the form of led or buzzer is sent to the subject. This process is continually repeated (Fig. 2).

4 Result and Simulation

Figure shows the two different waveforms of recorded EMG values. After obtaining the couple of readings through electromyography sensor from a group of people suffering from muscle fatigue and other group of people who are free from muscular

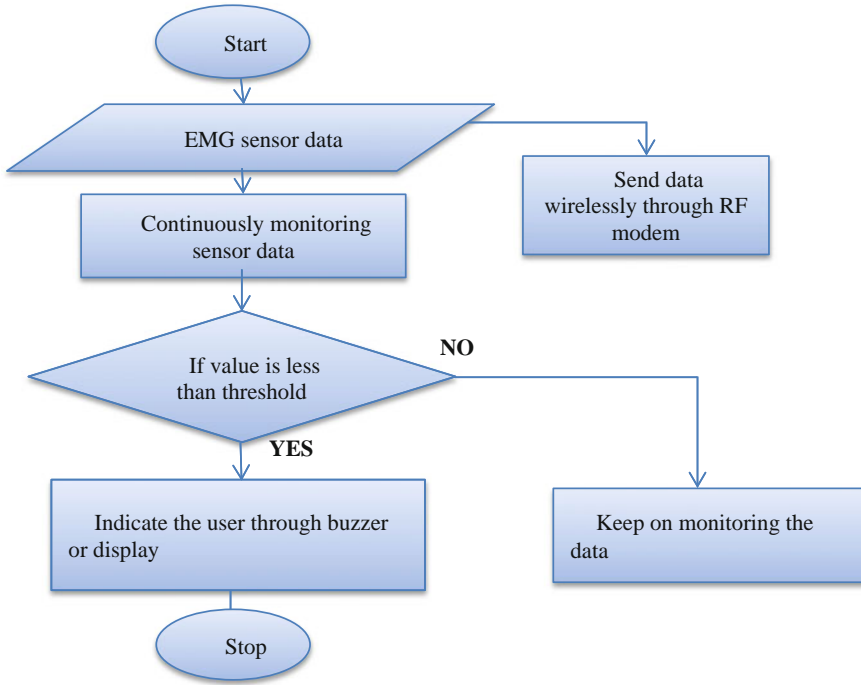


Fig. 2 Flow chart of the proposed system

fatigue, a threshold value is set. This value is decided. Now when the real-time monitoring is carried out, the data is continuously transferred to a handheld portable device with the help of RF module which is connected on both the end, i.e., transmitter and receiver end. When the value from the sensor is crossed above the threshold value, an indication in form of alarm or led is given as output (Figs. 3 and 4).

5 Discussion and Conclusion

Muscle fatigue has not only been observed in athletes but also in elderly people. Monitoring the muscle fatigue can also be useful in rehabilitation, because excessive exercises can be very dangerous to our muscles. Many technics are used to monitor the muscle fatigue some of them are using power spectrum, STFT, mean and median frequency observation and many more. The technique used here is to observe the average mean between the two groups (first group is for people where no muscle fatigue is observed and second one consists of people suffering muscle fatigue). So it is concluded that a wearable device is developed which can give the status of person's muscle contraction activity and can also alert them of the danger.

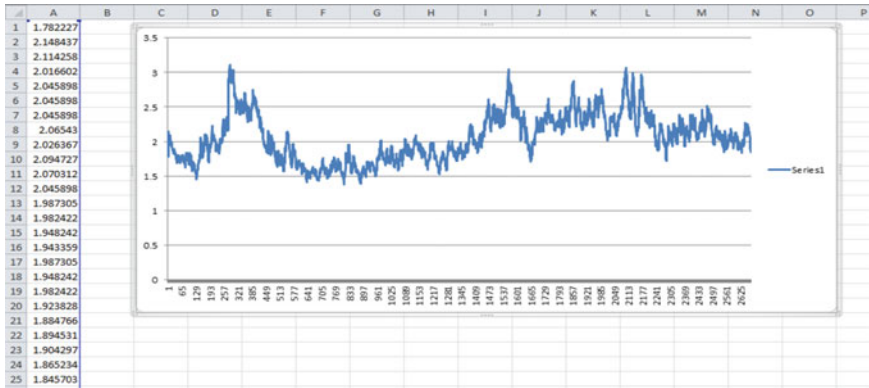


Fig. 3 shows waveform in presence of fatigue. As the waveform shows that the amplitude is decreasing at every instant which means person suffering from muscle fatigue cannot withstand more muscle contraction and failed to sustain the force. From initial stage to the final stage of recording procedure their muscles witness in pain

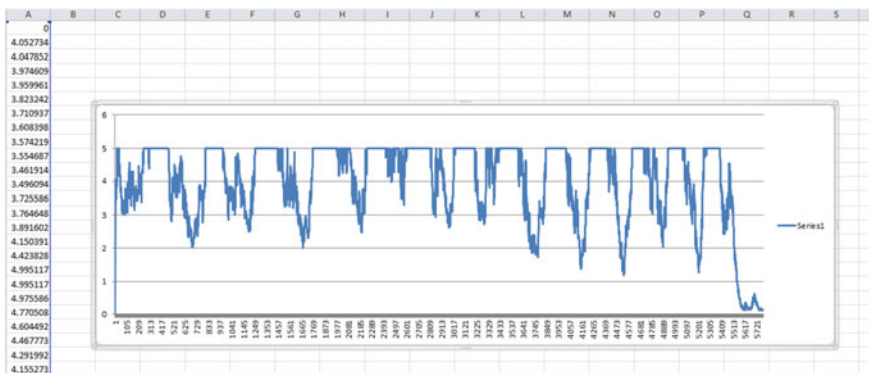


Fig. 4 shows the EMG values and the recorded amplitude waveform of persons not suffering from muscle fatigue. As the waveform shows here that after a particular value the graph is gradually falling down which shows the decline in muscle activity also referred to as initial stage of muscle fatigue

Of course, further experiments are required to confirm the validity of the monitoring system.

The research can be further extended from monitoring to controlling. Until now, a handheld portable monitoring system is developed but further these EMG signals can be used to control mechanical systems like robotic moments or automate home, i.e., it can control the turning on and off of lights, fans, or other gadgets. There are systems which can use EMG signals to control the forward and backward moment of the robot similarly further actions of the robot can be controlled.

References

1. Dayan, O., Spulber, I., Eftekhar, A., Georgiou, P., Bergmann, J., & McGregor, A. (2012, November). Applying EMG spike and peak counting for a real-time muscle fatigue monitoring system. In *Biomedical Circuits and Systems Conference (BioCAS), 2012 IEEE* (pp. 41–44). IEEE.
2. Ahamed, N., Sundaraj, K., Ahmad, R. B., Rahman, M., Islam, A., & Ali, A. (2012, November). Non- invasive electromyography-based fatigue detection and performance analysis on m. biceps brachii muscle. In *Control System, Computing and Engineering (ICCSCE), 2012 IEEE International Conference on* (pp. 302–306). IEEE.
3. Tanaka, Mami, Takeshi Okuyama, and Kazuhiro Saito. “Study on evaluation of muscle conditions using a mechanomyogram sensor.” *Systems, Man, and Cybernetics (SMC), 2011 IEEE International Conference on*. IEEE, 2011.
4. Pioggia, G., Tartarisco, G., Ricci, G., Volpi, L., Siciliano, G., De Rossi, D., & Bonfiglio, S. (2010, November). A wearable pervasive platform for the intelligent monitoring of muscular fatigue. In *Intelligent Systems Design and Applications (ISDA), 2010 10th International Conference on* (pp. 132– 135). IEEE.
5. Karagözoğlu, Bahattin, Waleed H. Sindi, and Ahmed A. Al-Omari. “Design and development of a practical muscle fatigue monitor.” *GCC Conference & Exhibition, 2009 5th IEEE*. IEEE, 2009.
6. Na, Y., Kwon, S., Kim, J., & Choi, C. (2013, October). Variation of dynamic muscle model during fatigue-inducing voluntary contraction. In *Systems, Man, and Cybernetics (SMC), 2013 IEEE International Conference on* (pp. 4854– 4859). IEEE.
7. Cifrek, M., Medved, V., Tonković, S., & Ostojić, S. (2009). Surface EMG based muscle fatigue evaluation in biomechanics. *Clinical Biomechanics*, 24(4), 327–340.
8. Chang, Kang-Ming, et al. “Exercise muscle fatigue detection system implementation via wireless surface electromyography and empirical mode decomposition.” *Engineering in Medicine and Biology Society (EMBC), 2013 35th Annual International Conference of the IEEE*. IEEE, 2013.

Effect of projectile on incomplete fusion reactions at low energies

Vijay R. Sharma^{1,*}, Mohd. Shuaib², Abhishek Yadav¹, Pushpendra P. Singh³, Manoj K. Sharma⁴, R. Kumar¹, Devendra P. Singh⁵, B. P. Singh^{2,**}, S. Muralithar¹, R. P. Singh¹, R. K. Bhowmik¹, and R. Prasad²

¹NP-Group, Inter University Accelerator Centre, New Delhi - 110 067, India

²Department of Physics, Aligarh Muslim University, Aligarh 202 002, India

³Department of Physics, Indian Institute of Technology Ropar, Punjab 140 001, India

⁴Physics Department, S. V. College, Aligarh - 202 001, India

⁵Department of Physics, University of Petroleum and Energy Studies, Dehradun - 248 007, India

Abstract. Present work deals with the experimental studies of incomplete fusion reaction dynamics at energies as low as $\approx 4 - 7$ MeV/A. Excitation functions populated via complete fusion and/or incomplete fusion processes in $^{12}\text{C}+^{175}\text{Lu}$, and $^{13}\text{C}+^{169}\text{Tm}$ systems have been measured within the framework of PACE4 code. Data of excitation function measurements on comparison with different projectile-target combinations suggest the existence of ICF even at slightly above barrier energies where complete fusion (CF) is supposed to be the sole contributor, and further demonstrates strong projectile structure dependence of ICF. The incomplete fusion strength functions for $^{12}\text{C}+^{175}\text{Lu}$, and $^{13}\text{C}+^{169}\text{Tm}$ systems are analyzed as a function of various physical parameters at a constant $v_{rel} \approx 0.053c$. It has been found that one neutron (1n) excess projectile ^{13}C (as compared to ^{12}C) results in less incomplete fusion contribution due to its relatively large negative α -Q-value, hence, α Q-value seems to be a reliable parameter to understand the ICF dynamics at low energies. In order to explore the reaction modes on the basis of their entry state spin population, the spin distribution of residues populated via CF and/or ICF in $^{16}\text{O}+^{159}\text{Tb}$ system has been done using particle- γ coincidence technique. CF- α and ICF- α channels have been identified from backward (B) and forward (F) α -gated γ spectra, respectively. Reaction dependent decay patterns have been observed in different α emitting channels. The CF channels are found to be fed over a broad spin range, however, ICF- α channels was observed only for high-spin states. Further, the existence of incomplete fusion at low bombarding energies indicates the possibility to populate high spin states.

1 Introduction

The study of breakup of heavy ions followed by the fusion of one of the fragments with the target has gained a resurgent interest. Several authors reported the competition of complete fusion (CF) and incomplete fusion (ICF) reactions at energies slightly above the Coulomb barrier [1–10], and a substantial ICF fraction has been observed at these energies. In general, the complete fusion (CF) process is considered to be the sole contributor to the total fusion cross section at low energies i.e. starting from threshold to 7 MeV/A.

Though, several studies and models [11–18] are developed to understand ICF phenomenon, but the dynamics of ICF at low incident energies is still not fairly understood and thus continues to be an active area of investigations. High quality data for ICF processes has been obtained and reported so far worldwide [1–8, 19, 20], and conclusively demonstrate the low energy ICF, but are limited only for a few projectile-target combinations. Therefore, for better understanding of ICF dynamics, several inclusive experiments at the Inter-University Accelerator

Center (IUAC), New Delhi, India were performed by our group [5, 7, 8, 21, 22]. Based on experimental findings an attempt has been made to correlate data with suitable set of physical parameters viz., (a) projectile energy, (b) mass-asymmetry of interacting partners (μ), (c) α -Q value, and (d) input ℓ values. In the present work, the percentage fraction of ICF were deduced from the analysis of experimental excitation functions of individual reaction residues for different projectile-target combinations. This suggests at the studied energy regime projectile structure plays an important role to understand ICF dynamics. To understand the role of ℓ values, a particle- γ coincidence experiments were performed and spin distribution of individual reaction residues have been measured. The spin distribution of various evaporation residues reveals that the mean input angular momenta ($\langle \ell \rangle$) associated with the ICF observable are found to be higher than those involved with CF. Further, the occurrence of ICF is due to the influence of centrifugal potential in peripheral interactions, where driving angular momentum limits do not allow CF to occur.

The present paper is organized as; the experimental details are presented in section 2. The observation from our recent experiments are given in section 3, where the influence of ICF on CF and its dependencies on various en-

*e-mail: phy.vijayraj@gmail.com

**e-mail: bpsinghamu@gmail.com

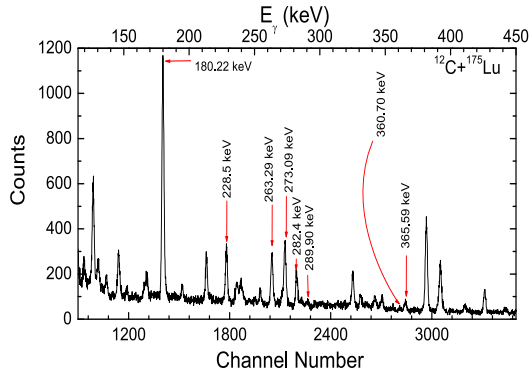


Figure 1. (Color online) Typical γ -ray spectrum of $^{12}\text{C}+^{175}\text{Lu}$ interaction at $\approx 78.36 \pm 1.08$ MeV

trace channel parameters are demonstrated. Summary of the present work is given in Section 4.

2 Experimental details

To explore the dynamics of incomplete fusion reaction processes, experiments were performed using 15 UD pellectron accelerator of Inter University Accelerator Centre (IUAC), New Delhi, India. These experiments were performed using two different setups (a) General Purpose Scattering Chamber (GPSC) and (b) Gamma Detector Array (GDA) coupled with Charged Particle Detector Array (CPDA). The detailed methodology and experimental setups have been discussed in refs.[5, 7, 21, 22]. However, a short account of experimental conditions are given here for the ready reference.

In order to achieve information on the behavior of fraction of ICF observable on various entrance channel parameters, the value of incomplete fusion fraction (F_{ICF}) has been deduced as a function of various physical parameters (discussed in sec 3) in a separate set of experiment. In this experiment, absolute production cross-sections of individual reaction residues populated via CF and/or ICF in $^{12}\text{C}+^{175}\text{Lu}$, and $^{13}\text{C}+^{169}\text{Tm}$ systems have been measured at energies starting from threshold to 7 MeV/A [7, 23]. The target foils of isotopically pure (99.9%) ^{175}Lu , and ^{169}Tm along with in ^{27}Al catchers were prepared using rolling technique. The thickness of the samples were determined from the observed change in the energy of the α -particles by using stopping power values and were found to ≈ 1.5 to ≈ 2.5 mg/cm² for both targets and ≈ 1.0 to ≈ 3.0 mg/cm² for Al-catchers. The thickness of the Al-catchers was chosen keeping in view the fact that even the most energetic residues produced due to the complete momentum transfer may be trapped in the catcher thickness. The irradiation has been carried out with a beam current ≈ 2 -3 pA. The evaporation residues (ERs) produced during the irradiations were counted off-line with two pre-calibrated HPGe detectors. The ERs have been identified by their characteristic γ -lines and are further confirmed by decay-curve analysis. A part of γ -ray spectra obtained at $E_{Lab} = 78.36 \pm 1.08$ MeV in $^{12}\text{C}+^{175}\text{Lu}$ system is shown in

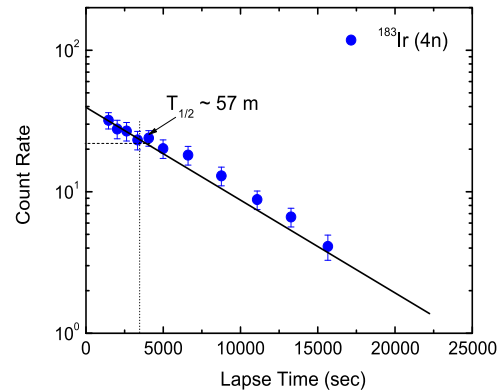


Figure 2. (Color online) Typical decay curve of ^{183}Ir residue observed in $^{12}\text{C}+^{175}\text{Lu}$ interaction at $\approx 78.36 \pm 1.08$ MeV beam energy.

Fig.1. Some of the peaks corresponding to different reaction residues are marked. As a typical example, the observed decay curve for one of the Iridium isotopes ^{183}Ir ($T_{1/2} = 57$ min) populated in $^{12}\text{C}+^{175}\text{Lu}$ system is shown in Fig. 2. Further, the production cross-sections (σ_R) of ERs have been calculated using standard formulation [23]. The overall errors in the present measurement are estimated to be $\approx 10\%$. A detailed discussion on error analysis is presented in Refs. [24].

To probe the role of ℓ -values in the onset of ICF at low projectile energies, the spin-distributions (SDs) of xn/pxn/ α xn channels has been measured in $^{16}\text{O}+^{159}\text{Tb}$ system using particle- γ coincidence technique. The experiment was performed at four set of projectile energies viz. $\approx 83.5 \pm 1.5$, 88.5 ± 1.5 , 93.5 ± 1.5 and 97.6 ± 1.4 MeVs, using GDA alongwith CPDA facility of IUAC, New Delhi, India. The particle- γ coincidences were recorded using 12 Compton suppressed, high resolution HPGe detectors installed at an angles 45° , 99° , 153° with respect to the beam axis in Gamma Detector Array (GDA). It may be mentioned that there were four detectors at each of these angles in GDA set up. Further, the GDA set up is coupled with the Charge particle detector array (CPDA) which is a set of 14-phoswich detectors housed in a 14 cm diameter scattering chamber. These particle detectors cover nearly 90% of the total solid angle. All 14 detectors of CPDA have been divided into the angular zones viz.; (i) Forward angle (F) 10° to 60° , (ii) Sideways (S) 60° to 120° , and (iii) Backward angle (B) 120° to 170° . Depending on the fast and slow components of the CPDA, proton and α -particles in each angular ring can be identified. For the experiment, isotopically pure, self-supporting ^{159}Tb (100%) target of thickness ≈ 1.5 mg/cm² (prepared by rolling technique) has been bombarded with $^{16}\text{O}^{+7}$ beams delivered from 15UD Pellectron Accelerator. A prompt γ -ray spectra was recorded in event-by-event multi parameter mode, which includes different coincidences i.e. particles ($Z=1,2$) detected in backward (B), forward (F) and 90° (S)-angles. Singles data have also been collected to identify xn-channels (pro-

duced via CF). Data analysis was done in two steps. In the first step, spin distributions of xn-channels have been measured by looking into singles spectra. For the identification of pxn-channels, backward (B)- α -gated spectra has been subtracted from backward(B)-particles($Z=1,2$)-gated spectra to achieve proton-gated spectra. However, α xn -channels populated via CF have been identified from the backward (B)- α -gated spectra. Further, the fast- α -particles (which are expected to be emitted only in forward cone) produced via ICF have been identified from forward(F)- α -gated spectra obtained by subtracting backward (B)- α -gated spectra from forward(F)- α -gated spectra. The intensity and area under the photo-peak (efficiency corrected) of the characteristic prompt α -transitions were used to determine the relative production yield [21]

3 Projectile Dependence of ICF: Recent Results

In the present work, a systematic investigation have been done to understand the effect of various entrance channel parameters (i.e. projectile energy, entrance channel mass-asymmetry of interacting partners, α -Q-value, and input ℓ -values) on the onset and strength of incomplete fusion. Interpretation of the data and results are presented in this section.

3.1 ICF dependence on incident energy

The excitation functions (EFs), expected to be populated via CF and/or ICF mode have been measured for $^{12}\text{C}+^{175}\text{Lu}$, and $^{13}\text{C}+^{169}\text{Tm}$ systems at energies starting from the Coulomb barrier to 7 MeV/A and analyzed in the framework of statistical model code PACE4 to probe the energy dependence of ICF. Details of code PACE4 can be found in ref. [25]. In this code, the nuclear level density ($a = A/K$) plays an important role which can be tuned to fit the experimental data. In order to choose the suitable value of level density to reproduce fusion EFs, different values of $K = 8 - 12$ have been tested. The evaporation residues (ERs) populated via xn/pxnchannels have been found to be in good agreement with that estimated from code PACE4. On the other hand, the experimental EFs of α -emitting channels have been found to be significantly enhanced as compared to the PACE4 predictions. This enhanced value of α ERs may be attributed to ICF. To have the enhanced value of ERs (i.e. ICF contribution), experimental EFs of α -emitting channels were subtracted from the PACE4 values ($\sigma_{ICF} = \sigma_{exp} - \sigma_{PACE4}$) [25]. For better insight into the onset and strength of ICF, the percentage fraction of ICF (F_{ICF}) has been deduced and is plotted as a function of projectile relative velocity (v_{rel}) [5] for $^{12}\text{C}+^{175}\text{Lu}$, $^{13}\text{C}+^{169}\text{Tm}$ and $^{12}\text{C}+^{169}\text{Tm}$ systems in Fig.3. It may be mentioned that F_{ICF} defines empirical probability of ICF.

As shown in this figure, the F_{ICF} increases linearly with normalized projectile energies in terms of relative velocity of projectile (i.e., v_{rel}). This suggests strong projectile energy dependence of ICF reactions. On the other

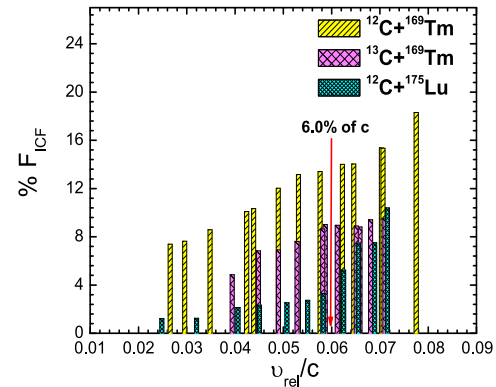


Figure 3. (Color online) The percentage fraction of ICF as a function of projectile relative velocity (v_{rel}) for $^{12}\text{C}+^{175}\text{Lu}$, $^{12}\text{C}+^{169}\text{Tm}$ and $^{13}\text{C}+^{169}\text{Tm}$ systems

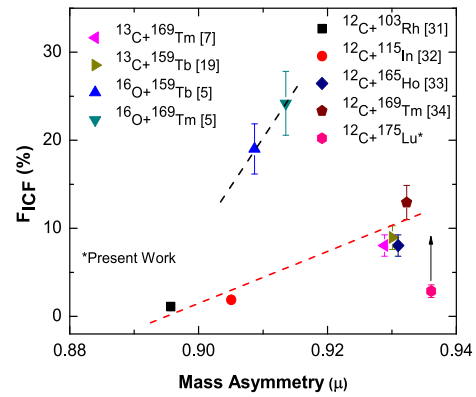


Figure 4. (Color online) The percentage fraction of ICF as a function of μ for 9 projectile-target combinations at a constant value of $v_{rel} \approx 0.053c$. Dashed lines are drawn to guide the eyes.

hand, Morgenstern systematics [26, 27] suggests that ICF contributes significantly above $v_{rel} \geq 0.06$ (6 % speed of light). However, in figure 3, the values of v_{rel} are in the range from ≈ 2.7 % of c to ≈ 7.8 % of c for $^{12}\text{C}+^{175}\text{Lu}$, and $^{12}\text{C}+^{169}\text{Tm}$ systems and from 2.3 % of c to 7.0 % of c for $^{13}\text{C}+^{169}\text{Tm}$ system. Hence, the results presented in Fig.3 clearly demonstrate the onset of ICF at relatively lower value of v_{rel} i.e. F_{ICF} is significant at well below the proposed onset value of v_{rel} . Further, for the same target the value of F_{ICF} for ^{12}C -projectile is lower than ^{13}C -projectile for the entire measured energy range. The difference in F_{ICF} for two systems (^{12}C , $^{13}\text{C}+^{169}\text{Tm}$) clearly points towards projectile structure and/or mass asymmetry effect on ICF.

3.2 Projectile structure dependence of ICF

To understand projectile structure and/or mass asymmetry (μ) dependence of ICF, the deduced percentage fraction of ICF for $^{12}\text{C}+^{175}\text{Lu}$, and $^{13}\text{C}+^{169}\text{Tm}$ systems along with

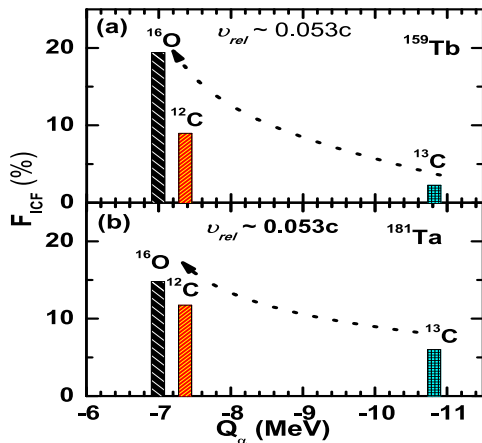


Figure 5. (Color online) Comparison of F_{ICF} on the basis of α -Q value of the projectile at a constant $v_{rel} = 0.053c$ for different projectile-target combinations

7 projectile-target combinations are plotted as a function of mass asymmetry at a constant value of $v_{rel} \approx 0.053$ in Fig.4. In order to understand projectile dependence on ICF more conclusively, data for the ^{16}O projectile is also added. It may be pointed out that ^{12}C , ^{13}C and ^{16}O are widely different projectiles and hence the probability of breakup depends on the input ℓ -values imparted into system in peripheral interactions. As can be seen from Fig.4, the Morgensterns systematics does not explain the variation of F_{ICF} with μ for given systems. However, the value of F_{ICF} increases with μ for ^{12}C , ^{13}C projectiles and individually for ^{16}O projectile. It is interesting to note that the ^{12}C , $^{13}\text{C}+^{169}\text{Tm}$ systems is a more mass asymmetric ($\mu \approx 0.9337$) system than $^{16}\text{O}+^{169}\text{Tm}$ system ($\mu \approx 0.9135$), but the value of F_{ICF} is $\approx 18\%$ higher than that observed for ^{12}C , $^{13}\text{C}+^{169}\text{Tm}$ system. The aforementioned observations based on 9 projectile-target combinations strongly contradict Morgensterns mass-asymmetry systematics, and suggest strong projectile dependence of ICF for alpha cluster projectiles. However projectile dependence of mass asymmetry is valid for same atomic number and different mass number projectiles (i.e. ^{12}C , ^{13}C , etc. on the same target) is a question of interest. As can be seen in Fig 3 the values of F_{ICF} for the ^{13}C projectile are less than for the ^{12}C projectile in the studied energy range. The difference in F_{ICF} for two systems (^{12}C , $^{13}\text{C}+^{169}\text{Tm}$) is clearly evident, and indicates the strong projectile dependence of F_{ICF} with some physical parameter other than μ . In order to explore this issue, the ICF strength functions for ^{12}C , $^{13}\text{C}+^{169}\text{Tm}$ systems have been studied in terms of projectile α -Q value.

3.3 Projectile α -Q value dependence of ICF

The percentage fraction of ICF is analyzed in terms of projectile α -Q-value for 6 projectile-target combinations. The value of F_{ICF} is plotted as a function of Q_α in Fig.5(a-b) at a constant $v_{rel} \approx 0.053c$. As shown in this figure, the probability of ICF for the ^{13}C projectile is smaller than that for the ^{12}C projectile. This clearly point towards the

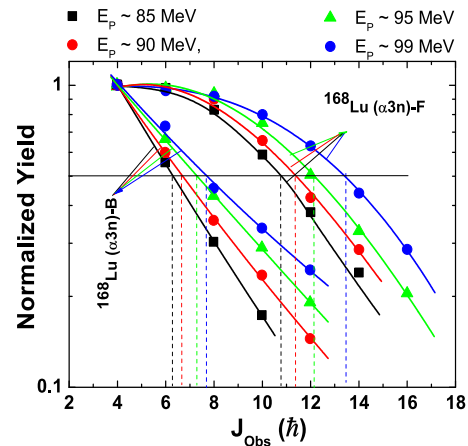


Figure 6. (Color online) Experimentally generated spin-distributions of $\alpha 3n$ -(B), and $\alpha 3n$ -(F) channels. Lines and curves are the best fit to the experimental data points.

projectile structure effect. It may be pointed out that ^{12}C is a well known α -cluster nucleus with $Q_\alpha = -7.37$ MeV. However, ^{13}C has a larger Q_α ($= -10.64$ MeV) than ^{12}C . The higher α -Q-value for ^{13}C translates into the smaller breakup probability into constituent α -clusters, resulting smaller ICF fraction than that found in ^{12}C induced reactions. In order to strengthen α -Q-value dependence, the value of F_{ICF} for the ^{16}O ($Q_\alpha = -7.16$ MeV)+ ^{159}Tb system is found to be 18% which is reduced to only 3% for the ^{13}C ($Q_\alpha = -10.64$ MeV)+ ^{159}Tb system. Similar trend was observed for the ^{181}Ta target. Hence, from the data presented in this figure, it can be inferred that the α -Q-value is an important entrance channel parameter which essentially dictates the probability of ICF.

3.4 ℓ dependence of ICF

In order to understand the physics of angular momentum involvement and de-excitation pattern of any residual nuclei, the spin distribution of various CF and ICF channels have been measured for $^{16}\text{O}+^{159}\text{Tb}$ system at laboratory energies (E_{lab}) $\approx 83.5 \pm 1.5$, 88.5 ± 1.5 , 93.5 ± 1.5 and 97.6 ± 1.4 MeV with beam intensities of ≈ 4 -6 p nA. It is expected that in case of CF residues (high E^* and low ℓ) the de-excitation pattern are more likely as statistical transitions, on the other hand, the ICF residues achieve low E^* (due to the involvement of partial degrees of excitations) and high ℓ (relatively higher values of impact parameters contribute to the high spin states) at a given projectile energy, therefore, the number of yrast-like transitions are much larger than that of statistical ones.

In view of the above, a comparison of the spin distribution pattern for the $\alpha 3n$ channel (^{168}Lu) populated via both CF mode (\rightarrow identified in the backward (B) α -gated spectra) and ICF mode (\rightarrow identified in the forward (F) α -gated spectra) are plotted in Fig.6. As shown in this figure, there is a difference in the spin-distributions which indicate the involvement of entirely different mode of reactions in the production of these residues. The intensity of $\alpha 3n$ (B)-

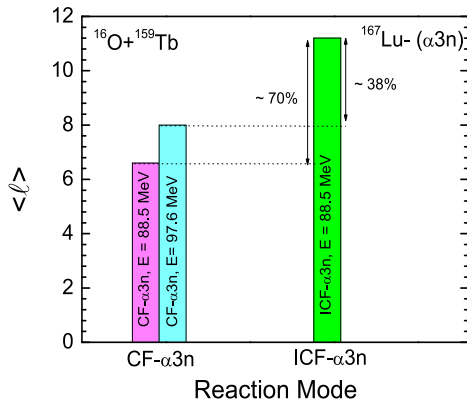


Figure 7. (Color online) The value of the mean angular momenta i.e., the value of $\langle \ell \rangle$ deduced from the best fitting procedure of spin distributions [21] involved in ^{167}Lu isotope populated via CF and ICF processes as a function of modes of reaction.

channels (CF residues) falls off rather quickly with observed spin (J_{obs}), indicating strong feeding and/or broad spin population during the de-excitation of CN. However, for $\alpha 3n$ (F)-channels (ICF residues), the intensity appears to be almost constant up to a certain value of J_{obs} , and then decreases towards band head. This indicates the absence of feeding to the lowest members of the Yrast band and/or the population of low spin states are strongly hindered in ICF-channels.

Concerning the usefulness of incomplete fusion as a tool to populate high-spin states in final reaction products the mean input angular momenta ($\langle \ell \rangle$) associated with $\alpha 3n$ channel (populated via both CF and ICF modes) have been deduced as suggested in Ref [21] and is plotted in Fig.7. As can be seen in Fig. 7, the $\langle \ell \rangle$ values involved in the production of ^{168}Lu via ICF- $\alpha 3n$ channel (i.e. $\approx 11.0 \hbar$) is found to be 70% larger than that via CF- $\alpha 3n$ channel (i.e. $\approx 6.5 \hbar$) at the same projectile energy, i.e., $E_{lab} \approx 88.5 \pm 1.5$ MeV. On the other hand, the value of ℓ involved in ICF- $\alpha 3n$ channel (i.e. $\approx 10.5 \hbar$) at 83.5 ± 1.5 MeV is found to be $\approx 40\%$ more than that involved in CF- $\alpha 3n$ channel (i.e. $\approx 7.5 \hbar$) even at highest experimental incident laboratory energy (E_{lab}) $\approx 97.6 \pm 1.4$ MeV. This clearly demonstrates the involvement of higher ℓ -values in the production of incomplete channels which may lead to the population of higher spin-states in the final reaction products which may not be possible otherwise. The present spin distribution measurement for $^{16}\text{O} + ^{159}\text{Tb}$ system supports earlier findings by Dracoulis *et al* [28], Lane *et al* [29], and Mullins *et al* [30] on the population of high spin states in final reaction products at low bombarding energies. Hence, ICF can be used as a spectroscopic tool to study the high spin states even at low energies.

4 Summary

This paper gives the recent experimental results for the excitation function and particle- γ coincidence experiments.

The EFs for several residues populated via CF and/or ICF in $^{12}\text{C} + ^{175}\text{Lu}$ and $^{13}\text{C} + ^{169}\text{Tm}$ systems have been measured at energies starting from threshold to ≈ 7 MeV/nucleon, and analyzed in the framework of statistical model code PACE4. A systematic analysis of ICF dependence on various entrance channel parameters has been performed. It has been found that ICF strongly depends on incident energy, projectile and target type, α Q-values. Results and analysis presented on projectile structure effects suggest more ICF fraction for less negative α Q-value projectiles. Results presented are in good agreement with the existing data.

The spin-distribution(s) associated with ICF are found to be originated from the narrow spin population, localized near and/or above to the critical angular momentum (ℓ_{crit}) for CF, where a given direct- α -fragment is emitted to release excess driving angular momenta. This reveals a competition from successively opened ICF channels for each value of ℓ above the ℓ_{crit} for normal fusion (CF). On the basis of the present analysis of experimental data, the mean angular momenta associated with ICF are found to be $\approx 70\%$ higher than that for CF at the same energy. Further, the mean input angular momenta associated with ICF residues at lowest energy is 40 % higher than that for the CF residue at the highest studied energy, this helps to understand the population of high spin states via ICF route.

5 Acknowledgements

The authors thank to the Director, IUAC, New Delhi, for providing all the necessary facilities to carry out this work. One of the author (VRS) thanks to DST for providing travel support.

References

- [1] P. R. S. Gomes, R. Linares, J. Lubian, C. C. Lopes, E. N. Cardozo, B. H. F. Pereira, and I. Padron, Phys. Rev. C 84, 014615 (2011).
- [2] K. Surendra Babu, R. Tripathi, K. Sudarshan, B. D. Shrivastava, A. Goswami, and B. S. Tomar, J. Phys. G 29, 1011 (2003).
- [3] K. Sudarsan Babu et al., Nucl. Phys. A 739, 229 (2004).
- [4] D.J. Hinde, M. Dasgupta, Phys. Rev. C 81, 064611 (2010), and the references therein.
- [5] P. P. Singh, B. P. Singh, M. K. Sharma, Unnati, D. P. Singh, and R. Prasad, Phys. Rev. C 77, 014607 (2008).
- [6] M. Dasgupta, D. J. Hinde, R. D. Butt, R. M. Anjos, A. C. Berriman, N. Carlin, P.R. S.Gomes, C. R. Morton, J. O. Newton, A. Szanto de Toledo, and K. Hagino, Phys. Rev. Lett. 82, 1395 (1999).
- [7] Vijay R Sharma et al., Phys. Rev. C 89, 024608 (2014).
- [8] Mohd. Shuaib, et al, Phys. Rev. C 94, 014613 (2016).
- [9] K. Sudarshan, et al, Phys. Rev. C 69, 027603 (2004).
- [10] R. Tripathi, et al, Eur. Phys. J. A 42: 25 (2009).
- [11] I. Tserruya et al., Phys. Rev. Lett. 60, 14 (1988).

- [12] E. Takada, T. Shimoda, N. Takahashi, T. Yamaya, K. Nagatani, T. Udagawa, and T. Tamura, *Phys. Rev. C* **23**, 772 (1981).
- [13] J. Wilczynski, K. Siwek-Wilczynska, J. Van Driel, S. Gonggrijp, D. C. J. M. Hageman, R. V. F. Janssens, J. Lukasiak, R. H. Siemssen, and S. Y. Van Der Werf, *Nucl. Phys. A* **373**, 109 (1982).
- [14] M. Blann, *Phys. Lett.* **27**, 337 (1971).
- [15] J. P. Bondroff et al., *Nucl. Phys. A* **333**, 285 (1980).
- [16] B. G. Harvey, *Phys. Lett. B* **130**, 373 (1983).
- [17] B. G. Harvey, *Nucl. Phys. A* **444**, 498 (1985).
- [18] A. Y. Abul-Magd, *Z. Phys. A* **298**, 143 (1980).
- [19] A. Yadav, V. R. Sharma, P. P. Singh, R. Kumar, D. P. Singh, Unnati, M. K. Sharma, B. P. Singh, and R. Prasad, *Phys. Rev. C* **86**, 014603 (2012), and references therein.
- [20] Manoj K Sharma *Physical Rev. C* **91**, 024608 (2015).
- [21] Vijay R. Sharma, et al., *J. Phys. G, Nucl. Part. Phys.* **42** 055113 (2015).
- [22] Pushpendra P. Singh, et al., *Phys. Lett. B* **671**, 20 (2009).
- [23] Vijay R. Sharma, Ph.D. Thesis, A.M. University, Aligarh-Unpublished, (2015).
- [24] B. P. Singh, M. G. V. Sankaracharyulu, M. A. Ansari, H. D. Bhardwaj, and R. Prasad, *Phys. Rev. C* **47**, 2055 (1993).
- [25] O. B. Tarasov and D. Bazin, *Nucl. Instrum. Methods Phys. Res., Sect. B* **204**, 174 (2003).
- [26] H. Morgenstern, W. Bohne, W. Galster, and K. Grabisch, *Z. Phys. A. Atomic Nuclei* **324**, 443 (1986).
- [27] H. Morgenstern, W. Bohne, W. Galster, K. Grabisch, and A. Kyanowski, *Z. Phys. A* **313**, 39 (1983); H. M. Morgenstern, W. Bohne, K. Grabisch, D. G. Kovar, and H. Lehr, *Phys. Lett. B* **113**, 463 (1982).
- [28] G.D. Dracoulis, et al., *J. Phys. G, Nucl. Part. Phys.* **23**, 1191 (1997).
- [29] G.J. Lane, G.D. Dracoulis, A.P. Byrne, A.R. Poletti, T.R. McGoram, *Phys. Rev. C* **60**, 067301 (1999).
- [30] S.M. Mullins, et al., *Phys. Lett. B* **393**, 279 (1997); S.M. Mullins, et al., *Phys. Rev. C* **61**, 044315 (2000).
- [31] Bindu Kumar, et al., *Phys. Rev. C* **59**, 2923 (1999).
- [32] S. Mukherjee, et al., *Int. J. Modern Phys. E* **15**, 237 (2006).
- [33] S. Gupta, et al., *Phys. Rev. C* **61**, 064613 (2000).
- [34] P. P. Singh, et al., *Jour. of Phys: Conf. Series* **590**, 012031 (2015).

Exploring 3D Network-on-Chip Architectures and Challenges

Sapna Tyagi

Department of Computer Science
Institute of Management Studies
Ghaziabad, India
sapna030280@gmail.com

Piyush Maheshwari

Department of Engineering
Amity University Dubai
United Arab Emirates
pmaheshwari@amityuniversity.ae

Amit Agarwal, Vinay Avasthi

Center for Information Technology
University of Petroleum & Energy
Studies, Dehradun, India
{[@ddn.upes.ac.in](mailto:aagarwal,vavasthi)}

Abstract— Network-on-Chip (NoC) is a nascent approach for reducing the communication bottleneck of multicore System-on-Chip (SoC). As the number of cores are increasing on SoC due to high performance demand of the consumer electronics and processing systems like servers, the low power and low latency NoC is required. Topologies are one of the most important parts of a NoC design, with considering the performance parameter as a constraint. The important parameters of networks-on-chip are latency, throughput, injection rate and average number of hops etc. In our work, various existing 3D NoC architectures and their performance are studied and presented. The basic concepts of NoC and motivation for 3D NoC and its advantages over 2D NoC are also focused in this paper. We have also investigated and demonstrated 144 nodes and 256 nodes 3D mesh architecture in terms of the latency, throughput and injection rate.

Keywords—Network-on-Chip (NoC); Topologies; Access Noxim

I. INTRODUCTION

Network-on-chip is a emerging design for communication where large number of functional and storage cores or commonly known as IP Core such as video and audio processors, memories, I/O peripherals, hardware accelerators, etc. are integrated onto a single chip to exchange data and commands for implementing emerging multimedia and networking services. Earlier system-on-chips communications are carried through by direct cross bar interconnections and shared buses. However these approaches restarint performance and are consider no longer reliable architecture for SoC due to lack of scalability and parallelism integration, high latency and power dissipation, and low throughput which degrades on-chip performance.

Network-on-Chip is the revolutionary methodology as comapred with traditional bus-based and point-to-point communication structures with a huge potential to handle the increasing complexity of current and future multicore SoCs [1][2]. In such arena, cores are connected via a packet-switching communication network on a single chip. NoC architecture is generally characterized by its topology, routing, switching, flow control, and arbiter techniques. On-chip network topology is a crucial factor of the chip in determining the parameters performance, cost, and energy

consumption. Various network topologies have been studied for NoCs. Especially, the two-dimensional mesh [12] and torus [13] are popularly used in NoCs, because their n-dimensional grid-based regular architecture is very simple and easy to understand and thus considered to be the most suitable choice for designing NoC. Routing algorithm calculates the path taken by a packet from source node to the target node. These routing algorithms must have the capability to prevent deadlock, livelock, and starvation situations [31]. The different classifications areas are presented in Table 1.

Table 1: Routing Algorithms

Criteria	Types
Number of Destinations	Unicast & Multicast
Routing Decision	Centralized Routing, Source Routing, Distributed Routing, Multiphase Routing
Adaptability	Deterministic Routing, Adaptive or Oblivious Routing
Path Length	Minimal and Non-Minimal routing
Network Condition	Delay & Loss

Switching strategy can be categorized into circuit switching and Packet switching. In circuit switching complete path from source node to destination node is reserved for entire message to traverse the network whereas in packet switching message broken into packets where each packet finds its own way to reach to destination.

Flow control deals about how the data flow is controlled between router to router. It provides the mechanism in the case of congestion in network. Data is temporarily stored in buffers, and re-routed to other nodes. Flow control also tells source node to temporarily halt, discard, etc.

The various important metrics of interest in NoC are:

- performance (latency, throughput, cross-section bandwidth, diameter)
- energy dissipation, power limits
- reliability (fault tolerance, other failures)
- scalability (increasing number of cores)

- Implementation cost (foot print area).

The industry has already entered into the NoC arena by developing different NoC-based architectures such as the *Ethereal NoC* [4] from Philips, the *STNoC* [5] from STMicroelectronics, *80-coreNoC* from Intel [6], *NOSTRUM* [14], *SoCBus* [15] and *Hermes* [16] are few examples.

The remaining part of the paper is organized as below. Section II provides an insight about why we need to migrate towards 3D-NoC. Section III explores various 3D-NoC Architecture and Routing Protocols for 3D-NoC. Section IV presents simulation and results using *Access Noxim 3D-NoC Simulator*. Finally, the conclusion and some challenges are discussed in Section V.

II. MIGRATING FROM 2D NoC TO 3D NoC

The two dimensional NoC presented acceptable performance for the current SoC;s applications but as future applications are getting more and more complex, the consumer products such as mobile phones, notebooks and personal handheld sets will have fabrication of thousands of IP core on single chip. Future devices will become faster, smaller-in-size, larger-in-capacity, lighter-in-weight, lower-in-power-consumption and cheaper. This trend will persistently continue and will demand the good architecture to ensure a satisfactory performance on the chip. Following this trend, we have to integrate hundred and thousands of IP cores onto a single chip for ultra high performance applications. The planar chip two dimensional fabrication technology is facing new challenges in the deep submicron regime [7]. 2D-NoC interconnect are not suitable candidate for future large scale many-core SoCs that are expected to accommodate hundreds of cores.

Planar 2D NoC has limitations for floor planning. Long global wires causes increased latency and therefore limits the performance improvements resulting from Network-on-Chip paradigm. This challenge comes basically from the high network diameter that NoC suffers from. The network's diameter is the number of hops that it traverses in the longest possible minimal path between a (source, destination) pair. The diameter is an important parameter for the NoC design and may have the negative impact on the performance of NoC because if a given packet traverses a large number of hops to reach its destination, it will increase the network diameter which will in turn increase the communication time (latency) hence the throughput will be low. Thus the need to optimize the 2D-NoC system arises and one of these proposed solutions was porting the 2D-NoC architecture to the third dimension to enhance the performance of NoC systems and alleviate their limitations [21]. Research in 3D-NoC is now emerging as new trend to implement future SoC's applications. A 3-dimensional Network on chip is a composite of multiple device layers of 2D NoC with direct vertical interconnects using *Through Silicon Vias (TSV's)*. There are various approaches to build the vertical interconnects which comprises of wire bonded approach, Micro-bonded 3D package, Micro-bonded face to face, contactless –capacitive with buried bumps, contactless – inductive and *Through Silicon Vias (TSV)* is one of the most popular choice [8, 9, 10].

Figure 1 shows 3D Mesh NoC in which nodes are placed as Manhattan-like grid. As NoC structures can be combined with benefits of 3D integration, low interconnects latency and area efficient solution can be realized [11].

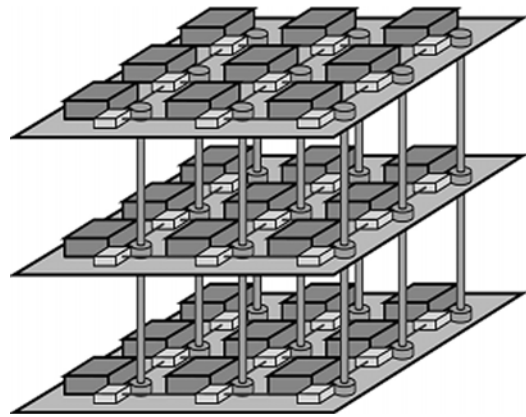


Fig. 1. 3D Mesh based NOC [10]

Three Dimensional NoC technology has several major advantages: (1) More IP/Core units can be added due to the stacking of layers, thus foot-print on each layer will remain smaller and thus leading to more compact chips and drastic increase in IP/Core density which will satisfy the high requirements of future large scale applications, (2) smaller footprints lead to short-length wires and higher transistor density within each layer which are the obvious obstacles for delay and power consumption but inter layer connections are obtained using efficient TSV's and these shorter wires decrease the average load capacitance, resistance and number of repeaters which consumes lot of power thereby leading to higher communication bandwidth, lower delay, low power consumption, lower noise and less jitter, (3) allows integration of plethora of technologies that are currently impossible in 2D planar technology, as each could be designed as a separate layer and will create hybrid circuit, and (4) layered architecture leads to reduced average hop count, fast inter layer and intra layer packet transmission and overall high-throughput network.

III. RELATED WORK: 3D-NOC ARCHITECTURES

This section presents various architectures that were proposed recently for 3D-NoCs. One of the well-known 3D-NoC architectures is the 3D Mesh as shown in Figure 1. In this 3D-NoC architecture each IP core is associated with 7 port router where one port is attached to the IP block, two ports to the routers above and below, and other four in each direction i.e North, South, East, and West. The drawback to this simple architecture is too much number of buffers at each port even when it is not required while travelling through upward and downward links because latency between tiers is too low as tiers are stacked very closely [23]. The number of ports depends on the position of the switch in the design, since we have to eliminate any unused links that have no connections with other switches in order to reduce power consumption.

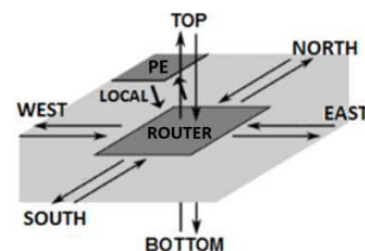


Fig 2. 7-Port 3D Router

3D-NoC Bus Hybrid Architecture [17] was proposed as a hybrid of packet switched NoC's and Shared Bus architecture where multiple 2D Mesh layers are individually implement with packet switched technology and vertically the layers communicate through Shared bus architecture. A router in this hybrid architecture has, at most, six ports: one port is connected to the IP, another to the bus, and rest four to the directions (N,S,E,W). This architecture was implemented in 3D NUCA L2 Cache for CMPs [43]. It suffers from lower bandwidth while communicating interlayer due to shred bus.

Ciliated 3D Mesh [3] was proposed as a variant of 3D basic Mesh based architecture where each switch/router accomodates two or more IP block. In a ciliated 3D Mesh network, each router/switch consist of at most $5+k$ ports (one for each direction (N, S, E, and W), one port either for up or down layers for 2Layer 3D Mesh and K ports are connected to each K IP blocks. This structure suffers from lower bandwidth as switch/router is shared by multiple IP core but power dissipation is low.

In [19], the vertical partial mesh-based 3D NoC (VPM3NoC) architecture is described. This architecture contains mesh-based stacked layers where each layer is differentiated with respect to technology, application and size. In each layer some nodes have vertical links to up and down layers. This structure employs varieties of routers i.e 2D router, 3D Router with upward link, 3D router with downward link, 3D Router with up and down link.

In [12], the authors have presented two 3D topologies i.e 3D star topology and 3D Recursive Network topology and compared them in terms of the parameters as follows: latency, energy dissipation and Network Diameter. In both the topologies, group of 4 node is formed which is termed as cluster with one node is designated as Cluster Head (CH) which can act as CH as well as node. A layer has four clusters, and the total number of nodes in a layer is 16. TSV's are used to connect the 3 layers vertically. The Performance of 3D RNT is evaluated and found better performing in comparison with 3D ST with respect to latency and energy dissipation parameters.

In [13], the authors have proposed 3D 2-layer and 3-layer architectures. In both the approaches the goal is to optimize the floorspace of the chip. In 3D 2-Layer approach, the layer 1 is dedicated to place hetrogenous IP cores where as layer 2 is used to place routers in mesh configuration, similarly In 3-layer architectures, layers 1 and 3 are used to place hetrogenous IP Cores and layer 2 implements mesh architectures of assigned routers. The 3 layers are connected with each other through silicon vias (TSV).

POC topology [20] was proposed as another variant of 3D Mesh topology which consists of two diffrent types of routers i.e 7-port router and 6-port router. 7 port routers are used to coonect with IP where 6-port router was only used for communication. The difference between 3D Mesh and POC topology is that the vertical links are only implemented at 6 port router. The advantage of this topology is fewer vertical links which leads to low energy dissipations.

Another 3D Mesh based NoC architecture called Lasio [22] is also presented where hops between layer (z axis) and hops within layer (X, Y axis) have same cost. The most important feature of this architecture is that all router ports are bidirectional. It implemented XYZ routing and used credit based flow control.

Another class of 3D-NoC topologies called Xbar-connected Network-on-Tiers (XNoTs) [24], consisting of multiple layers and each layer is customized with different topology according to the application .The layers are tightly connected via crossbar switches which reduces the average hop count and low power consumption.

3D Honeycomb NoC topology [25] is formed by stacking 2D honeycomb topology which is composed of hexagons. This topology suffers from the high implementation cost due to the large number of vertical communication links. This architecture has the network degree of 5 which leads to higher network cost.

IV. EXPERIMENTAL RESULTS

In this paper we analyze packet latency, throughput with respect to injection rate by using the Access Noxim [26] simulator which is extended version of Noxim Simulator for 3D-NoC Mesh.

The latency of the network is the synonym for delay and time taken for a packet, flit or message to reach from source to destination. It also includes the time taken for computing arbitration logic as well as routing computation and other contention delays. It is the elementary parameter of the performance evaluation of Networks on chip. The delay is mainly caused by the source-destination physical distance, and also by deflections due to traffic congestion inside the network. It is measured in clock cycles. Packet Latency can be calculated as:

$$\text{Packet Latency} = \text{Actul Transmit time} + \text{Routing Delay} + \text{Contention Delay}$$

Another related parameter i.e zero load latency [1] is also used widely as a performance metrics to evaluate the topology and where the total time taken by one packet to reach from source to destination is calculated in the absence ofcongestion.

The throughput of a network is the data rate in bits per second that the network can accept per input port. The rate at which the packets are injected into the network by a node is termed as packet injection rate [32]. It can be described through (packet/cycle/IP). Packet injection rate lies between 0 and 1. For example, the pir of 0.1 means that one node is capable of sending 1 packet every 10 clock cycles. The Packet Format is shown in Figure 3.

We have performed simulations involving 144-node and 256-node 3D mesh architectures and compared their performance. We have already described various advantages of 3D-NoC architecture over 2D-NoC in Section II.

For a range of injection rates within the simulation period, the average latency values and throughput are calculated which are shown in Table 3, Table 4, Figure 3, and Figure 4 respectively. The default parameters set as follows for conducting simulation with Access Noxim.

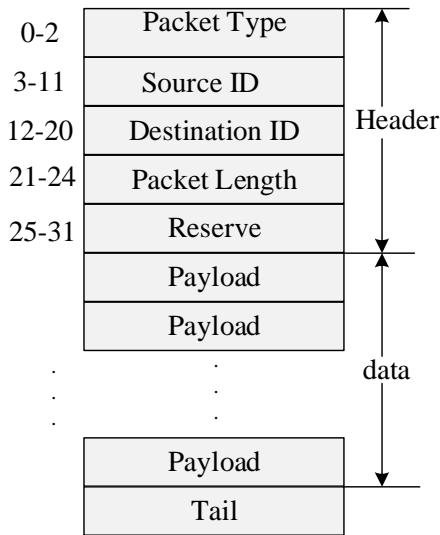


Fig. 3: Packet Format

Table 2: Default Parameters

Parameter Name	Values taken
Dim X, Dim Y, Dim Z (Mesh Size)	6*6*4 and 8*8*4
Buffer size (in flits)	Default 16
Simulation run	10000 cycles
Packet size	2-10 flits
Traffic Pattern	Random
Routing Algorithm	XYZ algorithm

Table 3: Injection rate vs throughput

Injection rate	throughput(6*6*4)	throughput (8*8*4)
0.01	0.0798705	0.0794013
0.02	0.157087	0.158455
0.03	0.235071	0.234774
0.04	0.309366	0.0193707
0.05	0.0178685	0.00817582
0.06	0.0127124	0.00608811
0.07	0.00861753	0.00552243
0.08	0.00783967	0.00471543
0.09	0.00870087	0.00426605
0.1	0.00712293	0.00379332

Table 4: Injection rate vs latency

Injection rate	Latency 6*6*4	Latency 8*8*4
0.01	48	52
0.02	72	110
0.03	118	193
0.04	170	370
0.05	256	270
0.06	216	220
0.07	201	212
0.08	244	202
0.09	254	245
0.1	184	219

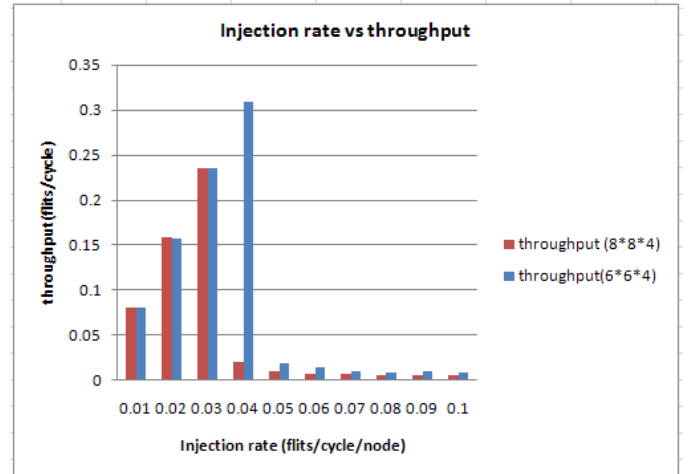


Fig. 4: Injection rate vs throughput

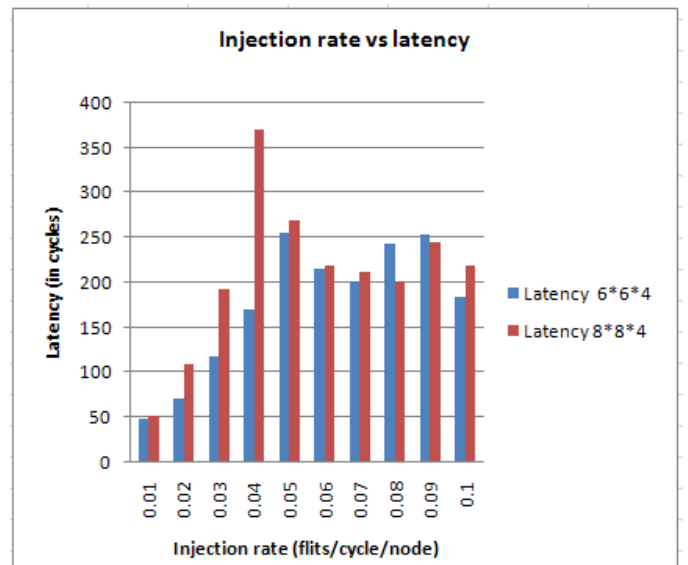


Fig. 5: Injection rate vs latency

V. CONCLUSION AND CURRENT CHALLENGES

The Network on Chip (NoC) is an enabling solution for integrating larger number of IP cores and the communication infrastructure among IP cores predominantly using packet-switched communication. Through pipeline packet transmission, NoCs permit a more efficient utilization of communication resources than traditional on-chip buses. 3D-NoCs are amalgamation of leading edge technology i.e. NoC and 3D IC's and contain multiple layers having the potential to dramatically achieve better chip performance, functionality, and device packing density in deep sub-micron technology. We have presented the performance of 3D Mesh topology with dimensions 6*6*4 and 8*8*4. From the various graphs obtained from simulation under random traffic pattern, it can be concluded from Figure 3 and Table 3 that, as the injection rate increases, the throughput of the network increases for both 144 nodes and 256 node architectures. The actual advantage of 3D mesh is visible; for 144 nodes and 256 nodes, the throughput does not vary too much, it is almost same. Similarly the latency values with respect to injection are also shown in Table 4 and Figure 4. This means the data transfer in 144 node architecture is faster than 256 node architecture. Results

obtained so far show that 3D-ICs can achieve better performances, more flexibility, and higher throughput compared to traditional ICs.

The Network-on-Chip paradigm has emerged as a fabrication technology for integrating thousands of intellectual property (IP) blocks on a single die as compared to the convention bus based System on chips. The kind of the IP blocks (their qualities, capacities) and in addition the topology, scheduling and routing plan assumes a vital part on how proficiently a NoC will perform for a certain application or set of applications. Up to now NoC designs were limited to two dimensions. But the currently emerging 3D integration technology targets at lower power consumption, lower communication delay, and higher system performance. Observing that current on-chip systems suffer from the critical memory bandwidth problems in the communications between on-chip components and off-chip memory. 3D-NoC architectures are proved to be outstanding in their performance and energy efficient against 2D-NoC systems, questions about their reliability to sustain their performance growth begun to arise [29]. Increased communication latency due to congestion and fault tolerance are challenges for modern 3D-NoCs due to complex and large scale application mapping structures. 3D-NoC systems are becoming susceptible to a variety of faults caused by crosstalk [27], impact of radiations [28]. However, prior works presented so many fault tolerant routing algorithms for 2D-NOCs, but only a few works have been designed for 3D-NOCs. The routing models that have been proposed until now usually have high overhead or routing tables, data redundancy and global route or fault information to tolerate faulty links [30]. These overheads increase area and power consumption that is not suitable for on-chip networks. However, the performance of earlier routing methodologies are not satisfied for 3D-NOCs. Hence in addition to providing high performance, the fault-tolerance and reliability of these networks is becoming a critical issue for future applications. We would like to extend our research work to develop a novel model for routing in 3D mesh-based network-on-chips.

VI. REFERENCES

- [1] W. J. Dally and B. Towles. Principles and Practices of Interconnection Networks. Morgan Kaufmann, 2004.
- [2] William J. Dally and Brian Towles. Route packets, not wires: On-chip interconnection networks. In Proceedings of the 38th Conference Design Automation, pages 684–689, 2001. DOI: 10.1109/DAC.2001.935594.
- [3] Feero B.S., Pande P.P. "Networks-on-Chip in a Three – Dimensional Environment": A Performance Evaluation. IEEE Transactions on Computers Vol.58; No. 1; Jan. 2009; pp. 32-45
- [4] Goossens, Kees, John Dielissen, and Andrei Radulescu. "Æthereal network on chip: concepts, architectures, and implementations." IEEE Design & Test of Computers 22.5 (2005): 414-421.
- [5] Palermo, Gianluca, et al. "Application-specific topology design customization for stnoc." Digital System Design Architectures, Methods and Tools, 2007. DSD 2007. 10th Euromicro Conference on. IEEE, 2007.
- [6] Vangal, Sriram, et al. "An 80-tile 1.28 TFLOPS network-on-chip in 65nm CMOS." IEEE International Solid-State Circuits Conference, ISSCC 2007, Digest of Technical Papers, San Francisco, CA, USA. IEEE, 2007.
- [7] Ebrahimi, Masoumeh, et al. Cluster-based topologies for 3d networks-on-chip using advanced inter-layer bus architecture. Journal of Computer and System Sciences 79.4 (2013): 475-491
- [8] Ebrahimi, Mojtaba, et al. Path-based partitioning methods for 3D networks-on-chip with minimal adaptive routing. Computers, IEEE Transactions on 63.3 (2014): 718-733
- [9] Eghbal, Ashkan, et al. "Analytical Fault Tolerance Assessment and Metrics for TSV-based 3D Network-on-Chip." 2015 IEEE Transactions on computers.
- [10] Somasundaram, K., Juha Plosila, and N. Viswanathan. Deadlock free routing algorithm for minimizing congestion in a Hamiltonian connected recursive 3D-NoCs. Microelectronics Journal 45.8 (2014): 989-1000
- [11] De Paulo, Vitor, and Cristinel Ababei. 3D network-on-chip architectures using homogeneous meshes and heterogeneous floorplans. International Journal of Reconfigurable Computing 2010 (2010)
- [12] Viswanathan, N., K. Paramasivam, and K. Somasundaram. "Exploring Hierarchical, Cluster based 3D Topologies for 3D NoC." Procedia Engineering 30 (2012): 606-615.
- [13] De Paulo, Vitor, and Cristinel Ababei. "3D network-on-chip architectures using homogeneous meshes and heterogeneous floorplans." International Journal of Reconfigurable Computing 2010 (2010)
- [14] M. Millberg, E. Nilsson, R. Thid, and A. Jantsch, "Guaranteed bandwidth using looped containers in temporally disjoint networks within the Nostrum network on chip," in Proceedings VLSI Design 15 of the Conference on Design, Automation and Test in Europe (DATE '04), vol. 2, pp. 890–895, Paris, France, February 2004.
- [15] D. Wiklund and D. Liu, "SoCBUS: switched network on chip for hard real time embedded systems," in Proceedings of 17th IEEE International Parallel and Distributed Processing Symposium (IPDPS '03), p. 8, Nice, France, April 2003.
- [16] F. Moraes, N. Calazans, A. Mello, L. Moller, and L. Ost, "HERMES: an infrastructure for low area overhead packetswitching networks on chip," The VLSI Journal, vol. 38, no. 1, pp. 69–93, 2004.
- [17] Rahmani, Amir-Mohammad, et al. "An efficient hybridization scheme for stacked mesh 3D NoC architecture." 2012 20th Euromicro International Conference on Parallel, Distributed and Network-based Processing. IEEE, 2012
- [18] F. Li et al., "Design and management of 3D chip multiprocessors using network-in-memory," In Proc. of Int. Symp. on Computer Architecture, pp.130–141, 2006.
- [19] Bahmani, Maryam, Abbas Sheibanyrad, and Frédéric Pétrot. "Vertical Partial 3D Mesh-Based NoC architecture."
- [20] Li, Min, et al. "A 3D topology based-on partial overlapped clusters for NoC." *IEICE Electronics Express* 11.19 (2014): 20140790-20140790.
- [21] G. Philip, B. Christopher, P. Ramm, Handbook of 3D integration: Technology and Applications of 3D Integrated Circuits, Wiley-VCH, Weinheim, 2008
- [22] Ghidini, Yan, et al. "Topological impact on latency and throughput: 2D versus 3D NoC comparison." Integrated Circuits and Systems Design (SBCCI), 2012 25th Symposium on. IEEE, 2012.
- [23] Matsutani, Hiroki, Michihiro Koibuchi, and Hideharu Amano. "Tightly-coupled multi-layer topologies for 3-D NoCs." 2007 International Conference on Parallel Processing (ICPP 2007). IEEE, 2007.
- [24] H. Matsutani et al., "Tightly-coupled multi-layer topologies for 3-D NOCs," in Proc. of International Conference on Parallel Processing, 2007, pp. 75-84.
- [25] Yin, Alexander Wei, et al. "Explorations of honeycomb topologies for network-on-chip." Network and Parallel Computing, 2009. NPC'09. Sixth IFIP International Conference on. IEEE, 2009.
- [26] Access Noxim: <http://access.ee.ntu.edu.tw/noxim/index.html>
- [27] M. Cuvliello, S. Dey, X. Bai, and Y. Zhao. Fault modeling and simulation for crosstalk in system-on-chip interconnects. In IEEE/ACM International Digest of Technical Papers on Computer-Aided Design, pp. 297303, 1999.
- [28] S. Borkar, Designing reliable systems from unreliable components: The challenges of transistor variability and degradation. IEEE Micro 25(6):1016, Nov-Dec 2005.
- [29] L. Benini and G. De Micheli. Networks on Chips: Technology and Tools. Morgan Kaufmann, 2006
- [30] Liu, Junxiu, et al. "Low cost fault-tolerant routing algorithm for Networks-on-Chip." Microprocessors and Microsystems 39.6 (2015): 358-372.
- [31] L. M. Ni and P. K. McKinley, "A Survey of Wormhole Routing Techniques in Direct Networks", IEEE Computer Magazine, v.26(2), February, 1993, pp. 62-76
- [32] Chau, H. F., H. Y. Chan, and F. K. Chow. "On the critical packet injection rate of a preferential next-nearest neighbor routing traffic model on Barabási-Albert networks." The European Physical Journal B-Condensed Matter and Complex Systems 72.4 (2009): 641-655.

Exploring 3D Network-on-Chip Architectures and Challenges

Sapna Tyagi

Department of Computer Science
Institute of Management Studies
Ghaziabad, India
sapna030280@gmail.com

Piyush Maheshwari

Department of Engineering
Amity University Dubai
United Arab Emirates
pmaheshwari@amityuniversity.ae

Amit Agarwal, Vinay Avasthi

Center for Information Technology
University of Petroleum & Energy
Studies, Dehradun, India
{[@ddn.upes.ac.in](mailto:aagarwal,vavasthi)}

Abstract— Network-on-Chip (NoC) is a nascent approach for reducing the communication bottleneck of multicore System-on-Chip (SoC). As the number of cores are increasing on SoC due to high performance demand of the consumer electronics and processing systems like servers, the low power and low latency NoC is required. Topologies are one of the most important parts of a NoC design, with considering the performance parameter as a constraint. The important parameters of networks-on-chip are latency, throughput, injection rate and average number of hops etc. In our work, various existing 3D NoC architectures and their performance are studied and presented. The basic concepts of NoC and motivation for 3D NoC and its advantages over 2D NoC are also focused in this paper. We have also investigated and demonstrated 144 nodes and 256 nodes 3D mesh architecture in terms of the latency, throughput and injection rate.

Keywords—Network-on-Chip (NoC); Topologies; Access Noxim

I. INTRODUCTION

Network-on-chip is a emerging design for communication where large number of functional and storage cores or commonly known as IP Core such as video and audio processors, memories, I/O peripherals, hardware accelerators, etc. are integrated onto a single chip to exchange data and commands for implementing emerging multimedia and networking services. Earlier system-on-chips communications are carried through by direct cross bar interconnections and shared buses. However these approaches restarint performance and are consider no longer reliable architecture for SoC due to lack of scalability and parallelism integration, high latency and power dissipation, and low throughput which degrades on-chip performance.

Network-on-Chip is the revolutionary methodology as comapred with traditional bus-based and point-to-point communication structures with a huge potential to handle the increasing complexity of current and future multicore SoCs [1][2]. In such arena, cores are connected via a packet-switching communication network on a single chip. NoC architecture is generally characterized by its topology, routing, switching, flow control, and arbiter techniques. On-chip network topology is a crucial factor of the chip in determining the parameters performance, cost, and energy

consumption. Various network topologies have been studied for NoCs. Especially, the two-dimensional mesh [12] and torus [13] are popularly used in NoCs, because their n-dimensional grid-based regular architecture is very simple and easy to understand and thus considered to be the most suitable choice for designing NoC. Routing algorithm calculates the path taken by a packet from source node to the target node. These routing algorithms must have the capability to prevent deadlock, livelock, and starvation situations [31]. The different classifications areas are presented in Table 1.

Table 1: Routing Algorithms

Criteria	Types
Number of Destinations	Unicast & Multicast
Routing Decision	Centralized Routing, Source Routing, Distributed Routing, Multiphase Routing
Adaptability	Deterministic Routing, Adaptive or Oblivious Routing
Path Length	Minimal and Non-Minimal routing
Network Condition	Delay & Loss

Switching strategy can be categorized into circuit switching and Packet switching. In circuit switching complete path from source node to destination node is reserved for entire message to traverse the network whereas in packet switching message broken into packets where each packet finds its own way to reach to destination.

Flow control deals about how the data flow is controlled between router to router. It provides the mechanism in the case of congestion in network. Data is temporarily stored in buffers, and re-routed to other nodes. Flow control also tells source node to temporarily halt, discard, etc.

The various important metrics of interest in NoC are:

- performance (latency, throughput, cross-section bandwidth, diameter)
- energy dissipation, power limits
- reliability (fault tolerance, other failures)
- scalability (increasing number of cores)

- Implementation cost (foot print area).

The industry has already entered into the NoC arena by developing different NoC-based architectures such as the *Ethereal NoC* [4] from Philips, the *STNoC* [5] from STMicroelectronics, *80-coreNoC* from Intel [6], *NOSTRUM* [14], *SoCBus* [15] and *Hermes* [16] are few examples.

The remaining part of the paper is organized as below. Section II provides an insight about why we need to migrate towards 3D-NoC. Section III explores various 3D-NoC Architecture and Routing Protocols for 3D-NoC. Section IV presents simulation and results using *Access Noxim 3D-NoC Simulator*. Finally, the conclusion and some challenges are discussed in Section V.

II. MIGRATING FROM 2D NoC TO 3D NoC

The two dimensional NoC presented acceptable performance for the current SoC;s applications but as future applications are getting more and more complex, the consumer products such as mobile phones, notebooks and personal handheld sets will have fabrication of thousands of IP core on single chip. Future devices will become faster, smaller-in-size, larger-in-capacity, lighter-in-weight, lower-in-power-consumption and cheaper. This trend will persistently continue and will demand the good architecture to ensure a satisfactory performance on the chip. Following this trend, we have to integrate hundred and thousands of IP cores onto a single chip for ultra high performance applications. The planar chip two dimensional fabrication technology is facing new challenges in the deep submicron regime [7]. 2D-NoC interconnect are not suitable candidate for future large scale many-core SoCs that are expected to accommodate hundreds of cores.

Planar 2D NoC has limitations for floor planning. Long global wires causes increased latency and therefore limits the performance improvements resulting from Network-on-Chip paradigm. This challenge comes basically from the high network diameter that NoC suffers from. The network's diameter is the number of hops that it traverses in the longest possible minimal path between a (source, destination) pair. The diameter is an important parameter for the NoC design and may have the negative impact on the performance of NoC because if a given packet traverses a large number of hops to reach its destination, it will increase the network diameter which will in turn increase the communication time (latency) hence the throughput will be low. Thus the need to optimize the 2D-NoC system arises and one of these proposed solutions was porting the 2D-NoC architecture to the third dimension to enhance the performance of NoC systems and alleviate their limitations [21]. Research in 3D-NoC is now emerging as new trend to implement future SoC's applications. A 3-dimensional Network on chip is a composite of multiple device layers of 2D NoC with direct vertical interconnects using *Through Silicon Vias (TSV's)*. There are various approaches to build the vertical interconnects which comprises of wire bonded approach, Micro-bonded 3D package, Micro-bonded face to face, contactless –capacitive with buried bumps, contactless – inductive and *Through Silicon Vias (TSV)* is one of the most popular choice [8, 9, 10].

Figure 1 shows 3D Mesh NoC in which nodes are placed as Manhattan-like grid. As NoC structures can be combined with benefits of 3D integration, low interconnects latency and area efficient solution can be realized [11].

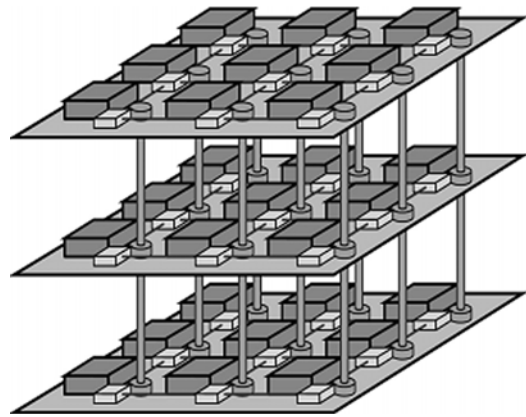


Fig. 1. 3D Mesh based NOC [10]

Three Dimensional NoC technology has several major advantages: (1) More IP/Core units can be added due to the stacking of layers, thus foot-print on each layer will remain smaller and thus leading to more compact chips and drastic increase in IP/Core density which will satisfy the high requirements of future large scale applications, (2) smaller footprints lead to short-length wires and higher transistor density within each layer which are the obvious obstacles for delay and power consumption but inter layer connections are obtained using efficient TSV's and these shorter wires decreases the average load capacitance, resistance and number of repeaters which consumes lot of power thereby leading to higher communication bandwidth, lower delay, low power consumption, lower noise and less jitter, (3) allows integration of plethora of technologies that are currently impossible in 2D planar technology, as each could be designed as a separate layer and will create hybrid circuit, and (4) layered architecture leads to reduced average hop count, fast inter layer and intra layer packet transmission and overall high-throughput network.

III. RELATED WORK: 3D-NOC ARCHITECTURES

This section presents various architectures that were proposed recently for 3D-NoCs. One of the well-known 3D-NoC architectures is the 3D Mesh as shown in Figure 1. In this 3D-NoC architecture each IP core is associated with 7 port router where one port is attached to the IP block, two ports to the routers above and below, and other four in each direction i.e North, South, East, and West. The drawback to this simple architecture is too much number of buffers at each port even when it is not required while travelling through upward and downward links because latency between tiers is too low as tiers are stacked very closely [23]. The number of ports depends on the position of the switch in the design, since we have to eliminate any unused links that have no connections with other switches in order to reduce power consumption.

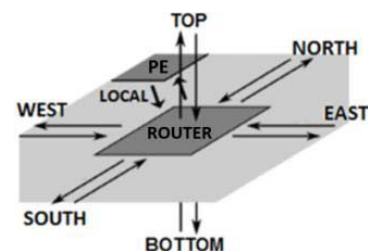


Fig 2. 7-Port 3D Router

3D-NoC Bus Hybrid Architecture [17] was proposed as a hybrid of packet switched NoC's and Shared Bus architecture where multiple 2D Mesh layers are individually implement with packet switched technology and vertically the layers communicate through Shared bus architecture. A router in this hybrid architecture has, at most, six ports: one port is connected to the IP, another to the bus, and rest four to the directions (N,S,E,W). This architecture was implemented in 3D NUCA L2 Cache for CMPs [43]. It suffers from lower bandwidth while communicating interlayer due to shared bus.

Ciliated 3D Mesh [3] was proposed as a variant of 3D basic Mesh based architecture where each switch/router accommodates two or more IP block. In a ciliated 3D Mesh network, each router/switch consist of at most $5+k$ ports (one for each direction (N, S, E, and W), one port either for up or down layers for 2Layer 3D Mesh and K ports are connected to each K IP blocks. This structure suffers from lower bandwidth as switch/router is shared by multiple IP core but power dissipation is low.

In [19], the vertical partial mesh-based 3D NoC (VPM3NoC) architecture is described. This architecture contains mesh-based stacked layers where each layer is differentiated with respect to technology, application and size. In each layer some nodes have vertical links to up and down layers. This structure employs varieties of routers i.e 2D router, 3D Router with upward link, 3D router with downward link, 3D Router with up and down link.

In [12], the authors have presented two 3D topologies i.e 3D star topology and 3D Recursive Network topology and compared them in terms of the parameters as follows: latency, energy dissipation and Network Diameter. In both the topologies, group of 4 node is formed which is termed as cluster with one node is designated as Cluster Head (CH) which can act as CH as well as node. A layer has four clusters, and the total number of nodes in a layer is 16. TSV's are used to connect the 3 layers vertically. The Performance of 3D RNT is evaluated and found better performing in comparison with 3D ST with respect to latency and energy dissipation parameters.

In [13], the authors have proposed 3D 2-layer and 3-layer architectures. In both the approaches the goal is to optimize the floorspace of the chip. In 3D 2-Layer approach, the layer 1 is dedicated to place heterogeneous IP cores where as layer 2 is used to place routers in mesh configuration, similarly In 3-layer architectures, layers 1 and 3 are used to place heterogeneous IP Cores and layer 2 implements mesh architectures of assigned routers. The 3 layers are connected with each other through silicon vias (TSV).

POC topology [20] was proposed as another variant of 3D Mesh topology which consists of two different types of routers i.e 7-port router and 6-port router. 7 port routers are used to connect with IP where 6-port router was only used for communication. The difference between 3D Mesh and POC topology is that the vertical links are only implemented at 6 port router. The advantage of this topology is fewer vertical links which leads to low energy dissipations.

Another 3D Mesh based NoC architecture called Lasio [22] is also presented where hops between layer (z axis) and hops within layer (X, Y axis) have same cost. The most important feature of this architecture is that all router ports are bidirectional. It implemented XYZ routing and used credit based flow control.

Another class of 3D-NoC topologies called Xbar-connected Network-on-Tiers (XNoTs) [24], consisting of multiple layers and each layer is customized with different topology according to the application. The layers are tightly connected via crossbar switches which reduces the average hop count and low power consumption.

3D Honeycomb NoC topology [25] is formed by stacking 2D honeycomb topology which is composed of hexagons. This topology suffers from the high implementation cost due to the large number of vertical communication links. This architecture has the network degree of 5 which leads to higher network cost.

IV. EXPERIMENTAL RESULTS

In this paper we analyze packet latency, throughput with respect to injection rate by using the Access Noxim [26] simulator which is extended version of Noxim Simulator for 3D-NoC Mesh.

The latency of the network is the synonym for delay and time taken for a packet, flit or message to reach from source to destination. It also includes the time taken for computing arbitration logic as well as routing computation and other contention delays. It is the elementary parameter of the performance evaluation of Networks on chip. The delay is mainly caused by the source-destination physical distance, and also by deflections due to traffic congestion inside the network. It is measured in clock cycles. Packet Latency can be calculated as:

$$\text{Packet Latency} = \text{Actual Transmit time} + \text{Routing Delay} + \text{Contention Delay}$$

Another related parameter i.e zero load latency [1] is also used widely as a performance metrics to evaluate the topology and where the total time taken by one packet to reach from source to destination is calculated in the absence of congestion.

The throughput of a network is the data rate in bits per second that the network can accept per input port. The rate at which the packets are injected into the network by a node is termed as packet injection rate [32]. It can be described through (packet/cycle/IP). Packet injection rate lies between 0 and 1. For example, the pir of 0.1 means that one node is capable of sending 1 packet every 10 clock cycles. The Packet Format is shown in Figure 3.

We have performed simulations involving 144-node and 256-node 3D mesh architectures and compared their performance. We have already described various advantages of 3D-NoC architecture over 2D-NoC in Section II.

For a range of injection rates within the simulation period, the average latency values and throughput are calculated which are shown in Table 3, Table 4, Figure 3, and Figure 4 respectively. The default parameters set as follows for conducting simulation with Access Noxim.

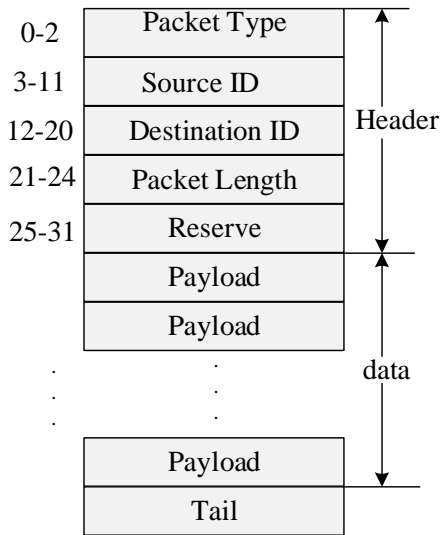


Fig. 3: Packet Format

Table 2: Default Parameters

Parameter Name	Values taken
Dim X, Dim Y, Dim Z (Mesh Size)	6*6*4 and 8*8*4
Buffer size (in flits)	Default 16
Simulation run	10000 cycles
Packet size	2-10 flits
Traffic Pattern	Random
Routing Algorithm	XYZ algorithm

Table 3: Injection rate vs throughput

Injection rate	throughput(6*6*4)	throughput (8*8*4)
0.01	0.0798705	0.0794013
0.02	0.157087	0.158455
0.03	0.235071	0.234774
0.04	0.309366	0.0193707
0.05	0.0178685	0.00817582
0.06	0.0127124	0.00608811
0.07	0.00861753	0.00552243
0.08	0.00783967	0.00471543
0.09	0.00870087	0.00426605
0.1	0.00712293	0.00379332

Table 4: Injection rate vs latency

Injection rate	Latency 6*6*4	Latency 8*8*4
0.01	48	52
0.02	72	110
0.03	118	193
0.04	170	370
0.05	256	270
0.06	216	220
0.07	201	212
0.08	244	202
0.09	254	245
0.1	184	219

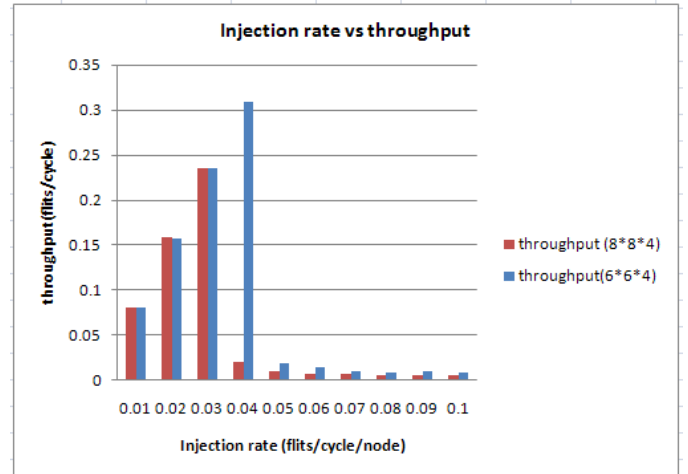


Fig. 4: Injection rate vs throughput

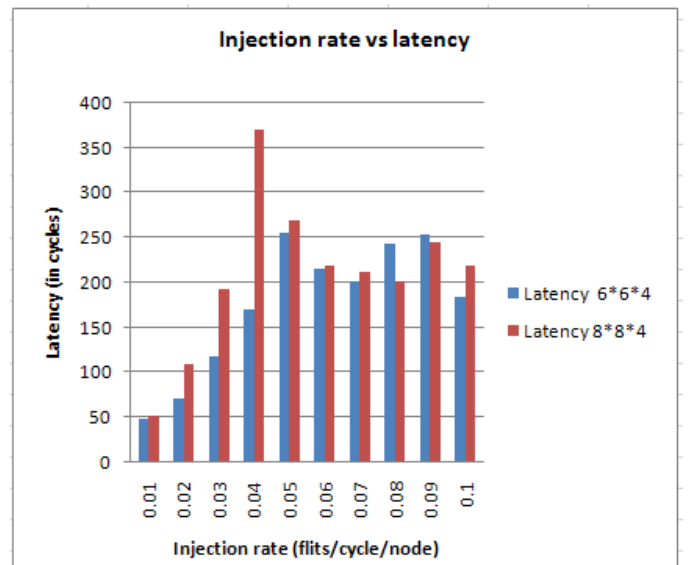


Fig. 5: Injection rate vs latency

V. CONCLUSION AND CURRENT CHALLENGES

The Network on Chip (NoC) is an enabling solution for integrating larger number of IP cores and the communication infrastructure among IP cores predominantly using packet-switched communication. Through pipeline packet transmission, NoCs permit a more efficient utilization of communication resources than traditional on-chip buses. 3D-NoCs are amalgamation of leading edge technology i.e. NoC and 3D IC's and contain multiple layers having the potential to dramatically achieve better chip performance, functionality, and device packing density in deep sub-micron technology. We have presented the performance of 3D Mesh topology with dimensions 6*6*4 and 8*8*4. From the various graphs obtained from simulation under random traffic pattern, it can be concluded from Figure 3 and Table 3 that, as the injection rate increases, the throughput of the network increases for both 144 nodes and 256 node architectures. The actual advantage of 3D mesh is visible; for 144 nodes and 256 nodes, the throughput does not vary too much, it is almost same. Similarly the latency values with respect to injection are also shown in Table 4 and Figure 4. This means the data transfer in 144 node architecture is faster than 256 node architecture. Results

obtained so far show that 3D-ICs can achieve better performances, more flexibility, and higher throughput compared to traditional ICs.

The Network-on-Chip paradigm has emerged as a fabrication technology for integrating thousands of intellectual property (IP) blocks on a single die as compared to the convention bus based System on chips. The kind of the IP blocks (their qualities, capacities) and in addition the topology, scheduling and routing plan assumes a vital part on how proficiently a NoC will perform for a certain application or set of applications. Up to now NoC designs were limited to two dimensions. But the currently emerging 3D integration technology targets at lower power consumption, lower communication delay, and higher system performance. Observing that current on-chip systems suffer from the critical memory bandwidth problems in the communications between on-chip components and off-chip memory. 3D-NoC architectures are proved to be outstanding in their performance and energy efficient against 2D-NoC systems, questions about their reliability to sustain their performance growth begun to arise [29]. Increased communication latency due to congestion and fault tolerance are challenges for modern 3D-NoCs due to complex and large scale application mapping structures. 3D-NoC systems are becoming susceptible to a variety of faults caused by crosstalk [27], impact of radiations [28]. However, prior works presented so many fault tolerant routing algorithms for 2D-NOCs, but only a few works have been designed for 3D-NOCs. The routing models that have been proposed until now usually have high overhead or routing tables, data redundancy and global route or fault information to tolerate faulty links [30]. These overheads increase area and power consumption that is not suitable for on-chip networks. However, the performance of earlier routing methodologies are not satisfied for 3D-NOCs. Hence in addition to providing high performance, the fault-tolerance and reliability of these networks is becoming a critical issue for future applications. We would like to extend our research work to develop a novel model for routing in 3D mesh-based network-on-chips.

VI. REFERENCES

- [1] W. J. Dally and B. Towles. Principles and Practices of Interconnection Networks. Morgan Kaufmann, 2004.
- [2] William J. Dally and Brian Towles. Route packets, not wires: On-chip interconnection networks. In Proceedings of the 38th Conference Design Automation, pages 684–689, 2001. DOI: 10.1109/DAC.2001.935594.
- [3] Feero B.S., Pande P.P. "Networks-on-Chip in a Three – Dimensional Environment": A Performance Evaluation. IEEE Transactions on Computers Vol.58; No. 1; Jan. 2009; pp. 32-45
- [4] Goossens, Kees, John Dielissen, and Andrei Radulescu. "Æthereal network on chip: concepts, architectures, and implementations." IEEE Design & Test of Computers 22.5 (2005): 414-421.
- [5] Palermo, Gianluca, et al. "Application-specific topology design customization for stnoc." Digital System Design Architectures, Methods and Tools, 2007. DSD 2007. 10th Euromicro Conference on. IEEE, 2007.
- [6] Vangal, Sriram, et al. "An 80-tile 1.28 TFLOPS network-on-chip in 65nm CMOS." IEEE International Solid-State Circuits Conference, ISSCC 2007, Digest of Technical Papers, San Francisco, CA, USA. IEEE, 2007.
- [7] Ebrahimi, Masoumeh, et al. Cluster-based topologies for 3d networks-on-chip using advanced inter-layer bus architecture. Journal of Computer and System Sciences 79.4 (2013): 475-491
- [8] Ebrahimi, Mojtaba, et al. Path-based partitioning methods for 3D networks-on-chip with minimal adaptive routing. Computers, IEEE Transactions on 63.3 (2014): 718-733
- [9] Eghbal, Ashkan, et al. "Analytical Fault Tolerance Assessment and Metrics for TSV-based 3D Network-on-Chip." 2015 IEEE Transactions on computers.
- [10] Somasundaram, K., Juha Plosila, and N. Viswanathan. Deadlock free routing algorithm for minimizing congestion in a Hamiltonian connected recursive 3D-NoCs. Microelectronics Journal 45.8 (2014): 989-1000
- [11] De Paulo, Vitor, and Cristinel Ababei. 3D network-on-chip architectures using homogeneous meshes and heterogeneous floorplans. International Journal of Reconfigurable Computing 2010 (2010)
- [12] Viswanathan, N., K. Paramasivam, and K. Somasundaram. "Exploring Hierarchical, Cluster based 3D Topologies for 3D NoC." Procedia Engineering 30 (2012): 606-615.
- [13] De Paulo, Vitor, and Cristinel Ababei. "3D network-on-chip architectures using homogeneous meshes and heterogeneous floorplans." International Journal of Reconfigurable Computing 2010 (2010)
- [14] M. Millberg, E. Nilsson, R. Thid, and A. Jantsch, "Guaranteed bandwidth using looped containers in temporally disjoint networks within the Nostrum network on chip," in Proceedings VLSI Design 15 of the Conference on Design, Automation and Test in Europe (DATE '04), vol. 2, pp. 890–895, Paris, France, February 2004.
- [15] D. Wiklund and D. Liu, "SoCBUS: switched network on chip for hard real time embedded systems," in Proceedings of 17th IEEE International Parallel and Distributed Processing Symposium (IPDPS '03), p. 8, Nice, France, April 2003.
- [16] F. Moraes, N. Calazans, A. Mello, L. Moller, and L. Ost, "HERMES: an infrastructure for low area overhead packetswitching networks on chip," The VLSI Journal, vol. 38, no. 1, pp. 69–93, 2004.
- [17] Rahmani, Amir-Mohammad, et al. "An efficient hybridization scheme for stacked mesh 3D NoC architecture." 2012 20th Euromicro International Conference on Parallel, Distributed and Network-based Processing. IEEE, 2012
- [18] F. Li et al., "Design and management of 3D chip multiprocessors using network-in-memory," In Proc. of Int. Symp. on Computer Architecture, pp.130–141, 2006.
- [19] Bahmani, Maryam, Abbas Sheibanyrad, and Frédéric Pétrot. "Vertical Partial 3D Mesh-Based NoC architecture."
- [20] Li, Min, et al. "A 3D topology based-on partial overlapped clusters for NoC." *IEICE Electronics Express* 11.19 (2014): 20140790-20140790.
- [21] G. Philip, B. Christopher, P. Ramm, Handbook of 3D integration: Technology and Applications of 3D Integrated Circuits, Wiley-VCH, Weinheim, 2008
- [22] Ghidini, Yan, et al. "Topological impact on latency and throughput: 2D versus 3D NoC comparison." Integrated Circuits and Systems Design (SBCCI), 2012 25th Symposium on. IEEE, 2012.
- [23] Matsutani, Hiroki, Michihiro Koibuchi, and Hideharu Amano. "Tightly-coupled multi-layer topologies for 3-D NoCs." 2007 International Conference on Parallel Processing (ICPP 2007). IEEE, 2007.
- [24] H. Matsutani et al., "Tightly-coupled multi-layer topologies for 3-D NOCs," in Proc. of International Conference on Parallel Processing, 2007, pp. 75-84.
- [25] Yin, Alexander Wei, et al. "Explorations of honeycomb topologies for network-on-chip." Network and Parallel Computing, 2009. NPC'09. Sixth IFIP International Conference on. IEEE, 2009.
- [26] Access Noxim: <http://access.ee.ntu.edu.tw/noxim/index.html>
- [27] M. Cuvillo, S. Dey, X. Bai, and Y. Zhao. Fault modeling and simulation for crosstalk in system-on-chip interconnects. In IEEE/ACM International Digest of Technical Papers on Computer-Aided Design, pp. 297303, 1999.
- [28] S. Borkar, Designing reliable systems from unreliable components: The challenges of transistor variability and degradation. IEEE Micro 25(6):1016, Nov-Dec 2005.
- [29] L. Benini and G. De Micheli. Networks on Chips: Technology and Tools. Morgan Kaufmann, 2006
- [30] Liu, Junxiu, et al. "Low cost fault-tolerant routing algorithm for Networks-on-Chip." Microprocessors and Microsystems 39.6 (2015): 358-372.
- [31] L. M. Ni and P. K. McKinley, "A Survey of Wormhole Routing Techniques in Direct Networks", IEEE Computer Magazine, v.26(2), February, 1993, pp. 62-76
- [32] Chau, H. F., H. Y. Chan, and F. K. Chow. "On the critical packet injection rate of a preferential next-nearest neighbor routing traffic model on Barabási-Albert networks." The European Physical Journal B-Condensed Matter and Complex Systems 72.4 (2009): 641-655.

HAAR like Feature-Based Car Key Detection Using Cascade Classifier

Paawan Sharma, Mukul K. Gupta, Amit K. Mondal
and Vivek Kaundal

Abstract The paper reports effective real-time implementation for specific object detection in an image or sequence of images. For the present work, car key has been taken as an object under consideration. The classifier is developed using OpenCV-Python. The procedure encompasses training and detection. A wide variety of object images are used for training purpose. The developed xml classifier is then tested on separate test images. The classifier has a good success rate with minimal false object detection rate.

Keywords Classifier · Haar-like features · OpenCV · Python · Machine vision · Pattern recognition

1 Introduction

Machine vision is a very crucial component of robotics and automation for various systems such as manufacturing plants, smart robots, etc. [1]. OpenCV [2] is an open source library for computer vision. Specifically in real-time applications, OpenCV exhibits a good computational efficiency. Classifier design is an important aspect of any machine vision-based application, and is practiced to implement a decision rule [1]. Classifier behavior depends on features which are extracted from images.

Paawan Sharma (✉) · M.K. Gupta · A.K. Mondal · Vivek Kaundal
Department of Electronics, Instrumentation and Control Engineering,
University of Petroleum and Energy Studies, Dehradun, India
e-mail: paawan.sharma@ddn.upes.ac.in

M.K. Gupta
e-mail: mkgupta@ddn.upes.ac.in

A.K. Mondal
e-mail: akmondal@ddn.upes.ac.in

Vivek Kaundal
e-mail: vkaundal@ddn.upes.ac.in

Every classifier has some description, which can be obtained using supervised or unsupervised learning [3]. In supervised learning, a training set of images is used to develop class representation in terms of various statistical parameters. An unsupervised learning is basically a clustering algorithm which links samples to the nearest cluster.

Viola-Jones generated [4] Haar-like features from Haar basis function $f(x)$ described in Eqs. (1) and (2), and constructed classifier using Adaboost [5] by successive combination in a cascade fashion resulting into detection speed improvement.

$$f(x) = \begin{cases} 1 & 0 \leq x < \frac{1}{2} \\ -1 & \frac{1}{2} \leq x \leq 1 \\ 0 & \text{else} \end{cases}; \quad (1)$$

$$f(x)_j^k \equiv f(2^j x - k) \quad (2)$$

In such process, a weak learning algorithm selects the single feature which best differentiates between positive and negative samples. This optimal function results into minimum number of wrong classifications.

2 Methodology

This section describes the overall process of generating a classifier as shown in Fig. 1. It starts with creating a vector file (.vec file) from positive and negative samples (images). Positive images are those which contain the desired object (car keys in this case), while negative images are those which do not contain the object. The utility `opencv_createsamples` in OpenCV [6] creates a vector file according to various options. The second utility `opencv_traincascade` [6] uses the *.vec file generated in previous step and set of background images to create the classifier (*.xml file).

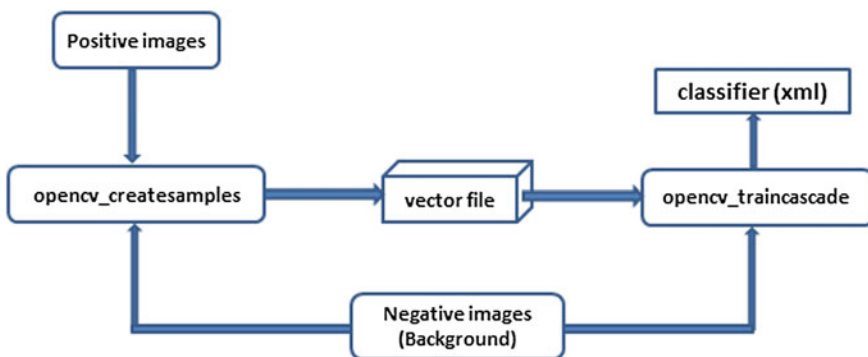


Fig. 1 OpenCV classifier (.xml) design process

Table 1 opencv_createsamples parameters

Parameter	Value	Description
-maxxangle	1.1	Maximum X-axis rotation angle
-maxyangle	1.1	Maximum Y-axis rotation angle
-maxzangle	0.5	Maximum Z-axis rotation angle
-w	24	Sample width in pixels
-h	24	Sample height in pixels

Table 2 Opencv_traincascade parameters

Parameter	Value	Description
-numPos	18	No. of positive samples
-numNeg	18	No. of negative samples
-numStages	20	Trainable cascade stages
-w	24	Sample width in pixels
-h	24	Sample height in pixels

Then, the classifier is applied on various test images using a simple Python program. The code for this purpose is expected to draw a polygon at the location where object is detected in the image.

As discussed in Sect. 2.1, the OpenCV utilities have many optional parameters which alters the training process. opencv_createsamples has -vec, -info, -img, -bg, -num, -bgcolor -bgthresh, -inv, -randinv, -maxidev, -maxxangle, -maxyangle, -maxzangle, -show, -w, -h as parameters, the values for which are mentioned in Table 1. opencv_traincascade has -data, -vec, -info, -img, -bg, -numPos, -numNeg, -numStages, -mode, -w, -h, -minHitRate as parameters, the values for which are mentioned in Table 2.

2.1 Code Syntax

OpenCV command usage

```
opencv_createsamples -info
E:\machine_vision\haarclassifier\imagess \info.dat -bg
E:\machine_vision\haarclassifier\imagess\bg.txt -vec
op_ft.vec -num 18
opencv_traincascade -data E:\machine_vision\ -vec
op_ft.vec -bg
E:\machine_vision\haarclassifier\imagess\bg.txt -numPos
18 -numNeg 18
```

Python code [7]

```

import numpy as np
import cv2
carkeys_cascade = cv2.CascadeClassifier('carkeys.xml')
img1 = cv2.imread('img1.jpg')
img2 = cv2.imread('img2.jpg')
gray1 = cv2.cvtColor(img1, cv2.COLOR_BGR2GRAY)
gray2 = cv2.cvtColor(img2, cv2.COLOR_BGR2GRAY)
faces1 = carkeys_cascade.detectMultiScale(gray1, 1.05,
1)
faces2 = carkeys_cascade.detectMultiScale(gray2, 1.05,
1)
for (x,y,w,h) in faces1:
    cv2.rectangle(img1 , (x,y) , (x+w, y+h) , (255,0,0)
, 2)
for (x,y,w,h) in faces2:
    cv2.rectangle(img2 , (x,y) , (x+w, y+h) , (255,0,0)
, 2)
cv2.imshow('img1',img1)
cv2.imshow('img2',img2)
cv2.imwrite('det1.png',img1)
cv2.imwrite('det2.png',img2)
cv2.waitKey(0) cv2.destroyAllWindows()

```

3 Results

Figure 2 shows the output of Python program, which clearly indicates the detection of car keys. However, a better success rate and minimal false object detection can be achieved by increasing the number of positive as well as negative samples. For present study, 18 images for each category were chosen for training purpose.

4 Conclusion

A practical method of object detection was analyzed in real-time yielding positive results. The biggest advantage of using OpenCV-Python for such purpose lies in the fact that both tools are available for Linux operating system also. This makes it possible to implement it on hardware platform such as Raspberry pi, etc., since users can select OS of their choice for the hardware platform. Hence, a combination of Linux-OpenCV-Python can be easily exploited over a hardware platform.

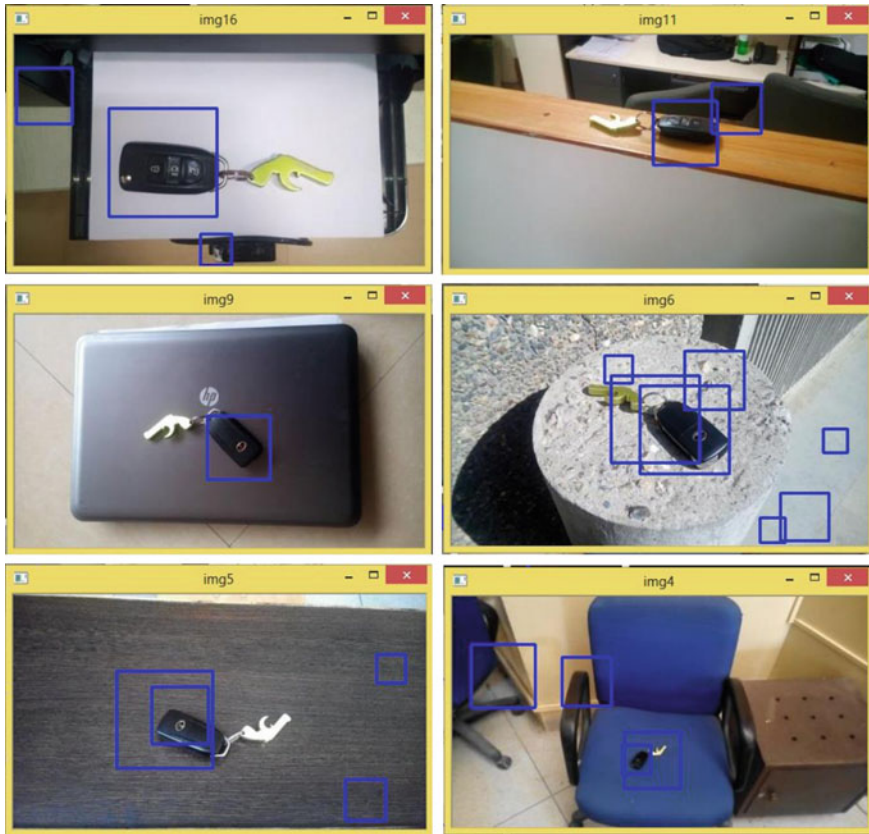


Fig. 2 OpenCV classifier performance

Acknowledgments Authors are thankful to Mr. Bhanprakash for his valuable help in collecting image samples.

References

1. Sonka, Milan, Vaclav Hlavac, and Roger Boyle. Image processing, analysis, and machine vision. Cengage Learning (2014).
2. Documentation for OpenCV, <http://opencv.org/documentation.html>.
3. Snyder, Wesley E., and Hairong Qi. Machine vision. Cambridge University Press (2010).
4. Viola, Paul, and Michael Jones. "Rapid object detection using a boosted cascade of simple features" In Computer Vision and Pattern Recognition, 2001. CVPR 2001. Proceedings of the 2001 IEEE Computer Society Conference on, vol. 1, pp. 1–511. IEEE (2001).

5. Freund, Yoav, and Robert E. Schapire. "A decision-theoretic generalization of on-line learning and an application to boosting" *Journal of computer and system sciences* 55, no. 1 (1997): 119–139.
6. Cascade Classifier Training, http://docs.opencv.org/3.1.0/dc/d88/tutorial_traincascade.html#gsc.tab=0.
7. OpenCV-Python Tutorials, http://docs.opencv.org/3.1.0/d6/d00/tutorial_py_root.html.

Implementation of Ladder Logic for Control of Pipeline Inspection Robot Using PLC

Varnita Verma, Roushan Kumar and Vivek Kaundal

Abstract In the modern world, the transportation of goods and services plays an important role in establishing good connections between the nations. The main source of transportation of major energy sources like fuel gases, petroleum, and other flow of gases and liquid has been done through pipelines, any crack, blow-holes, or damage inside the pipe may lead to major economic loss and can catches fire therefore the internal inspection of pipelines is needed. For inspection of narrow, deep, and hazardous environment inside the pipeline the robots is used. The control of robot has been done by programmable logic controller (PLC) and internal control of robot has been through human-machine interface (HMI). The control of robot has two parts in terms of programming. First, the development of ladder logic is done in Indraworks Engineering Software according to the sequence of operations and then simulates it on software itself to check the fulfillment of objectives. Second, developing the HMI Interface is for internal control of robot and easy access of operation. Touch screen has been used as HMI which is helpful in opting the size of pipe accordingly pipeline inspection robot will adjust its arms.

Keywords Pipeline inspection robot · Rexroth PLC · Industrial automation · HMI · Indraworks Engineering

Varnita Verma (✉) · Roushan Kumar · Vivek Kaundal
University of Petroleum and Energy Studies, Dehradun, India
e-mail: varnitaverma@yahoo.in

Roushan Kumar
e-mail: rkumar@ddn.upes.ac.in

Vivek Kaundal
e-mail: vkaundal@ddn.upes.ac.in

1 Introduction

The flow of gases and liquid has been done through pipelines and the inspection of pipeline is must for proper transportation of gases and liquids and related to safety issues, for internal inspection of pipe conventionally, humans go inside the pipe which is harmful to the health of human. Therefore, the device has been created which was inserted in pipes to check for obstruction or damage [1–3]. This robot is capable of adjusting its arm from 30 to 40 cm and able to detect the intensity of damage inside the pipe this could be done through inspection camera mounted on the robot which helps in capturing the real-time images and processes the image through image processing. This robot is very useful for internal inspection of underground pipeline, sewage pipes, gas pipes, ac vent, etc., and easy repair of pipeline can be done after knowing the defect location of pipeline. The most popular nondestructive testing (NDT) techniques has been done with the help of camera, ultrasonic sensor, microwave technique, and 3D optical sensor. The size and shape of robot are dependent on the layout of entire pipeline structure [2]. Many pipeline inspection robots have been implemented before like PIRAT robot which is a nonautonomous tethered robot for the quantitative and automatic assessment of sewer conditions. Visual camera and laser scanner have been used as a sensory device. A human operator can operate the robot from a surveillance unit via a cable, with a length of 250 m (maximum). An expert system running on a workstation was responsible for data interpretation and damage classification [1]. For sewer inspection, a platform has been developed which is semi-autonomous and connected with surveillance unit by a cable named as Kanalroboter (KARO), it is having an inclinometers which will correct the tilt poses by wheel of robot and balanced them accordingly [2]. Kanal–Untersuchungs–Roboter-testplattform (KURT) is a six-wheeled autonomous un-tethered robot. A map of pipe net is needed for the navigation. Ultrasonic sensor, inclinometer, and CCD camera are used for inspection [3]. For drain pipe inspection, wireless radio communication system has been used by Ishikawa Tekkousyo in “The robot was developed based on drain pipe inspection robot, Mogurinko 250” [4]. Rotating probes with piezo-electric element have been used by “The Indian Institute of Technology Kanpur for internal inspection robot [4]. There are many nondestructive techniques which have been mentioned above along with non-contact inspection technique [5]. Classification of non-contact inspection techniques results into two techniques optical and no optical techniques. Non-contact optical inspection techniques include machine vision system, conventional optical instruments (optical comparators and microscopes), laser system (scanning laser device), linear array devices, and optical triangulation techniques. Non-contact non-optical inspection techniques include: electrical field techniques, radiation techniques, and ultrasonic inspection methods. In in-pipe inspection, robot has used machine vision (computer vision) in most of them because of the distinction is that machine vision tends to imitate the capabilities of the human optical sensory system. This includes not only the eyes, but also the complex interpretive powers of the brain [6]. CCD-based technique that is

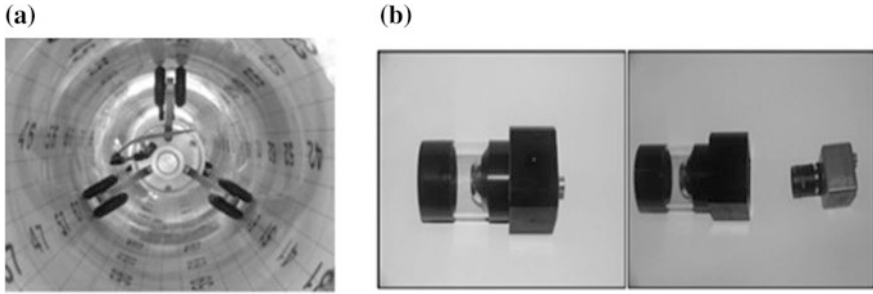


Fig. 1 a Image acquisition test pipe [7]. b CCD Camera and lens system

embedded in in-pipe inspection robot structure has some limitations that restrict their implementation like: (1) the lack of visibility in the interior of the pipes and (2) the poor quality of the obtained images because of difficult lighting conditions Fig. 1a, b.

2 Hardware System

The pipeline inspection robot is using the cable to control the robot and to transfer the information data to detect the defects inside the robot. Robot is controlled by wired remote to get a direct view to the pipe wall. PLC connection is also possible through wire and in case of failure of power we can easily access the robot. For control of robot, the Rexroth PLC L20 is needed along with Indraworks engineering software installed in laptops or PC's and the connection established between PLC and Indraworks engineering software can be used in many ways like Profibus, Ethernet cable, etc., after establishing the connections, the control of PLC input and output devices can be done by developing Ladder logic. Wall-pressed caterpillar-shaped robot consists of six motors in which three motor is used to control the length of arms and another three motors are used for linear motion control of robot. For each motor pushbutton switches have been provided. If Switch 1 is pressed then switch 4 cannot be true because at a time relay can move in single direction, this problem is been rectified with in the ladder logic program. In the motor switching Table S2 symbolizes the Switch_2 and, respectively, others have the same extension. The robot will have 3 DOF in X and Z direction and one rotatory shaft will rotate along 360 along with linear motion in x direction. Hence three motors which drive the standard wheel rotate in two directions that make robot to move in $+x$ and $-x$ direction and other three motor is used to adjust the arms of robot according to the size of pipe diameter which gave linear motion in $+z$ and $-z$ direction. The $+x$ and $-x$ direction motion can be done by developing the motor control circuitry which helps motor to rotate in clockwise and anticlockwise direction. The motor control circuitry consists of 24 V SPDT relay. For control of

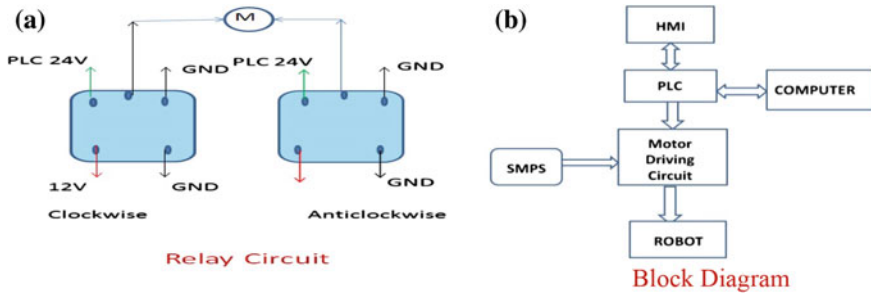


Fig. 2 a Relay circuit and b block diagram

each motor in clockwise and anticlockwise direction, two SPDT relays are used where common of two relays is connected to the motor and normally closed terminal (NC Terminal) has been grounded and normally open terminal (NO Terminal) has been connected to 12 V power supply and PLC output terminal has been connected to the one terminal of relay coil and other was grounded. When PLC output is high then accordingly relay got energized and rotates motor in either of direction (Fig. 2a).

3 Software Algorithms

Software algorithms are used to run the system according to the requirement. In this paper, the system has been controlled using Ladder Logic, which has been developed in Indraworks Engineering Software which is compatible with Rexroth L20 PLC. Software algorithms consist of two states naming of variables and Ladder logic implementation. The location of input switches and output port which are used in the ladder logic has been mentioned in the Figs. 3 and 4 with their data types.

The Ladder Logic for control of three arm motor in clockwise and anticlockwise direction in order to move the robot in clockwise and anticlockwise direction and three thread screw motor are used to adjust the size of robot. Start and stop switches are used to switch ON and OFF the device but the motor will run according to Switches allotted to them.

Control of each motor consists of a TON Timer and a TOF Timer to produce the square pulses which will run the DC motor attached to the arms and thread screw. The speed of motor can be controlled by adjusting the preset time of the timer which controls the pulse width and accordingly the speed of the motor is controlled. The flow chart of the system has been showed in Fig. 3.

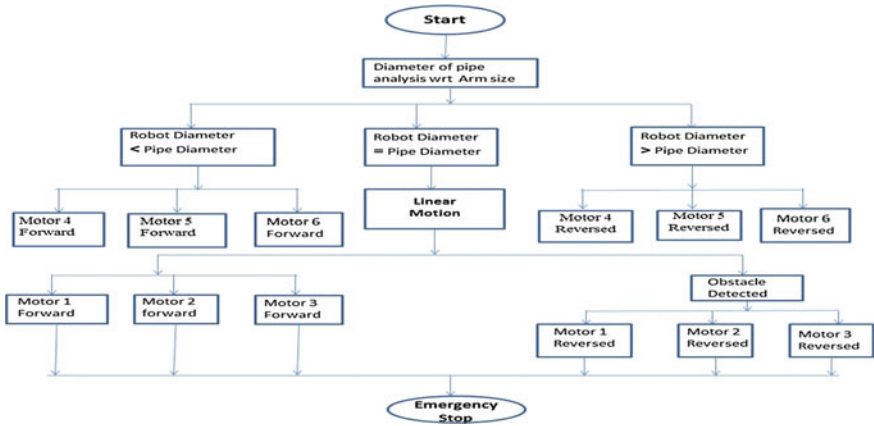


Fig. 3 System flow chart

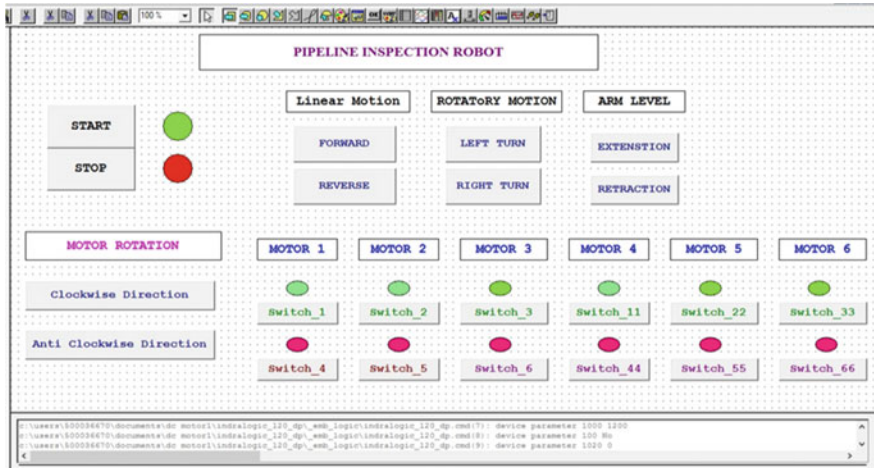


Fig. 4 HMI interface

4 Visualization and HMI

In Indraworks Engineering Software, the visualization tool provides an easy understanding of system parameters and gave visual platform to user to monitor the system and able to extract the useful content out of it. It works similarly as the SCADA software which builds the graphic user interface (GUI) between man and machine. It is used as indicator to know the status of switch whether the switch is pressed or not, various indicators are used in HMI to know the real-time operation. Monitor and control of robot can be done through HMI by pressing the pushbutton



Fig. 5 Experimental setup

S.No.	Motor Driver Type	Torque of Motor (oz-in)	Speed of Motor (RPM)	Time Latency (ms)
1	Relay Circuit	0.05	10,786.3	26ms
2	L293d motor Driver	0.075	10,324.85	40ms
3	Variable Speed driver	0.1	9,863.6	82ms
4	IXDN404PI	0.125	9,402	150ms
5	SCR Dc Driver	0.15	8,940.9	350ms

Fig. 6 Comparison table of motor driver wrt to time latency

on HMI. Hence it gave an advance safety feature to the system. The layout of HMI has been shown below in Fig. 4.

In the HMI displayed, the motor 1, motor 2, motor 3 are used for linear and rotatory motion of robot while motor 4, motor 5, motor 6 have been used for adjusting the arms of robot according to the size of pipelines. Switches are the manual control of robot and indicator will show the status of switches.

5 Result and Discussions

The experiment setup of pipeline inspection robot has been shown in Fig. 5 which consists of Rexroth L20 PLC, RS232 cable, Onboard and Inline I/O's, wall-pressed caterpillar-shaped pipeline inspection robot, motor driver circuit, different push-buttons, and toggle switches and HMI. The control robot through HMI has been properly done.

The total machine cycle used in ladder logic is of 13 rungs each rung will take 2 ms with timer hence total time taken by robot to complete one Scan cycle is 26 ms and comparison of different motor driver types with each other's is shown in Fig. 6. Hence implementation of ladder logic will control the pipeline inspection robot more effectively with less duration of time.

References

1. R. Kirham, P.D. Kearney, K.J. Rogers, J. Mashford, PIRAT: “A system for quantitative sewer pipe assessment”, *The International Journal of Robotics Research* 19 (11) (2000) 1033–1053.
2. H.B. Kuntze, H. Haffner: “Experiences with the development of a robotvb for smart multisensoric pipe inspection”, in: *Proceedings of the IEEE International Conference on Robotics and Automation*, Leuven, Belgium, 1998.
3. F. Kirchner, J. Hertzberg: A prototype study of an autonomous robot platform for sewerage system maintenance, *Autonomous Robots* 4 (1997) 319–331.
4. H. Schempf, Explorer-ii: Wireless Self-powered Visual and NDE Robotic Inspection System for Live Gas Distribution Mains, Tech. Rep., Carnegie Mellon University, 2006.
5. Zin, Md Raziq Asyraf Md,Sahari, Khairul Salleh Mohamed, Saad, Juniza Md, Anuar, Adzly, Zulkarnain, Abd Talip, Development of a Low Cost Small Sized In-Pipe Robot, *Procedia Engineering* 41, (2012), 1469–1475.
6. Skjelvareid, M.H., Birkelund, Y. and Larsen, Y., 2013. Internal pipeline inspection using virtual source synthetic aperture ultrasound imaging, *NDT & E International*, 54(0), 2013, pp. 151–158.
7. Choi, H.R. and Ryew, S.M., Robotic system with active steering capability for internal inspection of urban gas pipelines, *Mechatronics*, 12(5), 2002, pp. 713–736.

On solving complex reliability optimization problem using multi-objective particle swarm optimization

6

A. Kumar*, S. Pant*, M. Ram[†], S.B. Singh[‡]

*University of Petroleum & Energy Studies, Dehradun, India, [†]Graphic Era University, Dehradun, India, [‡]G. B. Pant University of Agriculture and Technology, Pantnagar, India

1 Introduction

Reliability is always a top customer concern and is increasingly vocalized by customers as a major factor in purchasing decisions. When someone assigns attribute “reliable” to a component or a system, it precisely means to say that the same will render service for a good or at least reasonable period of time [1]. Designing a highly reliable system is the most challenging task for a design engineer because it is mandatory for him/her to strike a balance between multiple competing objectives like to maximize reliability, minimize cost, minimize weight, etc. Optimization deals with finding the extreme (optimal) value of a function in a domain of definition, subject to various constraints on the variable values. In other words, optimization is the act of determining the value of certain parameters subject to constraints so that some measure of optimality is satisfied. The applicability of optimization methods is widespread (Science, Engineering, Mathematics, Economics, Commerce, Management etc.), reaching into almost every activity in which numerical information is processed. In single objective optimization problem (SOOP), the main objective is to find one optimum solution. Therefore, it cannot provide a set of alternative solutions that trade different objective against each other. On the contrary, the main objective of a multi-objective optimization problem (MOOP) is to find a set of compromised solutions (Pareto-optimal solutions) instead of finding a single optimal solution. These Pareto-optimal solutions help DM to find the most preferred optimal solution according to his/her subjective preferences [2]. As far as solution to multi-objective problem is concerned one can solve such problems either under single objective formulation or under multi-objective formulation. In the past two decades the problems of multi-objective reliability optimization have been extensively solved [3–12].

In general, obtaining optimal reliability design is a tedious task because of the non-deterministic polynomial-time hard (NP-hard) nature of reliability optimization problems [13]. So it is almost impossible to find the solution of those types of problems using exact methods or heuristics. Therefore, metaheuristic algorithms, particularly,

particle swarm optimization (PSO), gray wolf optimization (GWO) algorithm, genetic algorithm (GA), Cuckoo Search algorithm (CSA), ant colony optimization (ACO), etc. are suitable for solving reliability optimization problems. Recently, many meta-heuristics [2,14,15] have been employed to solve reliability optimization problems.

1.1 Multi-objective reliability optimization problems

$$\begin{aligned} \text{Max } F &= (f_1(r_1, r_2, \dots, r_n, x_1, x_2, \dots, x_n), f_2(r_1, r_2, \dots, r_n, x_1, x_2, \dots, x_n), \dots, \\ &\quad f_k(r_1, r_2, \dots, r_n, x_1, x_2, \dots, x_n)) \\ \text{subject to} \\ &f_i^c(r_1, r_2, \dots, r_n, x_1, x_2, x_n) \leq b_i, \quad \text{for } i = 1, 2, \dots, m \\ &l_j \leq x_j \leq u_j, x_j \in Z^+, \quad \text{for } j = 1, 2, \dots, n \\ &r_j \in (0, 1) \subset R, \quad \text{for } j = 1, 2, \dots, n \end{aligned}$$

where $f_k, \forall k = 1, 2, \dots, K$ is one of the objective functions of the problem and K is the total number of objective functions. In most practical situations involving reliability optimization, there are several mutually conflicting goals such as maximizing system reliability and minimizing cost, weight, volume, and constraints required to be addressed simultaneously. Some main objectives can be expressed as:

Objective 1 The most important objective is the maximization of system reliability (R_S). It enables the system to function satisfactorily throughout its intended service period

$$\text{Max } R_S$$

As in our approach we are considering all minimization problems. Hence, the above objective is equivalent to minimization of system unreliability ($Q_S = 1 - R_S$) that can be expressed as follows

$$\text{Min } Q_S$$

Objective 2 The addition of the redundant components increases not only the system reliability but also its overall cost (C_S). A manufacturer has to balance these conflicting objectives, keeping in view the importance of reducing the overall cost

$$\text{Min } C_S$$

Objective 3 As with cost, every added redundant component increases the weight of the system. Usually, the overall weight of a system needs to be minimized along with its cost even as reliability is maximized (or unreliability is minimized)

$$\text{Min } W_S$$

1.2 Pareto dominance

For any minimization problem, a solution \vec{x}^1 is said to dominate \vec{x}^2 (denoted by $\vec{x}^1 \prec \vec{x}^2$) iff \vec{x}^1 is no worse than \vec{x}^2 in all objectives, i.e. $f_i(\vec{x}^1) \leq f_i(\vec{x}^2), \forall i = 1, 2, 3, \dots, M$, and \vec{x}^1 is strictly better than \vec{x}^2 in at least one objective, i.e. $\exists i = 1, 2, 3, \dots, M : f_i(\vec{x}^1) < f_i(\vec{x}^2)$.

The definition for a maximization problem (\succ) is analogical. If \vec{x}^1 dominates \vec{x}^2 , it is also customary to write any of the following:

- \vec{x}^2 is dominated by \vec{x}^1 ;
- \vec{x}^1 is nondominated by \vec{x}^2 , or \vec{x}^1 is noninferior to \vec{x}^2 .

1.3 Particle swarm optimization

PSO, developed by Eberhart and Kennedy, is a swarm intelligence method for solving optimization problems [1]. PSO is inspired by the ability of flocks of birds, schools of fish, and herds of animals to adapt to their environment, find rich sources of food, and avoid predators by implementing “information sharing” approaches, hence, developing an evolutionary advantage [11, 16, 17]. PSO is initialized with randomly generated population of particles (initial swarm) and a random velocity is assigned to each particle that propagates the particle in search space toward optima over a number of iterations. Each particle has a memory remembering best position attained by it in the past, which is called personal best position (P_{best}). Each particle has its P_{best} and the particle with the best value of fitness is called global best particle (G_{best}). Suppose that the search space is D dimensional, the i th particle of the population can be represented by a D -dimensional vector $(x_i^1, x_i^2, \dots, x_i^D)^T$. The velocity of this particle can be represented by another D -dimensional vector $(V_i^1, V_i^2, \dots, V_i^D)^T$. The previously best visited position of i th particle is denoted by P_i and the best particle in the swarm is denoted by P_g . The update of the particle's position is accomplished by the following two equations. Eq. (1) calculates a new velocity for each particle based on its previous velocity and Eq. (2) updates each particle's position in search space.

$$V_{id}^{k+1} = wV_{id}^k + c_1r_1 [p_{id}^k(t) - x_{id}(t)] + c_2r_2 [p_g^k(t) - x_{id}^k(t)] \quad (1)$$

$$x_{id}^{k+1}(t+1) = x_{id}^k(t) + v_{id}^{k+1}(t+1) \quad (2)$$

where k =iteration number, $d=1,2,3, \dots, D$; $i=1,2,3, \dots, N$; N =swarm size, w =inertia weight, which controls the momentum of particle by weighing the contribution of previous velocity; c_1 and c_2 are positive constants called acceleration coefficients; r_1 and r_2 are random numbers uniformly distributed between [0,1].

2 Multi-objective particle swarm optimization incorporating the mechanism of crowding distance

MOPSO-CD is a swarm-based artificial intelligence-based technique. It is inspired from the food searching behavior of birds flocking or fish schooling. Crowding distance technique has been extensively applied in evolutionary multi-objective optimization algorithms to promote the diversity. The proposal for using crowding distance measure in MOPSO for G_{best} selection and archiving updating was first made by Raquel et al. [6]. This approach used a mutation operator proposed by Coello et al. [18] to produce a highly explorative behavior in the algorithm in such a way that it is applied only during a certain number of generations at the beginning of the process. This is helpful in terms of preventing premature convergence due to existing local Pareto optimal fronts in some optimization problems. The performance of this approach was highly competitive in converging toward the Pareto optimal front and generated a well-distributed set of nondominated solutions. MOPSO-CD has drawn some attention recently as it exhibits a relatively fast convergence and well-distributed Pareto optimal front compared with other multi-objective optimization algorithms [19,20]. Therefore, MOPSO-CD approach has been applied to solve multi-objective reliability optimization problems in this chapter. In this process, at each generation the following computation takes place: first the crowding distance is computed for selecting the global best particle and also for deleting particles from the external archive of nondominated solutions. The global best guide of the particles is selected from nondominated solutions with the highest crowding distance values. Selecting different guides for each particle in a specified top part of sorted repository based on a decreasing crowding distance allows the particles in the primary population to move toward those nondominated solutions in the external repository which are in the least crowded area in the objective space. Also, whenever archive is full, crowding distance is again used in selecting which solution to replace from the archive. This promotes diversity among the stored solutions in the archive since those solutions which are the most crowded areas are most likely to be replaced by a new solution. A flowchart showing the procedure of MOPSO-CD is provided in Fig. 1 [20,21].

Comparing with other evolutionary approaches, it has the following advantages [21–24]:

- (i) less parameters
- (ii) easy implementation
- (iii) fast convergence

3 Application of MOPSO-CD in reliability optimization problems

To evaluate the performance of MOPSO-CD for reliability optimization problems, a reliability test problem, namely series system is solved.

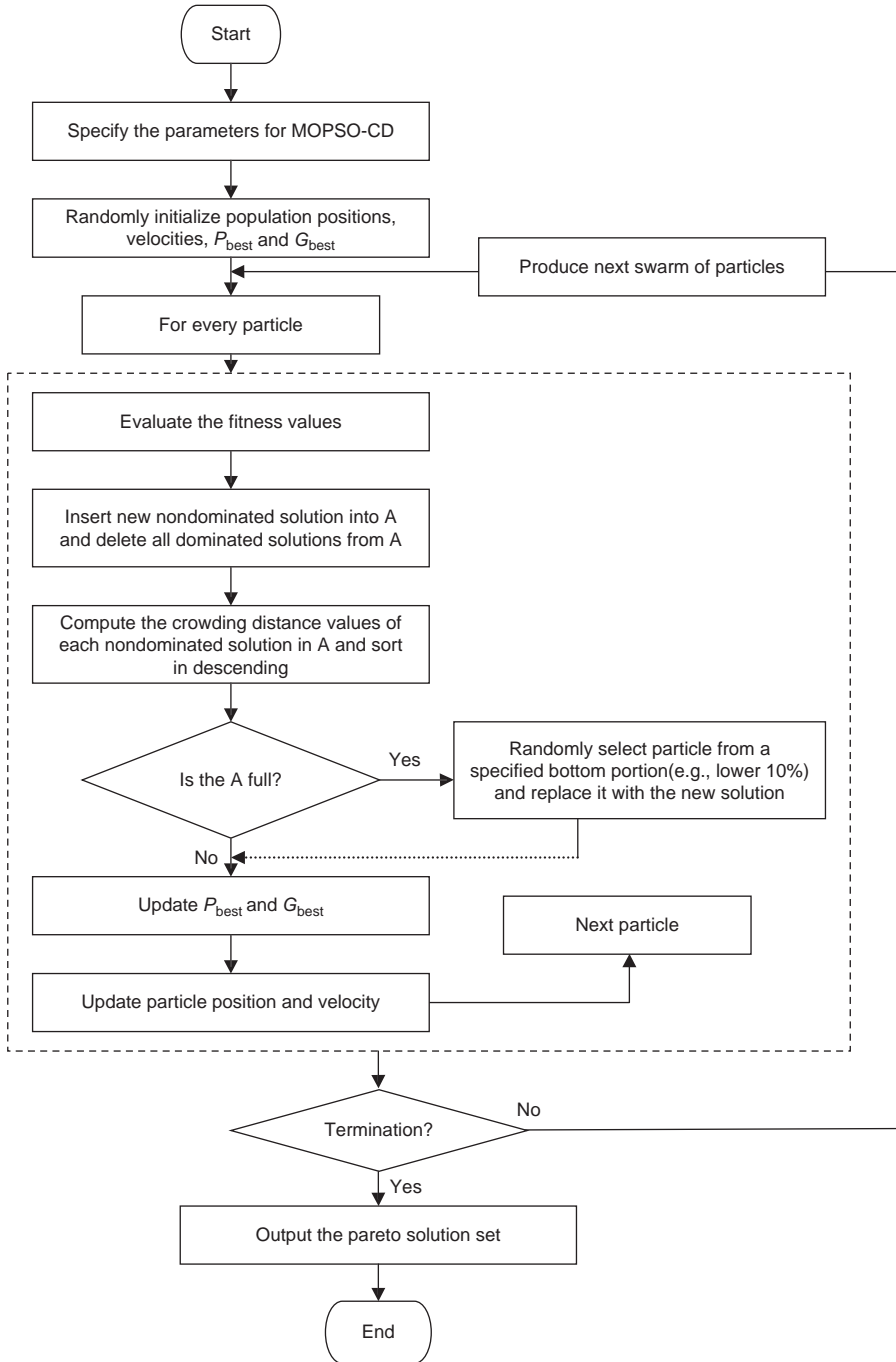


Fig. 1 The flow chart of MOPSO-CD.



Fig. 2 Block diagram of series system.

3.1 Series system

Suppose a certain series system as shown in Fig. 2 consists of five components, each having component reliability $r_j, j = 1, 2, 3, 4, 5$. The cost of j th component is assumed to be an increasing function of r_j in the form

$$c_j = a_j \log \left(\frac{1}{1 - r_j} \right) + b_j, j = 1, 2, \dots, 5 \quad (3)$$

where vectors of coefficients a_j and b_j are $a = (24, 8, 8.75, 7.14, 3.33)$ and $b = (120, 80, 70, 50, 30)$, respectively. Thus the system reliability R_S , system unreliability Q_S , and system cost C_S are given by

$$R_S = \prod_{j=1}^5 r_j \quad (4)$$

or

$$Q_S = (1 - R_S) = 1 - \prod_{j=1}^5 r_j \quad (5)$$

$$C_S = \sum_{j=1}^5 c_j = a_j \log \left(\frac{1}{1 - r_j} \right) + b_j \quad (6)$$

Then the MOOP problem is to determine the reliability of components, which maximizes the system reliability and minimizes the system cost or in other words, which minimizes both system unreliability and system cost. Thus the mathematical formulation of the problem is:

$$\begin{aligned} &\text{Find } (r_1, r_2, r_3, r_4, r_5) \text{ to minimize } (Q_S, C_S) \\ &\text{subject to} \\ &0 \leq r_j \leq 1, \quad j = 1, 2, 3, 4, 5 \end{aligned} \quad (7)$$

Huang [25] solved this problem using fuzzy approach and reported only three Pareto-optimal solutions using aggregation method. We applied MOPSO-CD to solve this problem. The Pareto optimal front obtained by MOPSO-CD is shown in Fig. 3. The parameters used to solve the problem are shown in Table 1. The different solutions represent different combinations of system reliability and cost. The user has the flexibility and choice to choose a particular combination depending on the needs and constraints with the aid of a proper decision making process.

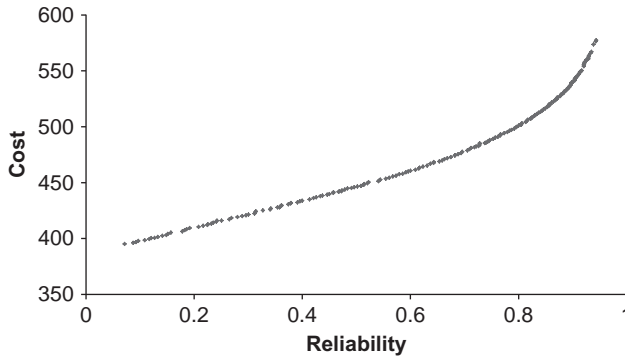


Fig. 3 Pareto front obtained by MOPSO-CD for series system.

Table 1 Parameters used in MOPSO-CD for series system

Pop size	Max gen	Mutation prob.	Archive size	c_1	c_2	w
200	300	0.25	220	1	1	0.3

4 Analysis of MOPSO-CD in reliability optimization problems

In this section, authors have analyzed the results obtained from MOPSO-CD for different parameter settings in reliability optimization problems of MOOP category. We have tried to check the different parameters on the optimization process. For each problem, first inertia weight is kept constant, and then the quality of Pareto optimal fronts for different mutation probabilities and acceleration coefficients is checked.

4.1 Series system

We have checked different settings of parameters and reported one of the best Pareto optimal fronts found during the investigation in Fig. 3. For further investigation we have tried to check the impact of different values of inertia weight, acceleration coefficient, and probability of mutation on the behavior of Pareto optimal front. Following three types of investigations have been made:

1. The Pareto optimal fronts for $w = 0.3, 0.6, 0.9,$ and 1.20 have been checked.
2. The acceleration coefficients are kept at 1 (as suggested in original MOPSO-CD) and 2.0 (as suggested in most of the previously reported literature of PSO) for each of the aforementioned inertia weight.
3. For each above values of inertia, weight, and different acceleration coefficients, the probability of mutation has been tested for 0.3, 0.6, and 0.9.

For the series system first we have kept $w = 0.3$ and acceleration coefficients c_1 and c_2 are kept at 1.0. Then we kept changing the probability of mutation. For the different probabilities of mutation we have got almost same Pareto optimal fronts. It is further observed that these Pareto optimal fronts have good diversity and different probabilities of mutation provided almost same Pareto optimal fronts. These Pareto optimal fronts are shown in Figs. 4–6. But when we change acceleration coefficients c_1 and c_2 to the value 2.0 for the same value of inertia weight and probability of mutation, the Pareto optimal fronts lose their diversity and uniformity. These Pareto optimal fronts are shown in Figs. 7–9. Same experiments have been carried out for other

Fig. 4 Pareto optimal front for series system for $w = 0.3$, $c_1 = c_2 = 1.0$, and $P_{mut} = 0.3$.

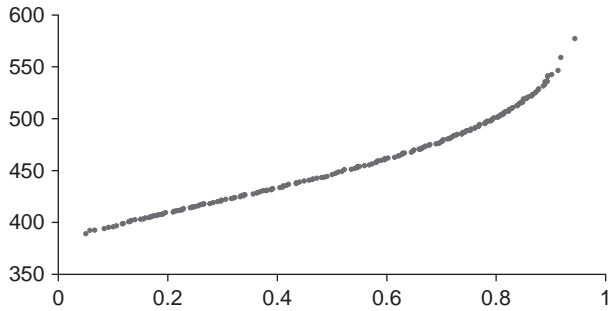


Fig. 5 Pareto optimal front for series system for $w = 0.3$, $c_1 = c_2 = 1.0$, and $P_{mut} = 0.6$.

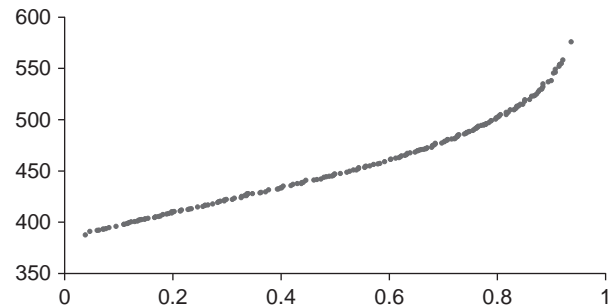
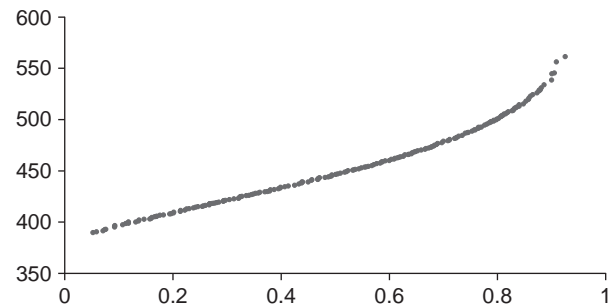


Fig. 6 Pareto optimal front for series system for $w = 0.3$, $c_1 = c_2 = 1.0$, and $P_{mut} = 0.9$.



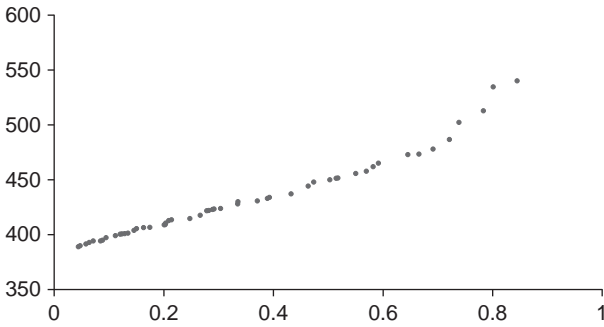


Fig. 7 Pareto optimal front for series system for $w = 0.3$, $c_1 = c_2 = 2.0$, and $P_{mut} = 0.3$.

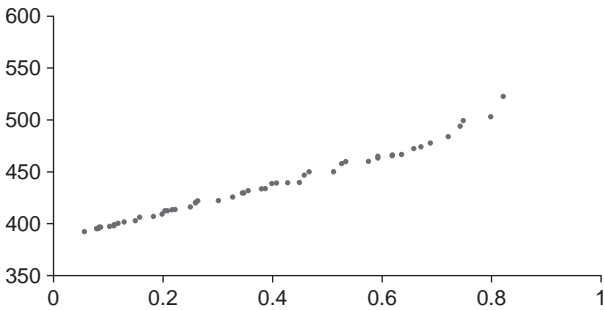


Fig. 8 Pareto optimal front for series system for $w = 0.3$, $c_1 = c_2 = 2.0$, and $P_{mut} = 0.6$.

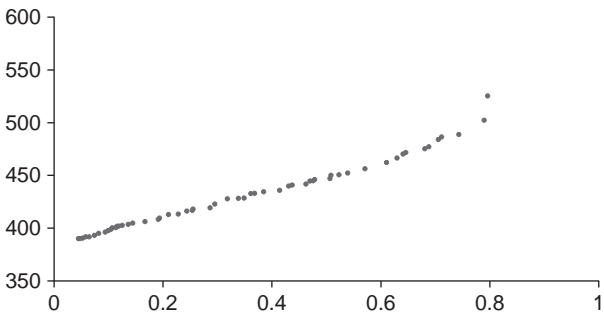


Fig. 9 Pareto optimal front for series system for $w = 0.3$, $c_1 = c_2 = 2.0$, and $P_{mut} = 0.9$.

different settings of parameters. Similarly many Pareto optimal fronts can be obtained varying the different parameters. When w is fixed at 0.6 and kept changing the probability of mutation and acceleration coefficients, we have got the same results. Although the Pareto optimal fronts for $w = 0.6$ are not as much good as for $w = 0.3$. Similar results are found for $w = 0.9$ and $w = 1.20$. These Pareto optimal fronts are shown in Figs. 10–27. It is clear from these plots that as we increase inertia weight from $w = 0.3$ to $w = 1.2$, diversity also decreases and at the same time by

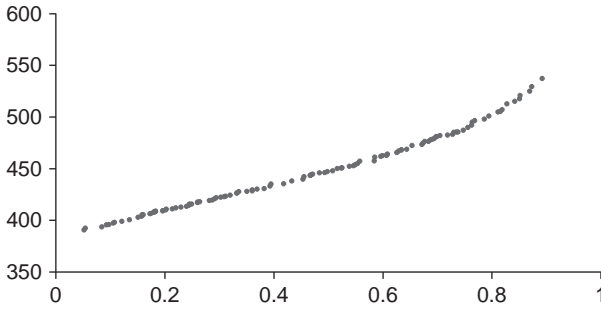


Fig. 10 Pareto optimal front for series system for $w = 0.6, c_1 = c_2 = 1.0,$ and $P_{mut} = 0.3.$

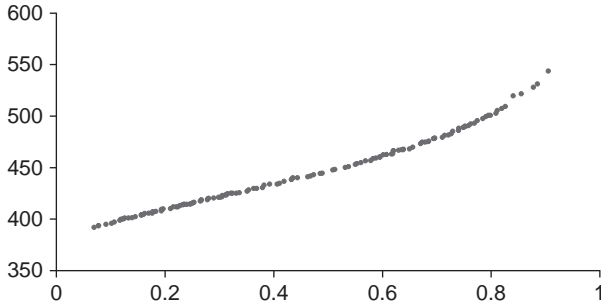


Fig. 11 Pareto optimal front for series system for $w = 0.6, c_1 = c_2 = 1.0,$ and $P_{mut} = 0.6.$

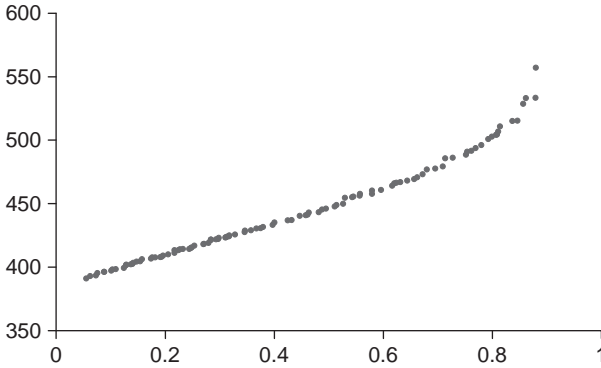


Fig. 12 Pareto optimal front for series system for $w = 0.6, c_1 = c_2 = 1.0,$ and $P_{mut} = 0.9.$

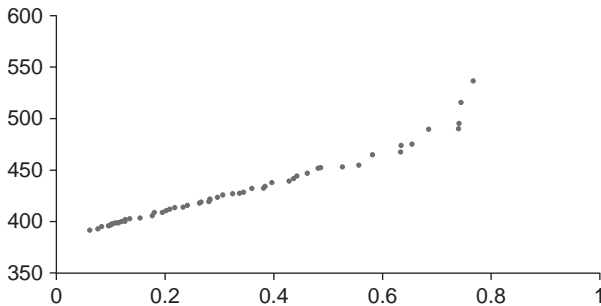


Fig. 13 Pareto optimal front for series system for $w = 0.6, c_1 = c_2 = 2.0,$ and $P_{mut} = 0.3.$

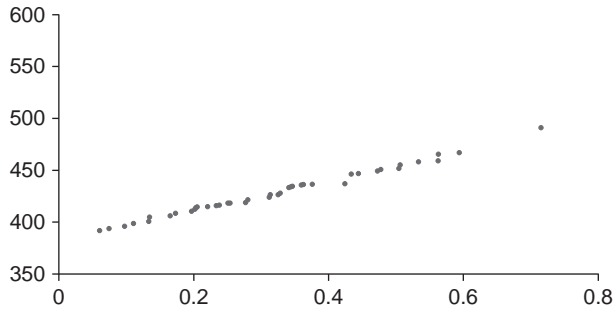


Fig. 14 Pareto optimal front for series system for $w=0.6$, $c_1=c_2=2.0$, and $P_{mut}=0.6$.

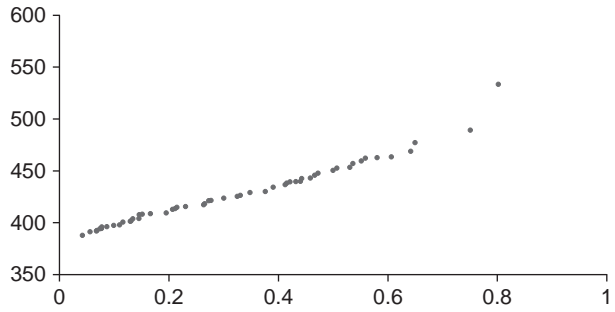


Fig. 15 Pareto optimal front for series system for $w=0.6$, $c_1=c_2=2.0$, and $P_{mut}=0.9$.

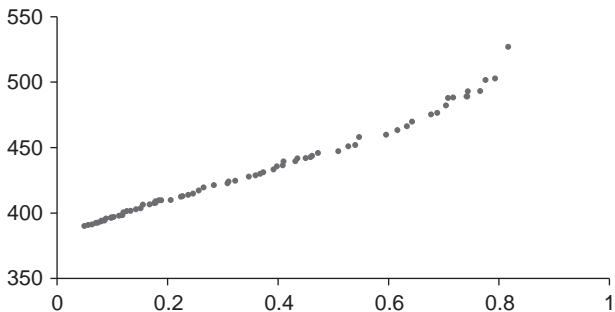


Fig. 16 Pareto optimal front for series system for $w=0.9$, $c_1=c_2=1.0$, and $P_{mut}=0.3$.

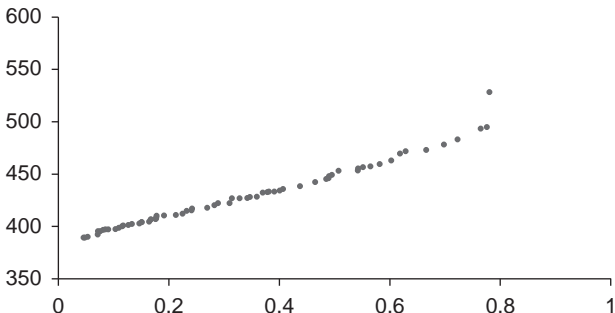


Fig. 17 Pareto optimal front for series system for $w=0.9$, $c_1=c_2=1.0$, and $P_{mut}=0.6$.

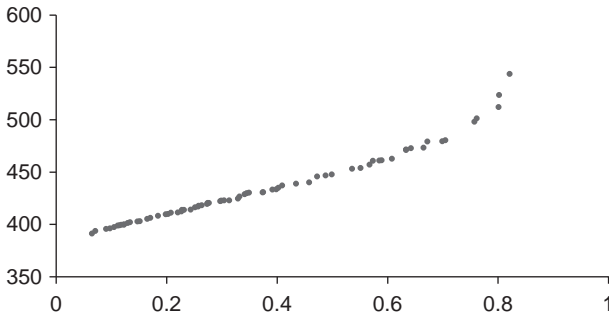


Fig. 18 Pareto optimal front for series system for $w = 0.9$, $c_1 = c_2 = 1.0$, and $P_{mut} = 0.9$.

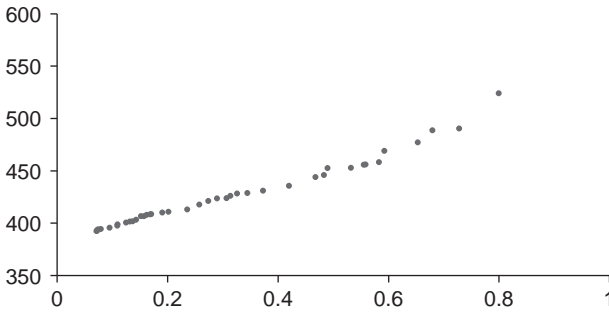


Fig. 19 Pareto optimal front for series system for $w = 0.9$, $c_1 = c_2 = 2.0$, and $P_{mut} = 0.3$.

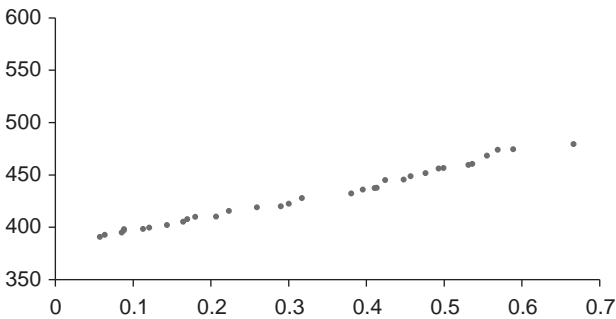


Fig. 20 Pareto optimal front for series system for $w = 0.9$, $c_1 = c_2 = 2.0$, and $P_{mut} = 0.6$.

increasing value of acceleration coefficients for the different values of mutation probability the Pareto optimal fronts get poorer and lose their uniformity. Hence, for the series system the value of acceleration coefficient and inertia weight should not be very high as it can disturb the convergence and diversity of the algorithm.

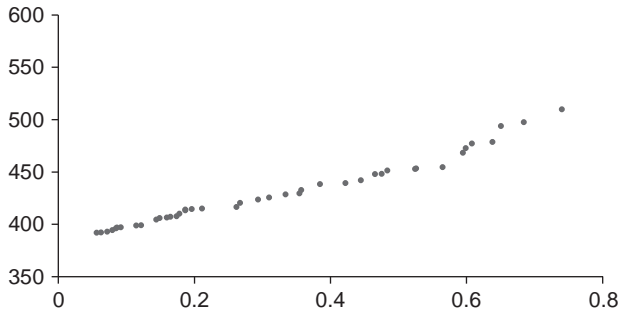


Fig. 21 Pareto optimal front for series system for $w = 0.9$, $c_1 = c_2 = 2.0$, and $P_{mut} = 0.9$.

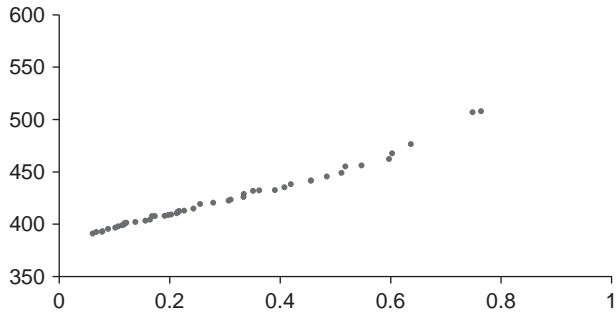


Fig. 22 Pareto optimal front for series system for $w = 1.2$, $c_1 = c_2 = 1.0$, and $P_{mut} = 0.3$.

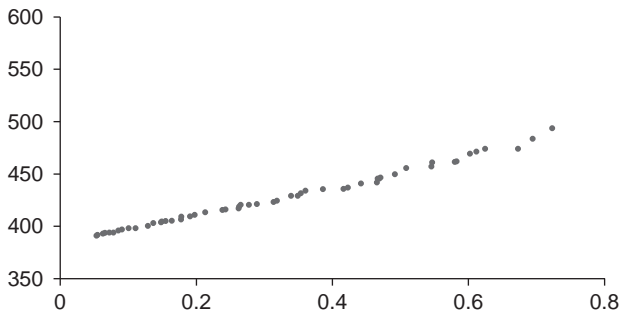


Fig. 23 Pareto optimal front for series system for $w = 1.2$, $c_1 = c_2 = 1.0$, and $P_{mut} = 0.6$.

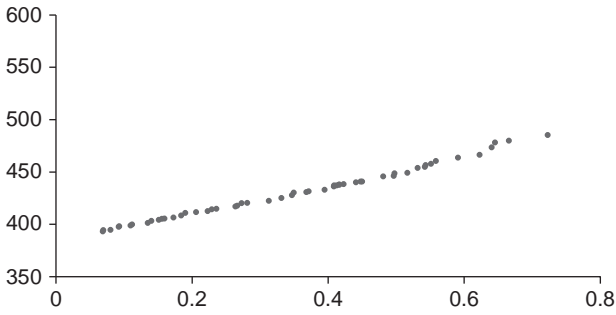


Fig. 24 Pareto optimal front for series system for $w = 1.2$, $c_1 = c_2 = 1.0$, and $P_{mut} = 0.9$.

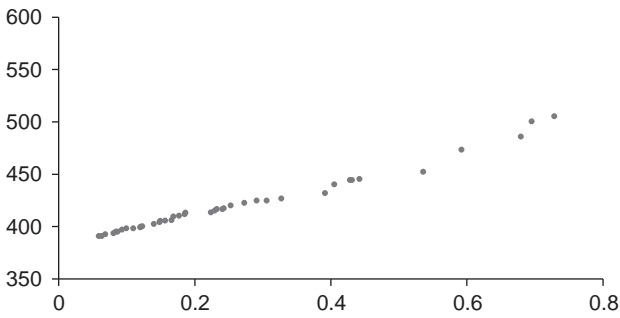


Fig. 25 Pareto optimal front for series system for $w = 1.2$, $c_1 = c_2 = 2.0$, and $P_{mut} = 0.3$.

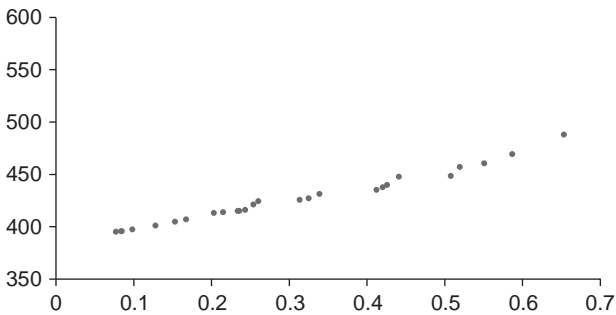


Fig. 26 Pareto optimal front for series system for $w = 1.2$, $c_1 = c_2 = 2.0$, and $P_{mut} = 0.6$.

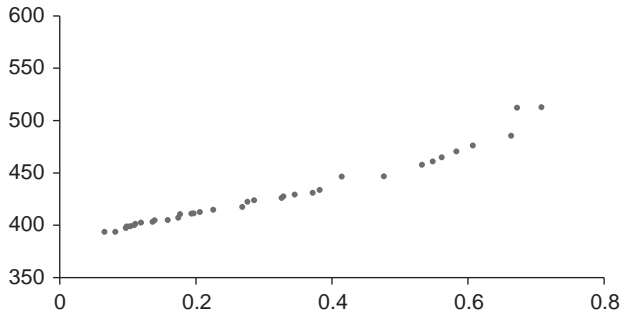


Fig. 27 Pareto optimal front for series system for $w = 1.2$, $c_1 = c_2 = 2.0$, and $P_{mut} = 0.9$.

5 Conclusion

Authors have applied MOPSO-CD for multi-objective reliability optimization problem. For this problem the MOPSO-CD algorithm evolves a good distribution of new Pareto-optimal solution set. The results are encouraging and suggest the applicability of the MOPSO-CD approach to more complex and real-world engineering problems. Apart from this, the MOPSO-CD is tested for different parameter settings. It is concluded that MOPSO-CD performed better for the lower value of acceleration coefficients and inertia weight but for higher values it can disturb the convergence and diversity of the algorithm.

Further, potential application of the well-proven technique MOPSO-CD in reliability optimization is presented. This theme links ideas and contributions that span the following areas:

- One of the most important practical advantages of the proposed PSO approach is that the mathematical models of real-life optimization problems can be solved.
- MOPSO-CD is examined for different settings of parameter, and it is concluded that inertia weight and acceleration coefficients have more effect on Pareto optimal front than the probability of mutation. The higher value (usually more than 0.6) of inertia weight is more responsible in lacking the diversity of swarm.
- The extension of the methodology especially to complex systems, and the results achieved, has demonstrated the efficiency of MPSO technique introduced in this work. The results obtained for reliability optimization problems are either better or comparable than those of previously reported results.

6 Future scope

- As part of future work plans, authors aim to develop a more efficient, optimized versions of the proposed algorithms so that it can tackle more complex problems. We have already identified some very interesting real-world problems coming from the wireless communication field (we have tried to optimize transmission/reception power, Antenna gain, date error rate,

size, cost, etc. of devices and systems), which we could not tackle using the existing implementation due to too long run time.

- Also, MOPSO-CD is implemented only for reliability allocation problems, which are continuous nonlinear programming problem. The further work can be carried out to implement MOPSO-CD in redundancy allocation and reliability-redundancy allocation problems, which are integer nonlinear programming and mixed integer nonlinear programming problems, respectively.

References

- [1] A. Kumar, S.B. Singh, Reliability analysis of an n -unit parallel standby system under imperfect switching using copula, *Comput. Model. New Technol.* 12 (1) (2008) 47–55.
- [2] S. Pant, A. Kumar, A. Kishor, D. Anand, S.B. Singh, Application of a multi-objective particle swarm optimization technique to solve reliability optimization problem, in: *Proceedings of IEEE Int. Conf. on Next generation Computing Technologies*, September 4–5, 2015, pp. 1004–1007.
- [3] A. Kishore, S.P. Yadav, S. Kumar, Application of a multi-objective genetic algorithm to solve reliability optimization problem, in: *Proceedings of IEEE International Conference on Computational Intelligence and Multi-Media Applications*, 2007, pp. 458–462.
- [4] A.P. Engelbrecht, *Fundamentals of Computational Swarm Intelligence*, John Wiley & Sons, Hoboken, New Jersey, USA, 2005.
- [5] B. Clow, T. White, An evolutionary race: a comparison of genetic algorithms and particle swarm optimization used for training neural networks, in: *Proceedings of International Conference on Artificial Intelligence*, 2004, pp. 582–588.
- [6] C.R. Raquel, P.C. Naval Jr., An effective use of crowding distance in multiobjective particle swarm optimization, in: *Genetic and Evolutionary Computation Conference*, 2005, pp. 257–264.
- [7] C.M. Rocco, A.J. Miller, J.A. Moreno, N. Carrasquero, A cellular evolutionary approach applied to reliability optimization of complex systems, in: *Proceedings of the Annual Reliability and Maintainability Symposium*, 2000, pp. 210–215.
- [8] H. Garg, M. Rani, S.P. Sharma, Y. Vishwakarma, Intuitionistic fuzzy optimization technique for solving multi-objective reliability optimization problems in interval environment, *Expert Syst. Appl.* 41 (7) (2014) 3157–3167.
- [9] H. Garg, S.P. Sharma, Multi-objective reliability-redundancy allocation problem using particle swarm optimization, *Comput. Ind. Eng.* 64 (1) (2013) 247–255.
- [10] S. Guangyong, L. Guangyao, G. Zhihui, C. Xiangyang, Y. Xujing, L. Qing, Multiobjective robust optimization method for drawbead design in sheet metal forming, *Mater. Des.* 31 (4) (2010) 1917–1929.
- [11] S. Pant, S.B. Singh, Particle swarm optimization to reliability optimization in complex system, in: *IEEE Int. Conf. on Quality and Reliability*, Bangkok, Thailand, September 14–17, 2011, pp. 211–215.
- [12] S. Pant, D. Anand, A. Kishor, S.B. Singh, A particle swarm algorithm for optimization of complex system reliability, *Int. J. Perform. Eng.* 11 (1) (2015) 33–42.
- [13] J. Kennedy, R. Eberhart, Particle swarm optimization, in: *Proceedings of IEEE International Conference on Neural Networks*, 1995, pp. 1942–1948.
- [14] A. Kumar, S. Pant, S.B. Singh, Reliability optimization of complex system by using cuckoos search algorithm, *Mathematical Concepts and Applications in Mechanical*

- Engineering and Mechatronics, IGI Global Publisher, Hershey, Pennsylvania, USA, 2017, pp. 94–110.
- [15] M. Mutingi, V.P. Kommula, Reliability optimization for the complex bridge system: fuzzy multi-criteria genetic algorithm, in: Proceedings of Fifth International Conference on Soft Computing for Problem Solving, Advances in Intelligent Systems and Computing, vol. 437, 2016, pp. 651–663, http://dx.doi.org/10.1007/978-981-10-0451-3_58.
 - [16] D. Salazar, C.M. Rocco, B.J. Galvan, Optimization of constrained multiple-objective reliability problems using evolutionary algorithms, *Reliab. Eng. Syst. Saf.* 91 (2006) 1057–1070.
 - [17] V. Ravi, B.S.N. Murty, J. Reddy, Nonequilibrium simulated-annealing algorithm applied to reliability optimization of complex systems, *IEEE Trans. Reliab.* 46 (2) (1997) 233–239.
 - [18] C.A.C. Coello, G.T. Pulido, M.S. Lechuga, Handling multiple objectives with particle swarm optimization, *IEEE Trans. Evol. Comput.* 8 (2004) 256–279.
 - [19] J. Safari, Multi-objective reliability optimization of series-parallel systems with a choice of redundancy strategies, *Reliab. Eng. Syst. Safe.* 108 (2012) 10–20.
 - [20] J. Zhao, Z. Liu, M. Dao, Reliability optimization using multi objective ant colony system approaches, *Reliab. Eng. Syst. Saf.* 92 (1) (2007) 109–120.
 - [21] R. Hassan, B. Cohanım, O. De Weck, G. Venter, A comparison of particle swarm optimization and the genetic algorithm, in: Proceedings of the 1st AIAA Multidisciplinary Design Optimization Specialist Conference, 2005, pp. 1–13.
 - [22] M.S. Chern, On the computational complexity of reliability redundancy allocation in a series system, *Oper. Res. Lett.* 11 (5) (1992) 309–315.
 - [23] R. Eberhart, J. Kennedy, A new optimizer using particle swarm theory, in: Proceedings of the Sixth International Symposium on Micro Machine and Human Science, 1995, pp. 39–43.
 - [24] R.J.W. Hodgson, Particle swarm optimization applied to the atomic cluster optimization problem, in: Proceedings of the Genetic and Evolutionary Computation Conference, 2002, pp. 68–73.
 - [25] H.Z. Huang, Fuzzy multi-objective optimization decision-making of reliability of series system, *Microelectron. Reliab.* 37 (1997) 447–449.

One pot green synthesis of α -aminophosphonates with D-Malic acid as an organocatalyst

Harish Mudila, Himanshu Kapoor, and Parteek Prasher

Citation: [AIP Conference Proceedings](#) **1860**, 020057 (2017); doi: 10.1063/1.4990356

View online: <http://dx.doi.org/10.1063/1.4990356>

View Table of Contents: <http://aip.scitation.org/toc/apc/1860/1>

Published by the [American Institute of Physics](#)

Articles you may be interested in

[Preface: RAFAS 2016](#)

AIP Conference Proceedings **1860**, 010001 (2017); 10.1063/1.4990299

[Antimicrobial and antioxidant activities of substituted 4H-1, 4-benzothiazines](#)

AIP Conference Proceedings **1860**, 020062 (2017); 10.1063/1.4990361

One Pot Green Synthesis of α -Aminophosphonates with D-Malic Acid as an Organocatalyst

Harish Mudila ^{1a)}, Himanshu Kapoor ¹ and Parteek Prasher ²

¹Department of Chemistry, Lovely Professional University,
Phagwara, Punjab, India-144401

²Department of Chemistry, University of Petroleum and Energy Studies,
Dehradun, Uttarakhand, India-248007

Corresponding author: ^{a)} harismudila@gmail.com

Abstract: A one pot multi-component reactions using D-Malic acid as a chiral organocatalyst was carried out to synthesize a series of α -aminophosphonates by the reaction of various aldehydes, aniline and diethyl phosphite under solvent free conditions in excellent yield and were compared to parallel reactions under same conditions in absence of catalyst. The compounds thus synthesized were analyzed through NMR. The obtained outcomes represents excellent results with the used catalyst signifying that D-malic acid could be a persuasive catalyst for certain organic synthesis.

Key words: D-Malic acid, organocatalyst, α -aminophosphonates, catalyst, organic synthesis

INTRODUCTION

α -aminophosphonates are considered to be structural equivalents of α -amino acids, also present in numerous natural products are in profound emphasis in the recent time in account to their copious properties and usage as an antimicrobial, anticancer/antitumor agent, [1-4] pesticides, [5-7] medicine/pharmacy [8, 9] due to their great potential to affect enzymatic activities related to various pathological ailments, etc. 10-12]. Time to time various synthetic processes and routes are being employed in the synthesis of these α -aminophosphonates viz., uncatylsed reaction, [11] use of certain Lewis acids such as $\text{Cu}^{2+}[\text{BF}_4^-]_2$, [13] SmI_2 , [14], $\text{Cu}(\text{OSO}_2\text{CF}_3)_2$, [15] $\text{H}_2\text{Ti}_3\text{O}_7$ nanotubes, [16] Bismuth triflate, [17] HClO_4 , [18] etc. however these compounds/catalyst are having drawback that they cannot be used for *insitu* synthesis as a consequence of production of various spinoffs, whereas certain catalyst viz., $\text{Mg}(\text{Cl}_2)_4$, [19] $\text{TaCl}_5\text{-SiO}_2$, [20] etc. take extended time to generate desired products.

In this perspective to deal with above limitations the route involving the use of chiral catalyst is of immense applicability. The chirality of organic molecules bequeaths various biological properties to them also there is immense use of chirality in venting off the unwanted inefficient molecule. Nevertheless chiral synthesis is one of the most challenging works in the field of organic synthesis [21, 22]. These asymmetric reactions are highly prolific and economical; hence combating the waste resulting from racemate resolution. Chiral catalyst for asymmetric synthesis is been in extensive use in recent times. Usually scheming of a chiral catalyst in workshop for asymmetric synthesis is an obstinate work, consequently naturally occurring chiral molecules can be employed for this, in this regard various naturally occurring organic compound are used viz. proline, [21, 23] oxalic acid, [22] binaphthol phosphate, [24] etc.

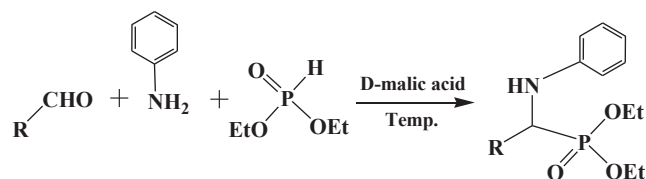
In this current work a chiral organocatalyst D-Malic acid is taken into consideration for exploring its probability as a potent chiral catalyst in the α -aminophosphonates synthesis. Synthesized products were subjected to ¹H-NMR for determination and time taken and percent yield were observed.

EXPERIMENTAL

Material and Method

This work reports asymmetric synthesis of α -aminophosphonates employing D-Malic acid as a potential chiral organocatalyst under solvent-free conditions at 50 ± 1 °C. Reactions were carried at room temperature (~35-40 °C) and higher temperatures of 50 °C-80 °C. The optimum temperature for reaction proceeding was found to be 50 °C. A magnetically stirred mixture of various aromatic aldehydes (10^{-2} mol), aniline (0.931 g, 10^{-2} mol), diethyl phosphite (1.380 g, 10^{-2} mol) and D-Malic acid (0.134 g, 10^{-3} mol) was kept at 50 ± 1 °C for the course of the reaction. The products obtained were filtered and washed repeatedly with deionized water. The obtained products (80-90 %) were recrystallized through chloroform to grow thick white/transparent needle shaped crystals. Along with catalyzed

reaction parallel unanalyzed reactions were carried out to conclude the worth of the catalyst (D-malic acid), (Scheme-1).

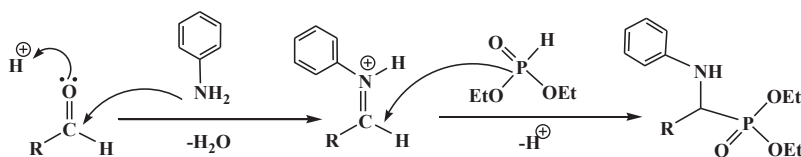


R= various aromatic aldehyde

Scheme-1: Reaction for synthesis of α -aminophosphonate

Mechanism

The reaction mechanism for one pot synthesis of aminophosphonates continues through generation of the imine from reaction of carbonyl with aniline, succeeded by nucleophilic attack of the diethyl phosphite.



Scheme 2: Mechanism of reaction for synthesis of α -aminophosphonate.

The results of reactions are presented in **Table 1**. It is apparent from the obtained results that the used catalyst reduces the reaction time and proliferate the yield percentage, irrespective of the substituents present on ring of aromatic aldehydes.

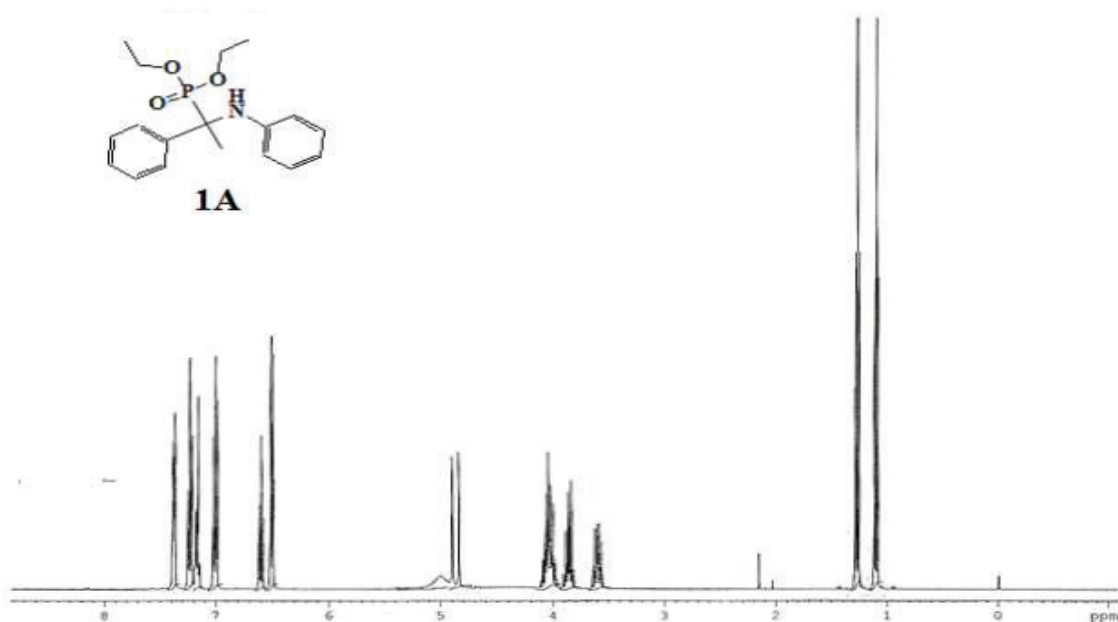
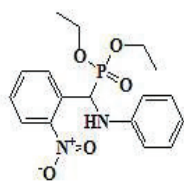


Figure 1. ^1H NMR of Diethyl [phenyl-1-phenylamino]-methylphosphonate



1B

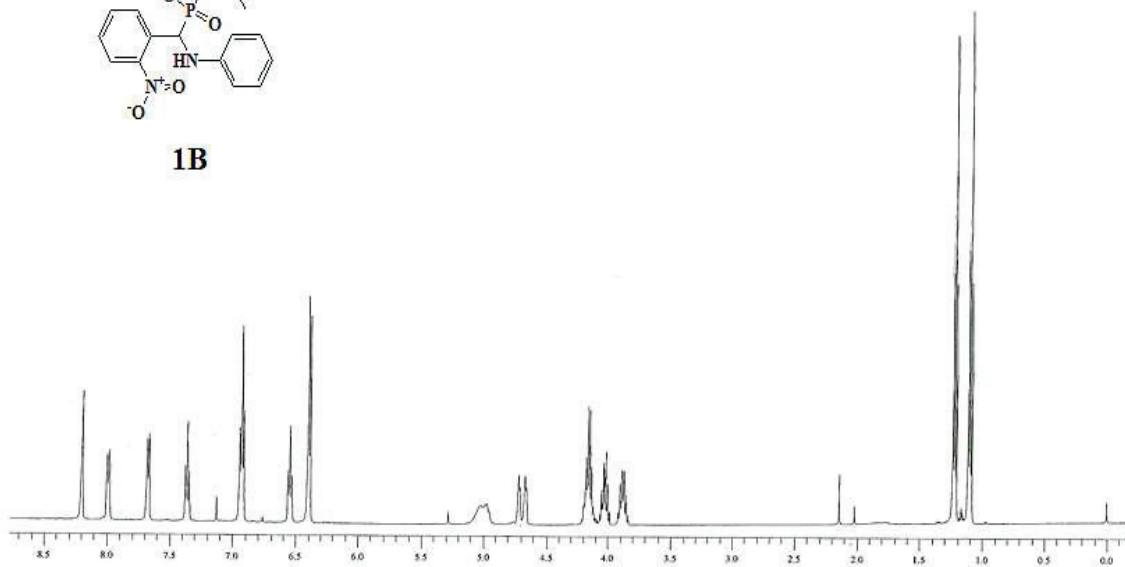
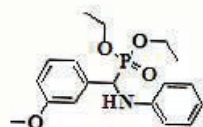


Figure 2. ¹H NMR of Diethyl [(o-nitrophenyl) (phenylamino) methyl]phosphonate



1C

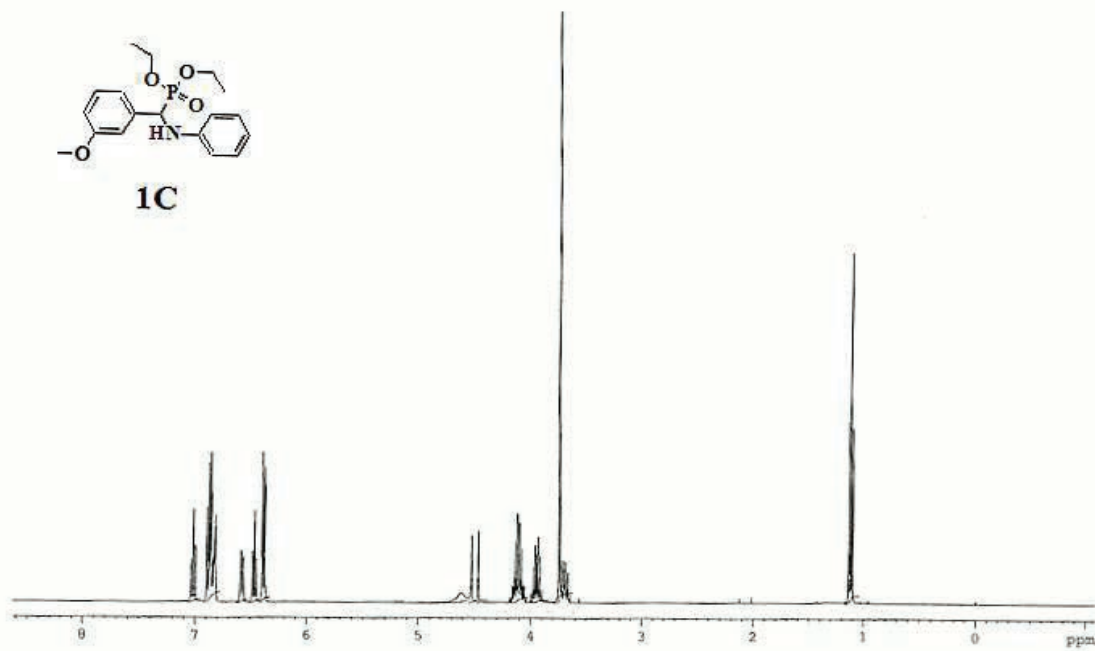


Figure 3. ¹H NMR of Diethyl [(m-methoxyphenyl) (phenylamino) methyl]phosphonate

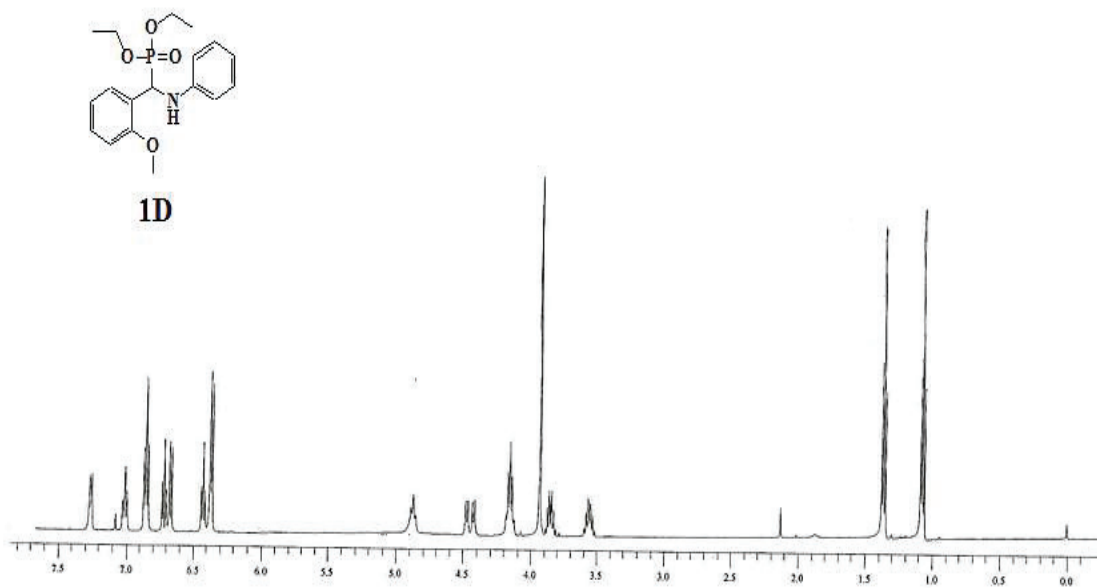


Figure 4. ¹H NMR of Diethyl [(o-methoxyphenyl) (phenylamino) methyl]phosphonate

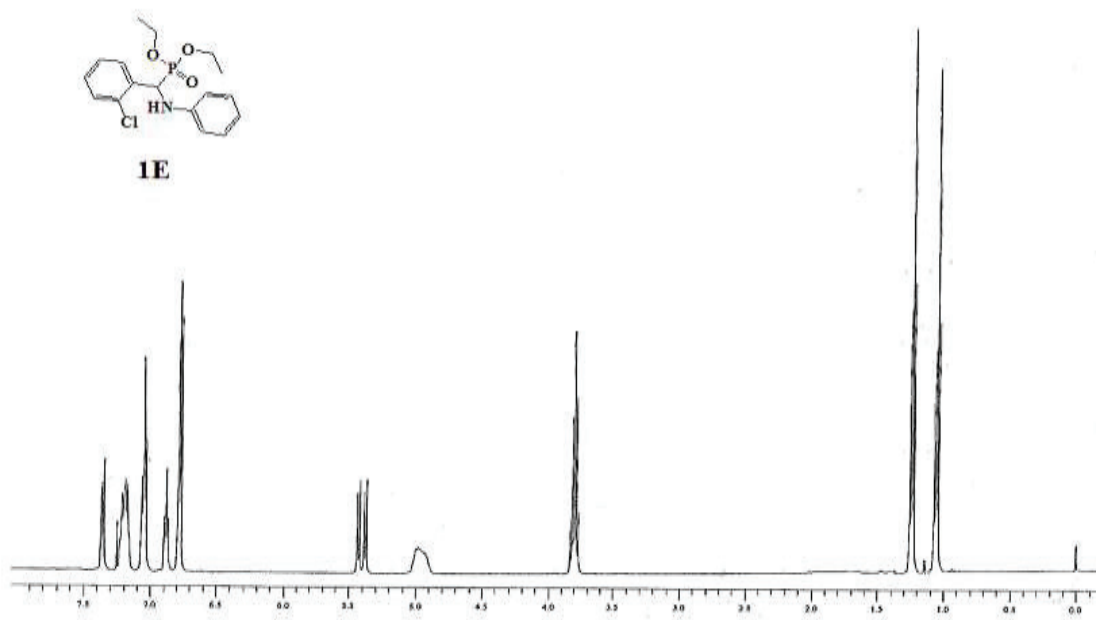


Figure 5. ¹H NMR of Diethyl [(o-chlorophenyl)(1-phenylamino) methyl]phosphonate

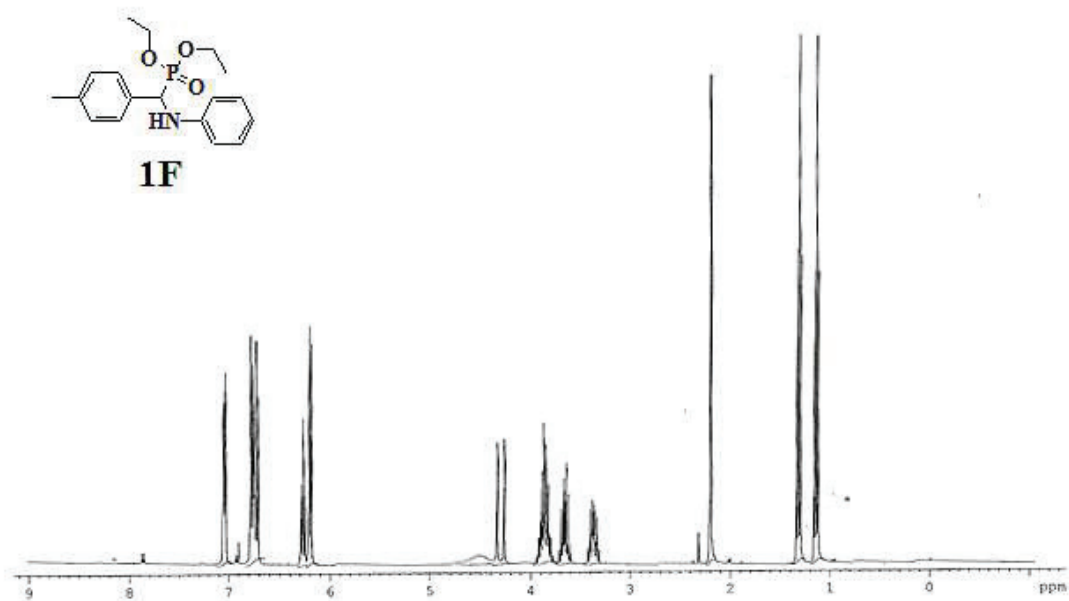


Figure 6. ¹H NMR of Diethyl [(p-methylphenyl)(phenylamino)methyl]phosphonate

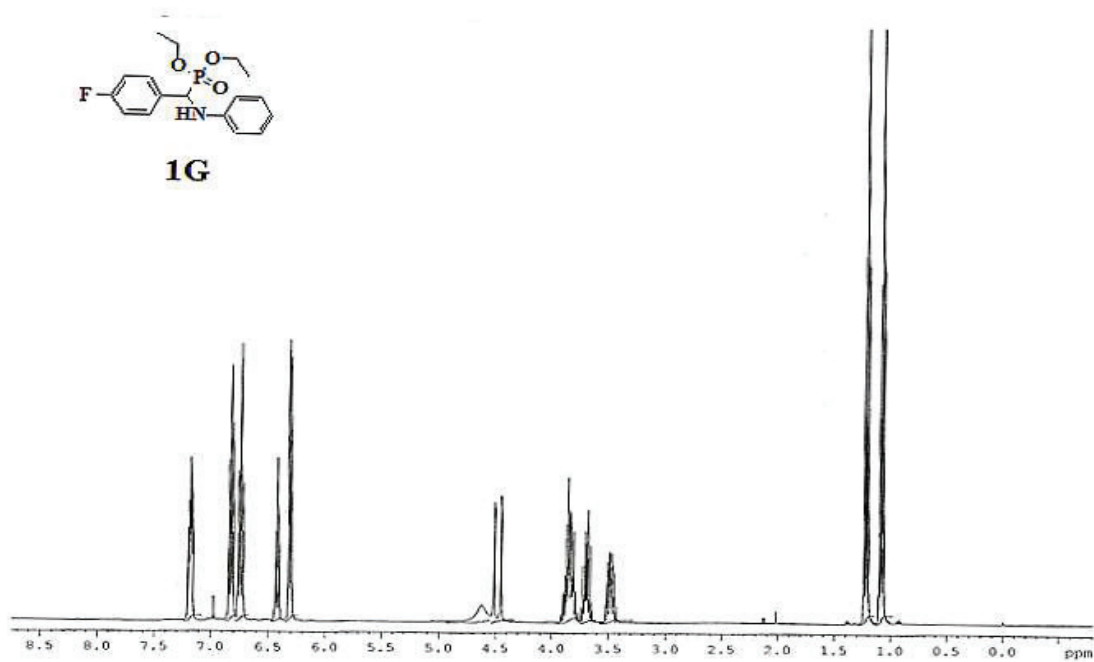
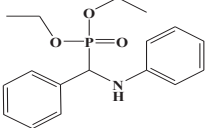
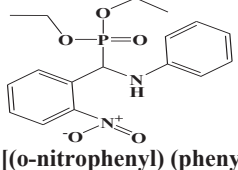
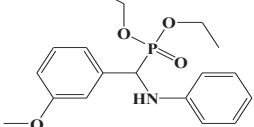
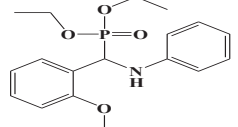
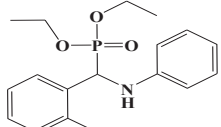
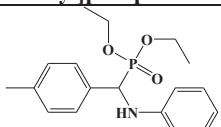
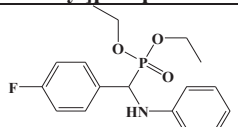


Figure 7. ¹H NMR of Diethyl [(p-fluorophenyl)(1-phenylamino)methyl]phosphonate

Table 1 Required time and percentage yield of synthesized α -aminophosphonates.

Code	Compound Name and Structure	% Yield		Time (Hr)	
		With Catalyst	Without Catalyst	With Catalyst	Without Catalyst
1A	 Diethyl [(1-phenylamino) methyl]phosphonate	89	81	1	3
1B	 Diethyl [(o-nitrophenyl) (phenylamino) methyl]phosphonate	82	67	3.5	9.0
1C	 Diethyl [(m-methoxyphenyl) (phenylamino) methyl]phosphonate	90	86	3.5	7.5
1D	 Diethyl [(o-methoxyphenyl) (phenylamino) methyl]phosphonate	90	80	1.0	1.5
1E	 Diethyl [(o-chlorophenyl) (1-phenylamino) methyl]phosphonate	92	83	3.0	7.5
1F	 Diethyl [(p-methylphenyl) (phenylamino) methyl]phosphonate	85	67	5.0	10.5
1G	 Diethyl [(p-fluorophenyl) (1-phenylamino) methyl]phosphonate	85	73	4.5	9.5

RESULT AND DISCUSSION

In the direction to synthesize α -aminophosphonates derivatives, a simplified procedure was anticipated. An instantaneous reaction of aniline, diethyl phosphite and aromatic aldehyde at $50 \pm 1^\circ\text{C}$ with organocatalyst D-Malic acid affords desired products in respectable yields (Table-1). The extant reaction has been relatively quicker, as

anticipated, compared to those in conventional solution phase synthesis. It is obligatory to remark that in all cases the conversion was never 100 %. Some quantity of starting material recovered after every reaction.

Structure Elucidation

Structures of synthesized α -aminophosphonates have been confirmed by their $^1\text{H-NMR}$ spectral analysis.

1. Diethyl [phenyl-1-phenylamino] methylphosphonate [1A]

M.P.: 93°C, **Colour:** White, **% Yield:** 89

$^1\text{H NMR}$ (CDCl_3 , TMS, 400 MHz): δ (ppm) 6.6-7.5 (9H, m, Ar-H), 5.0 (1H, br s, N-H), 4.8 (1H, d, $^2\text{J}_{\text{P-C-H}} = 24.2$ Hz, P-C-H), 3.64-4.16 (2H, m, P-O-CH₂-CH₃), 1.1-1.3 (3H, t, J= 7.2 Hz, P-O-CH₂-CH₃).

2. Diethyl [(o-nitrophenyl) (phenylamino) methyl]phosphonate [1B]

M.P.: 89°C, **Colour:** Yellow, **% Yield:** 82

$^1\text{H NMR}$ (CDCl_3 , TMS, 400 MHz): δ (ppm) 6.4-8.2 (9H, m, Ar-H), 5.00 (1H, br s, N-H), 4.7 (1H, dd, $^3\text{J}_{\text{H-N-C-H}} = 7.0$ Hz, $^2\text{J}_{\text{P-C-H}} = 24$ Hz, P-C-H), 3.8.10-4.20 (2H, m, P-O-CH₂-), 1.1-1.3 (3H, t, J= 7.0 Hz, P-O-CH₂-CH₃).

3. Diethyl [(m-methoxyphenyl) (phenylamino) methyl]phosphonate [1C]

M.P.: 112°C, **Colour:** White, **% Yield:** 90

$^1\text{H NMR}$ (CDCl_3 , TMS, 400 MHz): δ (ppm) 6.4-7.1 (9H, m, Ar-H), 4.5 (1H, br s, N-H), 4.45 (1H, d, $^3\text{J}_{\text{H-N-C-H}} = 24.2$ Hz, CH), 4.05-4.1 (1H, m, P-O-CH₂-CH₃), 3.73 (3H, s, -O-CH₃ group at benzene), 1.11 (3H, t, J= 7.0 Hz, P-O-CH₂-CH₃).

4. Diethyl [(o-methoxyphenyl) (phenylamino) methyl]phosphonate [1D]

M.P.: 115°C, **Colour:** White, **% Yield:** 90

$^1\text{H NMR}$ (CDCl_3 , TMS, 400 MHz): δ (ppm) 6.4-7.3 (9H, m, Ar-H), 4.85 (1H, br m, N-H), 4.45 (1H, dd, $^3\text{J}_{\text{H-N-C-H}} = 7.0$, Hz, $^2\text{J}_{\text{P-C-H}} = 24$, Hz, P-C-H), 4.1-4.2 (2H, m, P-O-CH₂-CH₃), 4.0 (3H, s, -O-CH₃ group at benzene), 3.7-3.6 (1H, m, O-CH₂-CH₃), 1.4 (3H, t, J=7.0 Hz, O-CH₂-CH₃).

5. Diethyl [(o-chlorophenyl)(1-phenylamino) methyl]phosphonate [1E]

M.P.: 92°C, **Colour:** White, **% Yield:** 92

$^1\text{H NMR}$ (CDCl_3 , TMS, 400 MHz): δ (ppm) 6.8-7.3 (9H, m, Ar-H), 5.4 (1H, dd, $^3\text{J} = 7.0$ Hz, $^2\text{J} = 24.0$ Hz, HN-CH-P), 5.0 (1H, br_s, N-H), 3.80 (2H, m, J= 7.0 Hz, P-O-CH₂-CH₃), 1.10 (3H, t, J= 7.0 Hz, P-O-CH₂-CH₃).

6. Diethyl [(p-methylphenyl) (phenylamino) methyl]phosphonate [1F]

M.P.: 67°C, **Colour:** Brown, **% Yield:** 85

$^1\text{H NMR}$ (CDCl_3 , TMS, 400 MHz): δ (ppm) 6.4-7.1 (9H, m, Ar-H), 4.5 (1H, br s, N-H), 4.3 (1H, d, $\text{J}_{\text{H-C-P}} = 24.0$ Hz, P-C-H), 3.6-3.9 (2H, m, P-O-CH₂-CH₃), 2.3 (3H, s, -CH₃), 1.2 (3H, t, J=7.1 Hz, P-O-CH₂-CH₃).

7. Diethyl [(p-fluorophenyl)(1-phenylamino) methyl]phosphonate [1G]

M.P.: 89°C, **Colour:** White, **% Yield:** 90

$^1\text{H NMR}$ (CDCl_3 , TMS, 400 MHz): δ (ppm) 6.3-7.2 (9H, m, Ar-H), 4.6 (1H, br s, N-H), 4.55 (1H, d, $^2\text{J}_{\text{P-C-H}} = 24.1$ Hz, P-C-H), 3.5-3.9 (2H, m, P-O-CH₂-CH₃), 1.1-1.3 (3H, t, J= 7.1 Hz, P-O-CH₂-CH₃).

CONCLUSION

A simple, competent, and environmentally benign method for the synthesis of α -aminophosphonates was developed, NMR studies suggests the synthesis of desired products with the help of chiral organocatalyst. Greater yield percentage of products and reduction in reaction time was observed for the catalyzed products as compared to uncatalysed ones.

REFERENCES

1. L. Gu and Jin C. *Org Biomol Chem.* **10**, 7098 (2012).
2. X. C. Huang, M. Wang, Y. M. Pan, X. Y. Tian, H. S. Wang and Y. Zhang. *Bioorg Med Chem Lett.* **23**, 5283 (2013).
3. J. F. Zhang, Z. W. Cui, Z. W. Miao and R. Y. Chen. *Chinese Journal of Organic Chemistry*, **28**, 946 (2008).
4. B. Song, Y. L. Wu, X. Q. He and M. G. Jiang. *Chinese Journal of Organic Chemistry*, **23**, 933 (2003).
5. G. C. S. Reddy, C. Radha Rani, M. V. N. Reddy and C. S. Reddy, *Arch. Pharm. Chem Life Sci.*, **347**, 819 (2014).
6. D. Bonarska, J. Sarapuk and H. Kleszczyńska. *Pol. J. Food Nutr. Sci.* **12**, 17 (2003).
7. N. Onița, I. Sisu, M. Penescu, V. L. Purcarea and L. Kurunczi. *Farmacia*, **58**, 531 (2010).
8. P. Zhang , C. Tang , Z. Chen , B. Wang , X. Wang , L. Jin , S. Yang and D. Hu. *Phosphorus, Sulfur, and Silicon and the Related Elements.* **189**, 530 (2013).
9. G. S. Reddy, K. U. M. Rao, C. S. Sundar, S. S. Sudha, B. Haritha, S. Swapna and C. S. Reddy. *Arabian Journal of Chemistry.* **7**, 833 (2014).
10. V. M. Dayalan, M. Arthanareeswari, P. Kamaraj, B. Siva Kumar, S. Devikala and T. K. Mohan. *International Journal of Advance Chemical Science and Applications.* **2**, 22 (2014).
11. M. H. Sarvari, *J. Iran. Chem. Soc.*, **5**, 118 (2008).
12. M. Sienczyk and J. Oleksyszyn. *Curr Med Chem.* **16**, 1673 (2009).
13. J. S. Yadav, B. V. S. Reddy, K. S. Shankar and K. Premalatha. *Org. Commun.*, **1**, 76. (2008)
14. F. Xu, Y. Luo, M. Deng and Q. Shen. *Eur. J. Org. Chem.*, **24**, 4728 (2003).
15. I. El Sayed, S. M. El Kosy, M. F. A. Magied, M. A. Hamed, A. A. A. El Gokha and M. M. A. El-Sattar. *Journal of American Science*, **7**, 604 (2011).
16. B. R. P. Reddy, P. V. G. Reddy and B. N. Reddy. *New J. Chem.*, **39**, 9605 (2015).
17. A. Banik, S. Batta, D. Bandyopadhyay and B. K. Banik. *Molecules*, **15**, 8205 (2010).
18. M. T. Maghsoodlou, S. M. H. Khorassani, R. Heydari, N. Hazeri, S. S. Sajadikhah, M. Rostamizadeh. *Arabian Journal of Chemistry.* **4**, 481 (2011)
19. J. Wu, W. Sun, H. G. Xia, and X. Sun, *Org. Biomol. Chem.* **4**, 1663 (2006).
20. S. Chandrasekhar, S. J. Prakash, V. Jagadeshwar and C. H. Narsihmulu. *Tetrahedron Lett.* **42**, 5561 (2001).
21. Y. Henmi, K. Makino, Y. Yoshitomi, O. Hara and Y. Hamada. *Tetrahedron: Asymmetry*, **15**, 3477 (2004).
22. S. M. Vahdat, R. Baharfar, M. Tajbakhsh, A. Heydari, S. M. Baghbanian. *Tetrahedron Lett.*, **49**, 6501 (2008).
23. I. Georgiou and A. Whiting. *European journal of organic chemistry.* **22**, 4110 (2012).
24. W. Xu, S. Zhang, S. Yang, L. H. Jin, P. S. Bhadury, D. Y. Hu and Y. Zhang. *Molecules*, **15**, 5782 (2010).

Pre-compound emission in low-energy heavy-ion interactions

Manoj Kumar Sharma^{1,*}, Mohd. Shuaib², Vijay R. Sharma³, Abhishek Yadav³, Pushpendra P. Singh⁴, Devendra P. Singh⁵, Unnati⁶, B. P. Singh^{2,**}, and R. Prasad²

¹Department of Physics, Sri Varsheny (Post Graduate) College, Aligarh (UP) - 202 001, India

²Department of Physics, Aligarh Muslim University, Aligarh 202 002, India

³NP-Group, Inter University Accelerator Centre, New Delhi - 110 067, India

⁴Department of Physics, Indian Institute of Technology Ropar, Punjab 140 001, India

⁵Department of Physics, University of Petroleum and Energy Studies, Dehradun - 248 007, India

⁶Department of Physics and Astrophysics, Delhi University, Delhi-110007 India

Abstract. Recent experimental studies have shown the presence of pre-compound emission component in heavy ion reactions at low projectile energy ranging from 4 to 7 MeV/nucleons. In earlier measurements strength of the pre-compound component has been estimated from the difference in forward-backward distributions of emitted particles. Present measurement is a part of an ongoing program on the study of reaction dynamics of heavy ion interactions at low energies aimed at investigating the effect of momentum transfer in compound, pre-compound, complete and incomplete fusion processes in heavy ion reactions. In the present work on the basis of momentum transfer the measurement of the recoil range distributions of heavy residues has been used to decipher the components of compound and pre-compound emission processes in the fusion of ^{16}O projectile with ^{159}Tb and ^{169}Tm targets. The analysis of recoil range distribution measurements show two distinct linear momentum transfer components corresponding to pre-compound and compound nucleus processes are involved. In order to obtain the mean input angular momentum associated with compound and pre-compound emission processes, an online measurement of the spin distributions of the residues has been performed. The analysis of spin distribution indicate that the mean input angular momentum associated with pre-compound products is found to be relatively lower than that associated with compound nucleus process. The pre-compound components obtained from the present analysis are consistent with those obtained from the analysis of excitation functions.

1 Introduction

The pre-compound (PCN) emission process in heavy ion reactions at relatively low energies ranging from 4 to 7 MeV/nucleon has been a topic of recent interest [1], since it is, generally, expected to occur at relatively high energies $\approx 10\text{--}15$ MeV/nucleon [2]. The PCN process may be understood as the fusion of two heavy nuclei in such a way so that a composite nucleus forms far from the statistical equilibrium, and a large fraction of its energy is considered to be in the form of an orderly translational motion of the nucleons of the projectile and target nucleus [3–8]. This orderly motion transforms slowly into chaotic thermal motion through a series of two-body interactions. The thermalization process completes when the composite nucleus reaches a state of thermal equilibrium referred to as compound nucleus (CN). During the thermalization of an excited composite system, it may be possible that a single nucleon or a cluster of nucleons having considerable energy is ejected into the continuum. As soon as the state of thermal equilibrium is attained, the accumulation of sufficient energy on a single nucleon or a cluster of nucleons

may occur in a random sequence of events and hence, may require much longer emission times favoring the emission of low energy particles. The emission of such light particles prior to the establishment of thermodynamic equilibrium of the composite system are termed as the PCN particles and the reaction mechanism is referred to as the PCN process.

The time scale at which PCN emissions occur is very short $\approx 10^{-21}$ sec., while for further evaporations from the equilibrated nucleus take a longer time $\approx 10^{-16}$ sec. The rate of emission of the PCN nucleons depends on the complexity of self-consistent mean-field interaction between the projectile and target nucleus, their structure effects [7, 9] and excitation energy availed by nucleons of composite system. This determines the initial energy distribution among the nucleons in the projectile and the target nuclei, which starts a cascade of nucleon-nucleon interactions as soon as the two nuclei touch each other. Some of the important experimental characteristics of the PCN process are; (i) the presence of a larger number of high-energy particles as compared to the spectrum predicted by the statistical model, (ii) forward-peaked angular distribution of the emitted particles through PCN process, (iii) ob-

*e-mail: manojamu76@gmail.com

**e-mail: bpsinghamu@gmail.com

ervation of smaller recoil range/linear momentum of the evaporation residues left over emission of PCN particles as compared to CN particles, (iv) observation of lower value of the spin with PCN process as compared to CN process, (v) slowly decreasing tails of the excitation functions (EFs) etc.,

In the earlier measurements, the relative strengths of the PCN and CN components in the reactions were estimated from the enhancement in the flux of emitted light particles in the forward direction over the backward direction. The other method often employed is to analyze the measured EFs of evaporation residues by comparing with the statistical model predictions. The observed deviation in EFs with statistical model predictions at relatively higher projectile energies side (tail portion of the EFs) is attributed to the PCN emission process. During last few decades the understanding of the PCN and the CN emission in light ion reactions has been well studied but in heavy ion reactions it needs to be further explored particularly for those associated with the emission of light particles in primary stage in a very short reaction time (10^{-21} s) prior to the establishment of equilibrated CN[7, 10–14]. The emission of such PCN particles reduces the momentum of the product residues. As such, the measurements of the momentum transfer during the interaction may provide a promising tool for the characterization of the reaction mechanism involved.

Although, information about the momentum transfer in heavy ion reaction may also be obtained by several methods[2, 15, 16], in the present measurements this information has been obtained from the study of the recoil range distributions (RRDs) and the spin distributions (SDs) of the reaction residues. Since emitted PCN particles takes away a significant part of angular momentum as compared to CN particles, the angular momentum associated with the PCN products is relatively lower than that associated with the CN process. Therefore, in PCN reactions, the residues are populated at relatively lower spin states as compared to those of the residues populated via CN process. This paper is organized as follows. The experimental details and analysis of RRDs, SDs and EFs are given in the subsections of the section 2. The conclusions drawn from the analysis are given in the section 3 of this paper.

2 Experimental details and analysis

In the present paper the following three self-consistent measurements i.e., (i) the recoil range distributions (RRDs), (ii) the spin distributions (SDs) of the product nuclei and (iii) the excitation functions (EFs), have been performed in the interaction of ^{16}O projectile with ^{159}Tb and ^{169}Tm targets. In both RRDs and EFs measurements, the detection of delayed γ -rays of product residues takes place through the recoil catcher off-line spectroscopy based activation technique. However, the measurements of the SDs is based on the detection of prompt γ -rays of product residues in a particle- γ coincidence experiments in forward and backward directions. A brief description on each experiment carried out in the Inter University Accelerator

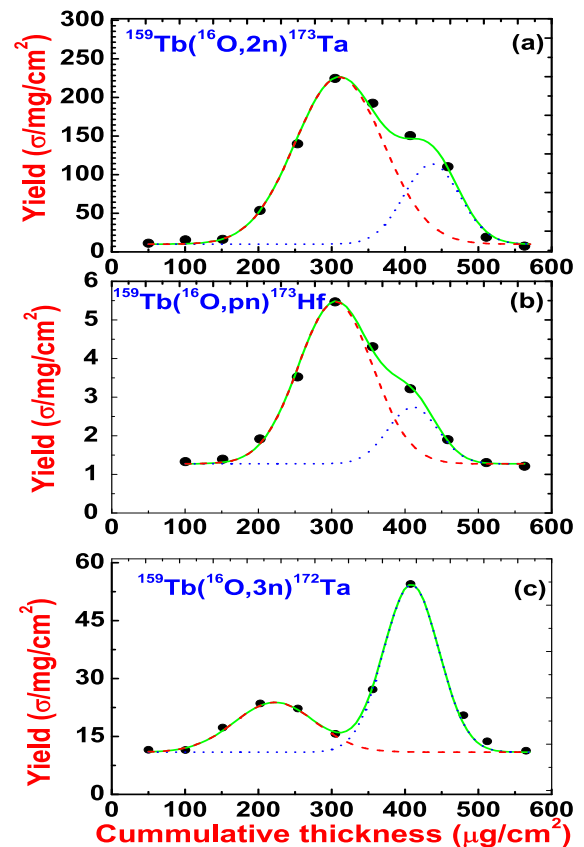


Figure 1. (Color online) The experimentally measured RRDs for the reactions $^{159}\text{Tb}(^{16}\text{O},2n)^{173}\text{Ta}$, $^{159}\text{Tb}(^{16}\text{O},pn)^{173}\text{Hf}$ and $^{159}\text{Tb}(^{16}\text{O},3n)^{172}\text{Ta}$ at energy ≈ 90 MeV. In this figure a Gaussian peak (blue dotted curve) obtained from ORIGIN software at higher cumulative thickness represents CN contribution while other Gaussian (red dashed curve) at lower thickness represents PCN contribution.

Centre (IUAC), New Delhi, India along with their results are given in following subsections;

2.1 Measurement and Analysis of Recoil Range Distributions

In order to investigate the role of linear momentum transfer in the PCN emission, the experiments have been carried out at in the General Purpose Scattering Chamber (GPSC) of IUAC, New Delhi, India to measure the RRDs of recoiling residues produced both by the CN and the PCN emission processes in the reactions $^{159}\text{Tb}(^{16}\text{O},2n)^{173}\text{Ta}$, $^{159}\text{Tb}(^{16}\text{O},pn)^{173}\text{Hf}$ and $^{159}\text{Tb}(^{16}\text{O},3n)^{172}\text{Ta}$ for the $^{16}\text{O}+^{159}\text{Tb}$ system at 90 MeV and for reactions $^{169}\text{Tm}(^{16}\text{O},2n)^{183}\text{Ir}$ and $^{169}\text{Tm}(^{16}\text{O},3n)^{182}\text{Ir}$ in the $^{16}\text{O}+^{169}\text{Tm}$ system at incident energy 88 MeV, respectively. The Coulomb barrier for systems $^{16}\text{O}+^{159}\text{Tb}$ and $^{16}\text{O}+^{169}\text{Tm}$ are ≈ 64 and 67 MeV respectively. In this experiment, the target (thickness $\approx 500 \mu\text{g}/\text{cm}^2$ for ^{169}Tm and $\approx 400 \mu\text{g}/\text{cm}^2$ for ^{159}Tb) followed by a stack of nearly fifteen thin Al catcher foils of varying thickness ($\approx 16\text{--}45 \mu\text{g}/\text{cm}^2$ prepared by vacuum evaporation technique) was mounted in the GPSC

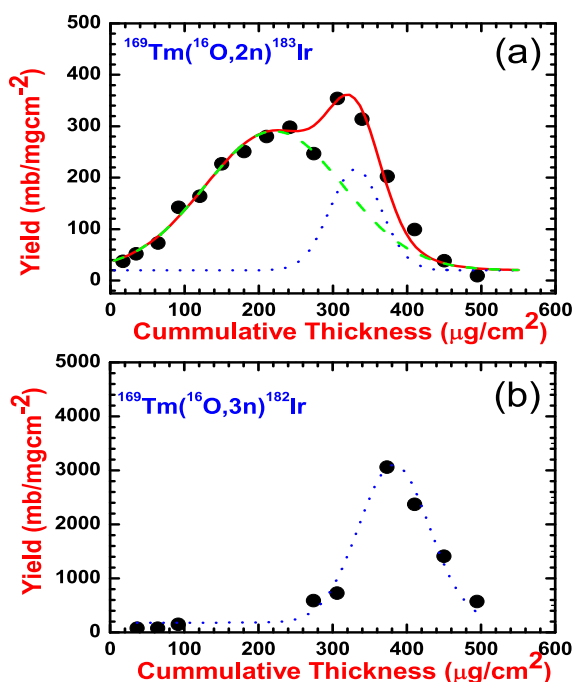


Figure 2. (Color online) (a-c). The experimental RRD for the reactions $^{169}\text{Tm}(^{16}\text{O},2n)^{183}\text{Ir}$ and $^{169}\text{Tm}(^{16}\text{O},3n)^{182}\text{Ir}$ at energy ≈ 88 MeV. In this figure a Gaussian peak (blue dotted curve) at higher cumulative thickness represents CN contribution while other Gaussian (red dashed curve) at lower thickness represents PCN contribution.

normal to the beam direction. Furthermore, SRIM[17] calculations of energy loss in the target sample has been performed to calculate the energy of recoiling residues at the mid of the target. Depending on the momentum carried away by the product residues, the recoiling residues were trapped at different ranges in the stack of thin Al-foils. The duration of irradiation was about 15 hrs. The thickness of the catcher foils was measured precisely prior to their use, by measuring the energy loss suffered in each catcher foil by 5.485 MeV α particles from ^{241}Am source. The code SRIM[17] was used for determining the thickness from the energy loss measurements.

The activities induced in each thin catcher were followed off-line for about two weeks using a pre-calibrated high resolution (2 keV for 1.33 MeV γ ray of ^{60}Co) HPGe detector. The experimental cross-section (σ) for the reaction products in different catcher foils were divided by its respective thickness that gives the resulting yield of experimentally measured RRDs. The experimental uncertainties in cross-section is $<10\%$ that arise due to various factors viz., uncertainty in the number of target nuclei due to non-uniformity in sample thickness, the fluctuations in the beam current, uncertainty in the determination of detector efficiency, statistical error in counts and the dead time of the counting system. The experimentally measured RRDs for reactions $^{159}\text{Tb}(^{16}\text{O},2n)^{173}\text{Ta}$, $^{159}\text{Tb}(^{16}\text{O},pn)^{173}\text{Hf}$ and $^{159}\text{Tb}(^{16}\text{O},3n)^{172}\text{Ta}$ at 90 MeV are shown in Fig 1 (a-c).

Solid curve in this figure guides the eye to the experimental RRD data. As can be seen from this figure that the experimental RRD data for these reactions has two peaks, one at a relatively lower value ($\approx 250\text{-}300\mu\text{g}/\text{cm}^2$, depending on straggling and number of evaporation residues) of cumulative catcher thickness and the other at $\approx 400\text{-}450\mu\text{g}/\text{cm}^2$. The peak at $\approx 400\text{-}450\mu\text{g}/\text{cm}^2$ corresponds to the fraction of residue produced through the CN process and is consistent with the full momentum transfer events in complete fusion reactions. The peak at relatively smaller range may be attributed to the fact that the residues ^{183}Ir are produced via the PCN process when emission of neutrons takes place prior to the establishment of thermodynamical equilibrium. The theoretical value (mean range) of the experimental RRD data is calculated with the help of energy loss program of the code SRIM and this value of mean range is fed in the program ORIGIN to fit the Gaussian peak of the experimental RRD. The Gaussian peak (shown by red dashed curve) at lower cumulative catcher thickness of larger width is obtained which shows the contribution of PCN emission. By using similar procedure, the RRDs for reactions $^{169}\text{Tm}(^{16}\text{O},2n)^{183}\text{Ir}$ and $^{169}\text{Tm}(^{16}\text{O},3n)^{182}\text{Ir}$ have also been measured at ≈ 88 MeV. The experimental RRDs with their theoretical simulations for these reactions are shown in Fig 2 (a-b), respectively. The peaks in the experimental RRD arise due to the overlap of the heavy residues produced via two different reaction mechanism i.e, the CN and the PCN emission of particles. As can be seen from this figure that the experimental RRD data for the reaction $^{169}\text{Tm}(^{16}\text{O},2n)^{183}\text{Ir}$ has two peaks, one at a relatively lower value ($\approx 200\text{-}250\mu\text{g}/\text{cm}^2$) of cumulative catcher thickness and the other at $\approx 330\text{-}380\mu\text{g}/\text{cm}^2$. The peak at $\approx 330\text{-}380\mu\text{g}/\text{cm}^2$ corresponds to the fraction of residue produced through the CN process. It is pointed out here that due to short half live (≈ 15 min) of the residue ^{182}Ir , we could measure only the RRD corresponds to CN component.

2.2 Measurement and Analysis of Spin Distributions

The second experiment based on particle-gamma coincidence technique has been performed for measuring the population of spin states during de-excitation of reaction residues. In the present work, the spin-distributions of the reaction $^{159}\text{Tb}(^{16}\text{O},2n)^{173}\text{Ta}$ at ≈ 93 MeV and for $^{169}\text{Tm}(^{16}\text{O},2n)^{183}\text{Ir}$ at ≈ 88 MeV have been measured using Gamma Detector Array (GDA) alongwith Charged Particle Detector Array (CPDA). The Experimental details are given in Ref. [21]. However, we mention them here in brief for ready reference. The GDA is an assembly of 12 Compton suppressed, high resolution HPGe γ -spectrometers arranged at 45° , 99° , and 153° angles with respect to the beam axis and there are four detectors at each of these angles. The CPDA is a set of 14-phoswich detectors housed in a 14 cm diameter scattering chamber, covering nearly 90% of total solid angle. The reaction residues have been identified from their characteristic prompt γ -transition lines [22]. The values of relative production yields of the residues (observed area under the peak of the experimentally measured prompt gamma

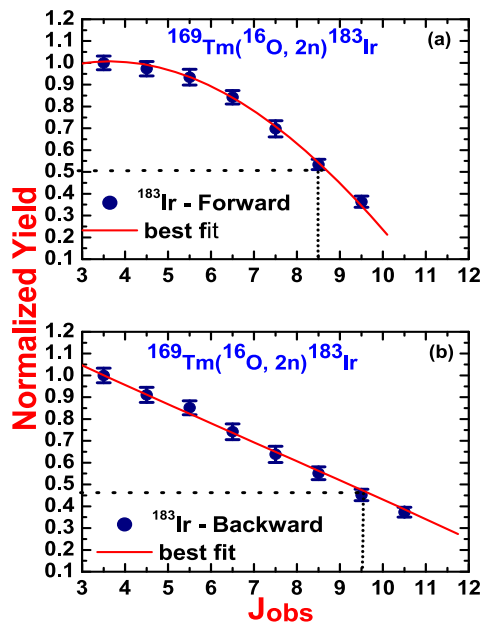


Figure 3. (Color online) The experimentally measured spin distributions for reactions $^{169}\text{Tm}(^{16}\text{O}, 2n)^{183}\text{Ir}$ in forward and backward directions. The curve and line in this figure guide the eye as a best fit to the experimentally normalized yield of spin distributions of PCN and CN processes.

lines with proper detector efficiency correction) have been plotted as a function of observed spin J_{obs} corresponding to prompt gamma-transitions[23]. The relative yield has been normalized with minimum observed spin (J_{obs}^{min}) at highest yield (Y_{obs}^{max}). As a representative case the experimentally measured SDs obtained from prompt γ -rays recorded in forward and backward directions for the reaction $^{169}\text{Tm}(^{16}\text{O}, 2n)^{183}\text{Ir}$ are shown in Fig 3 (a) and 3(b) at 88 MeV, respectively. As can be seen from these figures, the measured SD and hence its decay pattern for this reaction obtained in the forward and backward directions are distinctly different from each other indicating widely different reaction mechanisms involved. It may be pointed out the entirely different shapes of SDs in forward and backward directions indicate that the two processes are quite different in nature.

The observed lower value of the mean input angular momentum ($\approx 8.5\hbar$) in forward direction is due to the fact that emission of two PCN neutrons takes away a significant part of the angular momenta. On the other hand a relatively higher observed value of the mean input angular momentum in backward direction ($\approx 11.5\hbar$) is because of the emission of two equilibrated neutrons. As such, it is concluded that distinctly different SDs give a direct evidence of the PCN emission process. Thus, the results of the measurements of the SDs further supplement the conclusions drawn from the RRDs measurements.

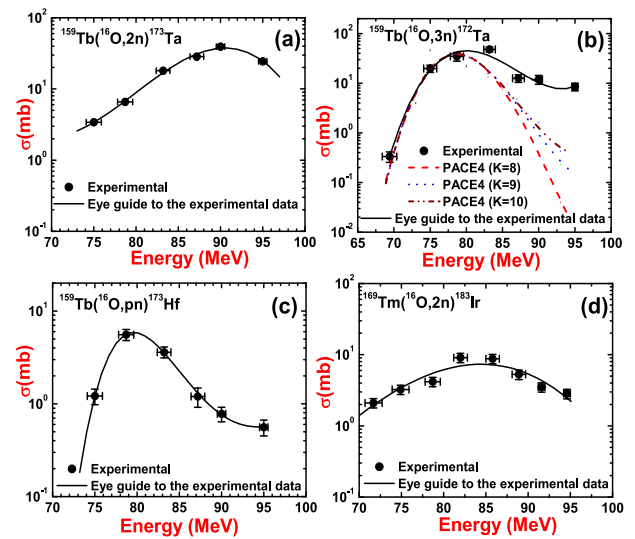


Figure 4. (Color online) (a-d) The experimentally measured EFs for reactions $^{159}\text{Tb}(^{16}\text{O}, 2n)^{173}\text{Ta}$, $^{159}\text{Tb}(^{16}\text{O}, pn)^{173}\text{Hf}$, $^{159}\text{Tb}(^{16}\text{O}, 3n)^{172}\text{Ta}$, and $^{169}\text{Tm}(^{16}\text{O}, 2n)^{183}\text{Ir}$, respectively. The theoretically calculated EFs by using code PACE4 gives negligibly small values of cross-sections for all these reactions except for $^{159}\text{Tb}(^{16}\text{O}, 3n)^{172}\text{Ta}$. The experimentally measured EFs and the PACE4 predictions with different values of parameter K from $K=8$ to $K=10$ for reaction $^{159}\text{Tb}(^{16}\text{O}, 3n)^{172}\text{Ta}$ is also shown in Fig 4(b).

2.3 Measurement and Analysis of Excitation Functions

The third experiment has been carried out for measuring the EFs by using stacked foil activation technique. In this experiment the stacks consisting of (^{159}Tb and ^{169}Tm) target samples followed by Al foils of suitable thickness have been irradiated for ≈ 8 -10 h in a GPSC of 1.5 m diameter having an in-vacuum transfer facility. The Al foils serve as energy degrader as well as catcher foil where the recoiling residues are trapped. The pertinent decay data required for cross-section measurements of the reaction residue has been taken from Ref.[24]. The activities produced in each target catcher assembly have been measured using a high resolution large volume (100 c.c.) High Purity Germanium Detector (HPGe). The reaction cross sections for the product residues have been obtained from the measured intensities of the characteristic γ -rays using the standard formulation[1].

The analysis of experimental EFs has been performed within the framework of statistical model calculations based on code PACE4[25] that calculates the reaction cross-section for evaporation residues (not for pre-compound residues) using the Bass formula[26]. The level density used in this code is calculated from the expression $a = (A/K)$, where, A is the mass number of the compound nucleus and K is a free parameter known as level density parameter constant. The experimentally measured EFs for the reactions $^{159}\text{Tb}(^{16}\text{O}, 2n)^{173}\text{Ta}$, $^{159}\text{Tb}(^{16}\text{O}, 3n)^{172}\text{Ta}$,

$^{159}\text{Tb}(^{16}\text{O,pn})^{173}\text{Hf}$ and $^{169}\text{Tm}(^{16}\text{O,2n})^{183}\text{Ir}$ in the energy range $\approx 70\text{--}95$ MeV are shown in Figs. 4 (a) to 4(d), respectively. The half-lives of these evaporation residues ^{173}Ta , 172 , ^{173}Hf and ^{183}Ir are 3.14 h, 36.8 m, 23.6 h and 57 m, respectively. The solid curves in these figures guide to the eye to the experimentally measured EFs. The theoretically calculated EFs by using code PACE4 gives negligibly small values of cross-sections for all these reactions except $^{159}\text{Tb}(^{16}\text{O,3n})^{172}\text{Ta}$, hence, the cross-section values obtained from code PACE4 are not shown in figures 4(a), 4(c) and 4(d). In the present calculations, the effect of variation of parameter K from $K=8$ to $K=10$ of code PACE4 on measured EFs for reaction $^{159}\text{Tb}(^{16}\text{O,3n})^{172}\text{Ta}$ is also shown in Fig. 4(b). As can be seen from this figure, by varying the value of K , the experimentally measured EFs could not be reproduced in higher energies (tail portion of EFs) side. The higher values of experimental cross sections in the tail portion of EFs for this reaction as compared to the theoretical calculations may be attributed to the PCN emission process, which is one of the dominant mode reaction channels and is not considered in the PACE4 calculations. It means that analysis of EFs with code PACE4 gives negligible contribution of CN process for the reactions $^{159}\text{Tb}(^{16}\text{O,2n})^{173}\text{Ta}$, $^{159}\text{Tb}(^{16}\text{O,pn})^{173}\text{Hf}$ and $^{169}\text{Tm}(^{16}\text{O,2n})^{183}\text{Ir}$, while the analysis of RRD for the same reactions gives energy dependent contributions of the CN and the PCN processes. This shows that RRD measurements are much sensitive as compared to those of EFs. The analysis of measured EFs for reaction $^{169}\text{Tm}(^{16}\text{O,3n})^{182}\text{Ir}$ gives a contribution of $\approx 35\%$ PCN and $\approx 65\%$ of CN at ≈ 88 MeV as shown in Fig 4 (b). This data is consistent with the corresponding values obtained from the RRD measurements at ≈ 88 MeV. Further, the reasonable agreement between the two sets of experiments speaks favorably on the consistency of these measurements.

3 Conclusions

The significant contribution due to PCN process has been observed. The results obtained by RRDs are supported by the SD measurements. The RRD measurements are found to be sensitive tool to decipher the CN and the PCN processes. The auxiliary experiments on the EF measurements is found to be consistent with both the RRD and SD measurements.

4 Acknowledgements

The authors are thankful to the Director, IUAC, New Delhi for extending all the facilities for carrying out the experiments. MKS thanks to the Council of Scientific and Industrial Research (CSIR), New Delhi, India vide the project number 03(1361)16/EMR-11 for financial support.

References

- [1] M. K. Sharma, P. P. Singh, D. P. Singh, V. Sharma, A. Yadav, Unnati, Indu Bala, R. Kumar, B. P. Singh, and R. Prasad, Phys. Rev. C **91**, 044601 (2015).
- [2] J. Gómez del Campo, D. Shapira, J. McConnell, C. J. Gross, D. W. Stracener, H. Madani, E. Chávez, M. E. Ortiz, Phys. Rev. C **60R**, 021601 (1999).
- [3] M. Blann, Ann. Nucl. Sci. **25**, 123 (1975).
- [4] M. Blann Nucl. Phys. A **235**, 211 (1974).
- [5] E. Holub, D. Hilscher, G. Ingold, U. Jahnke, H. Orf, and H. Rossner, Phys. Rev. C **28**, 252 (1983).
- [6] E. Holub, D. Hilscher, G. Ingold, U. Jahnke, H. Orf, H. Rossner, W. P. Zank, W. U. Scroder, H. Germeke, K. Keller, L. Lassen, and W. Lucking, Phys. Rev. C **33**, 143 (1986).
- [7] M. Cavinato, E. Fabrici, E. Gadioli, E. Gadioli Erba, P. Vergani, M. Crippa, G. Colombo, L. Redaelli, and M. Ripamonti, Phys. Rev. C **52**, 2577 (1995).
- [8] F. Amorini, M. Cabibbo, G. Cardelaa, A. Di Pietro, A. Musumarra, M. Papa, G. Pappalardo, F. Rizzo, and S. Tudisco, Phys. Rev. C **58**, 987 (1988).
- [9] H. Zheng, S. Burrello, M. Colonna and V. Baran, Phys. Lett. B **769**, 424 (2017).
- [10] H.C. Britt and A.R. Quinton, Phys. Rev. **124**, 877 (1961).
- [11] T. Otsuka and K. Haradav, Phys. Lett. B **121**, 106 (1983).
- [12] P. Vergani, E. Gadioli, E. Vaciago, E. Fabrici, E. Gadioli Erba, M. Galmarini, G. Ciavola, and C. Marchetta, Phys. Rev. C **48**, 1815 (1993).
- [13] C. Birattari et. al, Phys. Rev. C **54**, 3051 (1996).
- [14] H. Delagrance, A. Fleury, F. Hubert, and G. N. Simonoff, Phys. Lett. B **37**, 397 (1971).
- [15] H. Morgenstern, W. Bohne, K. Grabisch, D. G. Kover and H. Lehr, Phys. Lett. B **113**, 463 (1982).
- [16] B. B. Back et. al., Phys. Rev. Lett. **50**, 88 (1983).
- [17] The Stopping and Range of Ions in Matter (SRIM) code: [<http://www.srim.org/SRIM/SRIMLEGL.htm>].
- [18] M. K. Sharma et. al., Phys. Rev. C **70**, 044606 (2004).
- [19] D. P. Singh et. al, Phys. Rev. C **81**, 054607 (2010).
- [20] M. K. Sharma et. al., Phys. Rev. C **91**, 024606 (2015).
- [21] P. P. Singh, B. P. Singh, M. K. Sharma et al., Phys. Lett. B **671**, 20 (2009).
- [22] S. Andrd, J. Genevey-Rivier, et al., Phys. Rev. Lett. **38**, 327 (1977).
- [23] RADWARE Level Scheme
<http://radware.phy.ornl.gov/agsdir1.html>.
- [24] E. Browne and R. B. Firestone, 1986 Table of Radioactive Isotopes (Wiley, New York).
- [25] A. Gavron, Phys. Rev. C **21**, 230 (1980).
- [26] R. Bass, Nucl. Phys. A **231**, 45 (1974).

Quality of Service in Cloud Computing in Higher Education: A Critical Survey and Innovative Model

Jolly Upadhyaya

Ph.D. Scholar

Department of Computer Science and Engineering

Center for Information Technology

UPES, Dehradun

Dr. Neelu Jyoti Ahuja

Sr. Associate Professor

Department of Computer Science and Engineering

Center for Information Technology

UPES, Dehradun

Abstract— Cloud Computing, an emerging trend, in the e-learning sector has attracted number of service providers to the market in very less time, providing users with several applications at their disposal. However, while providing such service, not sufficient importance is given to the quality of the service, especially from the user's point of view. Hence it becomes necessary to monitor, track and quantify the QoS of the cloud computing e-learning applications in order to provide the right information to both the customers and the service providers. This information would help both the parties in terms of the comparison between the expectations and the capacity to meet them, but in this sector there is no standard model which defines the QoS parameters from the user's point of view. Thus, the need arises for developing a metrics model for enhancing the quality of service in cloud computing e-learning applications for higher education sector. In the current work, Quality of Service models are studied and comprehensive review of work done in this field is presented. Additionally an innovative QoS model for resolving this issue has been suggested.

Keywords—cloud computing;quality of service; innovative model;literature survey;higher education

I. INTRODUCTION

Cloud relies on sharing of resources to achieve coherence and economies of scale. Over the last ten years, due to the advent of technologies like cloud computing, big data etc, there have been major changes in the ICT sector and its services. These changes which are more economic in nature have led to many socio-cultural transformations with impact on user behaviour and increased performance expectations by the service providers. It has changed the way users perceive services. Currently, online learning applications are being hosted over cloud environment further promoting its necessity [20]. Surveys show that in the next five years, institutions of higher education expect to

cut 20% of their IT budget by moving their applications to cloud, thus representing a major shift in approach across the industry. The role of service quality in higher education has received increasing attention over the last few decades. All online education services should ensure that all service encounters are managed to enhance customer perceived quality (Brochado, 2009).

While there is a consensus on the importance of service, the identification and understanding of quality issue is a challenge. According to Maguad (2007), the future success of online learning services will increasingly depend on proper identification of the issues & variables related to quality of service.

Cloud Computing provides advantage to customers and service providers in terms of cost saving and resource utilization but it still has to earn the confidence of the customers in other aspects to become a commonly trusted technology. Due to the dynamic nature of cloud computing applications, the exact performance becomes unpredictable at times. Some Quality of Service requirements are specified in the SLAs but most of the points are only service provider specific. For example, Amazon Web Service (AWS) in its SLA with the customer commits the 99.9% availability of Amazon S3 during a month but no other QoS eg. quality of site, ease of use etc. is committed. This observation highlights the fact that the commitments in terms of Quality of Service made by the Service Providers in their SLAs are very simple and does not mention the user specific QoS criteria. Hence, a need arises to specify certain Quality of Service variables and their specification and quantification which could be representative of the user in the SLA. A QoS metrics model is an

important issue for developers, providers and users alike for improving performance and decreasing number of failures and anomalies that could affect their performance.

Initial survey of literature reveals that there is limited research work in the field of QoS of cloud applications in the area of online learning in higher education sector [21]. The primary goal of the current work is to address Quality of Service in the nascent paradigm of cloud computing in online learning. In reality, cloud service providers rarely provide Quality of Service beyond “you get what you are given.” Cloud users require more than that part of the commitment. With enhancement in Quality of Service, the range of deployable applications can improve and thus help in the overall adoption of cloud by higher education sector.

II. PROBLEM STATEMENT

With the increasing number of applications moving to cloud environment, the quality of service is deteriorating. This compels the scholar to develop a Quality of Service Metrics Model to recommend and fix the parameters of quality in cloud computing especially in the field of online higher education so that the relationship and accountability between the service provider and the end user gets enhanced.

III. MAIN RESEARCH QUESTION ?

How to develop a *Conceptual Model* and hence the prototype which improves *Quality of Service* over existing cloud environment particularly in the field of *online* higher education?

Supplementary questions which are associated with the main RQ:-

RQ1: How can Quality of Service be assured for cloud applications efficiently and effectively?

RQ2 : What are the current practices and are they sufficient and efficient?

RQ3: What is the current situation regarding QoS in cloud computing applications in the field of online education?

RQ4: Keeping in focus online learning in higher education sector, how can we identify and quantify the variables?

RQ5: How can the outcome variables are formulized further for theoretical classification and comparison?

RQ6: How can we prototype the model for validating the QoS of cloud applications at higher education level?

RQ7: How much significant advantage in QoS management through the proposed model is achieved?

IV. RELATED WORK

This section briefly discusses the related work that has been carried out by other researches and has been published in various journals and conferences. Special attention has been paid to select the relevant and recent work. Cloud computing applications may have many users at the same time and all may have different requirements in terms of quality of service. Providing a guaranteed QoS environment in such dynamic environment is a challenging task. But even then, over the time researches have tried to develop different mechanisms, systems and frameworks which can look into the aspect of QoS requirements of different services.

Buyya, Garg and Calheiros[24], proposed a framework for managing QoS requirements with special reference SLA management. It integrates the virtual technologies with the market based resource provisioning for flexible resource allocation to user applications. But the proposed model does not support different Cloud providers for IaaS, PaaS and SaaS together. According to NIST (Special Publication 500-307 in 2015), the Quality Model can be extended and integrated into Quality of Service (QoS) models that address the context of a quality metric, the observation and computing results based on a metric or the scenario that make use of metrics. Feng et al[12], have proposed an optimal resource allocation model for revenue maximization. But it considers only the mean response time as the QoS attribute to be satisfied. Den Bossche, Vanmechelen and Broekhove[26], proposed a system which attempts to maximize use of local resources while minimizing the use of external resources without compromising the QoS requirements. But it does not deal with the failures which may occur after the scheduling has been done which may result in increase in cost of execution and effect overall quality.

M.Salam et al[16], presented a QoS oriented federated cloud computing framework where multiple independent cloud providers can cooperate seamlessly to acquire more resources in peak time

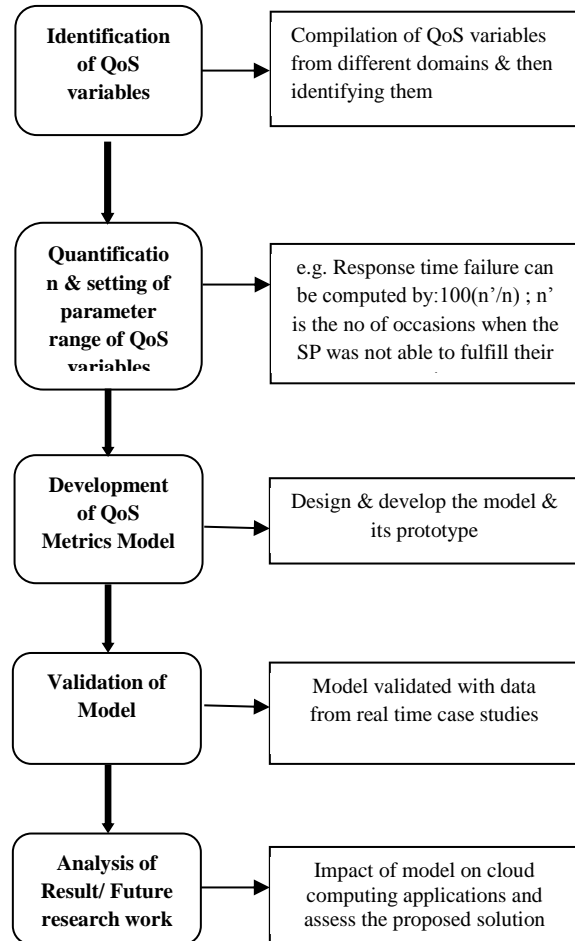
to fulfil their QoS targets and pre-defined SLAs. The distinct feature of this framework was QoS oriented capabilities to address dynamic resource management to improve the effective usage resources. But complex services were not constructed using services from different cloud providers and no provision was made for distributed denial of service attacks. R. Karim et al [25], proposed a mechanism to map the users QoS requirements of cloud services to the right QoS specifications of SaaS then map them to best IaaS service that offers the optimal QoS guarantee. The end to end QoS was calculated. They proposed a set of rules to perform the mapping process. A case study was used to illustrate and validate the solution. But no performance evaluation was done based on real QoS dataset of cloud services. S.Lee et al [28], proposed an architecture which employed the agent technology to handle the monitoring of requested QoS requirements and SLAs to support verification and validation. Its weak point was lack of self learning algorithms to determine the timing of automatic resource allocation. P.Zhang et al [23], presented a QoS framework for adaptive QoS management process and mobile cloud computing to manage QoS assurance in mobile cloud computing environment. But no good model with a suitable configuration was generated.

The literature discussed above is mainly concerned with the cloud workflow. None of it discusses the selection of QoS attributes and quantifying them from the user's point of view. During the literature study of QoS models in cloud computing that many researchers have proposed the scheduling techniques, admission controls, traffic control, dynamic resource provisioning etc. in order to handle the issue of QoS in cloud computing. But to the best of our knowledge no model has been proposed till now which deals with QoS issues from the perspective of user experience particularly in the sector of higher education.

V. INNOVATIVE MODEL

The main objective of the research is to develop an innovative model in which some specific measurable QoS variables will be identified and appropriate acceptable parameter range will be given for them which will go as an input and then will provide with the output. This will be enhanced QoS and will act like a guide to the customers and instil confidence in them. Through the model,

detecting expectations, malfunctioning and enhancement of QoS would help service providers to act proactively and maintain their service quality and cultivate confidence in users/customers mind. QoS parameters degradation can be detected and rectified through the development of a scalable, efficient and easy to use monitoring model and tool.



Flowchart for creating the QoS Innovative model

VI. EXPECTED OUTCOME

The expected outcome and significance of development of this model is manifold. Firstly, the model will act as a guide which would help both the customer and the provider to know the QoS variables their expected parameters to the services they are providing and receiving. Secondly, the model would help the service providers to prepare their services and maintain the quality of these services in accordance with the expectations of the customers. And lastly, the customers will be able to know beforehand what to demand in terms of quality of service from the service providers and will be able to monitor it.

VII. CONCLUSION

Quality of Service plays an important role in making cloud computing more reliable and adaptable. Knowing the expected parameters of the QoS variables is a key factor in ensuring that the quality of service is maintained. The conclusion of the proposed work is that it is expected to significantly contribute to the existing knowledge of QoS in cloud computing and develop a QoS model with special reference to enhancing the quality of service of cloud computing applications in higher education sector as this study can be beneficial to both the user to obtain a better service and by the provider to enhance their quality of services provided.

REFERENCES

- [1] Abdullah Alshwaier, Ahmed Youssef and Ahmed Emam, "A New Trend For E-Learnin in KSA Using Educational Clouds", ACIJ, Vol.3
- [2]Lutz Schubert and Keith Jeffery, "Advances in Clouds Expert Group Report", Public version 1.0
- [3]Aman Kumar Sharma and Anita Ganpati, "Cloud Computing: An Economic Solution to Higher Education", IJAEM, Volume 2, Issue 3, March 2013
- [4]Amid Khatim Bardsiri and Seyyed Mohsen Hashmi, "Quality of Service metrics for cloud computing services evaluation", IJISA, Vol. 6 No.12, Nov. 2014
- [5]Bariah Aljebreen, Prof. Ajantha Dahanayake and Liyakathunisa Syed,"Advances In Higher Educational Resource Sharing and Cloud Services for KSA", IJCSES, Vol.6, No.3, June 2015
- [6]BV Pranay kumar, Sumitha kommareddy and N.Uma Rani, "Effective Ways Cloud Computing can Contribute to Education Success", ACIJ, Vol.4, No.4, July 2013
- [7]Cloud 101: "Developing a Cloud-Computing Strategy for Higher Education", White Paper, CISCO 2011
- [8] "Cloud Computing in Higher Education: A Guide to Evaluation and Adoption", White Paper, CISCO 2009
- [9]Danilo Ardagna, Giuliano Casale, Michele Ciavotta, Juan F Pérez and Weikun Wang, "Quality-of-service in cloud computing: modelling techniques and their applications, Ardagna et al", Journal of Internet Services and Applications 2014
- [10]David Nunez, Carmen Fernandez-Gago, Siani Pearson and Massimo Felici, "A Metamodel for Measuring Accountability Attributes in the Cloud", Hewlett-Packard Laboratories, 2013
- [11]Eugene Gorelik, "Cloud Computing Models Working Paper" CISL, January 2013
- [12]G.Feng,S.Garg,R.Buyya and W.Li, "Revenue maximization using Adaptive resource provisioning in cloud computing Environments", Proc. 13th ACM/IEEE Int. Conf. Grid Computing,Pg. 192-200,2012
- [13]Girish J. Brahmamath, Rajeev R. Raje, Andrew M. Olson, Mikhail Auguston, Barrett R. Bryant and Carol Burt, "A Quality of Service Catalogue for Software Components"
- [14]"Innovating for Education & Research Excellence Oracle Cloud Solutions for the Modern Campus", Oracle White Paper, December, 2014
- [15]Kiran Yadav, "Role of Cloud Computing in Education", International Journal of Innovative Research in Computer and Communication Engineering, Vol. 2, Issue 2, February 2014
- [16] M. Salam and A. Shawish, "A QoS oriented inter cloud federation framework",IEEE Systems Journal, Pg. 642-643,2015
- [17]M.Xu, L.Cui,H.Wang and Y.B.Bi, "A multiple QoS constrained scheduling strategy of multiple workflows from cloud computing", IEEE International Symposium on Parallel and Distributed Proceedings with Applications, 2009, pg. 629-633
- [18]N.Ani Brown Mary and K.Jayapriya, "An Extensive Survey on Quality of Service in Cloud computing, IJCSIT, Vol. 5 (1), 2014, pg. 1-5
- [19]NIST, Cloud Computing Service Metrics Description, "NIST Cloud Computing Reference Architecture and Taxonomy Working Group", Special Report 2015
- [20] Pallavi Narang, Dr. I. S. Hudiera and Dr. Sawntar S. Khurmi, "Bring Into Play the Software Metrics in SAAS- A Cloud Computing Prospective", International Journal of Innovative Research in Science, Engineering and Technology ,Vol. 3, Issue 11, November 2014
- [21]Paul Manuel, "A trust model of cloud computing based on Quality of Service"
- [22] P.C.Hershey,S.Rao,c.b. Silio and A.Narayan, "System of systems for Quality of Service observation and response in cloud computing environment", IEEE Systems Journal, Vol.9, Issue 1, pg-1-5,2015
- [23]P.Zhang and Z.Yan, "A QoS aware system for mobile cloud computing", Proc. IEEE, pg.518-522,2011
- [24]R.Buyya, S.K.Garg and R.N. Calheiros, "SLA-Oriented Resource Provisioning for Cloud Computing:Challenges, Architecture and Solutions", Proc. Intl. Conf. Cloud and Service Computing,Pg.1-10,2011
- [25]R.Karim, C.Dinng,A.Mirri, "An end to end QoS mapping approach for cloud service selection", Proc. IEEE 9th world congress on services, pg.341-348,2013
- [26]R.V.den Bossche,K.Vanmechelen and J.Broeckhove, "Cost Efficient Scheduling Heuristics for deadline constraints workload on hybrid clouds", Proc. 3rd IEEE Intl. Conf. Cloud Comp. Tech. & Sc.(CloudCom),Pg. 320-327,2011
- [27]Stefan Frey, Claudia Luthje and Christoph Reich, "Key Performance Indicators for Cloud Computing SLAs", EMERGING 2013 : The Fifth International Conference on Emerging Network Intelligence

Smart Geyser with Usage Profiling to Reduce Electricity Consumption

Rohit Samkaria, Ambujaksh Shah, Bhupinder Singh
and Sushaban Choudhury

Abstract Geyser which is a pressurized hot water container utilized in household causes the high power consumption and at the same time degrading the efficiency of the heating element due to heat losses, i.e., overheating of the element. This paper presents the smart geyser which operates in two modes (i) Autonomous Mode (ii) User Mode. A temperature sensor probe is used as a control switch which is used to regulate the water temperature of geyser by adjusting the heating duration of the element. The study reveals the control topologies used to reduce the power consumption and to increase the efficiency of the geyser. The system consists of Atmega16 microcontroller which determines the hot water profile through temperature probe in Autonomous Mode and in User Mode the controller regulates the temperature of geyser as per the demand profile developed by user. From the result it is apparent that by controlling the temperature of the geyser, the heat losses in the Geyser element and saving of electricity power consumption can be made.

Keywords Geyser temperature control · Atmega16 microcontroller · Hot water profiling

1 Introduction

In daily life we use hot water for various purposes like cooking, bathing, or for industrial purposes and the process employed for the water heating uses the thermodynamics in which a source of energy is used to heat the water. Geysers used in households are pressurized hot water container which are operated by mains 220 V AC [1]. The element used for heating purposes inside the Geyser degrade due to

Rohit Samkaria (✉) · Sushaban Choudhury
University of Petroleum and Energy Studies,
Dehradun, India
e-mail: rohit.samkaria93@gmail.com

Ambujaksh Shah · Bhupinder Singh
Schematic Micro Electronics, Dehradun, India

the overheating of water, i.e., heat losses and at the same time causes the major consumption of the electricity power. The objective of continuously monitoring the environmental data of geyser, i.e., water temperature is to lowering the power consumption of household and to increase the power efficiency of heating element of the geyser [2]. A temperature sensor probe is utilized to monitor the temperature of the water [3]. When the temperature profile reached the maximum value in the Autonomous mode, the electronic circuit which uses electromagnetic relay is actuated [4] and then the geyser is automatically put in off mode in order to avoid over heating of the element [5]. In the User Mode, the microcontroller tracks the temperature of the Geyser as per the demand profile developed by the user [6] and when this demand profile reached to the actual heat profile then Geyser is automatically put in off mode [7]. In most populated country like India, the use of electricity by domestic sector is substantial during peak times and hot water geyser is one of the devices which cause the largest power consumption. So by making a sophisticated geyser control system, it is possible to make a sufficient reduction in the consumption of electricity during the peak demand [8]. This paper represents the development, design, and testing of such a sophisticated device which can reduce the electricity consumption and increases the efficiency of the geyser by avoiding the heat losses in the heating element.

2 Proposed System

Automatic Smart Geyser having capability to heat the water in two modes, i.e., Autonomous Mode and User Mode with power saving capability is proposed. Figure 1 shows the schematic model of the proposed system. The water is heated in geyser by two modes. In first mode when user switches on the geyser it starts heating the water up to a desired temperature which is continuously monitored by the temperature sensor probe inside the geyser and after this desired temperature the controlled relay switched OFF the main supply of the geyser and in the same time the RED LED over the Geyser starts blinking with the buzzer beeping out which is the indication of the overheating of the water. In the User Mode if user wish to heat the water up to his own desire he/she can select the temperature limit through the temperature selector switch board. After putting the desired value, the geyser starts heating with GREEN LED blinking showing the normal water condition. When the water temperature reaches up to the user's defined limit the control relay switch board will cut the supply off the geyser and buzzer starts beeping with RED LED blinking over the geyser. In some cases, it is the contact volume editor that checks all the pdfs. In such cases, the authors are not involved in the checking phase.

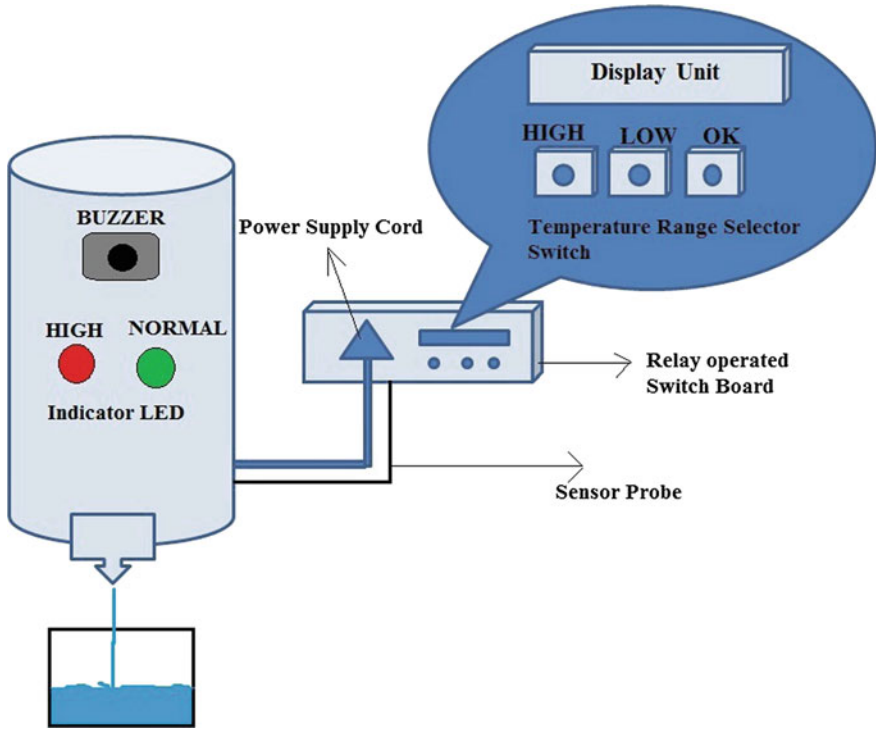


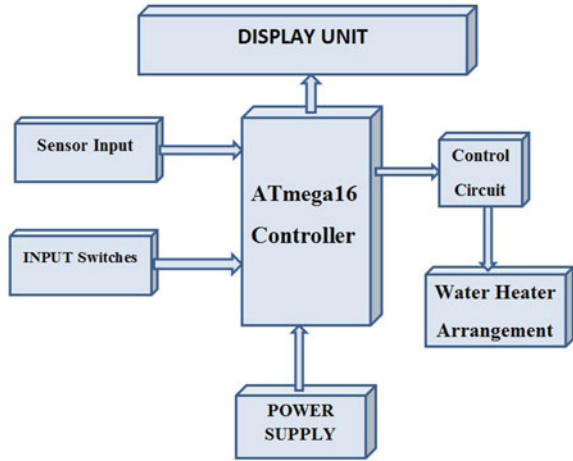
Fig. 1 Schematic diagram of model

3 Prototype Development

The hardware of the proposed system basically consists of the embedded system designed with a temperature monitor probe as a sensor unit for the system. Figure 2 shows the block diagram of the system having seven modules interconnected with each other.

In the block diagram, the main central control unit of the model is Atmega16 microcontroller which is termed as a single on chip computer which includes various numbers of peripherals device connected with it like EEPROM, RAM, etc., which perform some predefined task. Atmega16 having inbuilt 10-Bit ADC, SPI, PWM is much faster since it is modified RSIC processor. This microcontroller is capable of being programmed on board itself rather than first removing and then uploading the program. The monitoring and conditioning of data and taking the decision according to the predefined condition is done by the microcontroller unit. The temperature monitor probe which acts as the sensor unit for the module basically consists of the DS18B20 Programmable Resolution 1-wire digital thermometer which does not require external components and can be powered from the data line. The power supply required for the sensor is 3.0–5.0 V and measures the

Fig. 2 Block diagram of the model



temperature from the -55 to $+125$ °C (Fahrenheit equivalent to -67 to $+257$ °F). The sensor is made of stainless steel tube 6 mm diameter by 30 mm long. The cable is 36" long/91 cm, 4 mm diameter (1 m long). Input switches module is utilized when the circuit is used in autonomous mode and it consists of push button (SPST) which is connected with the input port of the microcontroller. These push buttons are used to select the predefined level of the heating of the water marked as UP, DOWN, and OK. UP and DOWN push buttons slide the value from maximum to minimum and OK to set that particular value of heating. The control circuit consists of SPDT relay with transistor 2N2222 as a switch to operate the relay. The relay circuit connects the mains supply to the Geyser and this relay is operated through the microcontroller. The display unit consists of the 16×2 LCD (Liquid Crystal Display) which provides the visual display of the level of heating and is connected to the microcontroller unit. To power up the whole system, a power supply is needed which is provided by the regulated IC. The module consists of step-down transformer followed by bridge rectifier with filter circuit. To obtain the regulated supply IC7805 is used in this module with indication circuit that consist of LED in series with a resistance.

4 Hardware Development

The hardware of the model of sensor module and input switches module which decide the operation of the circuit. Figure 3 shows the circuit diagram of the model.

In the circuit diagram, the temperature sensor probe is connected to the ADC0 pin of the Atmega16 microcontroller. The temperature sensor probe has three pins VCC, DQ, and GND and is connected to the +5 V supply. The Atmega16 has 10-Bit ADC which convert this 5 V supply into $2^{10} = 1024$ levels and these levels

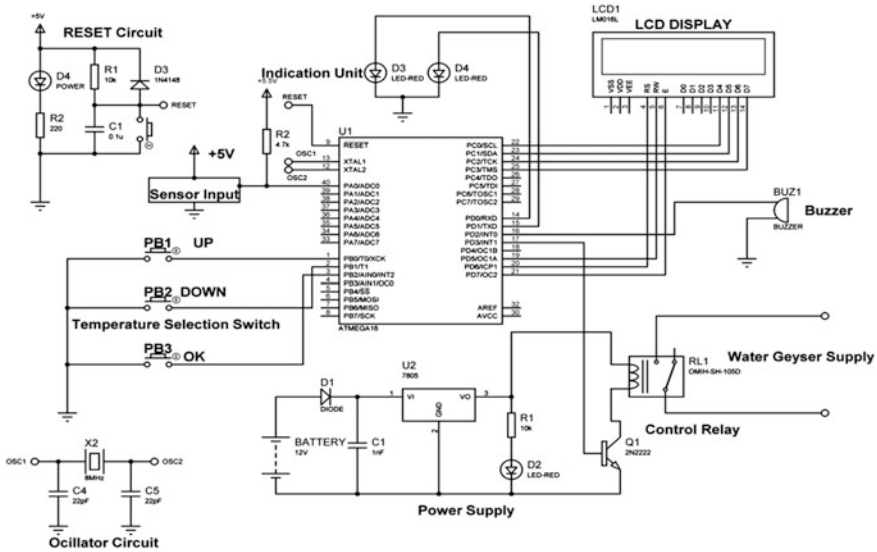


Fig. 3 Circuit diagram of the system

correspond to the temperature of the water. The input switches PB1, PB2, and PB3 are connected to the PB0, PB1, and PB2 pin of the microcontroller of the system. These three pins of the controller are internally pulled up and continuously read for a low voltage at these pins, so these push button are connected with the ground of the supply. LCD having 16 pins in which four data D11, D12, D13, D14 pins of the LCD are connected to the PC0, PC1, PC2, PC3 pin and the RS, R/W, and E pins are connected at PD6, PD5, and PD7 pin of the microcontroller. The two indications LED are connected at PD0 and PD1 pin of the controller which provides the status of the temperature. To provide the over temperature indication, the buzzer is connected to PD2 pin of the controller. The control circuit consists of 5 V operated relay which is controlled by a transistor 2N2222 that acts as a switch to ON/OFF the relay. The relay is connected at the collector of the transistor through a +5 V supply. The base of the transistor is connected at PD3 pin of the controller. By sending the high data over the PD3 pin, the transistor operates at saturation region and relay is connected at collector conducts. The whole circuit is powered up by regulated power supplies which consists of the regulated IC 7805.

5 Circuit Description

The circuit is operated in two modes (i) Autonomous Mode (ii) User Mode

- (i) **Autonomous Mode:** In the autonomous mode, the circuit operates in automatic mode. The user switches ON the power supply and the control circuit gets activated which provides the bridge between the main supply and the geyser supply and geyser starts working. Now the water temperature inside the geyser starts to rise. The temperature probe inside the geyser measures this rise in water temperature and provides the corresponded level over the display. When water temperature reached the maximum level which is determined inside the controller program, the microcontroller deactivates the control circuit which cuts off the geyser supply from main and the buzzer provides the beep sound with RED LED blinking which provides the indication of the overheating of water.
- (ii) **User Mode:** In the User Mode the predefined level of heating is selected from the selector switches, i.e., UP and DOWN switches can vary the range of the water heating and after that by pressing the OK button, system starts working. Now temperature probe monitors the rise in the temperature of the water and it compares the value defined by the user and the actual rise in temperature attained by the water. When the rise in temperature of water reaches equal to the defined value by the user, the microcontroller deactivates the control circuit which cuts off the geyser supply from the mains and buzzer starts beeping with RED LED blinking as an indication of overheating of the water.

The step-by-step working of the system is through algorithm in Fig. 4.

6 Software Development

The firmware for the system is developed using the WinAVR Compiler and AVR studio. The WinAVR is freeware, open source software development tool which is designed for the Atmel AVR series of RISC architecture microprocessor hosted on window platform and includes GCC compiler for C and C++. The software code for the desired system is written in the C language and the code is compiled by using the open source compiler avr-gcc (Fig. 5).

7 Proteus Simulator

Proteus simulator is used as the hardware simulation platform which is a powerful design tool in which various virtual components from the libraries are placed in the work space and connected with each other and the code is loaded inside the microcontroller and real-time hardware simulation by using virtual components is taken. The Proteus simulator has the ability to define most of the aspects of the drawing appearance and hardware feasibility is checked on Proteus simulation before actual hardware implementation.

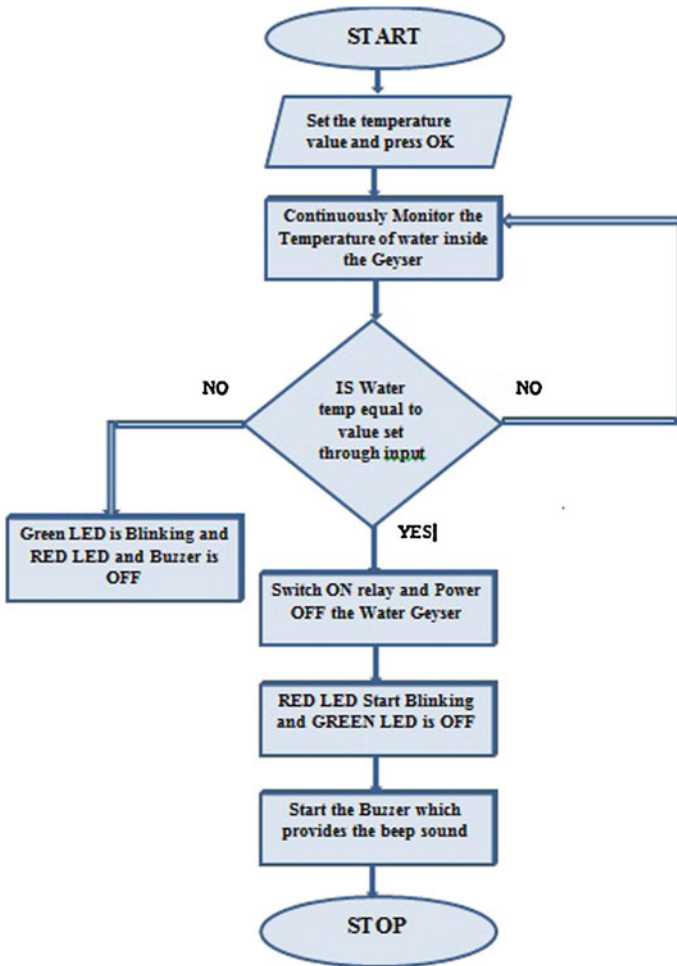


Fig. 4 Flow chart for working of the proposed system

Figure 6 shows the Proteus simulation of the model in which various virtual components from the Proteus libraries are placed on the work space and interconnected with each other. The code is loaded in the controller from the AVR studio in which coding is done by using C language. This code is compiled and the hex file created after compilation of the code is loaded into the microcontroller and then the Proteus simulation executed.

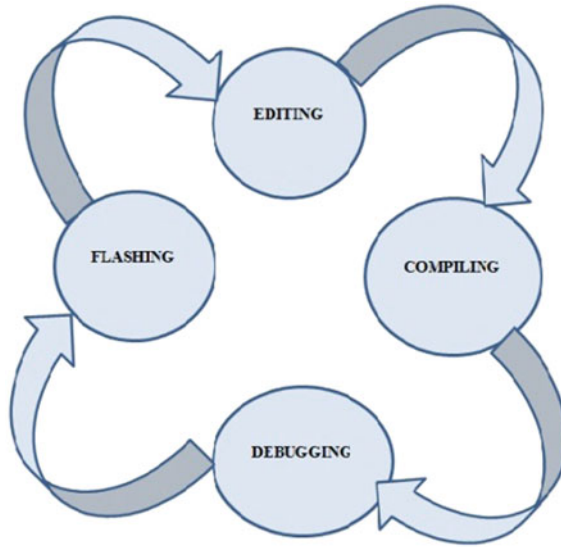


Fig. 5 Coding step

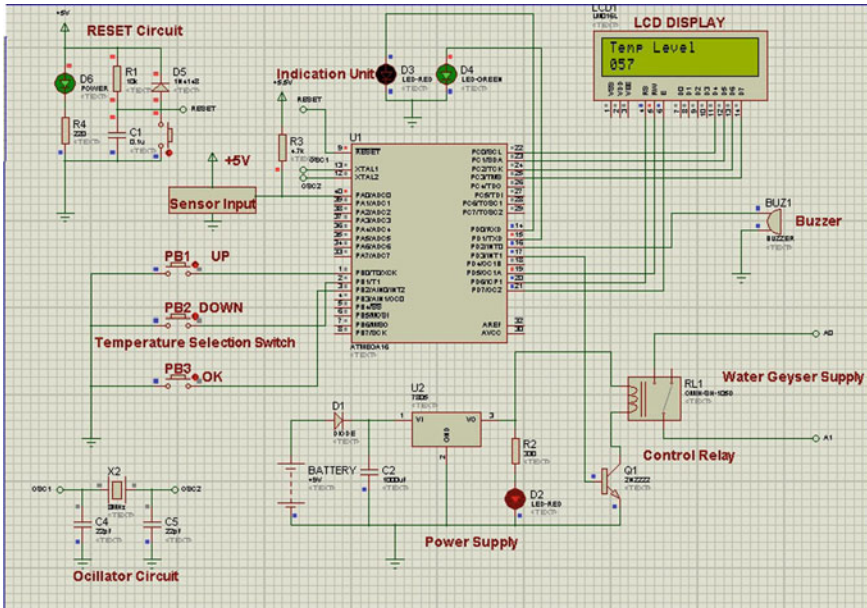


Fig. 6 Proteus simulation of the model

8 Result and Discussion

The proposed system is mainly focused to reduce the electric power consumption through smart geyser used in the domestic purposes which can save 7.48 (kWh) energy per month at a heating of 65 °C of heating element. There are two types of geyser which are mostly used in the domestic a 3 kW 150 L and 4 kW 200 L which causes an average energy loss of 2.3 kWh energy losses per day. So by this smart geyser these energy loss can be reduced and the efficiency of the heating elements can be increased three times that of the normal geyser where element degrades due to the heating loss.



9 Conclusion and Future Scope

From the result, we found that the average power consumption is reduced and at the same time the efficiency of the geyser increased by reducing the heat losses in the filament. Such type of geyser could in future also accommodate energy saving when connected with solar energy. By this system, it is possible to set predefined temperature profile.

As results have shown the net efficiency of geyser which would increase with reduction in the electricity consumption.

References

1. Catherine, Quinton, et al. "Hot water usage profiling to improve geyser efficiency." *Journal of Energy in Southern Africa* 23.1 (2012): 39.
2. Hulsbos, R., et al. "Design of a smart geyser controller unit." *AFRICON*, 2015. IEEE, 2015.

3. Haines, Eldon L., and Ralph E. Bartera. "Self-pumping solar heating system with geyser pumping action." U.S. Patent No. 4,478,211. 23 Oct. 1984.
4. Hayashi, Toshikazu. "Ventilation fan system with smoke detector speed control." U.S. Patent No. 3,826,180. 30 Jul. 1974.
5. Steyn, S. J. M., and R. Chetty. "Development of a residential appliance control interface (ACI) module using smart systems." Industrial Technology (ICIT), 2013 IEEE International Conference on. IEEE, 2013.
6. Elmahalawy, Ahmed Mustafa, Newal Elfishawy, and Mohamed Nour El-Dien. "Anticipation the consumed electrical power in smart home using evolutionary algorithms." Multimedia Computing and Information Technology (MCIT), 2010 International Conference on. IEEE, 2010.
7. Harris, James R. "Transistor circuit for operating a relay." U.S. Patent No. 2,718,613. 20 Sep. 1955.
8. Anderson, Larry L., Lawrence W. Shumaker, and Russell J. Van Rens. "Circuit for a power operated machine." U.S. Patent No. 4,195,722. 1 Apr. 1980. Appendix: Springer-Author Discount.

Stabilization of Underactuated Mechanical System Using LQR Technique

Akash Gupta, Varnita Verma, Adesh Kumar, Paawan Sharma,
Mukul Kumar Gupta and C.S. Meera

Abstract The two-link inverted pendulum on cart (TLIPOC) is a widely known system having underactuation property. TLIPOC is a highly unstable and nonlinear system. The modelling of TLIPOC is obtained using Euler–Lagrangian approach. In this paper use of optimal control minimizing a quadratic cost functional is discussed. The aim of the paper is to stabilize the TLIPOC using linear quadratic regulator (LQR) technique. MATLAB simulations are used to show the efficiency and feasibility of proposed approach.

Keywords Underactuated system · Linear quadratic regulator

1 Introduction

The two-link inverted pendulum on cart (TLIPOC) constitutes a challenging control problem because of underactuation property [1]. In underactuated systems there are fewer actuators than their degrees of freedom. These systems have many applications like robotics, mobile systems, aerospace systems and locomotion. The underactuation

Akash Gupta (✉) · Varnita Verma · Adesh Kumar · Paawan Sharma ·
M.K. Gupta · C.S. Meera
University of Petroleum and Energy Studies, Dehradun, India
e-mail: akashgupta646@gmail.com

Varnita Verma
e-mail: varnitaverma@yahoo.in

Adesh Kumar
e-mail: adeshkumar@ddn.upes.ac.in

Paawan Sharma
e-mail: paawan.sharma@ddn.upes.ac.in

M.K. Gupta
e-mail: mkgupta@ddn.upes.ac.in

C.S. Meera
e-mail: meera.cs@ddn.upes.ac.in

property is due to (i) dynamical property, (ii) failure of actuator, (iii) reduction of cost, (iv) forcefully reducing order of the system. Despite many control techniques, controlling of these systems remains challenging problem [1, 2]. The TLIPOC system is a highly nonlinear system so linear technique cannot be used. Linear quadratic regulator (LQR) is the technique to obtain the performance index function [3–6]. With the LQR technique, system stability can be achieved in a simpler manner as directly we can apply the LQR command whereas fuzzy logic or neural network is more challenging technique as compared to LQR.

2 A Two-Link Inverted Pendulum

The TLIPOC system is shown in Fig. 1. First we assume that the rod is lumped in nature and cart mass is denoted as M_0 , rod mass are m_{10} and m_{20} . There is external force applied on the cart, $x(t)$ represents position of the cart, $\theta_1(t)$ and $\theta_2(t)$ are the angle from the vertical position.

The difference between kinetic energy (K) and potential energy (V) is known as the Lagrangian of a system [7].

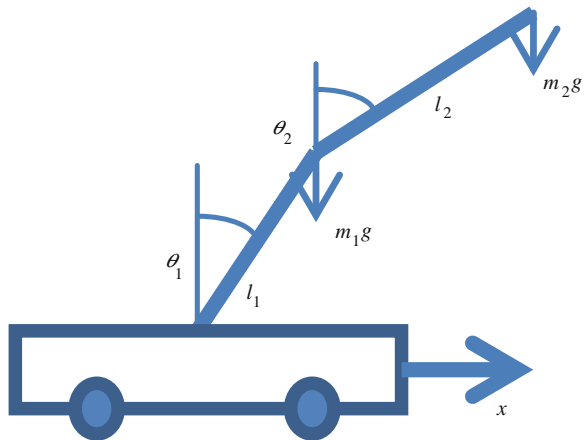
The Lagrangian will be calculated as the follows:

$$L = \frac{1}{2} [M + m_{10} + m_{20}] \dot{x}^2 + \frac{1}{2} m_{10} (l_1 \dot{\theta}_1)^2 + \frac{1}{2} m_{20} \{ (l_1 \dot{\theta}_1)^2 + (l_2 \dot{\theta}_2)^2 + 2l_1 l_2 \dot{\theta}_1 \dot{\theta}_2 \cos(\theta_1 - \theta_2) \} + [m_{10} + m_{20}] \dot{x} \dot{\theta}_1 l_1 \cos \theta_1 + m_{20} \dot{x} \dot{\theta}_2 l_2 \cos \theta_2 + (m_{10} + m_{20}) g l_1 (\cos \theta_1) + (m_{20}) g l_2 (\cos \theta_2) \quad (1)$$

The Lagrangian equations of motion will be calculated from the following:

$$\frac{d}{dt} \frac{\partial L}{\partial \dot{x}} - \frac{\partial L}{\partial x} = 0 \quad (2)$$

Fig. 1 The two-link inverted pendulum system



$$\frac{d}{dt} \frac{\partial L}{\partial \dot{\theta}_1} - \frac{\partial L}{\partial \theta_1} = 0 \tag{3}$$

$$\frac{d}{dt} \frac{\partial L}{\partial \dot{\theta}_2} - \frac{\partial L}{\partial \theta_2} = 0 \tag{4}$$

We get

$$(M + m_{10} + m_{20})\ddot{x} + (m_{10} + m_{20})\ddot{\theta}_1 l_1 \cos \theta_1 + m_{20} l_2 \ddot{\theta}_2 \cos \theta_2 - (m_{10} + m_{20})\dot{\theta}_1^2 l_1 \sin \theta_1 - m_{20} \dot{\theta}_2^2 l_2 \sin \theta_2 = u \tag{5}$$

$$(m_{10} + m_{20})l_1^2 \ddot{\theta}_1 + m_{20} l_1 l_2 \ddot{\theta}_2 \cos(\theta_2 - \theta_1) - m_{20} l_1 l_2 \dot{\theta}_2^2 \sin(\theta_2 - \theta_1) + (m_{10} + m_{20})g l_1 (\sin \theta_1) = 0 \tag{6}$$

$$m_{20} l_2^2 \ddot{\theta}_2 + m_{20} \ddot{x} l_2 \cos(\theta_2 + l_1 l_2 \dot{\theta}_1 \cos(\theta_1 - \theta_2)) - l_1 l_2 \dot{\theta}_1^2 \sin(\theta_1 - \theta_2 + m_{20} g l_2 \sin \theta_2) = 0 \tag{7}$$

After splitting the values of \ddot{x} , $\ddot{\theta}_1$, $\ddot{\theta}_2$ and substituting into nonlinear model as

$$\frac{d}{dt}(x) = f(x, u, t) \tag{8}$$

$$x_1 = x, x_2 = \dot{x} = \dot{x}_1, x_3 = \theta_1$$

$$\text{Let } x_4 = \dot{\theta}_1 = \dot{x}_3 \tag{9}$$

$$x_5 = \theta_2, x_6 = \dot{\theta}_2 = \dot{x}_5$$

State space representation is indicated as follows:

$$\frac{d}{dt} \begin{pmatrix} x_1 \\ x_2 \\ x_3 \\ x_4 \\ x_5 \\ x_6 \end{pmatrix} = \begin{pmatrix} x_2 \\ \dot{x}_2 \\ x_4 \\ \dot{x}_4 \\ x_6 \\ \dot{x}_6 \end{pmatrix} \tag{10}$$

Linearize the above equation at $(\underline{x}_0, \underline{u}_0) = (0, 0)$ and also taking the values of,

$$m_{10} = m_{20} = 0.2 \text{ kg}, M = 0.5 \text{ kg}, l_1 = l_2 = 1 \text{ m}, g = 10 \text{ (ms}^{-2}\text{)}$$

The linearized form of the system is

$$\frac{d}{dt}(\delta \underline{x}) = J_{\underline{x}}(\underline{x}_0, u_0)\delta \underline{x} + J_u(\underline{x}_0, u_0)\delta u \quad (11)$$

After solving the above equations we get the linearized matrix as [1]

$$\frac{d}{dt}(\delta \underline{x}) = \begin{bmatrix} 0 & 1 & 0 & 0 & 1 & 0 \\ 0 & 0 & -0.07 & 0 & 0.12 & 0 \\ 0 & 0 & 0 & 1 & 0 & 0 \\ 0 & 0 & -1.4 & 0 & -2.8 & 0 \\ 0 & 0 & 0 & 0 & 0 & 1 \\ 0 & 0 & 5.75 & 0 & 1.38 & 0 \end{bmatrix} \delta \underline{x} + \begin{bmatrix} 0 \\ 0.012 \\ 0 \\ -0.015 \\ 0 \\ -0.015 \end{bmatrix} \delta u \quad (12)$$

And the output matrix is

$$y = \begin{bmatrix} 1 & 0 & 0 & 0 & 0 & 0 \\ 0 & 0 & 1 & 0 & 0 & 0 \\ 0 & 0 & 0 & 0 & 0 & 0 \end{bmatrix} \begin{bmatrix} \dot{x} \\ x \\ \theta_1 \\ \dot{\theta}_1 \\ \theta_2 \\ \dot{\theta}_2 \end{bmatrix} \quad (13)$$

3 LQR Controller

For the design of LQR controller the main aim is to minimize the performance index J . The weighted matrix are positive definite in nature. The control input is taken as

$$u(t) = -Kx(t) \quad (14)$$

Weight matrices Q and R in performance index J are chosen randomly [8]. The selection that the elements of the matrix Q are larger than the matrix R means that controller is more sensitive to states than the control input. The elements of the Q and R matrices under consideration are

$$Q = \text{diag}([100010001000]); \quad R = 1$$

Table 1 Eigen values of Matrix A and Ac

S.no	E.V. of A	E.V. of Ac
1	0	-1.3802 + 1.3828i
2	0	-1.3802 - 1.3828i
3	-1.3772 + 1.3845i	-1.3743 + 1.3862i
4	-1.3772 - 1.3845i	-1.3743 - 1.3862i
5	1.3772 + 1.3845i	-0.2211 + 0.2213i
6	1.3772 - 1.3845i	-0.2211 - 0.2213i

The gain matrix is

$$K = [1.0000 \quad 5.9638 \quad -674.0980 \quad -59.0284 \quad -499.6924 \quad -297.1697] \quad (15)$$

The E.V. of Matrix A and Ac is given in Table 1.

4 Results and Discussion

Various trajectory plots of TLIP system are as shown in various figures. From the results it is clear that systems settling time is very low in almost all the output which is a very good indication. Here all the possible output is shown including cart for double inverted pendulum. There are other techniques also available like fuzzy control, neural network or LOR fuzzy, but for stability point of view it is the simplest technique as directly we can apply this technique with the MATLAB command. The main use of this control technique is to make the system stable in a simpler and effective manner (Figs. 2, 3, 4, 5, 6 and 7).

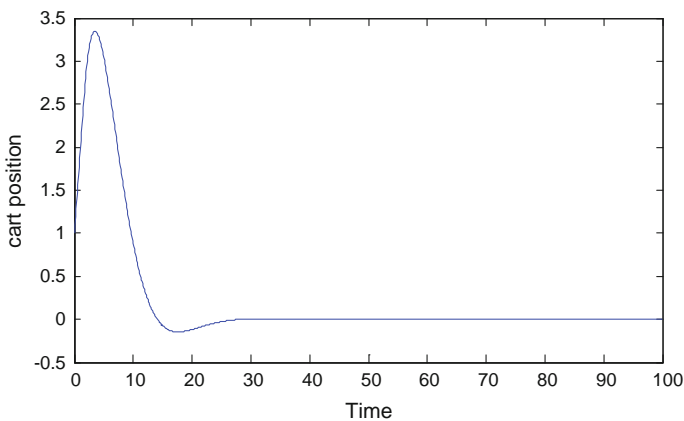


Fig. 2 Cart position

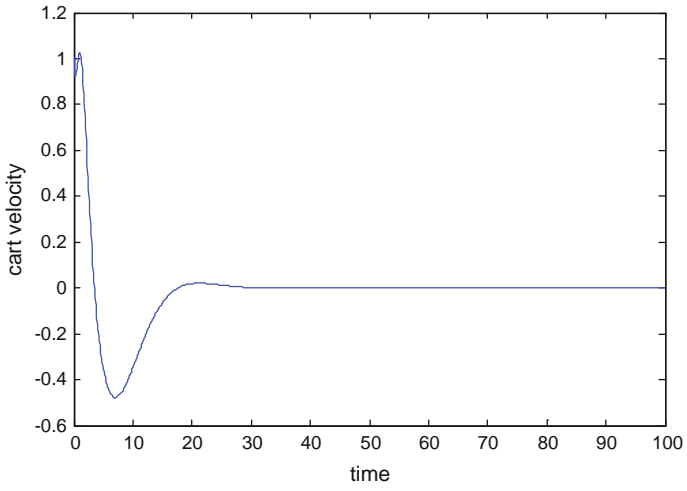


Fig. 3 Cart velocity

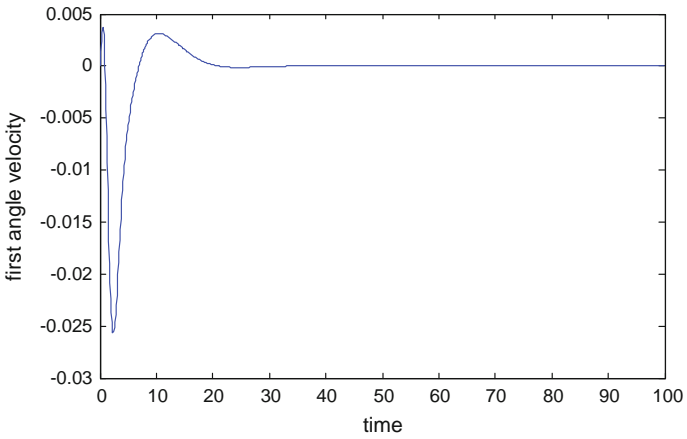


Fig. 4 First angle

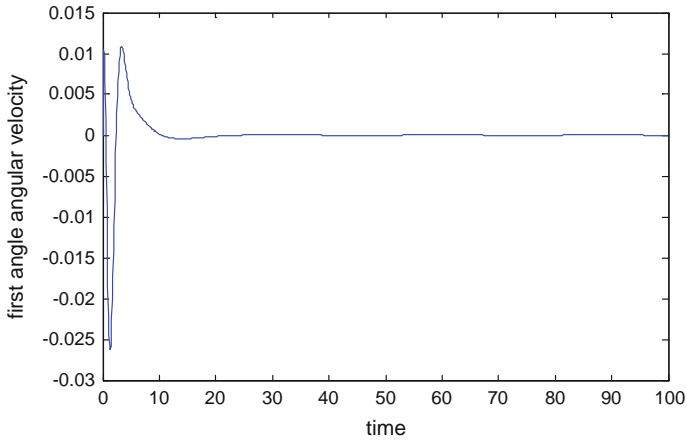


Fig. 5 First angle angular velocity

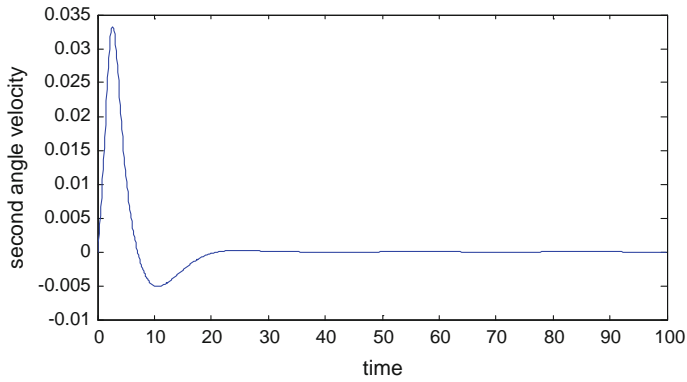


Fig. 6 Second angle

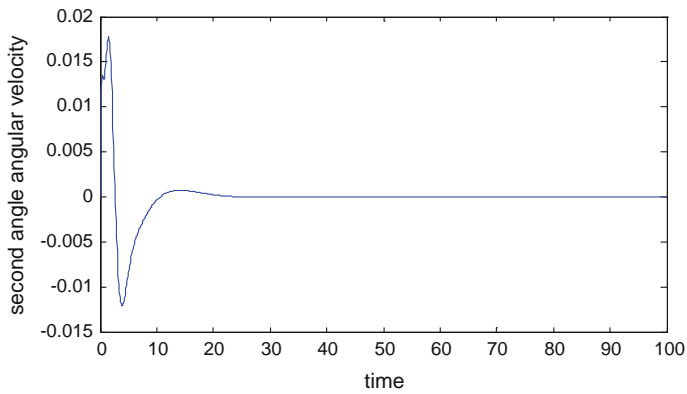


Fig. 7 Second angular velocity

5 Conclusion

The paper presents LQR technique to stabilize the TLIP system about its vertical position. The value of Q&R tried after various hit-and-trial methods and it is found that these are the most suitable value for optimal control. To balance a TLIP on a moving cart has been successfully designed using optimal control system. Simulation shows the validity of the suggested controller as the system's outputs are satisfactory. The main objective of this paper is to make output of TLIP stable in nature with least effort applied by the controller as compared with the other control techniques.

References

1. Abhaya Pal Singh, Faruk S. Kazi, N.M. Singh, Pallavi Srivastava, $PI\alpha D\beta$ Controller Design for Underactuated Mechanical Systems, 2012 12th International Conference on Control, Automation, Robotics & Vision Guangzhou, China, 5–7th December 2012 (ICARCV 2012).
2. C. Chevallereau, J.W. Grizzle and C.H. Moog. Nonlinear Control of Mechanical Systems with one Degree of Underactuation. "Robotics and automation", vol-3, 2222–2228, (2004).
3. Jinghu Xing, workers Chen, Ming Jiang. The study of inverted pendulum optimal control system based on LQR. Industrial Instrumentation and Automation. 2007.
4. Dan Huang, Shaowu Zhou, "Inverted pendulum control system based on the LQR optimal regulator. Micro Computer Information", 2004, 20(2): 37–39.
5. W. Zhong and H. Rock, Energy and passivity based control of the double inverted pendulum on a cart. In Proceedings of the IEEE international conference on control applications, Mexico City, Mexico, September 2001.
6. Desineni Subbaram Naidu, "Optimal Control Systems", Idaho State University, 2002, p. 129.
7. Lijuan Zhang, Yaqing Tu, "Research of Cart Inverted Pendulum Model Based on Lagrange Equation", Proceedings of the 6th World Congress on Intelligent Control and Automation, IEEE Press, June 2006, pp. 820–824.
8. Bogdanov Alexander, 2004, "Optimal Control of a Double Inverted Pendulum on a Cart", Technical Report CSE-04-006.Y.

Study of Performance of Transmit Beamforming and MU-MIMO Mechanisms in IEEE 802.11ac WLANs

N.S. Ravindranath*, Dr. Inder Singh, Dr. Ajay Prasad
College of Engineering Studies,
UPES, Dehra Dun, India
*nethins@yahoo.co.in

Dr. V. Sambasiva Rao
ECE Department,
PES University
Bengaluru, India

Abstract—Transmit beamforming and Multi User MIMO (MU MIMO) are key features in the 802.11ac WLAN standard. In this paper, we study these features and analyze the approaches suggested in the literature for enhancing the performance of 802.11ac WLANs using these features.

Keywords—WLAN; TxBF; MU MIMO; Aggregation, Precoding; TxOP;

I. INTRODUCTION

The IEEE 802.11ac Wireless Local Area Networks (WLAN) standard is designed to achieve the throughput rates on wireless networks from a minimum of around 1 Gbps and up to nearly 7 Gbps with increased bandwidth and multiple spatial streams (SS). As a result of these speeds, 802.11ac is used in numerous data hungry applications like video gaming/conferencing/ High Definition streaming.

Major performance improvements are expected in 802.11ac WLANs, the two features chiefly contributing to this being Transmit beamforming and Multi User MIMO. Transmit beamforming (TxBF) is achieved by introducing complex signal processing features in the WLAN chipset. An array of antennas are used to transmit with high gain to the 802.11 client, resulting in higher downlink signal-to-noise ratio (SNR), higher data rate over a longer range, and hence better overall system performance.

If the same data is transmitted from multiple antennas through a wireless channel, data received by the receive antennas has varied attenuations and phases due to reflection by different objects and also due to the different paths traversed along the channel. SNR at the receiver is affected by the phase of the multi path signals. Two signals with equal amplitude but opposite phases cancel at the receiver and on the other hand, two equi-phase signals will combine constructively. Hence, using signal processing methods, and by compensating the phase of individual streams at the receiver, we can maximize SNR at the receiver. This is the concept of TBF. TBF can thus be thought of as directing a beam using phase shifts towards a particular receive antenna. As the TBF technique can converge or cancel a beam by introducing appropriate phases, it can apply the same concept to cancel interfering signals in the direction of the receiver.

The MU-MIMO feature in 802.11ac introduces multiple SS distributed (maximum of four streams) between the clients. Data transmission is possible to more than one client concurrently; hence congestion delay is not an issue.

In 802.11ac, only downlink MU MIMO (DL MU-MIMO) is supported.

The contents of the paper are organized with the theoretical concepts of Transmit beamforming and Multi User MIMO discussed in Sections II and III respectively. Approaches adopted in literature for enhancing Transmit beamforming and Multi User MIMO are in Sections IV and V. Conclusion and future work are in section VI.

II. TRANSMIT BEAMFORMING

Channel sounding is a key functionality in TxBF. It is explained as follows:

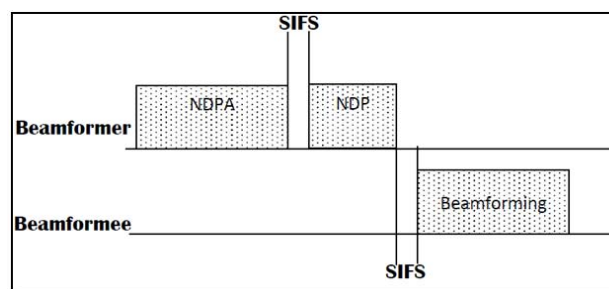


Figure-1 Channel Sounding - NDPA and NDP

Step 1: The Null Data Packet Announcement (NDPA) frame from the beamformer is to access the channel and discover beamformees. By responding to the NDPA the beamformee ensures that channel is not accessed by others until the end of the sounding sequence.

Step 2: An NDP from the beamformer follows the NDPA.

Steps 1 and 2 are explained through Figure 1

Step 3: On receiving the NDP, the beamformee analyses the OFDM training fields, processes the individual OFDM subcarrier associated with each (NTx,NRX) antenna pair and forms the V feedback matrix based on the amplitude and phase of each signal.

After matrix operations on the V matrix the angles by the beamformer are calculated, and the altered matrix is transmitted to the beamformer. One of operations performed is compression which results in a smaller frame and hence lesser airtime.

Step 4: The beamformer forms the steering matrix 'Q' based on the contents of the 'V' feedback matrix. The effect of the steering matrix on the data to be transmitted is to create a pointed beam from an omni-directional beam.

Figure 2 explains the steps 3 and 4.

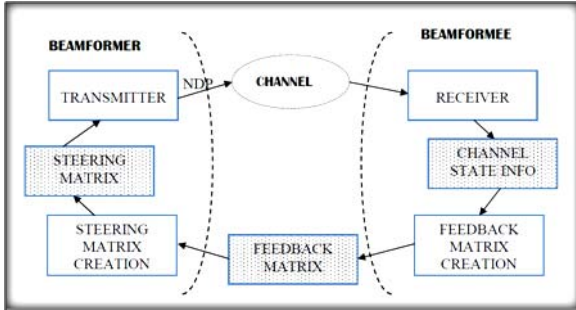


Figure-2 Channel Sounding- Feedback Matrix and Steering Matrix

III. MULTI-USER MULTI-INPUT MULTI-OUTPUT

The overall block diagram of 802.11ac PHY layer for supporting MU-MIMO is shown in Figure-3.

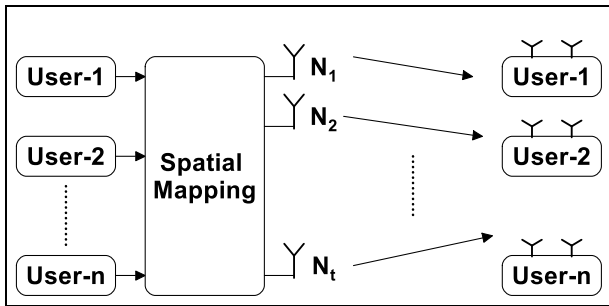


Figure-3 Structure of 802.11ac Downlink MU-MIMO

Modifications to the WLAN standard to support MU-MIMO in 802.11ac are examined with respect to MAC and PHY layer.

A. MAC

1) CSMA-CA and the Backoff Mechanism

A CSMA/CA is a medium access scheme and it requires a STA invoke a particular type of backoff procedure depending on the particular event which leads to the backoff. The backoff is activated when more than one station attempts to simultaneously access the channel. Changes have been made to the 802.11 standard to enhance the backoff mechanism in order to support DL MU-MIMO.

2) TXOP, Queuing and QoS

Transmit Opportunity (TXOP) was an enhancement in 802.11e to the existing Distributed Coordination Function (DCF) mechanism with the aim of providing contention-free access to the medium for a specific Access Category (AC).

The different ACs are Voice (VO), Video (VI), Best effort (BE) and Background (BK). As TXOP permits uninterrupted access to voice and video frames for a bounded period and also blocks low priority users from obtaining excessive channel duration, it is considered a major QoS mechanism. 802.11ac has enhanced TXOP with TXOP sharing concept to support DL-MU-MIMO feature. TXOP sharing works as follows:

- *Initiation of TXOP after gaining access to the medium:* At first, each EDCAF of an AP competes for the TXOP using its own parameters. Once an EDCAF wins a TXOP, it becomes the owner of that TXOP and its AC is the primary AC, where as other ACs are secondary ACs.
- *Sharing of TXOP:* The primary AC can then choose to share its TXOP with the secondary ACs for transmitting streams in parallel. Such a TXOP which is shared becomes a multi-user TXOP (MU-TXOP). The primary AC also can decide which secondary AC(s) to share with TXOP, and the destinations to which it needs to transmit.

3) Group ID Concept in IEEE 802.11ac WLAN

The Group ID field in the 802.11ac preamble is used to signal SU/MU transmission and the stations' position, to the potential recipients. The NSTS field indicates how many SS are destined for each of the potential recipients. In IEEE 802.11ac, up to four stations can be included in the downlink MU-MIMO transmission. Each can have up to four streams destined to it, with a maximum on the total number of streams equal to 8. A 6-bit field is assigned for the Group ID. 6 bits are sufficient to define up to 64 groups.

4) Aggregation

A-MPDU with Compressed Block ACK mechanism was introduced in IEEE 802.11n specification. In this mechanism, multiple MPDUs are aggregated into a single A-MPDU in order to improve MAC efficiency by reducing redundant protocol overhead such as backoff procedures, acknowledgments, inter-frame spacing, and protocol headers. All MPDUs within an A-MPDU are destined for the same receiver and have the same Traffic Identification (TID), and an A-MPDU cannot contain fragmented MPDUs even if the length of MAC Data Service Unit (MSDU) - a content of MPDU - exceeds the fragmentation threshold. The Compressed BlockAck mechanism is used as the acknowledgment for the A-MPDU.

IEEE 802.11ac amendment defines a VHT single MPDU that is a MPDU that is the only MPDU in an A-MPDU carried in a VHT PPDU. In this case, A-MPDU can only contain one fragmented VHT single MPDU, and its operating rules are the same as those for normal MPDU. Although it is useful to set the A-MPDU boundary for sharing EDCA TXOP, the use of fragmented MPDUs in A-MPDU is still not allowed, resulting in the wastage of medium by requiring that meaningless A-MPDU pads fill out the A-MPDU boundary.

B. PHY

1) Channel calibration/Sounding for MU-MIMO

Here, Channel State Information (CSI) is obtained from all related users, with the aim of identifying beamformees with orthogonal channel vectors. This result in total suppression of interference between the multiple streams directed towards the various users.

Figure-4 shows the channel sounding and MU-MIMO transmission protocols defined in IEEE 802.11ac. When the AP performs channel sounding at a given time, the beginning of sounding is announced by transmitting a null-data packet announcement (NDPA). After a short inter frame space (SIFS), AP transmits a null-data packet (NDP), in which each AP antenna sequentially transmits a known signal for channel estimation. It is seen from the figure that the multi-user mechanism necessitates a response from all beamformees, for which purpose, the Beamforming report poll frame is added. After a SIFS, a predestined node feeds back the CSI. After a SIFS again, the AP polls a next node, and the polled node feeds back the CSI after a SIFS until all the nodes have been polled for CSI feedback. The multiple responses are combined by the beamformer resulting in a master steering matrix.

The NDP announcement frame, NDP frame and compressed beamforming action frame are same as in Transmit Beamforming. The 802.11ac MAC protocol defines capability (number of SS, Modulation and Coding Scheme (MCS)) negotiation for all the transmissions happening in parallel.

After the AP transmits packets to the primary and secondary users, the primary user transmits a Block Acknowledgement (BA) after a SIFS. Next, the AP sends a BA Request (BAR) for one of the secondary users after a SIFS, and the polled node sends a BA after a SIFS till polling of all nodes is completed. This is shown in figure-5

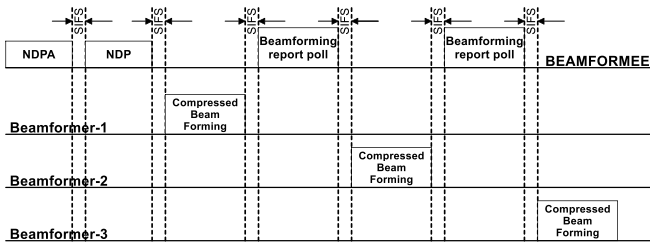


Figure-4: Channel Sounding in MU-MIMO Transmission

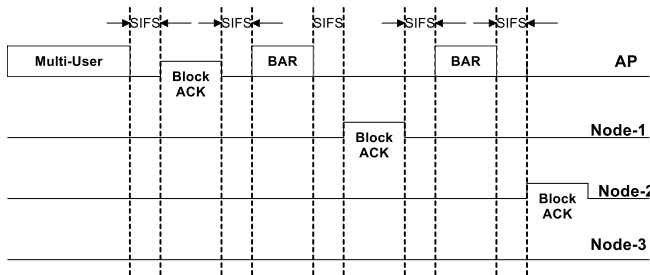


Figure-5: MU-MIMO Transmission

2) Precoding

Precoding techniques play a major role in the performance of MU-MIMO transmission. In this regard, there are two

major classes of precoding namely, non-linear and linear precoding.

Non-linear precoding techniques are recognized to be useful for obtaining the maximum throughput possible. Some of these non-linear precoding techniques are Tomlinson-Harashima precoding (THP), Vector Perturbation (VP) and Lattice Reduction Aided (LRA) methods. However, these techniques have a very high level of complexity caused by the requirement of additional processing at the receiver and are also not supported by 802.11ac.

Linear precoding techniques (Dirty Paper Coding (DPC), Zero Forcing and Block Diagonalization (BD)) on the other hand are low-complexity transmission techniques and are supported by 802.11ac.

3) User selection

Since total numbers of users are generally more than the number of users which can be supported at the AP, optimal users with good CSI can be selected to improve the throughput of MU-MIMO system.

4) Detection Mechanisms

Additionally, at the receiver side, the independent signals will need to be separated by using a technique called MIMO detection. Traditional MIMO detection methods include the well-known linear MMSE as well as the vertical-Bell laboratories layered space-time (V-BLAST) and LRA decoders.

IV. TRANSMIT BEAMFORMING ENHANCING MECHANISMS

A. Time Domain Quantization

In [1], a technique "time domain quantization" (TD-Q) is introduced wherein there is a feedback of time domain parameters. These are required, as in Sounding, to form the beamforming matrix at the transmitting end. It is proved that TD-Q reaches the same sum rate capacity of the conventional Givens rotation quantization GR-Q and requires less amount of feedback. However, TD-Q requires some additional complexity in that the transmitter must perform a FFT before the precoding process. Nevertheless, this can be easily supported because all the MIMO-OFDM systems equipment dispose of FFT component for OFDM demodulation.

B. Pre-coding and Temporal CSI

Reference [2] proposes a method of transmitting precise channel estimation to the transmitter which requires this to enable the calculation of precoding vectors. Since there is a huge amount of channel coefficients that is required for feedback, particularly when there more OFDM subcarriers and antennas, limited CSI feedback works out to be an advantage. Such a scheme that allows both the accuracy of the feedback to be improved and the feedback amount to be reduced based on the channel impulse response called Temporal CSI (TCSI) is proposed and is applied to a IEEE802.11n system.

C. *Explicit Feedback and Preamble Structure*

The authors in [3] suggest mechanisms to decrease overhead for Givens decomposition based feedback. It is demonstrated that the channel estimation smoothing gain may be larger than the beamforming gain, especially at low SNRs and also for low delay spread channels. Hence it is proposed to use a preamble structure that allows channel smoothing to be performed in a beamformed transmission. Also a non-precoded channel estimation for low delay spread channels is proposed.

D. *Directional Transmit and Receive Algorithm*

Reference [4] proposes a directional transmit and receive algorithm (DTRA) in WLANs with directional antennas for QOS purposes. The TDMA-based MAC algorithm utilizes the beamforming capabilities of smart antennas to adapt resource access based on to the services required for individual traffic flows. At the same time interference, probability of detection, and jamming in the network are also considered. In DTRA slots are reserved based on the traffic load. It is demonstrated from simulation results that DTRA performance is superior to IEEE 802.11.

E. *Beamforming with Multiple Spatial Streams*

Reference [5] analyses the theoretic throughput and coverage for a multi-element in home WLAN in the 5 GHz band. Results are provided for 802.11n MIMO deployments. It is seen that beamforming is mainly influenced by regulatory transmit power constraints. For long-range links, beamforming data throughputs decrease by more than half. When regulatory constraints are applied to the beamforming WLAN, the average data rate decreases by 14.3% whereas for a system with antenna selection, it result in an 8.9% reduction. Furthermore, it is seen that for long range links the average data rate is improved by 50% when the antenna selection replaces beamforming. While antenna selection uses single stream MIMO more commonly as compared to beamforming, beamforming is superior in performance with multiple spatial streams. Beamforming is shown to work best in the easy and medium-range channels.

F. *Single-User and Multi-User Beamforming*

In [6], the achievable rate formulas of STBC, SU-BF and MU-BF transmission modes in 802.11ac are derived. The rate losses are determined by the transmission mode, fading rate and frame length, i.e., feedback delay and operating SNR.

The space-time block code (STBC) is included in the open-loop category while transmit beamforming (BF) methods fit into the closed-loop category. The latter includes the single-user BF (SU-BF) in which an AP supports a single STA and multi-user BF (MU-BF) in which multiple STAs are served concurrently by an AP.

If a STA has no capability for closed-loop BF, the data should be sent by the AP employing STBC. With SU-BF and MU-BF, channel variation over time is a critical impairment. Under a severe condition, a STBC scheme can achieve higher throughput than the BF schemes even without channel feedback. When there is not much data to be delivered,

feedback turns out to be an overhead. In such cases, open-loop BF is a better choice compared to the close-loop BF. The rate loss due to channel variation is derived and the throughput is calculated by considering the frame structures as well as the overhead due to feedback. A guideline is provided for system design of 802.11ac following these investigations.

G. *Smart Antennas*

Prior to the application of smart antenna techniques in 802.11n, a study was undertaken in [7] to study the benefits of these techniques for general wireless networks. [7] discusses the circuit techniques involved in combining signals from various receive array elements and also for splitting signals to multiple transmit array elements. Also techniques to control the phase and the amplitude of signals from/to each array element are studied with the view of obtaining high data rates and manage interference.

V. MU MIMO ENHANCING MECHANISMS

Here, the various approaches which are mentioned in literature, with respect to MU MIMO are discussed. They are classified under General, MAC and PHY headings.

A. *General*

1) *Group ID*

Reference[8] focuses on the use of group membership for downlink (DL) MU-MIMO. The AP uses the Group ID to indicate to STAs which are group members about their positions and the spatial streams on which DL transmission will take place.

Reference[8] resolves the issue of assigning group membership and stations' positions given the available number of Group IDs. A heuristic algorithm was developed that implements the following steps:

- All associated stations are assigned letters of the alphabets. Transmission sets are organized in an alphabetical order.
- The AP computes the conditional probability that a station is in position x of a transmission set, given that the station is a member of that transmission set.
- Each station is assigned position x in a number of Group IDs proportional to the computed conditional probability.
- The AP can then choose the specific Group IDs for position x assignment.

Conclusions: Two methods are considered here for selecting specific Group IDs for position x assignment and their performance is compared to theoretical results. Results have shown that while the random selection method performs better, there is still more work needed to enhance the performance with respect to the success ratio and bring it close to results obtained theoretically.

2) *TxOP for DL MU-MIMO*

In [9], the technique of enhancing TXOP (TXOP sharing) for downlink MUMIMO transmission is discussed and the revised backoff procedures for secondary ACs is introduced.

Conclusions: Simulation results show that the proposed backoff procedure performs in a superior way, regarding fairness, than the traditional backoff mechanisms. The proposed TXOP Sharing mechanism has been accepted in the 802.11ac draft specification.

B. MAC Layer

1) MAC Mechanism

a) Backoff Mechanism: Reference [10] reports the work done by IEEE 802.11ac task group for enhancing the backoff schemes of the EDCA mechanism and points out its issues. Two different approaches are proposed to improve the limitations of the backoff schemes. OPNET simulations were conducted for performance evaluation. It may be noted that this suggestion has been implemented in the 802.11ac draft.

Simulation results indicate that these approaches decrease back offs and increase the channel time for voice traffic without obviously decreasing the channel time for video traffic. In addition, proposal #1 is able to increase downlink throughput without decreasing the uplink throughput. Simulation results have shown that the proposed backoff mechanism shows much better performance, in terms of fairness, than the conventional backoff procedures.

b) Network Allocation Vector - Problem: When there are more than one BSS, network allocation vector (NAV) may be set mistakenly due to MUMIMO and overlapping BSS. The redundant NAV settings contribute to reduction in throughput. To overcome this issue, [11] proposes a two-level NAV mechanism (with only minor changes to the standard) resulting in better throughput. Theoretical analysis is also performed on the proposed mechanism and the formulae of the achieved gain is derived.

2) MAC TXOP

a) Modified Backoff Procedure: In [12], it is proposed to enhance the TXOP Sharing mechanism, to obtain improved DL-MU-MIMO transmission. New definitions are provided about both events of successful and failed DL-MU-MIMO transmission. Then, a modified backoff procedure is designed for the primary AC. Simulation results show the advantages of the enhanced TXOP Sharing Mechanism with respect to throughput and channel utilization.

b) Markov Chain Model-1: In [13], an analytical Markov chain based model is introduced to assess performance of 802.11ac AP when TXOP sharing is enabled. While this model is an extension to the popular Bianchi's Model as also earlier models developed to analyze the EDCA TXOP, its chief advantage is in the integration of the TXOP sharing mode to the 802.11ac. Using the Markov chain output i.e., transmission probability of a given AC, a mathematical model is derived to estimate the achievable throughput of a given AC, namely, voice (VO), video (VI), best effort (BE), and background (BK). Using this model, it is possible to analyze how the TXOP sharing mechanism could enhance the

inadequate wireless bandwidth utilization while obtaining fairness among the multiple ACs in accessing the channel. Note that this paper only analyses the standard for TXOP and no enhancement is provided.

c) Markov Chain Model-2: In [14], an analytical model is discussed based on Markov chains for a non-saturated IEEE 802.11ac EDCA, supporting TXOP sharing. This model calculates the throughput assuming that the channel is ideal.

Simulation results demonstrate that the analytical model can accurately predict the throughput of the 802.11ac networks under non-saturated operation. As the average packet arrival probability increase, it is observed that the TXOP sharing can greatly improve the system throughput, whereas the throughput of IEEE 802.11ac without TXOP sharing slightly decreases. Another observation is that the TXOP sharing reduces the gap between the high priority AC and low priority AC, compared with the absence of TXOP sharing. Summarizing, these findings imply that the TXOP sharing mechanism has good effect on improving the system performance.

3) Aggregation

a) Comparison of MU-MIMO and Frame Aggregation Multiplexing Schemes: [15] compares the performance of the two downlink user multiplexing schemes: MU_MIMO and frame aggregation in IEEE 802.11ac. If each user's encoded data stream has a similar length, the MU_MIMO achieves better average throughput than frame aggregation. Conversely, if different lengths are present, average throughput of frame aggregation is better than MU_MIMO. In a fast-varying channel, because of the overhead of channel feedback, throughput of MU_MIMO is lesser than frame aggregation. Again, the average throughput of multi-user frame aggregation with STBC is always better than a single-user transmission with STBC because frame aggregation results in increased MAC layer efficiency.

- *Problem:* The multi-user spatial multiplexing combined with packet aggregation can improve system performance considerably. If the transmission times of the frames are different between different SS, the space channel time arises which is a period wherein data is carried by certain SS whereas the others do not have data. Due to space channel time downlink MU-MIMO channels transmission efficiency degrades.

In traditional aggregation, the selection of receiving terminals follows a FIFO policy for packets stored in a transmission buffer. In the setting of the lengths of the frames, APs uniform the number of packets aggregated into the frames on all the SS. However, under the current WLAN environment with various kinds of Mobile Terminals (MTs), the transmission time of the frames is not always equal in all the SS directed to individual receiving MTs. As a result, the space channel time problem arises.

The recent WLANs adopt multi-rate transmissions through Adaptive Modulation and Coding (AMC) to achieve transmission channel adaptation. Moreover, voice communications (VoIP service) is provided in the recent WLANs due to their diversification of communication

services. Because the VoIP service has the limitation of the transmission delay for each packet, it is necessary to give a higher priority to the VoIP packets than data ones when VoIP packets are likely to over an allowable delay limitation. Therefore, we have to consider both multi-rate transmission and VoIP packet transmission in packet aggregation schemes.

b) Aggregation for VoIP: The proposed scheme in [16] introduces the VoIP priority transmission, which performs the preferential selection of VoIP MT if the VoIP packets in the buffer likely exceed the allowable delay limitation. In the proposed wireless frame setting, the APs uniform the transmission times of frames as much as possible on all the SS to the different MTs considering their MCS level. As a result, the proposed aggregation scheme can minimize the space channel time while transmitting the VoIP packets within the allowable delay limitation. The proposed scheme is evaluated by computer simulation to demonstrate its effectiveness under the WLANs with multi-rate transmission providing VoIP services.

Conclusion: The results of computer simulations show that the new scheme improves the system throughput, the space channel time ratio, and maximum delay time for the VoIP packets in the WLANs with multi-rate transmissions and the VoIP service.

c) Fragmented MPDU-Problem: In EDCA TXOP sharing mode, A-MPDU pads must be added to the end of the A-MPDU for each user in order to fit within A-MPDU boundaries. The A-MPDU pads represents non-meaningful content that waste medium resources.

Solution: In [17], A-MPDU with Compressed Block ACK mechanism is modified to be able to contain a fragmented MPDU that is not even a VHT single MPDU. In the place of of A-MPDU pads, fragmented MPDU may be included to fill the length of A-MPDU boundary in EDCA TXOP sharing mode. The VHT Compressed Block ACK mechanism is also re-designed to acknowledge the fragmented MPDUs in the A-MPDU frame.

Conclusion: Using the new mechanism, more frames can be transmitted within the A-MPDU boundaries, leading to improved multi-user throughput. Simulation results indicate a multi-user throughput improvement, above 28% at low data rates and up to 3% at high data rates.

d) Combination of Aggregation and MU-MIMO: [18] proposes a combination of packet aggregation and MU-MIMO transmission to improve the system performance. The technique adopted is (a) RTS/CTS handshake is used to signal the selected STAs and also for channel sounding, (b) quantify the gain in performance that packet aggregation can provide and draw attention to the impact the buffer size can have on the attainable throughput, and (c) decide on buffer size to maximize the performance.

Conclusion: The following observations are made using the simulation results. If the number of STAs is very high, due to the heterogeneity of destinations in the packets present in the queue, complete benefit of packet aggregation is not realized. By increasing the queue size and thereby increasing the scheduling opportunities of a large number of packets at

each transmission, the throughput is enhanced - although it is at the expense of resulting in a higher delay.

e) Efficient Aggregation Scheme - Problem: The frame aggregation procedure consists of two steps in the downlink channels employing MU-MIMO transmission. The first step is a selection of receiving MTs, where an AP selects destination MTs for each SS channel. The second one is a setting of wireless frame, where the AP constructs aggregated MAC data frame in a wireless frame on each SS. To achieve efficient frame aggregation in downlink MU-MIMO transmission, we have to consider transmission efficiency in each SS channel. Different transmission time between frames on different SS causes space channel time, which is a time duration where a part of SS have user data whereas the other SS have no user data. This space channel time leads to the degradation in the transmission efficiency in downlink MU-MIMO transmissions. For reducing the space channel time, the data size based frame aggregation scheme has been proposed. This scheme uniform the amount of data size carried in the wireless frame on each SS channel. Under multi-rate transmissions, however, wireless frame duration (time length) generally differs between SS, and then, the space channel time arises in this scheme.

Moreover, due to first-in first-out (FIFO) based MT selection, it cannot always construct longer wireless frame, leading to large signaling overheads and then low transmission efficiency.

Against these problems, we have previously proposed the wireless frame duration based frame aggregation scheme considering multi-rate transmission for downlink MU-MIMO transmissions. This scheme achieves a reduction of space channel time by uniforming the wireless frame duration considering transmission rate of each receiving MT even under multi-rate transmissions. Signaling overhead reduction is also achieved by adopting receiving MT selection with descend order selection based on wireless frame duration. However, this receiving MT selection tends to prioritize MTs with lower transmission rate over higher one, leading to degradation in throughput performance. In addition, this scheme does not consider frame error occurring in wireless channel, so it also deteriorates transmission efficiency due to excessive retransmissions of errant frames under actual environments with transmission errors.

Solution: Aiming to provide an efficient MAC frame aggregation for downlink MU-MIMO transmissions in IEEE 802.11ac WLANs, [19] has proposed the efficient frame aggregation scheme which enhances system throughput and decreases frame error rate. Here, the receiving MT selection gives higher priority to MTs achieving higher throughput in the next MU-MIMO transmission while reducing signaling overhead, resulting in an improvement in throughput. The wireless frame setting in the proposed scheme, introducing hybrid frame aggregation method, provides lower frame error rate than acceptable level by using frame size adaptation.

This is an efficient frame aggregation scheme is an enhanced version of the previously proposed wireless frame length based frame aggregation scheme.

Conclusions: The transmission performance and its fairness between MTs have been evaluated through system-level simulation. From the results, the proposed scheme greatly improves both performances, compared with the conventional frame aggregation schemes. Accordingly, the proposed frame aggregation scheme is quite effective for performance improvement in downlink MU-MIMO transmissions on IEEE 802.11ac WLANs.

f) Sub-Channel Scheduling - Problem: The MAC layer in current WLANs randomly allocates the entire channel to only one user as a single resource, which, unfortunately, reduces the efficiency of WLANs. One way to significantly improve WLAN performance is to reduce the channel width and create many sub-channels. Based on the user's channel conditions and QoS requirements, the PHY layer resources can be dynamically allocated to several users at the same time.

A fundamental problem is that wireless channels suffer from time-varying losses due to mobility, interference and contention from hidden stations, leading to poor and inconsistent throughput performance. Since 802.11 standards were designed to support multiple types of traffic such as voice, video and data, the provision and control of QoS is a significant task as the QoS requirements differ among the diverse types of users. This makes system design difficult as the queuing delay and the number of re-transmissions have a large influence on the required QoS. The QoS requirement variations of different applications require the development of higher-layer protocols to take the PHY layer design into account when optimizing the wireless network performance. In the 802.11 PHY layer, the QoS for reliable data communications over the lossy wireless channels can be quantitatively characterized by measuring the Bit Error Rate (BER) or Signal-to-Noise Ratio (SNR). OFDM (Orthogonal Frequency Division Multiplexing) has become increasingly popular in modern wireless communications. It divides a spectrum band into many small and partially overlapping signal-carrying frequency bands called subcarriers. The subcarrier frequencies are chosen so that they are orthogonal to one another. Therefore, OFDM can pack subcarriers tightly together without inter-carrier interference, eliminating the need to have guard bands. Sub-channelization in OFDM refers to the grouping of subcarriers into sub-channels.

These sub-channels are assigned to users based on a static or dynamic procedure. The process of mapping subcarriers to sub-channels is called permutation. The basic objective of the mechanisms that define the combination of grouping subcarriers into sub-channels is to increase the frequency reuse ratio.

Permutations are of two kinds: i) contiguous and ii) diversity. Since the wireless channel conditions vary with respect to time and mobility, diversity methods are popular.

The two types of diversity permutations are FUSC (Fully Used Sub-Channelization) and PUSC (Partially Used Sub-Channelization).

Solution: In [20], to maximize the system performance, a new solution with 802.11 PHY and MAC layers is designed

with multiuser channel access and a dynamic sub-channel assignment method based on traffic priority.

The sub-channel scheduling access can be seen as selecting the best set of users to allocate subcarriers according to their channel state information. As data traffic has diverse characteristics and different transmission requirements, an advanced Multimedia-MAC layer should exist to classify outgoing data and dynamically adjust the bandwidth allocation in a shared-medium according to the instant traffic load status so that both network channel utilization and QoS for different types of traffic streams are enhanced dramatically.

In [20], the authors have formulated the resource allocation problem for WLANs and presented a distributed solution using which optimal scheduling in a practical system can be determined. Scheduling the access of flows in a non-interfering manner to avoid packet loss and adapt rates to changing channel conditions are important aspects of QoS in wireless networks. The goal of the rate adaptation scheme is to select the best set of transmission parameters for a given user considering its channel quality.

In particular, the designed approach can be used to support QoS traffic over an OFDM-based network. Assuming knowledge of the instantaneous channel gains for all users, we proposed an adaptive multiuser OFDM sub-channel allocation and modulation method.

A smart solution is designed for high-density wireless environments, which requires the support of hundreds or even thousands of wireless clients in a given area such as airports, campuses, sports stadiums, and concert halls. In addition, efficient resources are allocated for multiuser OFDMs over frequency selective channels with data and user priorities. For WLANs, the design of simple and fast execution time algorithms is critical because of the time-varying behavior of the channel and the requirement of adapting bandwidth allocation to the channel conditions.

Conclusion: The algorithm was evaluated for its performance compared to state-of-the-art systems, using NS-3 under a variety of network conditions. The performance of the proposed method was considered in a multiuser frequency selective fading environment with different time-delay spread values. The results indicate that the recommended solution leads to a real-time aggregation model with an almost stable throughput. In particular, it outperforms conventional multiuser OFDM systems with static TDMA or FDMA techniques, which employ fixed and predetermined time-slots. Therefore, the developed approach could prove to be an efficient solution to optimize the throughput performance of present and next generation WLANs.

C. PHY Layer

1) Precoding and Detection

a) Regularized Block Diagonalization Precoding - Problem: MIMO system can increase the capacity and spectral efficiency without consuming bandwidth greatly. MU-MIMO system can enhance the performance much more. But interference of multiple users must be considered in MU-MIMO system. Interference cancellation is the main goal of

precoding algorithm. Recently, BD precoding is widely employed for the sake of its low computational complexity and ability of eliminating the interference of other users. However, BD precoding doesn't consider the additive noise and it has a problem of limited dimensions antennas.

The MU-MIMO-OFDM based on bit-interleaved coded modulation (BICM) scheme is one of the enhanced air interface key technologies. In MU-MIMO, the transmitted information of different users will cause interference to each other, which can be removed by precoding. Due to its good performance and low complexity, Block Diagonalization (BD) precoding algorithm is widely used in MU-MIMO schemes. However, it also has obvious defects: the ignoring of additive Gaussian noise and the restrictions of antenna dimensions (i.e. number of receiving antennas < number of transmitting antennas).

Solution: In [21], we employ Regularized Block Diagonalization (RBD) with signal space diversity (SSD) to solve these problems. The proposed scheme makes full advantage of time, frequency and space diversity by using constellation rotation and Q-component interleavers to optimize the MIMO-OFDM, channel coding and modulation together.

Conclusion: Simulation results clearly show that the RBD-precoded mechanism surpasses the conventional bit interleaved coded modulation (BICM) scheme without SSD by 3.0 dB SNR gain. Also, the RBD precoding obtains 1.8dB SNR gain than the block Diagonalization (BD) precoding. Compared with BD precoding, RBD precoding not only reduces the interference of other users, but also reduces the effect of additive Gaussian noise. Besides, it eliminates the restrictions of antenna dimensions.

b) Study of Precoding Mechanisms: As precoding and user selection have an impact on MU-MIMO transmission, accurate CSI is required to select users and obtain precoding matrix. In [22], the performance of channel inversion (CI) and BD with limited CSI and compressed feedback are analyzed. The results compare the achievable sum-rate between the user selection metrics and provide the packet error rate (PER) performance under the realistic TGac channel models.

Conclusion: From the simulation results, it is observed that higher data rate can be obtained by greedy user selection algorithm with low complexity precoding schemes. Also, BD shows better PER performance than CI when the compressed feedback is used. Especially for MCS level 9, the quantization error caused error floor at high SNR for both precoding schemes. Note: This paper only analyses the standard for Precoding and no enhancement is provided.

c) MU-MIMO and SU-MIMO precoding: In [23] the precoding mechanisms in MU-MIMO and SU-MIMO are compared assuming perfect CSI at the Transmitter (CSIT) for both high and low correlation channels. Here, optimization of the BD, zero forcing and singular value decomposition based techniques have been proposed using an algorithm that reduces the computational calculations.

Mode switching SNR can be identified by verifying the impact of different precoding mechanisms in SU-MIMO and

MU-MIMO. This SNR measure is a critical metric which aids in selection between SU-MIMO and MU-MIMO and also to meet the demands of all users to an optimum extent. [23] discusses the maximum capacity that can be achieved with Block Diagonalization (BD) and zero forcing (ZF) in a MU-MIMO scenario and singular value decomposition (SVD) based precoding in a SU-MIMO scenario.

Conclusion: The performance analysis show that this optimized algorithm not only brings down the computational efforts drastically but also suffers from very less performance loss. The drop in computation is about 89 %. Only 11% of the original amount of computation is required which is really a great computational reduction. This paper also gives some idea about the mode switching of SU and MU MIMO cases with various receive antenna configurations. It also covers a very typical real time scenario of users having unequal receive antennas and mode switching in this case. In a low correlation channel the mode switching occurs around 10 dB while it is around 15 dB. For a high correlation channel, the mode switching occurs at 20 dB. Once this mode switching point is estimated, it becomes easier for the MAC layer to select SU-MIMO or MU-MIMO based on the SINR values.

d) Precoding with Detection Techniques: The performance improvements under realistic channel conditions is measured when BD and CI are paired with various MIMO detection techniques.

In [24], the bit error rate (BER) and packet error rate (PER) performance are examined. It is observed that high performance MIMO decoders such as LRA MMSE decoder, improve the uncoded BER performance of the BD precoding. However, it does not improve the uncoded BER performance of the CI precoding. Because the CI precoding is an inverse of the channel matrix, the effective channel matrix becomes the diagonal matrix at the receiver side. On the other hand, the effective channel matrix of the BD precoding is a block diagonal matrix. Hence MIMO decoders can take advantage of the diversity present in the inter stream interference within a single user.

When the channel model B and D are compared and the PER performance is measured, it is seen that the channel model D is better than the channel model B. The channel model B is high correlated, the wide distribution of the singular values of the inverse increases the precoded signal power at the transmitter, and noise enhancement at the receiver side.

We considered the PER performance of each MU-MIMO transmission methods when MIMO decoder is changed. Between the Linear MMSE and the V-BLAST MMSE decoders, the PER performance measured in the Linear MMSE is better than in the V-BLAST MMSE. While the uncoded BER performance of V-BLAST MMSE is better than Linear MMSE, performance degradation caused by error propagation limits the performance of coded V-BLAST MMSE. Also, we observe the substantial improvement of the PER performance of the BD precoding when using the LRA MMSE decoder.

Conclusion: From the simulation results, it is seen that (1) the PER performance of the BD precoding can be improved by the MIMO decoder and (2) the BD precoding is more effective compared to CI precoding.

e) SIC MIMO detectors with LR techniques: The challenges and concerns related to the application of lattice reduction (LR) techniques in IEEE 802.11ac systems in successive interference cancellation (SIC) receivers in SU and MU OFDM MIMO transceivers are investigated in [25].

The goal of [25] is to investigate the following hypothesis: the implementation of SIC MIMO detectors with LR techniques is a viable technique in order to obtain significant power gains when realistic operational aspects are taken into account. Finally, a comparative performance evaluation of the following OFDM MIMO detectors is undertaken: (1) MMSE; (2) ordered successive interference cancellation MMSE (OSIC/MMSE); (3) LR Zero-Forcing (LR ZF); (4) LR MMSE; (5) LR Zero-Forcing SIC (LR ZF-SIC); (6) LR MMSE-SIC.

Conclusion: The simulation results, validated using first-order techniques, assume realistic operational conditions faced in IEEE 802.11ac WLANs, such as, temporal autocorrelation synchronization algorithm, least square (LS) MIMO channel estimation scheme, spatial-correlated and frequency selective TGac channel models. It is demonstrated that the application of LR MMSE-SIC MIMO detectors with hard-decision Viterbi decoding in IEEE 802.11ac WLANs allows substantial power gains in relation to linear LR MMSE MIMO detectors over 8x8 MIMO channels in a SU scenario. On the other hand, these detectors allow a power gain of only 1 dB for 3x3 MIMO channels for the SU environment and no expressive power gains when a MUMIMO system with 4 transmit antennas, 2 receive antennas per user and 2 users is considered. Second, we verify that the OSIC MMSE detectors present severe performance degradation due to error propagation when realistic TGac MIMO channels models are simulated.

f) Precoding Simulation Framework: In [26], a framework to analyze and design the PHY layer of IEEE 802.11ac wireless LANs and focusing on MU operation is explained. The performance of CI, regularized CI and BD precoding mechanisms with ZF and MMSE MIMO detectors is evaluated over different configurations of 802.11 Task Group n (TGn) and TGac channel models.

Conclusions: A IEEE 802.11ac WLAN PHY simulator is first presented and validated. It is concluded that the performance of MU-MIMO 802.11ac systems presents a similar performance for both TGn and TGac channel models. Finally, a unified performance evaluation of five different transceiver MU-MIMO architectures tailored for IEEE 802.11ac systems was carried out: BD+ZF, BD+MMSE, CI+ZF, CI+MMSE and RI+MMSE. It is seen that for low SNR region the best performance is obtained with RI-MMSE schemes, while there is no significant differences on the attainable performance into high SNR regime.

g) Detection Mechanisms: [27] proposes to detect the SS in 802.11ac device using (2×2) , (4×4) , (8×8) MU-MIMO

systems using some of the MIMO detection algorithms. Here, the objective is to evaluate the effect of Detectors/Interference Canceller (IC) like ZF, MMSE and the proposed ZF-Successive IC (SIC) with Optimal Peak Power Ordering (OPPO), ZF-SIC-OPPO for WLAN on the performance of 802.11ac standard in a Rayleigh fading channel.

Conclusions: The Detection and IC techniques like ZF, MMSE and ZF-SIC-OPPO were simulated using number of antennas in the Rayleigh fading environment for the IEEE 802.11ac standard. The results of the proposed ZF-SIC-OPPO technique was compared to the existing method. The OPPO method for ZF-SIC gave an improvement in both the SNR and BER. ZF-SIC-OPPO detector outperformed ZF and MMSE with the lowest BER for a MIMO (8×8) 802.11ac system.

2) PHY Sounding

a) Multi-User Transmission enhancer(MUTE): In [28], the evaluation of a downlink MU-MIMO sounding protocol called MUTE is presented. In a practical system, the beamformer should compromise between the frequency of sounding and CSI accuracy. MUTE decouples the sounding set selection (used to collect CSI) from the transmission set selection, thereby helping in reducing the sounding overhead and simultaneously selecting the best users. The decoupling also offers the choice of sounding a particular user or not, separately from the set of users in the list meant for the next transmission. This, consequently, reduces overhead associated with sounding by exploiting the presence of users with stable channels. At the same time, adequately accurate data about channel statistics of associated users is given to the AP. Thus, the AP can pick the user group that maximizes an objective function such as achievable rate or a fairness criteria.

Conclusion: Using test bed experiments, it is shown that MUTE can decrease the sounding overhead appreciably while minimizing data rate losses resulting from inaccurate channel estimation. MUTE takes advantage of channel statistics to the multiple users to assess if a particular user's channel will stay acceptably stable, thus permitting the AP to prevent sounding before a MU-MIMO transmission.

b) Comprehensive Sounding Control Scheme: The sounding overhead may severely degrade the performance of a WLAN. In [29], a sounding control scheme for IEEE 802.11ac MU-MIMO is proposed which considers broadly the sounding control needs of the network environment, including channel coherence times, nodes' DL traffic loads, DL SNRs, etc.,. The sounding node set and sounding interval to maximize the long-term expected MU-MIMO throughput gain are jointly determined.

Although all the mobile nodes are in the same space, different wireless links experience different propagation environment variation due to mobility, behavior of nearby people, and so on. For example, some wireless links experience stationary propagation environments, such that their channel coherence times are several hundreds of milliseconds. On the other hand, some of the other wireless links are moderately time varying, such that their channel coherence times are several tens of milliseconds. Finally, the

remaining wireless links vary quite fast, such that their channel coherence times are several milliseconds. Thus, MIMO channel measurement are conducted in practical WLAN environments and the performance of the mechanism is evaluated by employing the real channel data traces.

Conclusion: The proposed scheme is shown to achieve remarkable performance improvement over the existing schemes which considers channel coherence times only.

Problem: In MU-MIMO, the AP selects both the user set and the mode (number of transmit and receive antennas) and after completing sounding and before commencing transmission. Thus, optimal user groups are selected given full CSI of a set of potential receivers (which is a major overhead) or by depending on intermittent probing or stale CSI to estimate the full CSI. The measured CSI can easily become stale between packets, making data collected from previous transmissions not useful in prediction of future environments.

c) Pre-sounding User and Mode selection Algorithm (PUMA): In [30], PUMA, an algorithm for selecting mode and user prior to sounding is designed, implemented and evaluated. PUMA, even without CSI, (i) exploits theoretical properties of MUMIMO system scaling with respect to mode, (ii) characterizes the relative cost of each potential mode, and (iii) estimates per-stream transmission rate and aggregate throughput in each mode for a potential user set. After PUMA chooses the appropriate mode and user group, the selected protocol's sounding mechanism is applied on the intended user subset to carry out the transmission.

The PUMA algorithm is executed before the start of any MU-MIMO transmission with only a priori information; i.e., without any information gathered from previous multi-stream communication or channel sounding.

Conclusion: It is seen that, on average, PUMA selects the mode and group that achieves an aggregate rate within 3% of the throughput of what would have been obtained by sounding all users.

VI. CONCLUSIONS AND FUTURE WORK

Transmit beamforming and MU MIMO are key features in the 802.11ac WLAN standard. Theoretical background is provided initially to get an understanding of these mechanisms. Approaches adopted in the literature for enhancing these mechanisms are next studied. The focus has been on selecting papers showcasing the range of approaches used. The majority of suggestions have been in the Aggregation and TXOP areas of the MAC layer and in Precoding, Sounding and detection mechanisms of the PHY layer.

Since the next WLAN standard, IEEE 802.11ax will be further enhanced with Uplink MU-MIMO, the recommendations, lessons learnt and studies conducted in the papers listed here will prove as useful pointers in the design of the new standard.

References

- [1] Calvin Iloki, Moustapha Mbaye, Moussa Diallo, "Feedback of the channel information for transmit beamforming in WLAN," 9th European Conference on Antennas and Propagation (EuCAP), 2015, IEEE Xplore.
- [2] Moussa Diallo, Maryline Hélar, Laurent Cariou, "A limited and efficient quantized feedback for IEEE 802.11n evolution," ICT 2013, DOI: 10.1109/ICTEL.2013.6632089, IEEE Conference Publications.
- [3] Pengfei Xia, Monisha Ghosh, Hanqing Lou, Robert Olesen, "Improved transmit beamforming for WLAN systems," 2013 IEEE Wireless Communications and Networking Conference (WCNC), IEEE Xplore.
- [4] Zhensheng Zhang, "DTRA: directional transmission and reception algorithms in WLANs with directional antennas for QoS support," IEEE Network, 2005, Vol 19, no 3, pp 27 - 32.
- [5] Di Kong, Evangelos Mellios, Geoffrey Hilton, Angela Doufexi, Andrew Nix, "The Impact of Regulatory Transmit Power Constraints on the Relative Performances of Wi-Fi Beamforming and Antenna Selection," 2015 IEEE 12th Malaysia International Conference on Communications (MICC), IEEE Xplore.
- [6] Heejung Yu, Heeyong Lee, "Comparison of MIMO schemes in IEEE 802.11ac under time-varying channels: analytical approach," 2014 IEEE Fourth International Conference Consumer Electronics - Berlin (ICCE-Berlin), IEEE Xplore.
- [7] Ada S. Y. Poon, Mazhareddin Taghivand, "Supporting and Enabling Circuits for Antenna Arrays in Wireless Communications," Proceedings of the IEEE, pp 2207 - 2218.
- [8] Osama Aboul-Magd, Uikun Kwon, Youngsoo Kim, Chunhui Zhu, "Managing downlink multi-user MIMO transmission using group membership," 2013 IEEE 10th Consumer Communications and Networking Conference (CCNC), pp 370 - 375.
- [9] Chunhui Zhu, Anirudh Bhatt, Youngsoo Kim, Osama Aboul-magd, Chiu Ngo, "MAC enhancements for downlink multi-user MIMO transmission in next generation WLAN," 2012 IEEE Consumer Communications and Networking Conference (CCNC), pp 832 - 837.
- [10] Chunhui Zhu, Chiu Ngo, Anirudh Bhatt, Youngsoo Kim, "Enhancing WLAN backoff procedures for downlink MU-MIMO support," 2013 IEEE Wireless Communications and Networking Conference (WCNC), pp. 368 - 373.
- [11] Baofeng Ji, Kang Song, Chunguo Li, Yongming Huang, Luxi Yang, "Throughput enhancement for VHT WLANs based on two-level network allocation vector," 2012 IEEE Globecom Workshops, pp. 881 - 885.
- [12] Mohand Yazid, Adlen Ksentini, Louiza Bouallouche-Medjkoune, Djamil Aïssani, "Enhancement of the TXOP sharing designed for DL-MU-MIMO IEEE 802.11ac WLANs," 2015 IEEE Wireless Communications and Networking Conference (WCNC), pp. 908 - 913.
- [13] Mohand Yazid, Adlen Ksentini, Louiza Bouallouche-Medjkoune, Djamil Aïssani "Performance Analysis of the TXOP Sharing Mechanism in the VHT IEEE 802.11ac WLANs," IEEE Communications Letters, 2014, Vol: 18, Issue: 9, pp. 1599 - 1602.
- [14] Zhiqun Hu, Xiangming Wen, Zhaoxing Li, Zhaoming Lu, Wenpeng Jing, "Modeling the TXOP Sharing Mechanism of IEEE 802.11ac Enhanced Distributed Channel Access in Non-Saturated Conditions," IEEE Communications Letters, 2015, Vol 19, Issue: 9, pp. 1576 - 1579
- [15] Jiyoung Cha, Hu Jin, Bang Chul Jung, Dan Keun Sung, "Performance comparison of downlink user multiplexing schemes in IEEE 802.11ac: Multi-user MIMO vs. frame aggregation," 2012 IEEE Wireless Communications and Networking Conference (WCNC), pp. 1514 - 1519.
- [16] Yoshihide Nomura, Kazuo Mori, Katsuhiko Naito, Hideo Kobayashi, "High efficient packet aggregation scheme for multi-rate and VoIP packet transmissions in next generation MU-MIMO WLANs," 2014 International Conference on Advanced Technologies for Communications (ATC 2014), pp. 517 - 521.
- [17] Chulho Chung, Taewook Chung, Byungcheol Kang, Jaeseok Kim, "A-MPDU using fragmented MPDUs for IEEE 802.11ac MU-MIMO WLANs," 2013 IEEE International Conference of IEEE Region 10 (TENCON 2013), pp. 1 - 4.

- [18] Boris Bellalta, Jaume Barcelo, Dirk Staehle, Alexey Vinel, Miquel Oliver, "On the Performance of Packet Aggregation in IEEE 802.11ac MU-MIMO WLANs," *IEEE Communications Letters*, 2012, Vol 16, Issue 10, pp. 1588 - 1591
- [19] Yoshihide Nomura, Kazuo Mori, Hideo Kobayashi, "Efficient Frame Aggregation with Frame Size Adaptation for Next Generation MU-MIMO WLANs," 2015 9th International Conference on Next Generation Mobile Applications, Services and Technologies, pp. 288 - 293.
- [20] Arafet Ben Makhoul, Mounir Hamdi, "Dynamic Multiuser Sub-Channels Allocation and Real-Time Aggregation Model for IEEE 802.11 WLANs," *IEEE Transactions on Wireless Communications*, 2014, Vol 13, Issue 11, pp. 6015 - 6026
- [21] Zhanji Wu, Xiang Gao, Yongtao Shi, "A novel MU-MIMO-OFDM scheme with the RBD precoding for the next generation WLAN," *MILCOM 2015 - 2015 IEEE Military Communications Conference*, pp. 565 - 569
- [22] Woochang Lim, Gibum Kim, Jinwoo Kim, Hyuncheol Park, Keunmoo Lee, Hanyoung Jang, "Performance of linear precoding and user selection in IEEE 802.11ac downlink MU-MIMO system," 2014 IEEE Wireless Communications and Networking Conference (WCNC), pp. 925 - 929
- [23] A P Theeksha, S. Srikanth, "Performance analysis and mode selection of SU-MIMO and MU-MIMO in 802.11ac," 2013 International Conference on Recent Trends in Information Technology (ICRTIT), pp. 732 - 737
- [24] Daisuke Nojima, Leonardo Lanante, Yuhei Nagao, Masayuki Kurosaki, Hiroshi Ochi, "Performance evaluation for multi-user MIMO IEEE 802.11ac wireless LAN system," 2012 14th International Conference on Advanced Communication Technology (ICACT), pp. 804 - 808
- [25] Roger Pierre Fabris Hoefel, "IEEE 802.11ac: On performance of lattice-reduction successive interference cancellation OFDM MIMO receivers," 2014 International Conference on Advanced Technologies for Communications (ATC 2014), pp. 691 - 696
- [26] Roger Pierre Fabris Hoefel, "Multi-user OFDM MIMO in IEEE 802.11ac WLAN: A simulation framework to analysis and synthesis," 2013 IEEE Latin-America Conference on Communications, pp. 1 - 6
- [27] Syed Moinuddin Bokhari B, Karthika S, Bhagyaveni M A, "Optimal Peak Power Ordering (OPPO) in ZF-SIC for IEEE 802.11ac industrial standard," 2015 IEEE International Conference on Electrical, Computer and Communication Technologies (ICECCT), pp. 1 - 6
- [28] Oscar Bejarano, Eugenio Magistretti, Omer Gurewitz, Edward W. Knightly, "MUTE: Sounding inhibition for MU-MIMO WLANs," 2014 Eleventh Annual IEEE International Conference on Sensing, Communication, and Networking (SECON), pp. 135 - 143
- [29] Junsu Choi, Sunghyun Choi, Kwang Bok Lee, "Sounding Node Set and Sounding Interval Determination for IEEE 802.11ac MU-MIMO," *IEEE Transactions on Vehicular Technology*, 2016, Vol 65, Issue: 12, pp. 10069 - 10074
- [30] Narendra Anand, Jeongkeun Lee, Sung-Ju Lee, Edward W. Knightly, "Mode and user selection for multi-user MIMO WLANs without CSI," 2015 IEEE Conference on Computer Communications (INFOCOM), pp. 451 - 459..

Threshold Modeling for Cellular Logic Array Processing based Edge Detection Algorithm

Surender Singh^{1,3}, Ajay Prasad¹, Kingshuk Srivastava¹, Suman Bhattacharya²

¹Center for Information Technology, UPES, Dehradun, India

²IPR Management Services, TCS, Bhubneswar, India

³Ambala College of Engg. & Applied Research, Devsthal, Ambala, India

surendahiya@gmail.com

Abstract--Edge detection is one of the basic methods for various image processing functions such as image analysis, image segmentation, pattern recognition etc. This is a process to find out discontinuity of intensity in image. If some or all neighboring pixels form a convex region of same gray level intensity, then there exists an edge. In order to distinguish between different level of intensities in edge detection, a threshold is required which is usually different for different type of images due to variation in level of intensities. This paper proposes and compares two methods namely global and local thresholding to model the value of threshold through quantitative empirical method for cellular logic array processing based edge detection method. The performance of the modeled algorithms is measured by F1-score, recall-precision break-even-points and performance ratio. Experimental results show that the local thresholding approach gives slightly better F1-score and performance ratio for all scenarios of six Berkeley Segmentation Database images and respective ground truths. It has also been found that best percentage of threshold value can be determined in a better way by break-even-point rather than by best F1-score. The proposed approach reduces false edge detection and make threshold selection automatic for every scenario.

Key Words--Cellular Logic Array processing, Edge Detection, Threshold modeling.

I. INTRODUCTION

An edge, within an image, is defined as a sudden change or discontinuity in the intensity of a pixel. It is regarded as a boundary between the object and its background. The process of edge detection characterizes an image into important features which can be further used in image processing functions of higher level. An ideal edge detection process is that which identifies less number of false edges or double edges and maximum number of real edges [1]. The edge detector should perform equally good in different environments and contexts.

Most of edge detection programs work on pixel level by identifying convex region of same gray level intensity and extracting edges by isolating pixel having differing level of intensity by thresholding. Two different images may be shot in quite different setup and they can differ in background intensities greatly due to variation in the reflectance, illumination, orientation, and depth of scene surfaces necessitating different values of threshold in edge detection process. This gives an idea that instead of fixing a single value for all types of images and scenarios or empirically identifying threshold values each time during edge detection process; a

formula must be devised which is dependent on background intensities so that good quality edge detection can materialize every time. This paper presents a model toward this direction.

Edge detection algorithm used for modeling in this paper is based on cellular logic array processing which works in quite different manner than standard algorithms such as Sobel, Pretwit's and Canny's methods. Cellular Logic Array processing (CLAP) is based on cellular automata which are homogeneous structures or iterative cells of ploy-dimensions. In cellular automaton, each cell can have a finite state and a neighborhood defined by the number of cells it surrounds. Initially at time $t=0$, a state is assigned randomly or seeded to each of cells and then a new generation of cells are evolved by following some rules. Typically, the updating rule is same for each cell and does not change over time, and is applied to the whole grid simultaneously. So, the CLAP is essentially a computer algorithm that exhibits discreteness in space and time that operates on arrays of elements. The concept was applied to scores of applications where time and space can be easily divided homogeneously. Edge detection is one such application.

This paper is distributed in the following way. Section I introduces the requirement of modeling the value of thresholding followed by Section II which discusses different edge detection methods and related works. Section III proposed a model for deciding threshold values for cellular logic array processing based edge detection method. Section IV describes the experimental setup for empirically evaluation of threshold values which is followed by comparative results and discussion in section V. Finally, the paper is summed up in concluding part.

II. EDGE DETECTION METHODS IN LITERATURE

Edge detection is one of the most basic procedures used in image processing application. Because of different variety of objects having different colors, texture and shapes, there are numerous object detection methods researched and discussed in literature during past years [4, 5, 9, 12]. Traditional algorithms can be classified into two categories:

i) *First Order Derivative Based Edge Detection*, in which edges are detected by computing the first derivative of the image. The magnitude of the gradient decides the sharpness of edge and the gradient vector gives the direction of maximum rate of change. Although the sharpening of image through first

gradient unravel the finer details but it also enhances the noise in the image. Another problem associated with first derivative is double edges. Most basic edge detectors in these categories are Roberts [19], Sobel [22] and Prewits [14]. These edge detection algorithms can be enhanced by post-processing techniques such as non-maximum suppression, Hysteresis Thresholding and non-major edge points removal [1] to get strong edges in the image.

ii) *Second Order Derivative Based Edge Detection (Laplacian)*, methods such as Laplacian of Gaussians (LOG), Difference of Gaussians (DOGs) [6] which searches for zero crossings in the second derivative of the image to find edges. These methods are limited by their huge complexity of time and sensitivity to noise.

Many attempts were made to extract edges with the help of morphological operations [11, 18, 26]. Neural Networks and fuzzy techniques were also devised for edge detection [3, 20]. Gao *et al* [24] proposed a hybrid method by combining Sobel edge detection operator with wavelet de-noising for edge detection in images containing white noise. Mohamed A. El-Sayed [10] proposed an entropy based high quality edge detection method for decreasing computation time. Priyadarshini *et al* [15] proposed an automatic threshold based edge detection method based on simple arithmetic and logic operations which claimed to perform better than Sobel's method and requiring less computation. Neha Mathur *et al* [8] developed a K-means segmentation method to obtain a local threshold values through histogram bins and cluster **center** for Sobel operator. Although they do not estimate time but it seems too heavy on real time processing.

Cellular automata in image processing applications was used first time in 1974 by Duff *et al.* [2] when he developed a hardware implementation of cellular logic array (CLIP3) for the use of image processing, intended for fast processing. But its' progress was too slow due to heavy computing requirements of image processing. EG Rajan in 1993 proposed software based *cellular automata* framework for high-throughput image processing [17]. This work assumed digital image as *cellular array* configuration and processing algorithm as *evolution* (update rule) of the automaton. This work demonstrated that cellular automata can be effectively used for various basic image processing operations such as thinning, edge detection, segmentation and morphological operations but failed to provide an adaptive thresholding for consistent performance across different types of images. In 2002, Popovici and Popovici [13] used two dimensional cellular automata for de-noising and edge detection applications. Both of these work claimed that the CLAP performance is better as compared to the traditional tools such as SUSAN [21]. Tapas Kumar *et al* [23] compared cellular automata based edge detection with standard methods but without any quantitative evidence.

III. OBJECT DETECTION FRAMEWORKS IN CELLULAR LOGIC ARRAY PROCESSING

Several edge detection algorithms use neighborhood principles for digital images to detect edges by locating edge points in the form of abrupt changes in gray levels. *The cellular logic array processing based algorithm also uses neighbourhood principle, but in a different way. Instead of finding points of abrupt changes in gray levels, it locates the regions of image where gray levels remain static.* In this method every pixel in digital image is investigated for its intensity difference with its surrounding neighbors as in cellular logic array and a uniform rule is defined to work on its intensity and that rule is: "if the difference between maximum and minimum intensity over the neighbourhood region is less than a threshold than the pixel value is changed to 0 otherwise it is changed to 255". Threshold value is chosen as the percentage value of Mean/Median Intensity Value of an image.

For practical implementation, the target digital image is scanned by a 3 x 3 pixels' window of five pixels forming convex region to find maximum and minimum gray level. If the difference of maximum and minimum intensities is less than a threshold value, then intensity of the center pixel is changed to 0 marking a uniform intensity region. This procedure is repeated for every pixel of the image resulting into creating uniform regions having similar gray level. Uniform intensity levels are labeled as background pixels which results into edge detection in the form of differing intensity level pixels. The pseudo code for global thresholding and local threshold procedure is given in figure 1 and 2 respectively.

```
S1: Find the Mean Intensity Value  $I_{gm}$  of image
S2: Set threshold  $Th_g = \alpha I_{gm}$ ;  $\alpha$  varies between 0 and 1
S3: Create a 3*3 neighborhood scanning structure consisting of only 5-neighborhood pixels
S4: for every central_pixel (i, j) of image {
    S4.1: find  $G_{min} = \text{Min}(5\text{-neighborhood structure})$ 
    S4.2: find  $G_{max} = \text{Max}(5\text{-neighborhood structure})$ 
    S4.3: if  $\text{diff}(G_{max}, G_{min}) < Th_g$  then central_pixel (i, j) = 0
        else Move structure to the next pixel as central pixel.
    end for
```

Fig. 1. The Global Threshold based CLAP Algorithm for edge detection

```
S1: Create a 3*3 neighborhood scanning structure consisting of only 5-neighborhood pixels
S2: for every central_pixel (i, j) of image {
    S2.1: find the Mean Intensity Value of 5-neighborhood pixels, set  $Th_l = \alpha I_{lm}$ ;  $\alpha$  varies between 0 and 1
    S2.2: find  $G_{min} = \text{Min}(5\text{-neighborhood structure})$ 
    S2.3: find  $G_{max} = \text{Max}(5\text{-neighborhood structure})$ 
    S2.4: if  $\text{diff}(G_{max}, G_{min}) < Th_l$  then central_pixel (i, j) = 0
        else Move structure to the next pixel as central pixel.
    end for
```

Fig. 2. The Local Threshold based CLAP Algorithm for edge detection

IV. THRESHOLD MODELING AND EXPERIMENTAL SETUP

As discussed in section I, threshold plays a great deal in determining the quality of edges. Adaptive threshold values can be decided by taking Global Threshold as the percentage value of *Mean Intensity Value* of an image i.e. Global Mean I_{gm} . We need to find out the optimal percentage value for proposing a model for automatic global threshold values for quality edge detection.

$$Th_{global} = \alpha \times I_{gm} \quad (1)$$

Another threshold can be a local value taken as the percentage of a local mean value from 5-neighborhood of five pixels which are evaluated for finding maximum and minimum values in CLAP algorithm. This is taken as

$$Th_{local} = \alpha \times I_{lm} \quad (2)$$

Six Berkeley segmentation database (BSD) images are taken for the empirical evaluation. There are various groundtruths for a single image in BSD data set, [7] but only one groundtruth-extractor image is taken to maintain the consistency in evaluation. For every image, hundred values of precision and recall are calculated using extracted edges and

corresponding groundtruths by varying global threshold or local threshold through percentage value α . Precision and Recall based F1-score, performance ratio (PR) and precision recall break-even-points (PR-BEP) are used to find out the optimum value of α separately for both methods. Precision, which is also called positive predictive value, is the percentage of retrieved instances that are relevant and on the other side recall (sensitivity) is percentage of relevant instances that are retrieved. Both in combined form give a better measure which is called F1-score. This is given by the following equation:

$$F1 = \frac{2 * Precision * Recall}{(Precision + Recall)} \quad (3)$$

Another popular measure for a classifier is a *Precision Recall Break-Even-Point*. Normally precision and recall are opposite to each other. At threshold zero, recall is at unity but as threshold increases it start decreasing and precision starts increasing. PR-BEP is that threshold point, where precision and recall are equal. Many papers reported that it is a better measure than F1-score [25]. The local and global threshold based CLAP methods are also compared by Average Recall (AR) and Average Precision (AP). Experiments are done using OPENCV software. The CLAP algorithm is developed using algorithms shown in figure 1 and figure 2.

TABLE 1. Different Measures extracted by CLAP algorithm for Global and Local Threshold when applied on six BSD images

BSD Image	Global Threshold						Local Threshold					
	No.	AR	AP	Mean F1-score	Mean PR	α Value for best measure α_{f1m}	α Value for PR-BEP α_{bep}	AR	AP	Mean F1-score	Mean PR	α Value for best measure α_{f1m}
35010	0.273	0.539	0.287	0.234	0.07	0.17	0.294	0.509	0.297	0.243	0.08	0.22
42049	0.235	0.576	0.274	0.225	0.03	0.11	0.380	0.553	0.403	0.365	0.04	0.27
118035	0.219	0.525	0.248	0.190	0.05	0.11	0.222	0.429	0.245	0.190	0.06	0.12
135069	0.255	0.645	0.312	0.272	0.05	0.8	0.316	0.628	0.370	0.330	0.08	0.12
189011	0.154	0.432	0.158	0.103	0.08	0.10	0.190	0.386	0.186	0.119	0.02	0.21
189080	0.175	0.474	0.169	0.110	0.10	0.13	0.233	0.373	0.200	0.137	0.19	0.22

V. RESULTS AND DISCUSSION

Table 1. gives the results of CLAP algorithm for taking threshold from global average of image and another from local average of 5-neighborhood. Average Recall (AR) and Average Precision (AP) measures and Mean Performance ratio for both methods are displayed for evaluation. The local thresholding based CLAP method fares well as compared to global thresholding CLAP in all measures except in precision measure. From this fact, it can be inferred that although global thresholding helps in better retrieval of pixels that are relevant, local threshold also retrieved higher fraction of relevant instances. So, local thresholding is better than global thresholding, as it is less noisy. This can be easily verified from qualitative analysis of images in figure 3 by visual inspection.

It is also found that there is considerable difference between the best values of alpha for highest F1-score (α_{f1m}) and for PR-BEP (α_{bep}) for each method and image. In figure 3, columns (d) to (g) shows the edge detection for all six images for these two best values of alpha and clearly it can be established that PR-BEP measure works better than F1-score in deciding the threshold value for automatic edge detection.

Finally, for different images, it is found that there is greater spread of alpha values for both measures F1-score and PR-BEP. Although a single value can be deduced by taking average of α_{bep} of different images for automatic thresholding in local thresholding and global thresholding based CLAP, but we need to work further on this area for better results. A hybrid of global and local threshold may give better result.



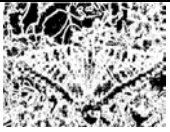
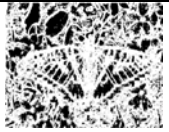
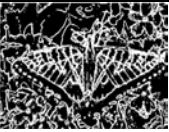
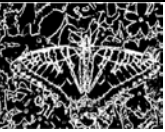




















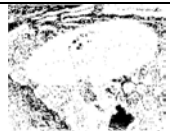









(a) BSD Sr. No.	(b) BSD Image	(c) Ground Truth	(d) CLAP Edge Detection with Global Threshold with α_{f1m}	(e) CLAP Edge Detection with Local Threshold with α_{f1m}	(f) CLAP Edge Detection with Global Threshold with α_{bep}	(g) CLAP Edge Detection with Local Threshold with α_{bep}
35010						
42049						
118035						
135069						
189011						
189080						

Fig 3. Comparatively evaluation for CLAP Edge Detection with Global Threshold and CLAP edge detection with Local Threshold when best alpha is taken based on F1-score and PR-BEP.

VI. CONCLUSION

This paper proposes an empirical evaluation method for determining the automatic thresholding value for the CLAP based edge detection from an image. Global thresholding can be assessed from image global mean while local thresholding can be determined separately for each pixel by taking the mean intensity value of local region surrounding the pixel. Local thresholding based CLAP has given slightly better empirical results. Six Images of BSD data set is taken for training and evaluation purpose. Threshold value is modeled as a percentage value of global mean or local mean. Two

measures F1-score and PR-BEP are used to determine the best thresholding method. Alpha value which are percentage of global mean and local mean are determined for best F1-score and PR-BEP. From experiments, it has been found that PR-BEP is a better evaluation method, at least in our case. Although a single value of alpha can be determined for automatic edge detection for all images but wide spread of these values may limit us in this approach.

ACKNOWLEDGMENT

We thank Dr. E. G. Rajan, Founder Director, Pentagram Research Centre (P) Limited, Hyderabad, who provided

insight and expertise on cellular logic array that greatly assisted the research.

REFERENCES

- [1]. J. Canny, "A computational approach to edge detection", *IEEE transactions on pattern analysis and machine intelligence PAMI-8* (6) pp: 679-698, 1986.
- [2]. M. J. B. Duff, D. M. Watson, T. J. Fountain and G. K. Shaw, "A cellular logic array for image processing," *Pat. Recog.* 5, 229-234, 1973.
- [3]. R. Ezhoosh Hamid, "Fast Fuzzy Edge Detection". *Pattern Recognition and Machine Intelligence Lab Systems Design Engineering*, University of Waterloo Waterloo, Ontario, N2L 3G1, Canada.,2010
- [4]. S.Lakshmi and V. Sanka Ranarayanan, "A study of Edge Detection Techniques for Segmentation Computing Approaches," *IJCA Special Issue on "Computer Aided Soft Computing Techniques for Imaging and Biomedical Applications"* CASCT, 2010.
- [5]. Lee Tzu- HengHenry, "Edge Detection Analysis", *IJCSI International Journal of Computer Science Issues*, Vol. 5, Issue 6, No 1, September 2012.
- [6]. D. Marr andE. Hildreth "Theory of Edge Detection," *Proceedings of the Royal Society of London. Series B, Biological Sciences*, 207 (1167): 187-217, 1980.
- [7]. D. Martin, C. Fowlkes,D. Tal and J. Malik, "A Database of Human Segmented Natural Images and its Application to Evaluating Segmentation Algorithms and Measuring Ecological Statistics," *Proc. 8th Int'l Conf. Computer Vision*, vol. 2, pp. 416-423, July 2001.
- [8]. N. Mathur S. Mathur andD. Mathur, "A Novel Approach to Improve Sobel Edge Detector," 6th International Conference On Advances In Computing & Communications, ICACC 2016, Cochin, India,6-8 September 2016,
- [9]. M. Basu, "Gaussian Based Edge -Detection Methods: A Survey", *IEEE Transactions on System, man, and cybernetics part c: Application and Reviews*, Vol. 32, No. 3, August 2002.
- [10]. A. Mohamed El- Sayed, "A New Algorithm Based Entropic Threshold for Edge Detection in Images", *IJCSI International Journal of Computer Science Issues*, Vol. 8, No 1, September 2011.
- [11]. C. NagaRaju, "Morphological Edge Detection Algorithm Based on Multi - Structure Elements of Different Directions", *IJICT*, Vol. 1 No: 1, May 2011.
- [12]. G. Papari andN. Petkov, "Edge and line oriented contour detection: State of the art," *Image and Vision Computing* 29, 79 - 103, 2011.
- [13]. A. Popovici and D. Popovici, "Cellular automata in image processing," in *Proceedings of the 15th International Symposium on the Mathematical Theory of Networks and Systems*, D. S. Gilliam and J. Rosenthal, Edition; electronic proceedings, pp. 1-6,2002
- [14]. J.M.S.Prewitt., "Object Enhancement and Extraction," In "Picture Processing and Psychopictorics", Academic Press,1970
- [15]. S. Priyadarshini andG. Sahoo, "A New Edge Detection Method based on additions and Divisions," *International Journal of Computer Applications* (0975 - 8887) Volume 9, No.10, November 2010.
- [16]. S. Qiucheng, H. Yueqian, T. Qingchang, L. Chunjing and L. Ming, "A robust edge detection method with sub-pixel accuracy", *Optik - International Journal for Light and Electron Optics*, Volume 125, Issue 14, Pages 3449-3453, 2014
- [17]. E. G.Rajan, "Cellular logic array processing techniques for high-throughput image processing systems", *Trends in Computer Vision*, Sadhana, Volume 18, Issue 2, pp 279-300, June 1993
- [18]. M. RamaBai, V. Krishna, and J. SreeDevi, "A new Morphological Approach for Noise Removal cum Edge Detection," *IJCSI International Journal of Computer Science Issues*, Vol. 7, Issue 6, November 2010.
- [19]. L. G. Roberts, "Machine Perception of Three-Dimensional Solids". Massachusetts Institute of Technology. Department of Electrical Engineering, Massachusetts Institute of Technology, Dissertation, 1963
- [20]. N. G. See, and C. Khuehiang, "Edge Detection using supervised Learning and voting scheme," *Nanyang Technological University, National university of Singapore*, Singapore, 2010.
- [21]. S. M. Smith and J. M. Brady, "SUSAN a new approach to low level image processing," *Intl. Journal of Computer Vision*, 23(1):45-78. May 1997.
- [22]. I. Sobel, and G. Feldman, "A 3x3 isotropic gradient operator for image processing, presented at a talk at the Stanford Artificial Project," in *Pattern Classification and Scene Analysis*, R. Duda and P. Hart, Eds., pp. 271-272, John Wiley & Sons, 1968.
- [23]. T. Kumar and G. Sahoo, "A Novel Method of Edge Detection using Cellular Automata" *International Journal of Computer Applications* 9(4):38-44, November 2010.
- [24]. W. Gao, L. Yang, X. Zhang and H. Liu, "An Improved Sobel Edge Detection," *IEEE international conference on computer science and information technology (ICCSIT)*, vol. 5, 67-71, 2010.
- [25]. T. William, "Logging, Bioinformatics and Computational Biology in Drug Discovery and Development," Cambridge University Press, 2016
- [26]. S. Zhu, "Edge Detection Based on Multi -structure Elements Morphology and Image Fusion," *ICIE, IEEE 2nd International Conference* Vol. 2, 2011.